Flinders University

College of Medicine

Understanding the Mechanisms Underlying Cardiac Fibrillation: Insights from Computational Approaches for Studying Re-entrant Circuits in Atrial and Ventricular Fibrillation

Author:

I Gusti Ayu Agung Dhani Dharmaprani

Supervisor:

Associate Prof. Anand Ganesan

Co-Supervisor:

Prof. Andrew McGavigan

Co-Supervisor:

Associate Prof. Kenneth Pope

A thesis submitted for the degree of

Doctor of Philosophy

April 20, 2020

Abstract

Cardiac fibrillation is characterised by aperiodic turbulence of wave propagation. This can occur in the atria, known as atrial fibrillation (AF), or the ventricles, constituting ventricular fibrillation (VF). Despite over 100 years of research, the mechanisms by which these arrhythmias are maintained unfortunately remain incompletely understood, but are of great significance as AF is the most common cardiac arrhythmia in humans, and VF the leading cause of sudden death in the world.

Although the atria and ventricles possess vastly different geometries, ionic mechanisms and global structures, they share similar electrical wave propagation dynamics. A defining characteristic of both AF and VF is the presence of re-entrant circuits that appear during ongoing fibrillation. This has led many to believe that these rotational phenomena play a key role in perpetuating cardiac fibrillation. With this in mind, the primary goal of this research is to investigate the nature of re-entrant events to gain insights into their role in perpetuating cardiac fibrillation, and to explore new avenues for possible treatments.

Chapters 3 and ***4*** begin by investigating the spatial and temporal stability of re-entrant circuits. It is hypothesised that these sites can be used to create a targeted ablation strategy to treat AF, wherein focal burns are applied at, or in the vicinity of, stable and dominant re-entrant circuits (rotors). Targeting these sites is hoped to result in AF termination or modification. Keeping in line with this thinking, chapter 3 investigates the spatiotemporal stability of rotors using an entropy-based mapping approach to determine whether targeted-ablation strategies may be feasible. It was found, however, that there was only a relative stability of the highest 10% of entropy regions, and that an overarching dynamic global instability was present.

Due to the intrinsic instability of re-entrant circuits implied by the findings of the entropy study in chapter 4, the focus of the PhD subsequently moved towards understanding the origin of this instability. The presence of unstable reentrant circuits in fact echoes much of the findings of many independent AF and VF studies conducted thus far. Consequently, ***Chapters 5-9*** aim to collectively understand the unstable nature of reentrant circuits using a branch of mathematics known as stochastic process theory. Specifically, these chapters aim to develop quantitative statistical approaches for understanding the consistently observed, yet unexplained, unstable behaviour of re-entrant circuits plaguing the field for over a century. Collectively, these chapters suggest that cardiac fibrillation should perhaps be redefined as an arrhythmia not governed by singular, autonomous drivers, but instead by the continuous regeneration cycle of phase singularity birth and death.

Thesis Declaration

I certify that this thesis does not incorporate without acknowledgement any material previously submitted for a degree or diploma in any university; and that to the best of my knowledge and belief it does not contain any material previously published or written by another person except where due reference is made in the text.

Dhani Dharmaprani (18/12/19)

Acknowledgements

I would like to thank the many people who have provided me with support and guidance throughout the course of my candidature. First and foremost, a tremendous thank you to my supervisor A. Prof Anand Ganesan, who provided me continuous mentorship, direction and support. His unique clinical insights and original ideas serve as a constant source of inspiration. A thank you also to my co-supervisor Prof. Andrew McGavigan who has always very kindly provided an immense amount of support, insight and a wealth of experience through the entirety of my PhD. Thank you also to my secondary co-supervisor A. Prof Kenneth Pope, who has not only been a source of support through my candidature, but also throughout my academic career thus far.

I would also like to extend a sincere thank you to all of our research collaborators and those who have provided their assistance, insight and support. Thank you to Prof. Stanley Nattel, Martin Aguilar and Dr. Feng Xiong for providing me with optical mapping data of rat AF and for the kind advice and support. Thank you also to Dr. Pawel Kuklik for kindly providing his insights, and to him along with Dr. Christian Meyers and Prof. Stephan Willems for kindly providing me with a subset of the human AF basket recordings. Thank you to Dr. Fadi Akar and Dr. Benjamin Strauss for providing the optically mapped rat VF data, and to Prof. Richard Clayton and Prof. Martin Nash for providing the unique epicardial sock recordings of human VF.

I am also beyond blessed for the unwavering support of my family and loved ones. A thank you to my mother and father Kencana and Darmawan for always being a huge source of inspiration and for always doing everything in their power to support my education. A thank you to my sisters and brother Dyah, Cintya and Dipta for being a source of joy and laughter. And finally, thank you to my wonderful partner Justin for his unwavering support, encouragement and love. Thank you for constantly believing in me.

Publications and communications to learned societies

Chapter 3: Part I. Literature Review: An Overview of Information Theory

- **Published manuscript:** Dharmaprani, D., Dykes, L., McGavigan, A.D., Kuklik, P., Pope, K. and Ganesan, A.N., 2018. Information theory and atrial fibrillation (AF): a review. Frontiers in physiology, 9.

Chapter 4: Investigating the spatiotemporal characteristics of re-entrant circuits

- **Published manuscript:** Dharmaprani, D., McGavigan, A.D., Chapman, D., Kutlieh, R., Thanigaimani, S., Dykes, L., Kalman, J., Sanders, P., Pope, K., Kuklik, P. and Ganesan, A.N., 2019. Temporal stability and specificity of high bipolar electrogram entropy regions in sustained atrial fibrillation: Implications for mapping. Journal of electrocardiology, 53, pp.18-27.
- **Presentation:** Presented at the Heart Rhythm Society (HRS) annual scientific meeting, May 2018, Boston, USA.
- **Presentation:** Presented for the Heart Rhythm Prize Award at the Cardiac Society of Australia and New Zealand (CSANZ) annual scientific meeting, August 2018, Brisbane, Australia.
- **Presentation:** Presented for the Young Investigator of the Year Award at the Asia Pacific Heart Rhythm Society (APHRS) annual scientific meeting, October 2018, Taipei, Taiwan.

Chapter 6: A universal framework to characterise the continuous regeneration of phase singularities

- **Published manuscript:** Dharmaprani, D., Schopp, M., Kuklik, P., Chapman, D., Lahiri, A., Dykes, L., Xiong, F., Aguilar, M., Strauss, B., Mitchell, L., Pope, K., Meyer, C., Willems, S., Akar, F.G, Nattel, S., McGavigan, A.D, Ganesan, A.N., 2019. Renewal theory provides a universal quantitative framework to characterise the continuous regeneration of phase singularities in cardiac fibrillation. bioRxiv, p.599142.
- **Presentation:** Presented at the Heart Rhythm Society (HRS) annual scientific meeting, May 2019, San Francisco, USA.

- **Presentation:** Presented at the Computing in Cardiology (CinC) annual scientific meeting, September 2019, Singapore, Singapore.
- **Presentation:** Presented for the Asia Pacific Heart Rhythm Society (APHRS) Young Investigator Award, October 2019, Bangkok, Thailand.
- **Presentation:** Presented for the Australian Physiology Society (AuPS), December 2019, Canberra, Australia.

Chapter 7: Investigating the temporal stability of phase singularity formation and destruction processes

- **Submitted manuscript:** Dharmaprani, Dharmaprani, D., Schopp, M., Kuklik, P., Chapman, D., Lahiri, A., Dykes, L., Mitchell, L., Pope, K., Meyer, Nattel, S., McGavigan, A.D, Ganesan, A.N., 2019, Atrial fibrillation phase singularity formation and destruction are stationary processes that are stable in the time domain.

MANUSCRIPTS IN PREPARATION

Chapter 8: Self-regeneration of atrial fibrillation can be summarised and predicted using a Markov birth-death framework

- **Manuscript (to be submitted Dec 2019):** Dharmaprani, Dharmaprani, D., Schopp, M., Kuklik, P., Chapman, D., Lahiri, A., Dykes, L., Mitchell, L., Pope, K., Meyer, Nattel, S., McGavigan, A.D, Ganesan, A.N., 2019, Markov-chain processes explain the perpetuation of atrial fibrillation via a regenerative cycle of phase singularity birth and death.

Chapter 9: Phase singularity formation and destruction processes in cardiac fibrillation are scale-dependent

- **Manuscript (to be submitted Dec 2019):** Dharmaprani, Dharmaprani, D., Schopp, M., Kuklik, P., Chapman, D., Lahiri, A., Dykes, L., Mitchell, L., Pope, K., Meyer, Nattel, S., McGavigan, A.D, Ganesan, A.N., 2019, Phase singularity birth-death processes in cardiac fibrillation are scale-dependent.

Prizes and Awards During Candidature

- Winner of Cardiac Society of Australia and New Zealand (CSANZ) Heart Rhythm Prize (2018, Australia)
- Winner of the Asia Pacific Heart Rhythm Society (APHRS) Young Investigator Award (2018, Taiwan)
- Finalist for the Cardiac Electrophysiology Society (CEPS) Young Investigator Award (2019, United States)
- Heart Rhythm Society Travel Grant 2019
- Hospital Research Travel Grant 2019
- Flinders University Travel Grant 2019
- Finalist for the Flinders University 3-minute thesis competition (2019, Australia)
- Finalist for the Asia Pacific Heart Rhythm Society (APHRS) Young Investigator Award (2019, Thailand)
- Flinders University College of Medicine Publication Prize (2019, Australia)
- Tom Simpson Trust Fund Equipment Grant from The National Heart Foundation of Australia (2020, Australia)

Contents

List of Figures

List of Tables

List of abbreviations

- AF: Atrial Fibrillation
- AP: Action Potential
- ApEn: Approximate Entropy
- BDP: Birth-death process
- CFAE: Complex Fractionated Electrograms
- DF: Dominant Frequency
- ECG: Electrocardiogram
- EGM: Electrogram
- En: Entropy
- EP: Electrophysiology
- MaxEnt: Maximum Entropy
- PS: Phase Singularity
- FFT: Fast Fourier Transform
- LA: Left Atrium
- RA: Right Atrium
- SampEn: Sample Entropy
- ShEn: Shannon Entropy
- VF: Ventricular Fibrillation

Chapter 1

Introduction

1.1 Motivation

The human heart is responsible for the mechanical job of pumping blood throughout the body, and although it is tasked with a single and seemingly straightforward duty, the rhythmic contraction that causes this pumping emerges from an elegant interplay between individual cells. In some cases, this interplay becomes compromised, and this can manifest as heart rhythm disorders known as arrhythmias. Arrhythmias exist in many forms, with perhaps one of the most notable examples being cardiac fibrillation. This condition, which is generally characterised by aperiodic turbulence of wave propagation [96, 171, 214], results in an irregular heart rhythm and exists in two forms depending on whether the atria or ventricles are affected: atrial fibrillation (AF) and ventricular fibrillation (VF).

AF is the more common of the two disorders, and is in fact the most prevalent cardiac rhythm disorder in the world [148]. The condition causes symptoms including palpitations, fatigue, chest discomfort, light-headedness and dyspnoea [54, 148, 214]. While these symptoms themselves may not be life-threatening, the downstream consequences of AF are much more severe, ranging from stroke [268], dementia [189], heart failure [255] and a doubled mortality rate for those affected [28, 52]. In Australia alone, AF affects over 350,000 Australians, and has emerged by 2019 to be the leading cause of cardiac hospitalisation. Coupled with the fact that the prevalence of AF increases with age, presenting in almost 9% of those aged 80-89 [122], this figure is predicted to double or triple within the next few decades due to the ever increasing aging population [214]. In fact, Australia has seen a relative increase of 295% for AF hospitalisations over the last 20 years, signifying a doubling of hospitalisations since the beginning of the century and an annual increase of 5.2% in AF hospitalisations [82]. Further exacerbating the AF burden is the economic strain placed on the health-care system, which is estimated at AU$ 1.25 billion per annum.

On the other hand, VF is the world's leading cause of sudden death, surpassing stroke, cancer and myocardial infarction [26]. When it occurs, incoordinate-type contractions arise which, despite producing a high metabolic rate of the myocardium, do not produce useful beats and hence results in no cardiac output [260]. Without adequate treatment, VF can lead to death within minutes [49]. Fewer studies have investigated the epidemiology of VF in Australia, however, it estimated to be responsible for the majority of the 25,000 sudden deaths that occur nationally per annum [26].

While the atria and ventricles possess vastly different geometries, ionic mechanisms and global structures, they share similar electrical wave propagation dynamics [192], and chaotic electrical wave turbulence characterises both atrial and ventricular fibrillation. Research aiming to understand the mechanisms underlying this chaotic electrical activity has increased exponentially over the last 100 years but unfortunately, this subject remains incompletely understood [116, 214]. This potentially underpins the difficulty of developing effective and reproducible strategies for the treatment of AF and VF. Showcasing this is the recent NIH-funded CABANA trial, which compared anti-arrhythmic drug therapy to catheter-based ablation of AF. Findings showed that less than 50% of patients demonstrated 4 year freedom from persistent AF for both drug and ablation therapy [190]. Few new AF treatments have also emerged in the past decade, with no new drugs approved in Australia since 2002. In the context of VF, defibrillation remains the only definitive treatment, but achieves low-success rates in out-of-hospital settings [75].

These failures may, at least partly, be attributed to a fundamental incongruity between treatment strategy and mechanism. Multiple hypotheses exist concerning the primary mechanism responsible for AF and VF, but this remains a topic of contention [254]. In several of these theories, a common theme is the presence of re-entrant circuits: spinning cyclone-like vortices of electricity that move in a rotational fashion. Re-entrant circuits are postulated to randomly excite the myocardium, resulting in fibrillation. Such re-entrant electrical circuits have been observed since early work by Mines [161] and Garrey [89] in 1914, and have since remained a consistent observation in mapping studies, both experimental models and in humans, as well as in computational models of AF and VF. Given the consistent observation of re-entrant circuits during fibrillation, the preliminary goal of this research is to investigate the nature of these re-entrant events to gain insights into the mechanisms responsible for cardiac fibrillation, and avenues for possible treatments.

In Part I (chapters 3-4), the spatiotemporal stability of re-entrant circuits is investigated, to determine whether targeted-ablation strategies may be feasible. This work stems from the hypothesis that localised re-entrant circuits drive and maintain cardiac fibrillation in an autonomous fashion, hence targeting these regions in a 'point-and-shoot' approach may lead to termination. Towards this goal, I investigate entropy-based mapping, and apply this strategy to determine the spatial and temporal stability of re-entrant circuits in atrial fibrillation episodes acquired from a fibrillation-type computer simulation model, an ovine model of sustained AF, and human persistent

AF patients [69].

Due to the intrinsic instability of re-entrant circuits implied by the findings of the entropy study in Part I, the focus of the PhD subsequently moved towards understanding the origin of this instability. Specifically, in Part II (chapters 5-9) I explore the formation and destruction processes of re-entrant circuits using various stochastic process theory approaches to better understand how these circuits are generated. This framework was applied to a computer simulation model, rat AF and VF, ovine sustained AF, and human persistent AF patients [70]. Using this framework, I further explore the temporal stability of the rate of formation and destruction of re-entrant circuits, and deduce that despite the apparent superficial randomness of fibrillation, the underlying dynamics are robustly stable and can be accurately summarised from short-duration recordings. Additionally, I explore how the formation and destruction of these re-entrant events can be summarised, understood and even predicted using a compact, Markov chain birth-death framework, and use this to explain the contribution of re-entrant circuit regeneration in the perpetuation of fibrillation. In the final chapter, I demonstrate that these birth-death processes during cardiac fibrillation are scale-dependent, enabling translation of these findings to both mechanistic and clinical mapping.

Collectively, these chapters aim to use computational approaches to develop gain insights into the consistently observed, yet unexplained, unstable behaviour of re-entrant circuits plaguing the field for over a century.

1.2 Aims of the thesis

This thesis aims to obtain insights into the potential mechanisms underlying persistent atrial fibrillation (AF) and ventricular fibrillation (VF) through:

- Understanding the temporal and spatial characteristics of re-entrant circuits using Entropy-based mapping of re-entrant circuits in long duration human, sheep and computer simulated persistent AF
- Development of a universal quantitative framework to measure the process of re-entrant circuit formation and destruction of in AF and VF
- Investigating the temporal characteristics of re-entrant circuit formation and destruction processes
- Investigating whether the formation and destruction of re-entrant circuits can be summarised, understood and predicted using a compact birth-death Markov chain framework
- Investigating whether re-entrant circuit formation and destruction is a scale-dependent process governed by the field of view of mapping

- Investigating whether the formation and destruction rates of re-entrant circuits can predict the likelihood of spontaneous AF termination

1.3 Structure of the thesis

Fundamental basic, clinical and technical background

Chapter 1 provides an introduction and establishes the motivation behind this thesis.

Chapter 2 provides an overview of cardiac anatomy and electrophysiology, the theorised mechanisms of AF and VF, approaches for AF/VF mapping and currently available treatments.

Part I: Investigates the spatiotemporal characteristics of re-entrant circuits using entropy-based mapping

Chapter 3 provides a literature review about current AF analysis approaches, AF mapping and information theoretic measures of entropy and its applications in cardiology.

Chapter 4 details the results from mapping re-entrant circuits in long duration AF using entropy, in addition to the temporal stability and specificity of high entropy regions.

Part II: Investigates the formation and destruction of re-entrant circuits using stochastic process theory

Chapter 5 provides a literature review about probability and stochastic process theory, and its application in cardiac electrophysiology.

Chapter 6 details the development of a universal quantitative framework to characterise the regeneration of re-entrant circuits in cardiac fibrillation.

Chapter 7 details an investigation into the temporal stability of re-entrant circuit formation and destruction processes.

Chapter 8 investigates whether a Markov birth-death processes can be used to summarise, understand and predict fibrillatory behaviour and spontaneous AF termination.

Chapter 9 investigates whether phase singularity formation and destruction processes are scale-dependent.

Part III: Summary, concluding remarks and supplementary material

Chapter 10 provides a summary about the body of work outlined in this dissertation, and discusses future direction for research.

Supplementary Results and Materials provides supplementary material for the research outlined in this dissertation.

Part IV: Additional publications during candidature

Additional publications during candidature includes additional publications published during candidature that are not included in this dissertation.

Chapter 2

Basic Foundations

2.1 Cardiac Anatomy and Electrophysiology

2.1.1 The Anatomy of the heart

The human heart is a vital organ in the circulatory system, situated in the middle of the thoracic cavity. The heart itself is enclosed by a membranous and double-layered pericardial sac, which comprises of a tough and fibrous layer and a secretory lining. The fibrous outer layer helps to anchor the heart and maintain its position within the chest by attaching itself to the connective tissue separating the lungs. The second secretory lining discharges pericardial fluid to provide lubrication and prevent friction within the pericardial layers during the beating action of the heart [111, 221].

Functionally, the heart can be thought of as a 'dual pump', with the left and right sides of the heart behaving as separate pumps [221]. The organ comprises of four chambers, namely an upper left and right atria, and lower left and right ventricles. A wall of tissue called the interatrial septum separates the left and right chambers of the atria, allowing the right atrium (RA) to receive deoxygenated blood returning from the inferior and superior vena cavae, while the left atrium (LA) receives oxygenated blood from the pulmonary veins. The atrial wall itself is composed of three layers that include connective tissue, endothelium and cardiac muscle. These layers are known as the outer epicardium, the middle myocardium and inner endocardium [226, 259].

In comparison, the ventricles are situated on the lower portion of the heart, as shown in Figure 2.1, and pump blood to the rest of the body. The right ventricle (RV) receives blood passing through the tricuspid valve from the right atrium, and pumps it to the pulmonary artery through the pulmonary valves upon ventricular contraction. From here, the pulmonary artery extends from the right ventricle, branching off into the left and right pulmonary arteries. The left ventricle

(LV) works in a similar fashion but receives blood passing from the left atrium through the mitral valve. As the ventricles contract, blood in the left ventricle is pumped to the aorta through the aortic valve, distributing oxygenated blood throughout the body. Like the atria, the ventricles are separated into left and right chambers by the septum, and comprise of the same three-layered heart wall. Unlike the atria however, the middle myocardial layer found in the ventricles is much thicker, allowing the ventricles to generate the necessary force needed to pump the blood out of the heart chambers and to the rest of the body. The ventricle walls also consists of papillary muscles, which attach to the atrioventricular valves to control their opening and closure [226, 259].

In a typically functioning heart, these chambers work harmoniously to deliver blood to the lungs and various organs in the body, with the left and right ventricles being primarily responsible for this pumping action. In comparison, the atria play an important role in directing blood flow through the heart during the different phases of a normal cardiac cycle [25, 221].

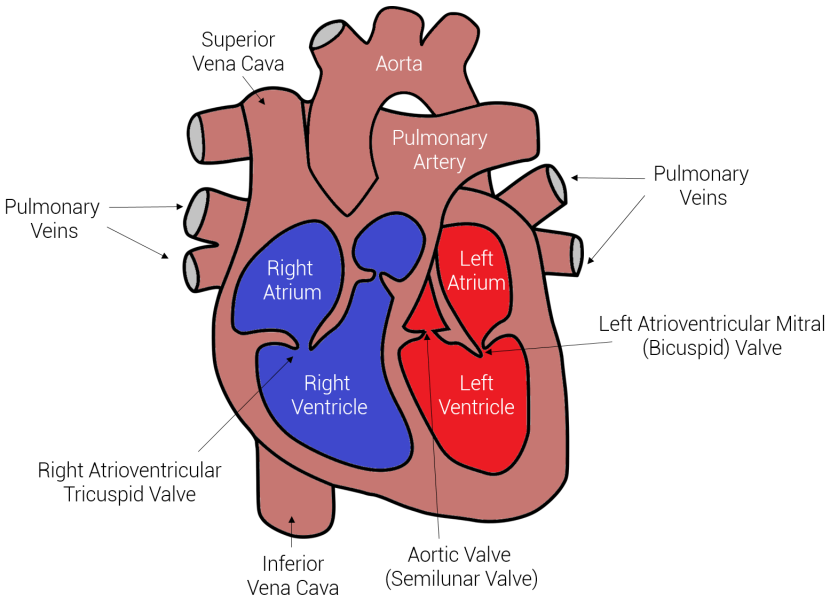

Figure 2.1: Anatomy of the human heart

2.1.2 Basic Cardiac Electrophysiology

Under normal function, the atria and ventricles contract with coordinated rhythmicity, allowing blood to be ejected effectively to various organs and around the body [221]. Specialised cardiac cells help this contractile motion to occur, and there are two types of such cells found in cardiac tissue. Namely, these cells are: i) contractile cells and ii) autorhythmic cells, with the latter being primarily responsible for electrical conduction throughout the heart. While contractile cells account for 99% of cardiac muscle cells, they normally do not initiate their own action potentials and are responsible for the mechanical work of pumping. In comparison, autorhythmic cells do not contract but are specialised for conducting and initiating the action potentials that cause

contraction of the working contractile cells [220]. The self-generated action potentials initiated by the autorhythmic cells consequently allows the heart to generate its own rhythm, a property known as autorhythmicity [121].

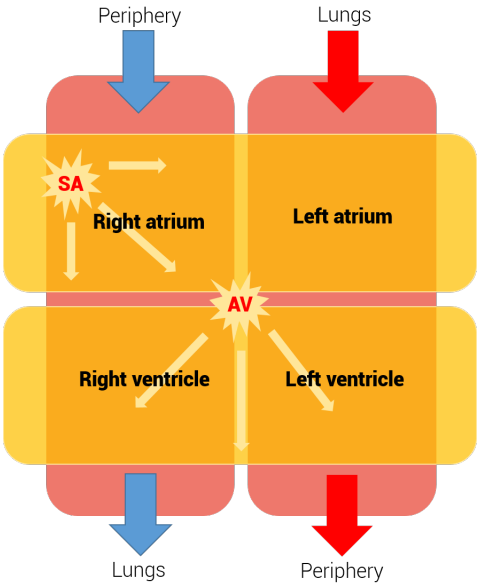

Figure 2.2: Schematic of electrical activity throughout the heart

Electrical activity is typically initiated in the atria by the sinoatrial (SA) node, and transmitted to the ventricles through the atrioventricular (AV) node.

Unlike contractile cells that can be found more prevalently in the heart, autorhythmic cells are found at specific sites. These electrically excitable sites allow action potentials, which provide electrical activation, to propagate along a specialised pathway, resulting in coordinated contraction of the heart muscle [121]. These electrically excitable regions include the sinoatrial node (SA node), the atrioventricular node (AV node), the bundle of His (atrioventricular bundle) and Purkinje Fibres [221].

It can be noted that the rates at which various autorhythmic cells generate action potentials differ, as these cells have varied rates of slow depolarisation to threshold. The SA node, a small specialised region located in the upper lateral wall of the right atrium, possesses the heart cells with the fastest rate of action potential initiation, and hence, the fastest rate of autorhythmicity. Consequently, other autorhythmic tissues are activated by action potentials propagating from the SA node before they can reach their own slower pace and hence, the heart subsequently beats at the pace set by the SA node (this typically ranges from 70-80 beats per minute). It is because of this that the SA node is termed the 'pacemaker' of the heart [221] (Figure 2.2).

As such, under normal physiologic rhythm, also known as sinus rhythm, the action potentials initiated in the SA node generate electrical impulses that pass to the atrio-ventricular (AV) node through the conductive atrial tissue. As the atria and ventricles are isolated from one another

due to the fibrous AV valves, the AV node is the only physiological pathway that allows electrical conduction to flow between them. Once electrical activation reaches the AV node, a specialised tissue called the His-Purkinje system, otherwise known as the His-bundle, spreads out in a web-like fashion throughout the ventricles to allow the ventricular muscle to become electrically activated and contract. Consequently, the ventricles are coordinated to contact synchronously to maximise the expulsion of blood from the heart and to the rest of the body [25] (Figure 2.2).

2.1.3 The Action Potential

The cardiac action potential describes the electrical activity within the heart's cardiac cells, known as cardiomyocytes. This arises from the flow of ions through membrane-bound proteins know as ion channels. These ion channels form the basis of cardiac electrical excitability. Due to changes in the electrical potential across the membrane, ion channels will open to allow ions in or out of the cell along their electrochemical gradients [221]. The flow of charged ions produces an electrical current, altering the membrane potential towards the equilibrium potential E, which represents the potential at which the electrochemical gradient for that ion species becomes zero. Different ionic species will possess different equilibrium potentials, given mathematically by the Nernst equation [270] (equation 2.1):

$$E_{ion} = \frac{RT}{zF} \ln \frac{[ion]_{internal}}{[ion]_{external}} \tag{2.1}$$

where E_{ion} is the equilibrium potential for the ion species, R is the universal gas constant, T the temperature in kelvins, z the ionic charge, F Faraday's constant and $[ion]$ the ionic concentration. The Nernst equation gives the electric potential whereby the flow of ions across a cell membrane, permeable to only a single ion, changes or reverses in direction. As such, it is also oftentimes referred to as the reversal potential [270].

In reality, however, cardiomyocytes possess several various ion channels, and therefore the true equilibrium potential will result from a balance between all the concentration and electrical gradients of individual ions. For monovalent ions, this is described by the Goldman-Hodgkin-Katz (GHK) equation [173] (equation 2.2):

$$V_m = \frac{RT}{F} \ln\left(\frac{\sum P_i[ion_i^+]_{internal} + \sum P_i[ion_i^-]_{internal}}{\sum P_i[ion_i^+]_{external} + \sum P_i[ion_i^-]_{external}}\right) \tag{2.2}$$

where V_m is the equilibrium membrane potential and P_i the permeability of positively charged ions (cations) or negatively charged ions (anions). To predict the equilibrium potential with consideration to the presence of divalent ions (e.g. Ca^{2+}), higher order equations can be used, however, due to the low resting permeability of these ions their contributions are usually considered negligible. Solving the GHK equation using experimental values for permeability and concentration

will accurately predict the resting membrane potential of cardiomyocytes, which is approximately -90mV.

At resting potential, if the membrane potential is significantly perturbed above a threshold of approximately -60mV, depolarization will occur. This occurs due to rapid opening of the sodium Na^+ channels, which allows sodium ions to flow into the intracellular space. In turn, this simultaneously leads to an increase in the membrane potential [116]. The change in the transmembrane voltage triggers calcium Ca^{2+} and potassium K^+ channels to open, leading to a decrease in the transmembrane voltage. The inflow of calcium into the intracellular cells is a unique feature of myocardial cells, and allows delayed repolarisation to occur, indicated by the plateau in Figure 2.3. This phase is referred to as the absolute refractory period, and during this phase, the cell becomes unexcitable until the transmembrane voltage decreases to approximately -20mV. As more K^+ enters the cell, the transmembrane voltage continues to decrease and the action potential reaches the relative refractory period, whereby the cell is excitable again but is inhibited. When the cell reaches resting potential once again, ionic concentrations and distributions are completely recovered [116] (Figure 2.3).

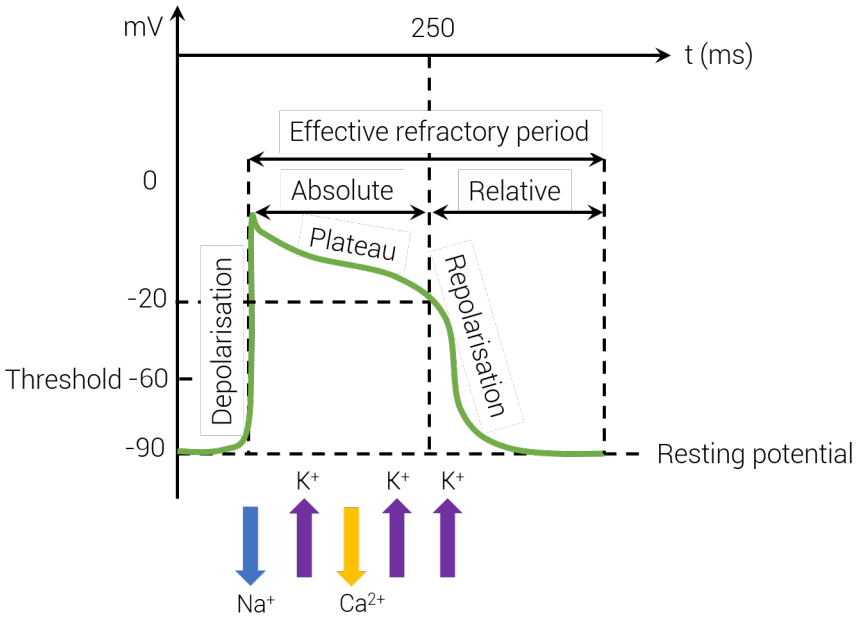

Figure 2.3: Action potential of the human myocardium. Adapted from [Malmivuo,1995]

2.1.4 Atrial Fibrillation

Atrial fibrillation (AF) is the world's most prevalent arrhythmia. When an individual suffers from atrial fibrillation, the rhythmic sequence of electrical conduction is disturbed and as such, synchronous ventricular contraction is not achieved. In addition, the frequency of atrial activation increases drastically in comparison to normal sinus rhythm, rising from 1-2Hz (60-120 beats per minute) to 6-10 Hz. Activation in various parts of the chamber also becomes spatially asynchronous,

which in turn causes uncoordinated and irregular contraction of the atria. Although the AV node acts as somewhat of a low-pass filter, stopping high-frequency atrial impulses from propagating to the ventricles, ventricular rate can increase up to 140-180 beat/min during AF. This increased ventricular rate is stipulated to be the cause of most AF-related symptoms including chest pain, palpitations and cardiomyopathy. An increased risk of stroke is also thought to be caused by stasis of blood within the atrium [25].

Individuals with AF typically seek medical attention to treat symptoms associated with the arrhythmia [214]. Common clinical manifestations of such symptoms include palpitations, fatigue, chest discomfort, light-headedness and dyspnoea [54, 148, 214]. While these symptoms may not be life-threatening, the downstream consequences of AF are much more serious, including an increased risk of stroke [267], dementia [189] [189], heart failure [255] and mortality rate for those affected [28, 52]. In fact, AF triggers 20-25% of all strokes, and these are more severe compared to those of other origins [162]. Additionally, the presence of AF alone increases the likelihood of stroke five-fold, marginally larger than other risk factors such as coronary heart disease and hypertension, which increase the risk of stroke by only two and three fold respectively [267]. The prognosis of individuals with heart failure and acute myocardial infarction is also worsened by the presence of AF [28, 176].

Clinically, atrial fibrillation is classified into different phenotypes using an internationally recognised nomenclature [125]. Specifically, AF can be classified as:

- **Paroxysmal atrial fibrillation (PAF)** typically self-terminating in most cases within 48 hours. Also describes AF episodes that terminate spontaneously or with intervention (pharmacological or electrical cardioversion) in less than 7 days.
- **Persistent atrial fibrillation (PersAF)**: atrial fibrillation that typically sustains for more than 7 days and does not spontaneously terminate, but can be terminated with pharmacological therapy or with direct-current cardioversion. After cardioversion, sinus rhythm can sustain for several days to months.
- **Long standing persistent**: atrial fibrillation that persists for over a year, and may or may not be terminated by pharmacological therapy or electrical cardioversion.
- **Chronic or permanent atrial fibrillation**: atrial fibrillation that does not terminate with both electrical and pharmacological cardioversion.

It is theorised that atrial fibrillation is caused by the interaction between initiating trigger and the underlying atrial substrate. An initiating trigger may include rapid focal discharges from the pulmonary veins, or an extrasystole. On the other hand, atrial substrate can refer to structural or electrical characteristics. The AF phenotype classifications as listed above are thought to be influenced differently by triggers and substrate (2.4). Paroxysmal AF is thought to be mainly

trigger-based, arising often from ectopic foci in the pulmonary veins, whilst persistent AF is thought to be the result of a complex interplay of triggers and the underlying substrate. Consequently, the mechanisms underlying the more persistent forms of AF are less well understood [272].

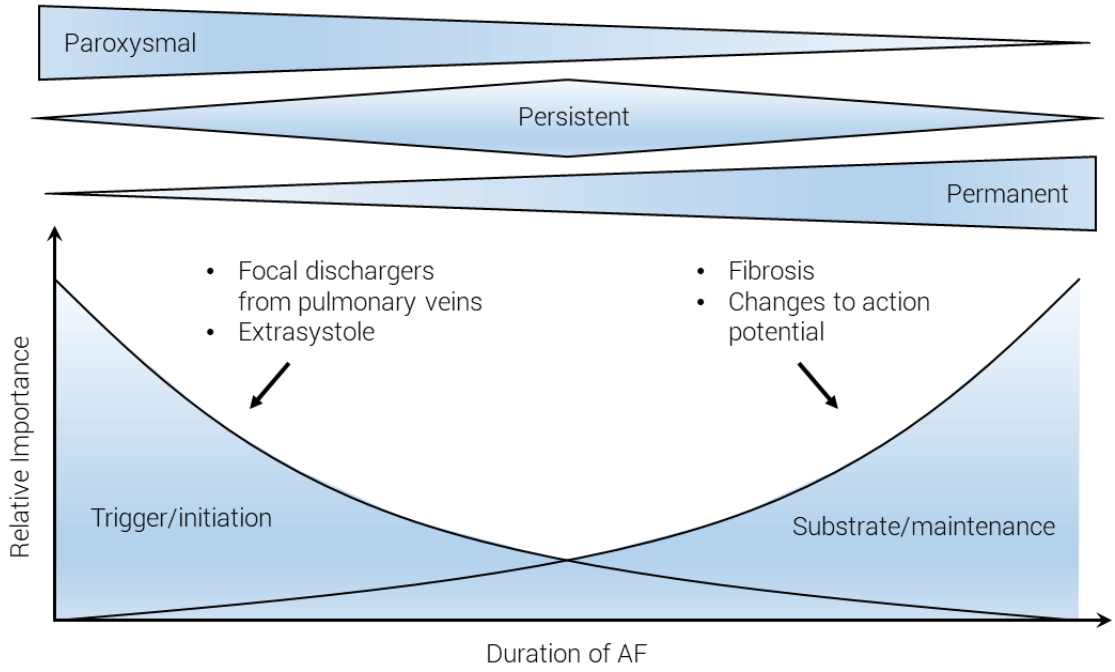

Figure 2.4: The influence of trigger vs substrate on AF phenotypes. Adapted from [Wyse,2004]

2.1.5 Ventricular Fibrillation

Ventricular fibrillation (VF) is the most common cause of sudden death in the world, and is characterised by high and uncoordinated depolarisations typically occurring at > 550 excitations per minute [115]. As a result, the ventricles do not contract effectively and fail to pump blood into the pulmonary and systemic circulation system, which can cause death within minutes [260]. Typically, VF will occur as ventricular tachycardia (VT) deteriorates, whereby VT is a more organised arrhythmia characterised by high but regular excitation and contraction rates (> 100/min). VF can result from the following [152]:

Impulse conduction:

- Functional and anatomical re-entrant circuit(s) can encourage VF to sustain

Abnormal impulse formation:

- Ectopic foci or extrasystoles can arise when after-depolarization, both early and late, overcome the refractory threshold
- Purkinje cells around ischemic areas during an MI can increase automaticity and initiate VT, leading to VF

VF typically manifests as sudden collapse, usually due to cardiac arrest, which eventually leads to sudden cardiac death (SCD). Patients may also demonstrate signs of acute myocardial infarction such as chest pain, vomiting, nausea and shortness of breath prior to the event. If patients have a known history of congestive heart failure or coronary artery disease, they may show a worsening of chronic symptoms such as dyspnea, orthopnea, angina and pedal edema. Often patients will be unresponsive, unconscious and have no palpable pulse at the time of presentation [152].

Epidemiological studies of VF in Australia are few, however, it is estimated that VF is responsible for the majority of SCDs that occur [26]. As of 2015, the overall incidence rate of SCD in Australia was 99.4 per 100,000 [269], and VF is thought to account for the majority of the 25,000 SCDs that happen nationally per annum. However, it is likely this number is an underestimate as the true incidence rate of VF is not well reported.

Like atrial fibrillation, various substrate are thought to promote the occurrence of ventricular fibrillation. VF is often associated with an acute myocardial infarction (MI), with 3-12% of cases of MI developing VF [91]. Another 5% will also develop VF or VT within 48 hours of an MI [6]. VF can also come about due to other ischemic conditions (e.g. sub-acute ischemia or from cellular abnormalities) within a scar border zone from the healed MI. Other forms of myocardial damage such as progressive heart failure or channelopathies (e.g. Brugada and long QT syndrome) can also favour VF. Such substrates can lead to alterations to the electrophysiological properties of the cardiac cells (myocytes), leading to changes in the action potential dynamics [114].

Acid base disturbances as well as electrolyte disturbances, such as hyperkalaemia and hypokalaemia, are also thought to increase the risk of ventricular fibrillation. Other homeostatic disturbances such as hypo/hyperthermia, hypo/hypervolemia and hypoxia are also thought to increase the risk of developing VF [114].

2.2 Theorised Mechanisms Underlying Atrial and Ventricular Fibrillation

Cardiac fibrillation is a phenomena that has been observed since ancient times. In 1543, Andreas Vesalius published his classical anatomy book titled 'De Humani Corporis Fabrica', which noted 'worm-like' movements that occurred in the hearts of animals just prior to their death [2]. Since then, debate has ensued about the precise mechanism responsible for cardiac fibrillation, and although this has been intensely investigated, these mechanisms remain elusive to this day. This is stark contrast to many other arrhythmias, such as AV nodal tachycardia, for which well-defined mechanisms have been identified and can be safely targeted with fairly high rates of success [254]. While the atria and ventricles possess vastly different geometries, ionic mechanisms and global structures, they share similar electrical wave propagation dynamics [192] and as such AF and VF

share many of the same theorised mechanisms.

Generally, it is thought that AF and VF may be perpetuated by either 'hierarchical' or 'anarchical' mechanisms, whereby hierarchical mechanisms describe fibrillation that is being driven by a rapid localised source, and anarchical mechanisms an arrhythmia that includes multiple, non-localised sources that act chaotically to sustain the arrhythmia.Whether the complex wave dynamics of fibrillation arise due to hierarchical versus anarchical mechanisms is a question that has remained unresolved for over a century. Below, I discuss some of these theorised mechanisms and their influence on the field.

2.2.1 Ectopic Foci

Ectopic foci classically describe a form of hierarchical mechanism constituting of rapidly firing focal sources of electrical activity (Figure 2.5A). These focal sources may either be a single focus with fibrillatory conduction, or multiple foci that discharge simultaneously. As myocardium remote from this source is not driven in a 1:1 fashion, irregular conduction will occur at lower frequencies. Such a theory is clinically attractive, as the ability to locate this source activity would allow targeted treatments such as AF ablation procedures [172]. Although ectopic foci are often thought of as a hierarchical mechanism, it is theorised that 'polytopic ectopy' in the form of disseminated focal charges may cause anarchical behaviour and also result in fibrillation. However, at this present time no convincing experiments have been reported to support this mechanism [214].

In the seminal study by Haïssaguerre et al., focal discharges emanating from the pulmonary veins (PV) were shown to initiate AF [102]. Catheter ablation to isolate the ectopic beats arising from the pulmonary veins can be achieved using a procedure known as pulmonary vein isolation (PVI), which has proven fairly effective for the paroxysmal AF populace [56, 102, 187]. Ectopic activity in the PVs is thought to occur due to cellular proarrhythmic mechanisms such as triggered activity, micro-reentry and automaticity, and it is hypothesised that this is due to the presence of abnormal myocytes [214]. However, there are divergent reports about the contribution of abnormal cell types on focal behaviour and the occurrence of these cells in the myocardial sleeves [107, 108, 158,214,247]. It has also been suggested that the relative contributions of these distinct mechanisms are likely varied amongst individual patients, which cannot be determined at the present time [102].

Although ectopic activity arising from the pulmonary veins seems to play an important role in paroxysmal AF, PVI procedures have unfortunately been less successful for cases of persistent AF [56, 184]. Underlying this may be the fact that separate mechanisms may be responsible for triggering and sustaining fibrillation, which is a line of thinking that has recently become more accepted. Further, it is postulated that as atrial fibrillation becomes more persistent, the interplay between these mechanisms likely evolves, and that the maintenance of fibrillation likely involves a separate mechanisms including some form of re-entry [254].

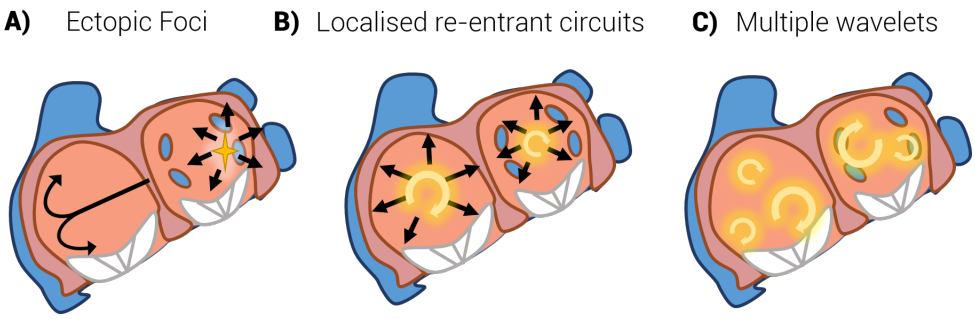

Figure 2.5: Classical theorised mechanisms of cardiac fibrillation. Adapted from [Nattel,2002]

2.2.2 Re-entrant activity

A recurring and consistent observation seen in both AF and VF are re-entrant circuits. Re-entrant activity was first noted by Garrey [89] and Mines [161] in the early 1900s, who noted that fibrillatory contractions organise themselves into 'vortex-like' rotating waves. By the 1950's it was generally agreed that these re-entrant circuits could occur and disrupt the ability of neighbouring tissue to conduct regularly, therefore giving rise to the chaotic appearance of fibrillation [115].

Generally speaking, a dissociation of refractoriness between different tissue zones is believed to result in re-entrant activity, and consequently generates abnormal impulse propagation that characterises fibrillation. The simplest model of re-entry is described by the leading circus model, first described by Allesie [14] (Figure 2.6). In this model, a unidirectional wavefront creates circus movement, leading to constant centripetal activation of the centre of the circuit rendering it continuously refractory. Consequently, this forms a functional barrier that is able to sustain re-entry in a similar vein to anatomical barriers such as scarring. The unidirectional block in tissue allows circus movement to be initiated in one direction, and the impulse simultaneously radiates outwards to activate neighbouring myocardium, and inwards towards the centre of the circuit. The wavelength of the circuit is a critical feature of this re-entry, given by the product of the tissue refractory period and the impulse conduction velocity. The smallest 'leading circle' circuit is one in which its path-length/circumference is equivalent to its wavelength, as anything smaller will mean the circulating wavefront will encounter refractory tissue and will therefore not sustain (2.6).

Special types of functional re-entry, known as rotors or spiral waves, are a modification of this leading circus movement originating from observations of chemical reactions in excitable media [263]. Instead of exhibiting a circular circuit, rotors have a curved or spiral wavefront (Figure 2.6). The wavefront meets the wavetail of the rotor at a point known as a phase singularity (PS). The wavefront velocity of the rotor is not constant unlike the leading circus model, due to the wavefront curvature governing the current source-sink mismatch, whereby the 'source' of a wavefront refers to the diffusion current generated by excited tissue tending to depolarise downstream cells, which acts like a 'sink' [214]. The area closest to the PS will have the slowest conduction velocity as it is also

the area with the highest curvature and in fact, the curvature is so high and conduction velocity so slow that the propagating wavefront is unable to excite the centre of the rotor, rendering this core effectively unexcitable. This creates an area of function block that is similar to the leading circus circuit [254].

The critical difference between these two models is their behaviour in space. A leading circus re-entrant circuit must remain fixed in space due to the centre of the circuit being completely unexcitable. However, a rotor is able to move through space due to the constant source-sink mismatch. Consequently, rotors under certain conditions can meander in complex trajectories and forms, which has important implications on its sustainability and behaviour [254].

Localised re-entrant circuits

Although re-entry seems to be a key feature of fibrillation, it is argued whether they perpetuate hierarchical or anarchical mechanisms as there has been support for both theories. In the former hypothesis it is believed that stable, localised rotors can act as driver sources. This theory is clinically attractive as localised re-entry can be targeted using ablation techniques to terminate the arrhythmia.

Mapping studies have demonstrated the presence of localised, organised and high frequency drivers during atrial fibrillation, thought to represent rotors (Figure 2.6B). The rotor model of fibrillation in these studies postulates that despite the disorderly and chaotic appearance of fibrillation, the arrhythmia is actually continuously being driven by the highly organised activity of a handful of high frequency re-entrant circuits. As a consequence, wavefronts are produced that eventually degenerate into chaotic activity [244].

Schuessler et al. demonstrated early evidence of such organised, high frequency drivers using a perfused canine right atrial model whereby AF was induced using various concentrations of acetylcholine (ACh). It was found that at lower concentrations of Ach, activation mapping revealed multiple re-entrant wavelets and circuits. At higher concentrations of ACh, the re-entrant circuits collapsed and formed a singular stable, high-frequency circuit that governed the resulting fibrillatory activity [217].

Evidence for high-frequency re-entrant activity has also been shown in a Langendorff-perfused sheep heart model using ACh. Bipolar mapping and optical fluorescence was used to sample fibrillatory activity at various left and right atrial sites. The Fast Fourier Transform (FFT) was used to determine the dominant frequency (DF) of local activation at each of the sites, and revealed an ordered gradient of stable DFs between the LA and RA [155]. Subsequent studies extended this approach to DF mapping in humans, and demonstrated DF gradients in paroxysmal AF. LA to RA DF gradients in patients with paroxysmal AF were eliminated with successful ablation [142]. However, these gradients were not present in persistent AF patients, again suggesting a difference in

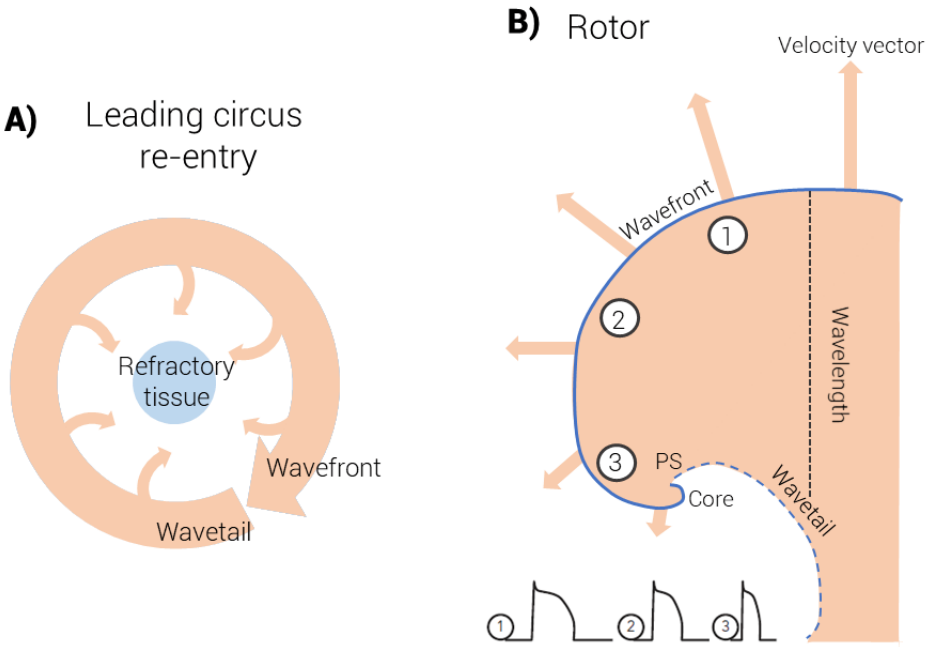

Figure 2.6: Models of re-entry: Leading circus model (left) and rotor model (right). Adapted from [Waks, 2014]

the mechanisms responsible for these varying AF phenotypes. Additionally, an important caveat of DF analysis is that although animal studies have correlated maximal DF sites to rotor-like activity, it is unclear whether all maximal DF sites are associated with rotors, especially in humans, or if they can also present other types of electrical activity [254].

Lastly, studies conducted by Narayan et al. have also supported the existence of a small number of rotors in relatively fixed spatial locations, which are thought to maintain the arrhythmia [169]. Although the original studies reported very high rates of success when ablating these regions, several subsequent studies have been unable to reproduce the initially reported outcomes, even using the same technology [227].

Multiple wavelet hypothesis

In 1959 Moe and Abildskov [163] proposed an alternative mechanism of fibrillation that extended on the concept of re-entry. Using a computer simulated model of AF based on simple assumptions about conduction velocity and refractoriness, Moe and Abildskov build on this in their 1964 study to show that re-entrant wavelets are able to travel through an excitable medium in a seemingly disorganised and chaotic pattern (Figure 2.5C) [165]. This is known as the 'multiple wavelet hypothesis'. The theory postulated that wavefronts continuously interact and result in wavebreak, leading to the generation of new wavefronts. Simultaneously, the blocking, collision and fusion of existing wavefronts will annihilate already existing wavelets. Therefore, as long as a critical number of these re-entrant wavefronts exist in an appropriate substrate (e.g. atrial size and mass,

tissue refractoriness and conduction velocity), these wavefronts hypothetically would be able to re-excite the atria and give rise to chaotic fibrillatory conduction.

The existence of multiple wavefronts was demonstrated for the first time by Allessie et al. in 1985, shown in a canine atrial model after administration of ACh [12]. A number of reported clinical observations also seemingly correspond to the multiple wavelet hypothesis. For example results from the Maze procedure wherein subdividing the atria into multiple electrically independent compartments causes it to become unable to sustain the arrhythmia [61, 62]. Additionally, prolonged refractoriness has also been shown to decrease the stability of fibrillation [44, 195].

Mother rotor

More recently, reports have emerged suggesting that the presence of multiple wavelets does not necessarily exclude the co-existence of localised sources [124, 170]. It is argued that under certain substrates, stable rotors known as the 'mother rotor' might actually generate multiple wavelets referred to as 'daughter wavelets' [118, 244]. This is known as the 'mother wavelet hypothesis'.

In this theory, stable circuits split into excitation wavefronts because the tissue is not able to conduct with a 1:1 ratio [177]. Subsequently, daughter circuits move into other parts of the myocardium, causing irregular rhythm. Support for this theory has been shown in cases of VF, in which large wavefronts have been shown to follow distinct pathways across the epicardium during the initial few minutes of VF [168].

2.2.3 Other theorised mechanisms

Outside of the classical theories aforementioned, other mechanisms have been recently proposed as the underlying mechanism of AF and VF. Development of advanced computational methods and mapping has allowed deeper investigation into the relevant mechanisms pertaining to the maintenance of fibrillation, including a high-level inverse solution-based analysis of surface electrogram data [103] and the use of in vivo high-density contact mapping arrays [241]. These recent advancements have offered new novel mechanisms that may potentially contribute to our understanding about the maintenance of fibrillation.

Reports from Haïssaguerre et al. suggest that rotors are present but are evanescent in nature, and although they tend to cluster at the edge of fibrotic regions, their location does not remain fixed temporally [103]. In these studies, the median rotor duration was only 2.6 rotations, in comparison to the minutes or hours reported by Narayan et al. Practically, if short-lived rotors located in fibrotic regions do play a critical role in maintaining fibrillation, targeting rotors in a 'point-and-shoot' approach would likely prove ineffective, though several groups are at present working towards targeting zones with specific patterns and degrees of fibrosis [5, 156].

Another theory stems from results from van der Does et al., who suggest a key role for endocardial-epicardial dissociation, which provides a large number of breakthrough activations on either surface to maintain fibrillatory behaviour [241]. Again practically, this would pose challenges in developing an effective ablation or treatment strategy, as endocardial-epicardial dissociation would likely produce a constant multiplication of fibrillation-maintaining sources via large numbers of regional breakthroughs.

2.3 Measuring and mapping cardiac activity during fibrillation

The measurement and mapping of cardiac activity is central to the analysis of fibrillatory behaviour. Advancements in technology have resulted in numerous methods for achieving this in recent years, however, this brief review will summarise the mapping and measurement methods relevant to this research.

2.3.1 The surface electrocardiogram (ECG)

The potential (voltage) differences arising from the electrical activity of the heart can be visualised using an electrocardiogram (ECG). The ECG is commonly used to provide information about the regularity and rate of the heart, in addition to the size and position of chambers, the effect of drugs or therapeutic interventions, and whether any damage is present. As electrical activity propagates through the myocardium, this gives rise to manifold potentials of various sizes. Summation of these small manifold potentials can be approximated as the potential on the body's surface and can therefore be measured using electrodes placed on the skin. The ECG becomes the projection of the spatial cardiac activity on the axis between these electrodes (Figure 2.7). Because the electrical biopotential measured by the electrodes are usually small in magnitude, they must be amplified before being recorded by an ECG recorder [256]. Under normal function, a physiologically normal ECG will consist of the following (Figure 2.7) [221]:

- **P wave:** Occurs during atrial depolarization. The positive wave of depolarization propagates from the SA node, and is conducted through atrial cells via gap junctions.
- **PR interval:** Corresponds to depolarization of the AV node (when electrical current passes through the AV node). This causes a delay which allows ventricles to fill. On the ECG trace, the PR interval appears as a flat line as the wave is too small to be recorded.
- **QRS interval:** A combination of the Q, R and S waves. The QRS complex occurs due to depolarization of the ventricles, which in turn triggers contractions primarily responsible for pumping blood throughout the body.

- **ST segment:** Corresponds to the beginning of ventricular repolarization. As all of the ventricular myocardium has a positive charge, there is no potential difference and hence the segment appears as a straight line on the ECG trace.

- **T wave:** Represents ventricular repolarization.

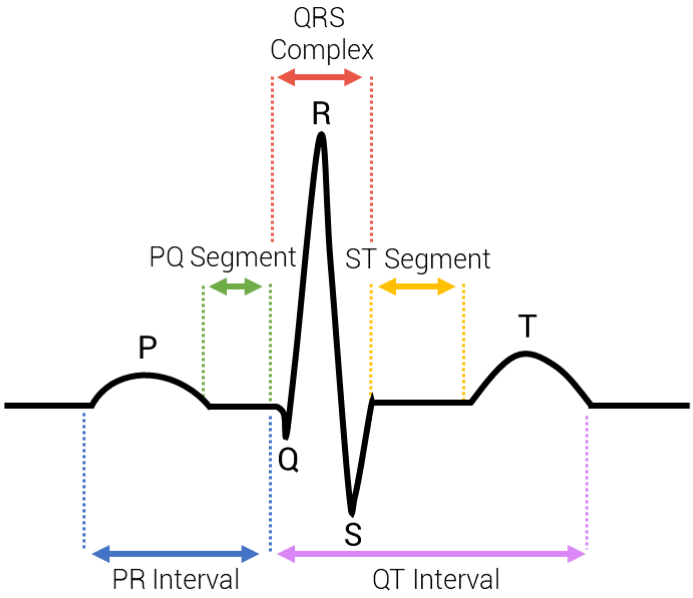

Figure 2.7: Schematic of a 'normal' ECG trace

The ECG is usually measured using conventional leads defined by Einthoven [74], Wilson [261] and Goldberg [93]. The leads as described by Einthoven are bipolar, measuring the voltage between the right arm (RA), left arm (LA) and left leg (LL) (Figure 2.8). In contrast, Goldberg's lead formation uses the same electrode locations but measures the voltage between one lead and the remaining two leads, which are interconnected via a resistor (aVR, aVL, aVF, Figure). Wilson's definition included an additional 6 electrode positions on the chest, located in close proximity to the heart. Voltage is measured on one of the chest electrodes using Wilson's central terminal (WCT) as the reference electrode. The WCT is produced by connect the R, L and F electrodes using a resistive network that gives an average action potential across the body.

Atrial fibrillation will appear in the ECG as shown in Figure 2.8. Low amplitude, irregular waves appear in the ECG due the irregular rhythm and feeble, uncoordinated twitching of the atria. Likewise, ventricular fibrillation causes feeble, uncoordinated twitching of the ventricles that results in no blood being pumped from the heart. On the ECG, this appears as extremely uncoordinated electrical activity as shown in 2.8.

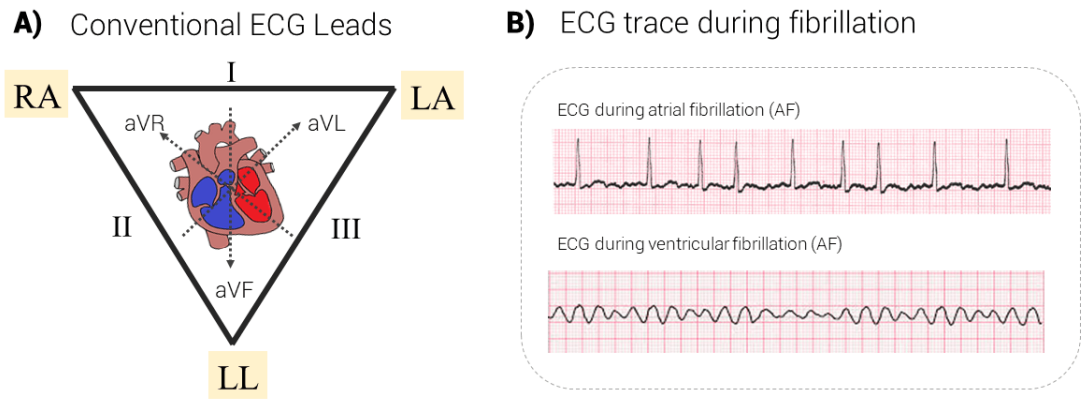

Figure 2.8: Standard ECG leads and example surface ECGs during fibrillation

A: Conventional ECG leads for Einthoven (I, II, III) and Goldberger (aVR, aVL, aVF) configurations. B: Example ECG traces for AF (top) and VF (bottom)

2.3.2 The intracardiac electrogram (EGM)

The cardiac electrogram (EGM) provides a trace of the electrical potentials of myocardial tissue by means of placing electrodes directly on the tissue (intracardially), versus on the surface of the body. The EGM is able to measure the tissue's electrical potential as transmembrane currents in the extracellular space create potential differences as cardiac muscle depolarizes, due to the differences in the axial voltage gradient between inactivated and activated cells [25]. Like the ECG, the cardiac EGM is measured as a potential difference recorded between two recording electrodes during the cardiac cycle, referred to as a differential recording. Potentials are usually measured from one source that is connected to the positive (anodal) input of the recording amplifier, and the second from a source connected to the negative (cathodal) input [228]. Depending on the placement of these electrodes, unipolar or bipolar electrogram configurations can be achieved.

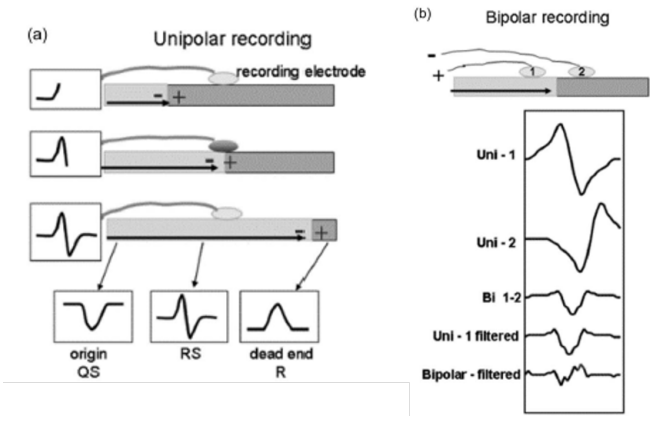

Figure 2.9: Schematic illustrating unipolar and bipolar electrograms during the cardiac cycle. Adapted and reproduced from [Stevenson, 2005] with permission.

Unipolar EGMs can be obtained by positioning the exploring electrode within the heart, and placing a second electrode (referred to as the indifferent or reference electrode) distant from the heart such that it will record little to no cardiac activity. Usually, by convention the recording electrode is in physical contact with the myocardium and is connected to the anodal input of the amplifier, whilst the indifferent electrode is connected to the cathodal input. This configuration results in the characteristic EGM morphology as wavefronts propagate towards the recording electrode. Specifically, a small positive deflection is initially seen as the depolarisation wavefront propagates towards the recording electrode. As the wavefront passes the electrode, the deflection becomes steeply negative, which results in the characteristic biphasic complex as shown in Figure 2.9A. The maximum negative slope coincides with the depolarization of cardiac tissue that is directly underneath the recording electrode [228]. It should be noted that one of the limitations of the unipolar EGM is that it is vulnerable to external electromagnetic interference arising from mains power, as well as electrical activity from other parts of the chamber (known as far-field activity) [25].

For most clinical mapping, EGMs are recorded in the bipolar configuration (Figure 2.9B). This is achieved by subtracting two unipolar EGM that have been recorded at proximate sites, which in practice are usually adjacent poles of an intracardiac catheter. This mode is preferred in clinical settings as far-field activity is largely overcome, which is particularly useful for recording AF activity as ventricular depolarisations tend to be much larger in amplitude. However, when compared to unipolar EGM, the timing of local activity is much less easily determined [220].

During sinus rhythm, the morphology of unipolar EGM demonstrate a relatively uniform appearance and predominantly negative deflections. Likewise, bipolar EGMs in sinus rhythm show discrete complexes separated by periods of isoelectric activity. Contrastingly, EGMs during AF are irregular and disorganised, with a more complex morphology. EGMs recorded during VF are similarly irregular and complex (Figure 2.10).

Figure 2.10: Typical electrograms during sinus rhythm, AF and VF

2.3.3 Fluoroscopy and 3D electroanatomical mapping

During experimental studies, it is often important to know exactly where in the heart data is being collected from. This is also important during clinical procedures, as often the exact location of the catheter is needed in order to perform an ablation. To achieve this, fluoroscopy is commonly used. Fluoroscopy is a medical imaging modality that provides continuous, real-time X-ray images on a monitor, achieved usually by passing an X-ray beam through the body. In this way, fluoroscopy is able to provide a two-dimensional image of the heart and the location of any medical instruments introduced into the body. However, a disadvantage is that it cannot relate local electrograms to their spatial orientation, and radiation exposure also poses a risk to the patient, clinician and medical staff [256].

To overcome these issues, 3D electroanatomical mapping systems are often utilised. These systems have the benefit of reducing radioactive exposure, while also providing the ability to measure the 3D anatomical location of catheters and the electrograms being measured. Commonly, mapping systems such as the EnSite Velocity (Abbott), and CARTO (Biosense Webster, Diamond Bar, CA, USA) are used clinically. Both systems use corresponding catheters that come in an array of shapes and sizes (e.g. circular, spiral, straight), useful for various applications [245].

The EnSite Velocity system is an impedance-based system, using the electrode on the cather to sense a 5.68 kHz low current signal, coupled onto the body using three pairs of large patches/-electrodes placed on the thorax to produce a transthoracic orthogonal electric field surrounding the heart. A sampling rate of 93 Hz is used to measure the field, allowing close to real-time measurement of anatomical location [245].

The CARTO system instead uses an ultra-low magnetic field emitter, placed under the operating table beneath the patient's thorax, and a small passive magnetic sensor embedded onto the distal electrode of the catheter. The magnetic field emitted will decrease in strength and change in direction as a function of its distance to the catheter [245].

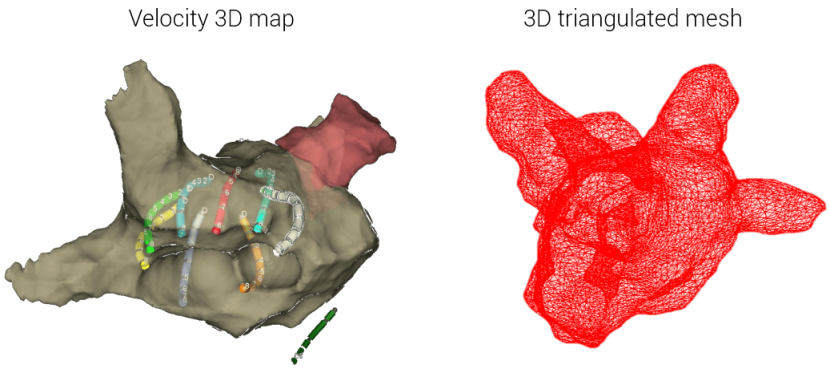

Figure 2.11: Anatomical 3D electroanatomical mapping
3D anatomical map acquired from EnSite Velocity (left) and a 3D triangulated mesh constructed in Matlab from exported 3D point-cloud (right)

From these systems, the 3D point cloud and triangular mesh vertices used to construct the 3D anatomical map, as well as electrograms and ECG data can be exported (2.11), allowing analyses to be performed outside of the CARTO and Velocity systems.

2.3.4 Phase Mapping

In mathematics and physics, a signal can be characterised by three fundamental characteristics: its amplitude, frequency and phase. The amplitude of a signal refers to the magnitude of the physical quantity measured over a particular time interval, for instance the voltage of an electrogram. Frequency is the number of cycles undergone during one unit of time, which is the fundamental repetition cycle of the signal. We can also describe a signal using its phase- a descriptor that defines the relative 'stage' of a signal within its full cycle (2.12).

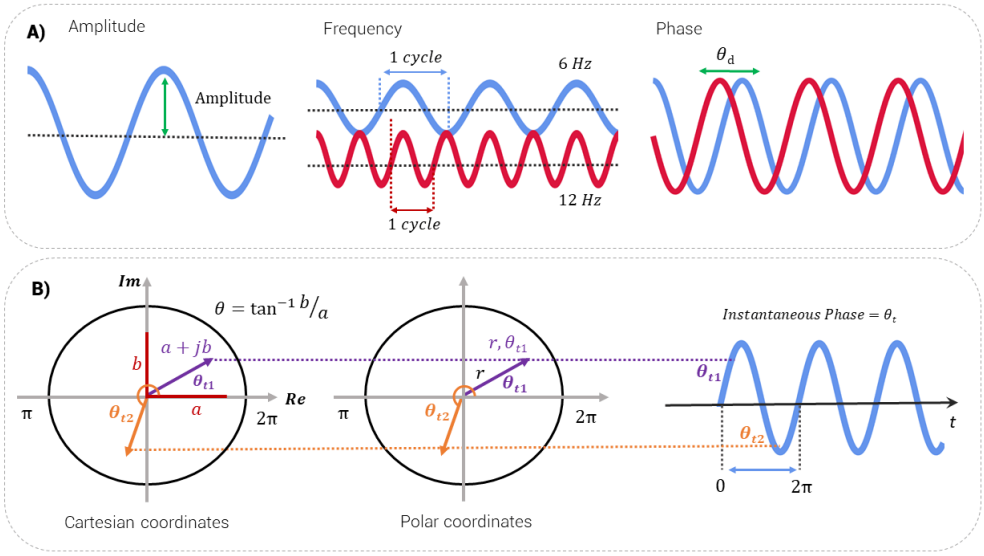

Figure 2.12: Descriptors of a signal and understanding phase

A: Descriptors of a signal: A signal can be characterised by its amplitude, frequency and phase. Here, two sinusoidal waves with a phase delay ϑd (equivalent to the phase difference) of 90° is shown (right). B: The phase of a signal can be given by ϑ, calculated by taking the position of its vector along the unit circle. This position can be expressed either as Cartesian coordinates (left) or in polar coordinates (right). The instantaneous phase, ϑt, gives the phase of the signal at a given time t.

Graphically, this concept of phase is illustrated further by the sinusoidal signal shown in Figure 2.12B. The phase of the signal at time instant t, known as the instantaneous phase, is given by the relative position of the vector to the origin on the unit circle, whereby the unit circle represents one full cycle (0 to 2π). This position can be given by the length of the vector r and angle ϑin polar co-ordinates, or in the complex form $a + jb$ in Cartesian co-ordinates, whereby j represents the imaginary part of the complex number.

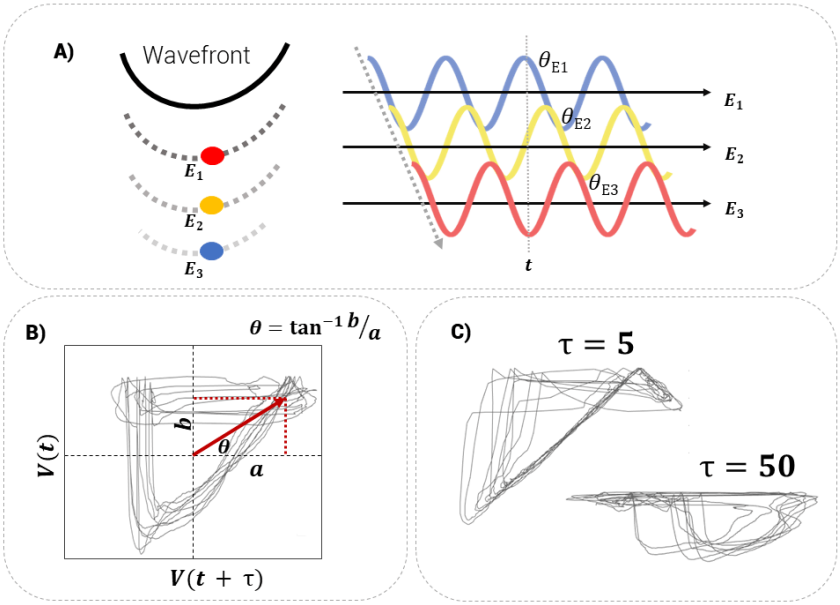

Figure 2.13: Conceptualisation of phase mapping in cardiac electrophysiology, phase space plots and the time embedding delay τ

A: An activation wavefront hits three electrodes at a slightly different times, and recorded activity (depicted as sinusoids for simplicity) at t will correspond to a slightly different stage of the action potential cycle. The phase difference, ϑ_d, can be used to track wave propagation. B: The phase ϑat time t (instantaneous phase) is given by position of the vector relative to the origin on the phase space plot. C: Phase reconstruction is reliant on τ.

In the context of cardiology, phase can be used to study electrical wave propagation. Specifically, phase is used to track the progression of a region of myocardium relative to the action potential by measuring the phase difference between signals measured at proximate electrodes [237]. An example of this is shown in Figure 2.13, whereby an activation wavefront is travelling through the heart across three electrodes (E1, E2 and E3). Due to the spacing between the electrodes, the activation wavefront hits each electrode at slightly different times, meaning that the activity recorded at each electrode for the same referenced time point t will correspond to a slightly different stage of the action potential cycle. This results in a measurable phase difference, which is proportional to the distance between the electrodes and the velocity of the travelling action potential. Using this principle, the phase distribution over time across these electrodes can be measured to understand the wave propagation dynamics of the activation [237].

Practically, in order to track wave propagation over time the phase at each recorded site of the heart must be obtained for each time step t. This can be achieved using time series analysis to reconstruct a phase space plot, which takes the transmembrane potential $V(t)$ as the state variable and plots this against its time delayed version $V(t+\tau)$, whereby τis the chosen time delay (also referred to as the time delay embedding) [39] [113]. Essentially, the method of reconstructing phase from a phase space plot is based on the concept that the cardiac action potential can be represented by a closed-loop trajectory through 2-D space. Because the phase space plot graphs $V(t)$ on the x-axis, and $V(t+\tau)$ on the y-axis, this allows the vector position with respect to the

origin to be determined as shown in 2.13. Hence the instantaneous phase θ can be found using:

$$\theta = tan^{-}1\frac{b}{a} \tag{2.3}$$

where b represents the vertical component of the vector, and a the horizontal component. Although the phase space plot can be used to measure the instantaneous phase, this approach is sensitive to the chosen time delay embedding τ. This is shown in Figure 2.13C, whereby a choice of τthat is too small causes the values of *V(t)* and *V(t+τ)* to become highly correlated, resulting in trajectories that are concentrated along the diagonal of the phase space plot (Figure 2.13C, left). Contrastingly, choosing a value of that is too large causes decorrelation of the data and in turn stretching and deformation of the phase space plot (Figure 2.13C, right) [39].

As an alternative, the Hilbert transform can be used as a substitute to more robustly compute the instantaneous phase, and is now widely implemented in contemporary phase mapping studies [131, 147, 170, 205]. The Hilbert transform works by transforming a real signal into a complex signal by removing its negative frequencies. This is achieved in simple terms by generating a phase shifted version of the original signal, and adding it as the imaginary part to the original real signal, causing all negative frequencies to cancel out [113, 237]. Mathematically, this is given by:

$$H[x(t)] = \frac{1}{\pi}\int_{-\infty}^{\infty}\frac{x(\tau)}{t-\tau}d\tau \tag{2.4}$$

Once this is done, the signal will have the complex form $a + jb$, which is practically useful as it simplifies calculation of the instantaneous phase to simply the arctangent of b (the imaginary component) divided by a (the real component) using equation 2.3.

Plotting the phase values at each recorded site of the heart for all time points t results in phase maps such as those shown in Figure 2.14. Phase is colour coded, allowing visual interpretation of the propagation of electrical activity. An example of a single, localised rotor is shown in Figure 2.14A, whereby the beginning of an action potential cycle corresponds to a phase of -πshown in blue, and the end of the cycle with a phase +$\pi$of shown in red. The rotational movement of the rotor can clearly be seen. Similarly, Figure 2.14 shows phase maps for human persistent AF. Propagation in this instance shows multiple complex wavefronts.

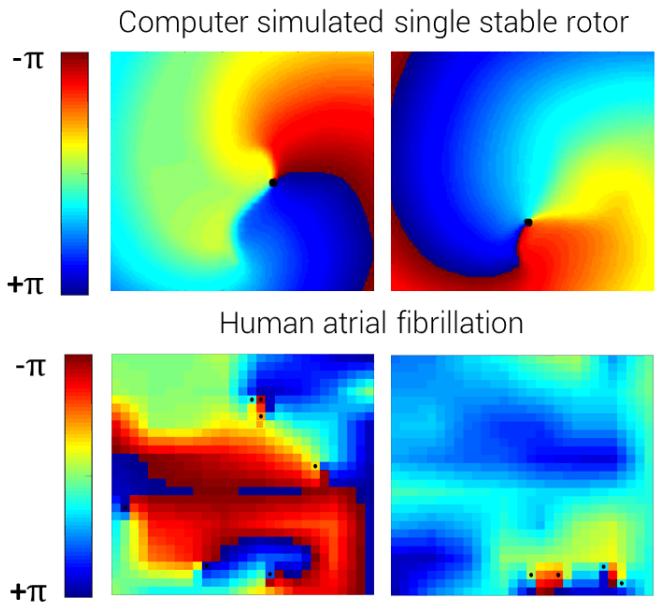

Figure 2.14: Example phase maps from computer simulations and human AF

Example phase maps showing electrical wave propagation of a stable localised rotor from computer simulated fibrillation (top), and complex wave propagation in an example case of human persistent AF.

2.3.5 The Phase Singularity

An important feature of phase mapping is the phase singularity (PS), regions in which activation wavefronts hinge and rotate about in an organised manner (Figure 2.15). Physiologically, they therefore coincide with re-entrant activity such as rotors and wavelets. The reason for this is that in phase space, a phase singularity is a topological defect that occurs only when surrounding points progress through a complete cycle from $-\pi$ to $+\pi$ (e.g. cycles through all colours from blue to red). Consequently, all the surrounding phase values converge and the phase at the central point itself becomes undefined [39].

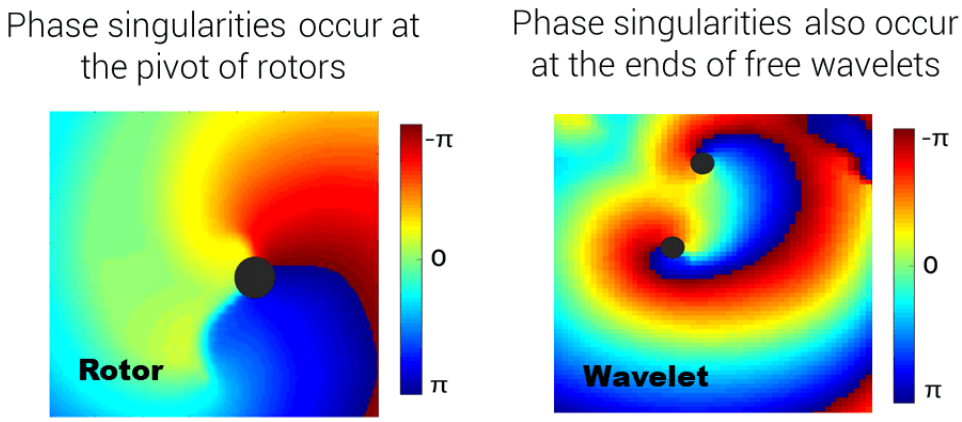

Figure 2.15: Conceptualisation of a phase singularity (PS), with PS indicated by black circle

To locate PS, a number of methods have been developed. Bray et al. [38] defined a phase singularity in terms of topological charge, n_t, given by 2.5:

$$n_t = \frac{1}{2\pi} \oint_c \nabla\phi \cdot \vec{dl} \tag{2.5}$$

where $\phi(\vec{r})$ is the local phase, and the line integral is taken over a path l around a closed curve c, which surrounds the PS. In this formulation, a phase singularity is evaluated using the gradient of the phase as a wave vector, k:

$$(\nabla \times \vec{k}) \cdot \hat{z} \equiv \lim_{a \to 0} \frac{1}{\pi a^2} \oint_c \vec{k} \cdot \vec{dl} \tag{2.6}$$

where a is the radius of the circular path c. If a small circular path is evaluated, then the topological charge n_t (given by equation 2.6) will be proportional to the curl of the wave vector k. The curl of k should be 0 everywhere that the phase ϕ is differentiable, and non-zero only at the phase singularity itself where ϕ is indeterminate [38].

In contrast, Iyer and Gray developed an automated algorithm to perform this PS detection, using the notion that although the phase at the centre of the rotation is undefined, neighbouring sites show a continuous progression of phase equal to 2π around the centre [113]. Consequently, the location of a PS on a phase map can be given by evaluating the difference in phase over a discrete path, and if this path is equal to $\pm$ 2π, then the path surrounds a PS:

$$\oint_c \nabla\phi \cdot \vec{dl} = \pm 2\pi \tag{2.7}$$

where equation 2.7 is a rearrangement of equation 2.5. Although the path length can be varied, Iyer and Gray implement a path length of 8 pixels as shown in Figure 2.16A. Consequently, the algorithm identifies 4 pixels wherein the surrounding path equals $\pm$ 2π, and the intersection of these 4 pixels locates the PS (Figure 2.16A) [113].

More recently, Kuklik et al. built on this to develop an extended topological charge method that more robustly detects PS (Figure 2.16B). In cases where a discrete number of electrodes are used, the integral has to be discretised and approximated. The loop c therefore becomes a ring of electrodes encircling the point to be evaluated for a PS. This means that for a low number of electrodes, false detections can occur much more easily as the path may encompass more than one wavefront, leading to artificial phase differences. To avoid this, a double ring approach was developed whereby the loop comprised of two paths: an inner 2 x 2 path, and a larger 4 x 4 path. Such a formation results in a positive PS detection only if one phase difference greater than π is present in both the inner and outer ring [136].

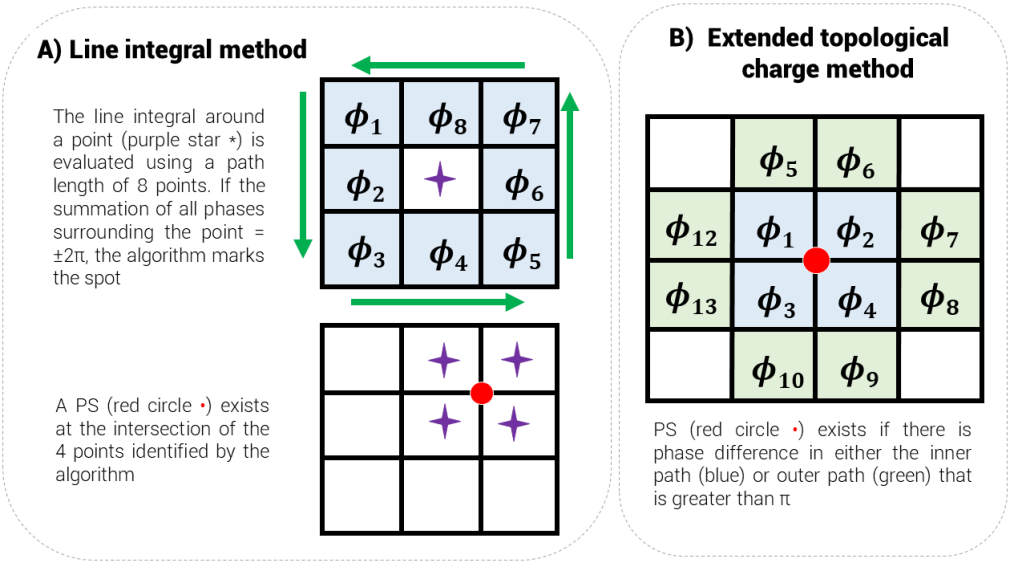

Figure 2.16: Line integral method (adapted from [Iyer,2001]) vs. extended topological charge method (adapted from [Kuklik, 2017])

2.4 Current AF and VF Treatments

Currently, cardioverting the AF to sinus rhythm either electrically or pharmacologically remains the most commonly used strategy, as these methods can help address the two main concerns associated with AF: (i) reducing thromboembolic risk and (ii) alleviating the haemodynamic effects associated with poor cardiac output [148]. Pharmacological methods of cardioversion employ various antiarrhythmic drugs to restore and maintain sinus rhythm [139]. Unfortunately, such drugs can often be ineffective or poorly tolerated and are associated with adverse side effects. Virtually all antiarrhythmic drugs have shown evidence of increased proarrhythmic effects, with the potential of inducing life-threatening arrhythmias. Furthermore, the success of such drugs is limited; AF is found to recur in 42-67% of treated patients [139]. In comparison, electrical cardioversion uses a transthoracic direct current to revert the patient's heart back into sinus rhythm, a method that has been used since first described by Lown et al. in 1962 [151]. The initial success rate of electrical cardioversion is reportedly between 50-90% [242, 243], though AF often quickly recurs and only 27-42% of patients remain in sinus rhythm after 1 or 2 years [138, 243].

An appealing alternative treatment that has been gaining interest within the last decade is catheter ablation. Catheter ablation is a potentially curative treatment for atrial fibrillation (AF), which uses percutaneously induced catheters to apply focal burns to specific areas of heart muscle in order to cease or modify the AF. This method was first popularized following the breakthrough investigation published by Haïssaguerre et al. in 1998 [102], which reported successful termination of up to 90% of paroxysmal AF (PAF) cases using catheter ablation on ectopic triggers located at the pulmonary veins. Although pulmonary vein isolation (PVI) is recognized as a landmark development for the treatment of paroxysmal AF, the extending application of ablative therapies

for the persistent AF populace has seen relatively lower rates of success. In fact, current literature has reported that less than 50% of patients maintain sinus rhythm following a single ablation procedure, irrespective of the ablation targets that are used [56, 190]. Consequently, the optimal approach to ablation in the persistent AF population is currently the subject of ongoing debate, as effective ablation targets remain unknown.

Treatment of ventricular fibrillation is a little more complex as the onset of this arrhythmia often happens suddenly and leads to sudden cardiac death (SCD). Subsequently, treatments typically focus on trying to restore blood flow to prevent damage to organs during a VF episode [22]. This usually includes cardiopulmonary resuscitation (CPR) to help maintain blood perfusion throughout the body, and delivery of an electrical shock via defibrillation. Oftentimes, the electrical current provided by the defibrillator will interrupt the abnormal rhythm and allow conduction to resume. If normal rhythm isn't resumed after CPR and defibrillation alone, medications such as epinephrine and amiodarone may be given. Unfortunately, however, the success rates for defibrillation are low in out-of-hospital settings [75]. Additionally, success rates of resuscitation decrease the longer the VF episode persists, hence it is vital that VF is detected as promptly as possible.

To prevent future episodes, medications including beta-blockers may be prescribed, especially in patients at high risk of VF and SCD. An implantable cardioverter-defibrillator (ICD) is also often used to monitor heart-rhythm and send an electrical signal to the heart if the rhythm is too slow, or if ventricular fibrillation or tachycardia is detected. In some cases of severe heart coronary artery disease, blood flow may be improved via surgeries such as a coronary angioplasty and stent placement, or a coronary bypass surgery [133].

Part I

Investigating the spatiotemporal characteristics and specificity of entropy-based rotor mapping

Chapter 3

Part I foundations and literature review

3.1 Introduction

As discussed in chapter 2, although atrial fibrillation is the most common cardiac rhythm disorder in the world, treatment of AF is unfortunately complicated by the efficacy of the current treatments available. Although touted as a potentially curative treatment, catheter ablation outcome in persistent AF patients remains poor, with studies reporting maintenance of sinus rhythm in less than 50% of patients following a single ablation procedure [56, 190]. From this, it is clear that improvements to ablation strategies are required.

At the heart of this is the highly complex wave dynamics of AF, which have thus far been responsible for the difficulties in identifying effective ablation targets. In recent years, the prevailing school of thought is that rotors play a key role in maintaining the arrhythmia, and hence may be effective ablation targets. However, ablation of rotors hinges on their stability both spatially and temporally (spatiotemporal stability), as instability would make targeting these rotors in a 'point-and-shoot' approach incredibly difficult and even close to impossible.

A number of AF mapping approaches have attempted to identify rotors using various technologies and methods but unfortunately, these have lead to conflicting outcomes [166, 169] or are still undergoing investigation [35, 211, 218]. A major limitation of many of these approaches is that they utilise internal or company-specific proprietary technology algorithms, which has had important consequences for reproducibility and independent validation, and has also led to growing scepticism regarding the viability of individual patient-level mapping in the AF ablation field.

In light of this, it is clear that in order to improve ablation outcomes, three important factors

must be considered:

- The identification of effective AF drivers
- Establishing more open source, non-proprietary AF mapping methods
- Investigating whether rotors are in fact stable in both time and space, such that they can be targeted

The purpose of ***Part I*** of this research, therefore, was to address these fundamental knowledge gaps through exploration of computational, entropy-based (information-theoretic) approaches for AF mapping.

An overview of information theory in cardiac fibrillation

The material contained within this chapter has been published in Dharmaprani, D. et al., 2018. ***Information theory and Atrial Fibrillation (AF): A review***. Frontiers in physiology, 9. The core theme of the chapter is to detail the use of information theory in atrial fibrillation. Dhani's contribution to the paper was conducting the literature research, and formulating and writing the manuscript.

3.2 Current AF mapping and electrogram analysis approaches

To date, a number of signal processing based approaches designed to guide clinical AF ablation have been explored. Such approaches typically rely on analysing AF electrograms to extract certain characteristics that are potentially useful for the selection of ablation targets. An example of one such potentially useful characteristic is fibrillatory rate. As the frequency of atrial activation increases drastically during AF in comparison to normal sinus rhythm, rising from 1-2 Hz (60-120 beats per minute) to 6-10 Hz [25], extracting fibrillatory rate is thought to infer regions of interest. Measuring fibrillatory rate in the time domain is usually achieved through measuring the AF cycle length (AFCL), which is based on the interval between consecutive local activation times (LAT) [33, 181]. Unfortunately, acquiring precise annotations of LATs from bipolar electrograms proves difficult in practice, as bipolar EGM signals rely heavily on the alignment of the electrode bipole in relation to the activation front, and hence are prone to providing incorrect and ambiguous activation times. Unipolar signals can also become misinterpreted, as these signals integrate considerable far-field activation [279].

Analysis of fibrillatory rate in the frequency domain has also been explored, primarily through dominant frequency (DF) analysis [25,30]. The frequency spectrum of the EGM in AF is analysed to extract the spectral peak, also known as the dominant frequency, which is often considered a substitute for the local activation rate in the frequency domain [155]. Although DF is often considered a surrogate measure, poor correlation of DF to the activation rate and local cycle length in the time domain has been previously reported [76,174]. The temporal dynamics of EGM signals also severely impact the ability to accurately analyse DF [174]. Additionally, the spatiotemporal stability of DF has been widely debated, with some studies claiming to observe short periods of stability [134], whilst others instability [100, 119], hence imposing implications for AF mapping. Clinical results using DF analysis are also somewhat mixed, with AF termination occurring in 72% of paroxysmal AF patients, but only 11% of persistent AF patients as reported by Atienza et al.

[18].

Electrogram analysis approaches also commonly examine the complexity of the EGM signals to help identify possible ablation targets. In 2004, Nademanee et al. [166] introduced EGM fractionation based approaches to ablation. In the study, complex fractionated atrial electrograms (CFAE) were defined as electrograms with a very short AFCL (<120 ms) averaged over a 10 second segment, or an EGM comprising of two or more deflections and/or perturbation of the baseline with continuous deflection [166]. Selection of CFAEs in the initial study were highly subjective however, as these were identified via visual inspection. In a bid to standardise the selection of CFAE sites, automated methods utilising quantitative approaches were developed, and even implemented in commercial mapping systems [196, 212, 250]. Unfortunately, these still require user inputs for parameter definitions and thresholds, and hence make replicability difficult [25]. The spatiotemporal stability of CFAE sites also poses a further issue, as basket recordings with a stable position have reported that CFAE sites are highly temporally unstable, with sequential maps failing to identify CFAE sites in one third of cases [100]. Clinical studies using CFAE guided ablation have also had minimal success, with many studies failing to replicate the promising results as reported in the initial study conducted by Nademanee et al. [166], showing instead a lack of incremental benefit with CFAE ablation [184–186, 251].

Another approach to analysing electrograms is multivariate electrogram analysis, which aims to assess the spatiotemporal relationship of atrial activity using multi-electrode recordings as opposed to EGMs acquired sequentially at various atrial sites [25]. One specific multivariate EGM analysis technique is Hilbert phase mapping, which allows the phase of atrial signals to be observed and hence, the spatial propagation of local activation waves (LAWs) [237]. Phase mapping techniques were the first to portray spiral waves as the drivers of fibrillation [98, 113], and have been demonstrated in both ventricular and atrial fibrillation models [155]. Unfortunately, a meaningful interpretation of the Hilbert transform relies on the signal being of one mode and hence, the complex nature of EGMs makes Hilbert phase estimation challenging [25]. Clinically, Hilbert phase maps have been utilised most notably by Narayan et al., with an approach known as focal impulse rotor modulation (FIRM) [169]. FIRM based ablation reported the identification of rotors during human AF in a number of cases, and a slowing or termination of the AF in 86% of patients using FIRM guided techniques [169]. In a second case series however, AF slowing or termination was achieved in only 50% of patients [27].

Whilst this summary provides only a brief overview of some of the commonly used AF analysis approaches, it is evident that current methods provide variable results that are also hard to reproduce. As such, this warrants the exploration of new AF analysis techniques, which may improve the selection of ablation targets and in turn the success of ablation procedures.

3.3 A new avenue for mapping using information theory

Information theory is a branch of mathematics that incorporates probability theory and statistics [18, 19]. Modern information theory was established after the publication of Claude E. Shannon's seminal original paper [219], which earned him the title of pioneer and founding father of information theory. Shannon's work introduced, for the first time, a number of key ideas that shaped the field of information theory, including the concept of digitizing information into binary digits known as 'bits', the formal architecture of communication systems, and source coding, which deals with the efficiency of data representation. In short, the scope of information theory focuses on the transmission, processing, storage and receiving of messages [246]. Although information theory was initially developed for use in communication systems, principally concerning itself with the transmission of telecommunication signals, it is now commonly used in a number of fields.

Information theoretic-based approaches may be an appealing new avenue in AF mapping, as they have i) a strong theoretical foundation in mathematics [68] and ii) use quantitative definitions rooted in intrinsic signal properties, instead of arbitrary, empirically derived definitions. In addition, although information theoretic approaches are seldom used in the field of cardiology, such techniques are already prevalent and widely accepted in other disciplines such as engineering [1], neurology [41], computer science [201], physics [157], quantum computing [175] and linguistics [31].

3.4 What is information and how can it be measured?

As Shannon argued, the semantic aspects of communication can be thought of as irrelevant to the engineering problem [219]. Consequently, the term 'information' in reference to information theory does not refer to the meaning of a message as one might assume intuitively, but instead how much can be learnt from that message [150]. To conceptualize this further, take for example the scenario in which someone is asked to guess a number from 1 to 10, whilst obtaining help from a friend through clues. With respect to information theory, the clue itself does not matter, but the amount of information that can be inferred from the clue does. As such, if they are told that the number is less than 11, then this clue is deemed uninformative. On the other hand, if they are told that the number is even, then this fact is considered much more informative, though revealing that the number is odd would also be equally as informative, as these both reduce the possible selections to 5. In this respect, information can be thought of as how much is learnt, rather than what is learnt [219].

Relating to this concept is the information theoretic measure known as 'entropy'. As information can alternatively be thought of as the amount of uncertainty that is eliminated or resolved, measuring this uncertainty will intuitively quantify information. Conceptually speaking, entropy utilizes this principle to measure information content, with greater uncertainty in turn generating

higher entropy [60, 99, 219]. As entropy increases with uncertainty, it will be maximal for completely random systems [58]. Such metrics have potentially useful clinical implications, particularly with respect to diagnostic tools using biological signals and understanding the underlying dynamic properties of physiological systems [59].

Although there are several ways that information can be measured outside of entropy, it is one of the most prevalently used classical measures of information theory, particularly in the context of AF. With this in mind, entropy-based approaches to quantifying information will be the focus of this review, and an overview of the various entropy algorithms commonly used to analyze AF will be described in the following.

3.4.1 Shannon Entropy (ShEn)

Named after Claude E. Shannon himself, Shannon entropy is the classical measure of information theory and measures the Shannon information content of a random variable [219]. It was first introduced by Shannon to describe the relationships between information, noise and power in a digital communication stream [3], quantifying the amount of storage required to store a signal (in bits) [238]. Now, it is also commonly used as a measure of information content across many fields. Shannon entropy (ShEn) can be defined as:

$$ShEn = -\sum_{i=1}^{M} p(i) log_2 p(i) \tag{3.1}$$

where M is the number of discrete values the variable can take, and *p(i)* the probability density function of the variable x assuming the i^{th} value. Note that Shannon entropy is given in the unit bits [219].

An intuitive example of how information is quantified using ShEn is the simple coin toss. A fair coin with a head and tail will result in maximum entropy, as the outcome cannot be predicted. As a result, the probability of choosing the correct outcome is $\frac{1}{2}$, as there are two possible outcomes that may occur with equal probability. Each coin toss will deliver one bit of information, as [219]:

$$ShEn = -\sum_{i=1}^{2} \frac{1}{2} log_2 \frac{1}{2} = 1 \ bit \tag{3.2}$$

Conversely, a double-headed coin will result in an entropy of zero, as the probability of the outcome is 1/1. Hence there is no uncertainty, and no information is gained from the outcome of

the coin toss [219]:

$$ShEn = -\sum_{i=1}^{2} 1log_2 1 = 0\ bits \tag{3.3}$$

In AF analysis, ShEn is often used to measure the information content of an ECG or EGM. Typically, this is achieved by constructing the amplitude distribution or histogram of the signal [25, 84] . Specifically, a voltage histogram can be acquired by binning signal samples according to its amplitude. Following this, the relative probability density function $p(i)$ is obtained by dividing the sum of counts in each amplitude bin by the total number of counts. In effect, ECG or EGM with regular morphologies (i.e. signals that only possess a few states) will yield a narrow amplitude distribution [84]. Conversely, complex morphologies containing a number of dissimilar deflections, such signals in AF, will lead to more varying amplitudes and in turn a broader amplitude distribution (Figure 3.1). In effect, as ShEn is taken a sum of the probabilities, broader amplitude distributions will result in higher ShEn [83, 84]. The ShEn equation defined in 3.1 can be classified as a 'static' measure, as it does not consider any temporal information when describing the observed probability distribution. In other words, it measures information content by quantifying the amount of information contained only in the present value of the time series [273].

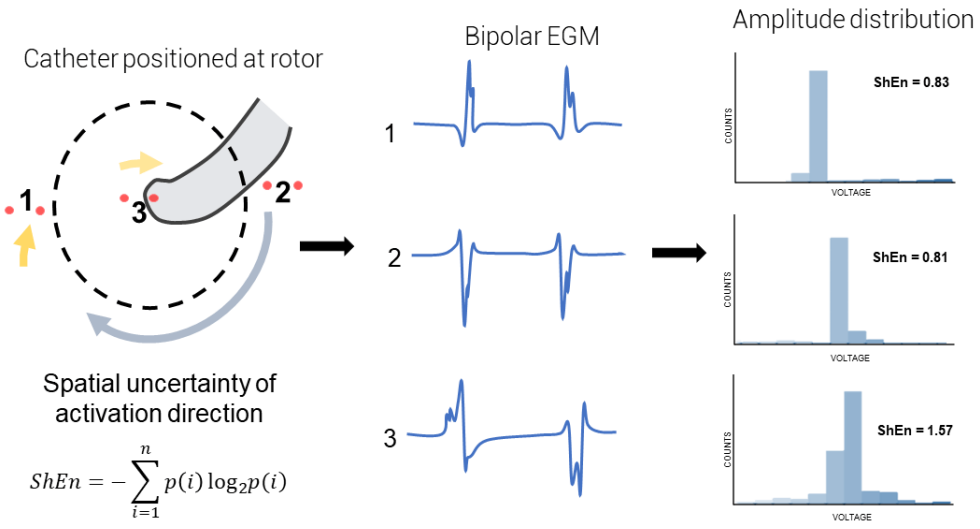

Figure 3.1: Schematic showing high ShEn correlating to centre of rotors. Adapted from [Ganesan,2012]

Schematic showing relationship between ShEn and the amplitude distribution in a simple rotating wave. Amplitude distribution (histogram) is generated by binning samples of the signal in amplitude bins. Bipoles positioned in location 1 and 2 (at the periphery of the rotating wave) experience consistent activation direction, leading to more regular EGM morphology and a narrow amplitude histogram. Conversely, the bipole at position 3 (at the rotor pivot) experiences sharp local deflection, but secondary activity as the wavefront changes direction, including intermediate activity and an inverted potential. Consequently, signal values are binned over a broader range of amplitudes, leading to higher ShEn

3.4.2 Approximate Entropy (ApEn)

In contrast to the 'static' measure of ShEn described in 3.1, 'dynamic' measures of entropy are those that study the information content of a process representing the activity of a system that is changing over time. An example of such a dynamic measure of entropy is conditional entropy [273].

Conditional entropy, also referred to as the Kolmogorov-Sinai entropy, is defined as the average rate of creation of new information [73]. Generally speaking, the current state of an observed process is partly determined by its past, but also conveys some amount of new information that can't be inferred from the past. Conditional entropy measures this residual information to quantify the rate of creation of new information [273]. In mathematical notation, this can be given by:

$$C(X) = (H(X_n)|X_n^-) = (H(X_n^-, X_n) - H(X_n^-) = -E[logp(x_n|x_1, ..., x_{n-1})] \tag{3.4}$$

where $p(x_n|x_1, ..., x_{n-1})$ is the conditional probability that X assumes the value x_n at time n, given that previous values are taken at $x_1, \ldots, x_{n-1}$. In effect, if the process is fully predictable, the system will not create new information and hence the conditional entropy is equal to zero. Contrastingly, a fully random process produces information at the maximum rate and will yield maximum conditional entropy. If the process is stationary, the system will produce information at a constant rate, and therefore the conditional entropy will not change over time [273].

A number of entropy estimates and measures have been developed to quantify conditional entropy. One specific example, which is commonly used to study physiological signals, is Approximate Entropy (ApEn). ApEn is a regularity metric that was originally developed for physiological signals such as heart rate. As accurate entropy calculation using regularity statistics is often found unfeasible in real-life applications due to the influence of system noise and the large amounts of data required, Steve M. Pincus developed ApEn to manage these limitations [194]. It can be noted that the approximate entropy family of statistics has been widely implemented in clinical cardiovascular studies [65, 79, 92, 109, 149, 208, 216, 234].

Specifically, ApEn quantifies the amount of regularity in a signal by measuring the logarithmic likelihood that runs of patterns similar to one another will remain similar when incrementally compared [204]. The prevalence of repetitive patterns in a signal is identified by forming a sequence of vectors using the time series data, and measuring the difference between them. If the relative difference between any pair of corresponding measurements is less than the length of the pattern, the pattern is deemed similar. In mathematical notation, this can be expressed using the equation:

$$ApEn(S_N, m, r) = ln\frac{Cm(r)}{Cm + 1(r)} \tag{3.5}$$

where m is the pattern length, r is the similarity criterion or threshold, and $Cm(r)$ the prevalence of patterns of length m in the sequence S_N [194]. ApEn is quantified in bits. Conceptualizing ApEn further, take for example two time series, t_1 and t_2:

$$\begin{aligned} t_1 &= (1,2,1,2,1,2,1,2,1,2\ldots) \\ t_2 &= (1,2,1,1,1,2,1,2,2,1\ldots) \end{aligned} \tag{3.6}$$

As t_1 follows a very regular pattern alternating between 1s and 2s, knowing that a term is valued at 1 will consequently allow the next value to be predicted, which in this case is always 2. Thus, t_1 possesses high predictability and low conditional entropy. Conversely, t_2 demonstrates a much more random pattern and hence will possess greater conditional entropy. Translating this to the cardiac space, a signal in normal sinus rhythm will exhibit periodicity and relatively uniform complexes, thus ApEn will detect the presence of similar patterns and identify this regularity (Figure 3.2). On the other hand, signals with complex morphologies will exhibit less regular patterns, hence yield higher ApEn [194].

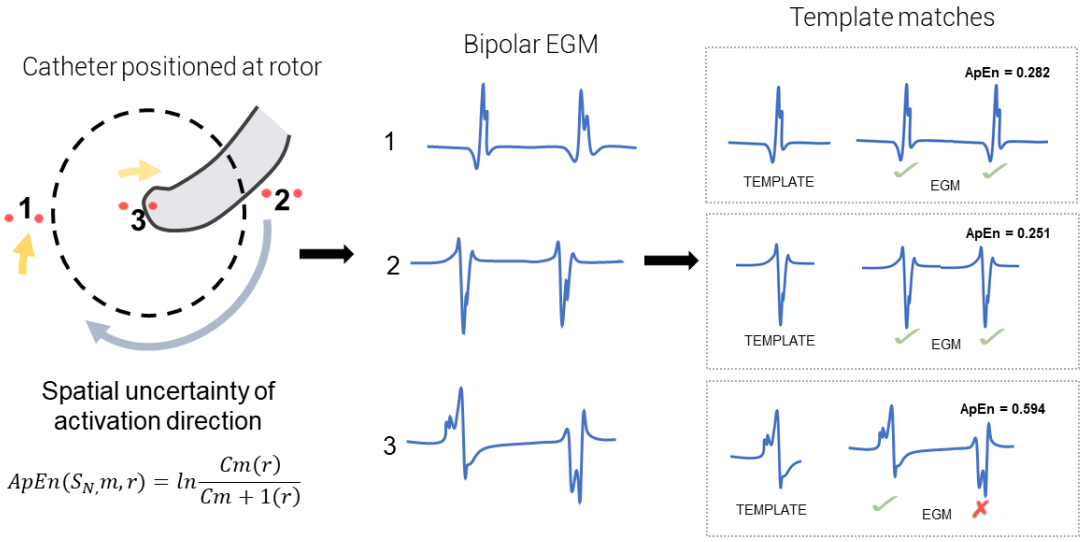

Figure 3.2: Schematic showing high ApEn correlating to centre of rotors

ApEn examines the presence of repetitive patterns by measuring the difference between the template vector and the rest of the time series data. As ApEn will compare a vector to itself, the regularity of the overall signal is increased.

Computationally speaking, as opposed to the binning method used in ShEn algorithms, a kernel estimator is often used when calculating ApEn. Specifically, the kernel estimator is a model free approach of constructing a probability distribution of a variable, which centers kernel functions at each outcome of the variable and uses the estimated probabilities to compute appropriate entropy estimates [273]. The distance of each point in the time series to the reference point is weighted depending on the kernel function, and commonly, a Heaviside kernel function is used. The Heaviside kernel sets a threshold r as the weight for each point, which is equal to the width of the Heaviside

kernel function and determines the precision of the density estimation. A small r obtains a more detailed estimate, but requites more data points to ensure accuracy, whilst a larger r yields coarse probability estimates as too many points neighboring the reference will be included. With this in mind, r is typically set to a fraction of the data variance in practical applications, e.g. a function of the standard deviation of the dataset, to remove the dependence of entropy on the amplitude of the observed process. Other estimators, such as linear and nearest neighbor estimators, are also available but are not as widely utilized in ApEn computation [273].

Another important computational consideration is the length of the compared runs or window length m. The window length m allows the ApEn algorithm to search through the sequence S_N and measure the likelihood or prevalence, *Cm(r)*, that runs of patterns similar for m observations remain close on the next incremental observation [274]. Although there is no established consensus for ApEn parameter selection, it is typically suggested that an $m = 2$ be used for clinical data. Though such a value is frequently used in literature and allows comparison of study results to other published findings, it is important to acknowledge that ApEn estimates depend strongly on the combination choice of m,r and the epoch length N. Hence, thoughtful consideration with respect to what m represents in a biological sense is necessary for each individual dataset [274].

3.4.3 Sample Entropy (SampEn)

Another estimate of conditional entropy is sample entropy (SampEn). SampEn is a modified rendition of ApEn that works in much the same fashion [204]. Computationally, however, SampEn differs in two primary ways: i) it is not length dependent and ii) it does not include self-comparison of the template vector. In ApEn calculations, the template vector (the vector being matched to) is compared to all others in the time signal, including itself. As a consequence, the probability of the vector $Cm(r)$ will never equal zero. As a result of this, the overall ApEn is lowered, since a self-match will create the appearance of increased regularity. By foregoing comparisons between a vector and itself (Figure 3.3), Richman et al. were able to create the SampEn family of statistics with an ability to avoid this biased regularity [204]. SampEn is derived from previous approaches established by Grassberger et al. [94, 95], and uses the natural logarithm of the conditional probability that two vectors that are similar at m points will remain similar at an incremental point. Specifically, SampEn can be defined mathematically as:

$$SampEn = -log\frac{\sum A_i}{\sum B_i} = -log\frac{A}{B} \tag{3.7}$$

where A_i is the number of matches of length $m+1$ with the i^{th} template, B_i the number of matches of length m with the i^{th} template and SampEn the entropy measured in bits.

Like ApEn, SampEn is also commonly computed using kernel estimators. Computationally,

estimation of SampEn using kernel estimation is achieved using the conditional entropy equation 3.4, which is implemented with the Heaviside kernel function and uses the maximum norm to compute distances [273]:

$$C(X) = H(X_n|X_n^m) = -ln\frac{\langle p(x_n, x_n^m\rangle)}{p(x_n^m)} \tag{3.8}$$

where $p(x_n^m)$ is used to estimate the joint probability distributions $p(x_{n-1}), ..., x_{n-m}$ and $p(x_n, x_n^m)$ in the m-dimensional and $(m+1)$ dimensional spaces spanned by X_n^m and (X_n, X_n^m). Note that $\langle . \rangle$ represents the averaging across patterns, and K represents the Heaviside kernel function:

$$K = \Theta = (\|x_n - x_i\|) = \begin{cases} 1, & \text{if } \|x_n - x_i\| \leq r \\ 0, & \text{if } \|x_n - x_i\| < r \end{cases} \tag{3.9}$$

and $p(x_n)$ the kernel estimate of the probability distribution:

$$p(x_n) = \frac{1}{N}\sum_i = 1^N K(\|x_n - x_i\|) \tag{3.10}$$

where $\|.\|$ is the maximum norm. Consequently, this kernel estimate of conditional entropy reduces the bias seen in ApEn [273].

In studies, SampEn demonstrated greater robustness over a broad range of conditions, potentially making it a more useful algorithm in studies analyzing physiological data [203]. SampEn also showed greater performance with short datasets, showing less dependency on the data length in comparison to ApEn estimates [274]. Like ApEn however, SampEn is also sensitive to parameter choice, though showed greater relative consistency over a broad range of possible combination values for r,m and N [59]. Despite this, care should still be taken when choosing SampEn parameters.

3.4.4 Multiscale Entropy (MSE)

As discussed, ApEn and SampEn approaches evaluate the appearance of repetitive patterns to compute the regularity of a signal and calculate entropy. One potential limitation of these methods, however, is that increased entropy may not always translate to increased dynamical complexity. As Costa et al. argue, entropy-based measures such as the Kolmogorov complexity and entropy rate, grow monotonically with randomness [58]. Consequently, such measures will yield high entropies for uncorrelated random signals such as white nose, which possess low predictability but are not structurally 'complex'. A randomized time series will also yield higher entropy than the original

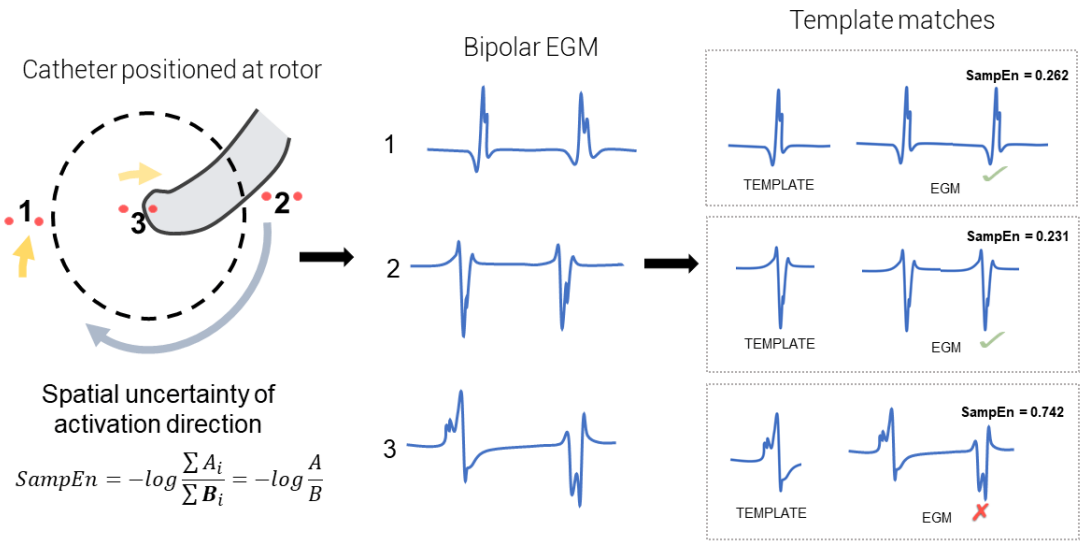

Figure 3.3: Schematic showing high SampEn correlating to centre of rotors

Like ApEn, SampEn also examines the presence of repetitive patterns by measuring the difference between the template vector and the rest of the time series data. Unlike ApEn, SampEn excludes self matches and avoids biased regularity

signal, despite the fact that the process of creating surrogate data destroys correlations and degrades the information content of the time series. With this in mind, Costa et al. aimed to develop a quantitative measure of dynamical complexity with three basic hypotheses in mind: i) that the complexity of a biological system reflects its ability to function and adapt in an evolving environment; ii) biological systems operate between multiple spatial and temporal scales, thus possessing multiscaled complexity; and iii) a number of disease states that reduce the adaptive capacity of the individual seemingly degrades the information carried by output variables. As such, Costa et al. introduce a multiscaled entropy (MSE) approach that quantifies entropy over a range of time scales [59].

Using MSE, measurements have the ability to reflect that both completely ordered and completely random signals are not truly complex, and identifies that correlated random signals are more complex than uncorrelated random signals [58, 59]. The inclusion of measurements from a variety of temporal scales also includes two major advantages: i) the ability to assess complexity at longer and shorter time scales and ii) quantification of the overall system complexity, which is equal to the sum of entropy values over all temporal scales [42].

Computationally, MSE implements the SampEn algorithm to assess complexity. The primary motive for using SampEn as opposed to ApEn is its greater consistency over a broad range of r,m and N values, as well as its reduced dependency on the time series length [59]. In comparison to the multiscaled complexity approach introduced by Zhang et al. for physical systems [277], which is based on ShEn, the use of SampEn also allows MSE to become better suited to physiologic time series. The use of Shannon's definition of entropy in Zhang's method requires a large amount of

virtually noiseless data in order to accurately map to a discrete symbolic sequence, which introduces limitations when applied to free-running physiologic signals [59].

In recognizing these considerations, Costa bases MSE on a modification of Zhang's and Pincus' approaches. Specifically, MSE comprises of two steps: i) 'coarse-graining' of the time series, which derives the representations of a system's dynamics at varying temporal scales (a form of resampling) and ii) application of SampEn on each of the coarse-grained time series [59]. Specifically, construction of a coarse-grained time series involves averaging a successively increasing number of data points using non-overlapping windows. Mathematically, each element of the coarse-grained signal is computed using:

$$y_j^{(\tau)} = 1/\tau \sum_{i=(j-1)\tau+1}^{j\tau} x_i \tag{3.11}$$

where τ represents the scale factor and $1 \leq jN/\tau$. In effect, the length of each coarse grained data will equal the length of the original time series divided by the scaling factor τ [271].

Following this, SampEn is used to calculate an entropy estimate for each coarse-grained time series plotted as a function of the scaling factor τ. This step is referred to as the multiscale entropy analysis. In traditional uses of SampEn, data from certain pathologic time series that may be chaotic/unpredictable but arise from less physiologically complex systems and mechanisms, such as data from episodes of atrial fibrillation, will result in higher SampEn. This is because such SampEn estimates are based on a single scale and hence will not account for features related to structure and organization on other scales. The MSE results published by Costa et al. support this, showing that at a single scale, the entropy assigned to the time series of atrial fibrillation and congestive heart failure patients is higher than those of healthy patients. Contrastingly, when analyzed at multiple scales, the time series of healthy subjects are assigned with highest entropy, reflecting that healthy cardiac dynamics are the most physiologically complex [59]. Whilst these results contradict those obtained using traditional ShEn, SampEn and ApEn algorithms, they more accurately reflect the physiological complexity of the underlying system.

It is important to note that although Costa's MSE algorithm is widely used in multiple fields, this approach still suffers from limitations. First, spurious MSE oscillations are introduced due to the inefficient process of eliminating fast temporal scales, and the original coarse graining procedure also artificially reduces MSE. To rectify these issues, Valencia et al. develop a refined multiscale entropy approach (RMSE) [240]. The RSME approach utilizes a low-pass Butterworth filter instead of an FIR filter to eliminate fast temporal scales, which ensures a more accurate elimination of components above the specified cut-off frequency. In addition, RMSE uses a refined coarse graining procedure that implements a continuously updating r, defined as a percentage of the standard deviation of the filtered series. In effect, this compensates for the decrease in variance related to the filtering procedure for removal of the fast temporal scales [240].

Though RSME overcomes spurious MSE oscillations and biased reduction of MSE estimates, it is difficult to reliably compute over short time series. In response, Faes et al. introduce the linear MSE (LMSE) method [77], which utilizes linear state-space models to provide a multiscale parametric representation of an autoregressive process observed at multiple time scales. LMSE exploits the state-space parameters to quantify the complexity of the process. Results show that in comparison to both RSME and MSE, application of LMSE to short cardiovascular data provides a better description of the physiological mechanisms producing biological oscillations at different temporal scales [77].

Another limitation of MSE is that the statistical reliability of SampEn for a coarse-grained time series is reduced as the time scale factor τ increases. This is because for an N point time series, the length of the coarse-gained series at scale factor τ is N/τ. Consequently, the larger the scaling factor, the shorter the coarse-gained series and hence, the variance of the estimated entropy will increase as the scaling factor increases. To overcome this, Wu et al. developed the concept of a composite multiscale entropy (CSME) to reduce the variance of estimated entropy values at large scales [254]. Specifically, CSME achieves this by calculating the sample entropy of all coarse-gained time series and finding the mean of the τu entropy values, rather than only the first coarse-grained time series as proposed by Costa [254].

3.4.5 Wavelet Entropy (WE)

While the aforementioned algorithms all compute entropy in the time domain, entropy estimates can also be calculated in the frequency space. Broadly speaking, computing entropy in the frequency domain consists of transforming the time series using methods such as the Fourier transform or wavelet decomposition [207]. Although signals used within the medical field are predominantly presented in the time domain, representation in the frequency domain may provide advantages in certain applications. For example, studies have postulated that the frequency band with the highest strength correlates to the cycle length derived from time domain analysis [174], which is annotated as the dominant frequency (DF) [211]. This becomes potentially useful in signals with deflection, varying amplitudes and more complex temporal patterns, wherein time domain measurements of the cycle length are likely to be inaccurate [20]. As this is often the case during AF, frequency-based analyses may provide a better measurement of the atrial rate. It should be noted, however, that the frequency spectrum may also be determined by other factors outside of cycle length, such as morphology and amplitude. As such, wavelet entropy methods that combine both entropy and frequency analysis may provide additional insights and more robust analyses in comparison to DF analysis alone [76, 174].

Specifically, wavelet entropy (WE) combines entropy and wavelet decomposition to provide an estimate of the degree of disorder present within a signal [207]. The wavelet entropy of a signal

can be given by:

$$WE = -\sum_{j=1}^{N} E_j log(E_j) \tag{3.12}$$

Where E_j is the relative energy associated with the wavelet coefficient at scale j and N the number of wavelet decomposition levels. Calculating entropy in this way provides a measurement of the amount of order or disorder in a signal, wherein WE will assume a value that is very low and close to zero for an extremely organized signal such as a periodic mono-frequency event, and high WE for random signals such as white noise [209]. Consequently, EGM or ECG signals with greater complexity and irregularity will result in high WE.

3.4.6 Transfer Entropy (TE)

Transfer entropy (TE) is an information theoretic measure that can be used to understand the information transfer between joint processes [24]. In systems consisting of more than one component or variable, understanding information transfer between these variables can be extremely useful in determining its structure and mechanism. Many studies have attempted to study such relationships using an alternate information-theoretic measure known as mutual information (MI), which provides a model-free approach to quantifying information overlap between two variables [252]. Specifically, this is achieved by measuring the amount of information that can be learnt from one random variable by observing another. Unfortunately, MI measures do not capture dynamical and directional information exchange, and hence poorly describe causal relationships [215]. For example, MI is symmetric under the exchange of signals and cannot differentiate between response and driver systems. Secondly, MI captures only the amount of information that is shared by two signals, rather than the information being exchanged (which better relates to causal dependence). To provide an asymmetric measure, delayed MI, which measures MI between a signal and another lagged signal, has been proposed. Though delayed MI reflects certain dynamical structures as a result of the time lag, it is still flawed and can cause issues when shared information from a common input or history is present. To address these problems, Schreiber et al. develop transfer entropy (TE) to provide an alternative information theoretic measure that shares some of the desired properties of mutual information, but also considers the dynamics and directionality of information transfer [215].

To measure TE between two variables X and Y, one needs to measure the amount of uncertainty (entropy) that is reduced in future values of Y by knowing past values of X, given the past values

of Y. In mathematical notation, the TE between X and Y can be given by:

$$TE(X \rightarrow Y) = \sum_{y_{t+1}, y_t^n, x_t^m} p(y_{t+1}, y_t^n, x_t^m log \frac{p(y_{t+1}|y_t^n, x_t^m)}{p(y_{t+1}|y_t^n)} \tag{3.13}$$

where $x_t^m = (x_t, \ldots, x_{t-m+1}), y_t^n = (y_t, \ldots, y_{t-n+1})$, and m and n the orders of the Markov processes X and Y respectively [252]. Typically, TE estimations use the Shannon entropy algorithm during computation to provide a measure of the uncertainty between X and Y [215].

It can be noted that the concept of transfer entropy shares some overlap with the statistical notion of causal influence termed Granger causality (GC) [24], which uses prediction via vector auto-regression to measure causality. Specifically, given sets of inter-dependent variables X and Y, Granger causality will say X Granger-causes Y if Y assists in predicting the future of X, beyond what X already predicts about its own future. In contrast, the information theoretic notion of transfer entropy is framed in the context of resolving uncertainty. For example, it can be said that the transfer entropy from Y to X is the degree to which Y disambiguates the future of X, beyond what X already disambiguates about its own future. This relationship was explicitly explored and detailed by Barnett [24], who shows that under Gaussian assumptions the concept of Granger Causality and Transfer entropy are in fact equivalent.

Although TE is prevalently used in neuroscience to understand the causal relationships between parts of the brain and responses to stimuli [252], it has thus far received little attention in the cardiac space.

3.5 Limitations of entropy

Although entropy is widely used in many fields, reliable estimation of information-theoretic quantities from empirical data can prove difficult. Firstly, the sensitivity of entropy estimates with respect to parameter selection can be problematic. Discretization of a time series using bins as commonly done in ShEn algorithms can pose potential problems, as inappropriately selecting bin-widths can lead to greater bias and reduce the accuracy of entropy estimates [197].

Additionally, both ApEn and SampEn show significant 2-way and 3-way interactions between m, r and N, hence are influenced heavily by the combination choice of these parameters [274]. Appropriate parameter selection is particularly critical when analyzing short data sets, as ensuring there is a sufficient number of matches can be problematic [140]. This can be seen in rapid diagnosis of AF. In such cases, choosing an m that is too large or r that is too small will result in too little template matches to estimate the conditional probabilities accurately. Conversely, if m is too small and r too large, all templates will match each other and cardiac different rhythms cannot be discerned. Although SampEn is relatively more stable across varying data lengths in comparison to

ApEn, inappropriate parameter selection, particularly in the choice of r, can still lead to inaccurate entropy estimates [140].

In addition, although bipolar EGM entropy-based approaches of AF mapping (such as ShEn mapping) have been proposed for identification of rotational activity, problems may be encountered in areas where wave propagation dynamics mimic such rotational sources. For example, areas in which multiple waves precess and cross propagate in varying directions may instead appear to originate from a single rotational source and hence, result in high entropy estimates similar to those seen for rotors. This could potentially present problems for a targeted entropy guided ablation strategy in the future.

3.6 Information theory and the intracardiac electrogram

Relating to the electrogram (EGM) morphology is the previously discussed concept of entropy. When applied to the intracardiac electrogram, entropy approaches have the potential to provide clinical insights into the underlying dynamics of AF. As entropy is linked to the information content of a signal, EGM with complex, non-uniform morphology will result in greater uncertainty and higher entropy. Conversely, an EGM with a regular, periodic morphology will result in lower entropy [84]. This characteristic makes entropy particularly useful in AF applications in which the ability to distinguish between AF and non-AF signals is required (AF detection algorithms), and where changes in the EGM morphology are thought to correlate to important AF triggers or substrates (AF mapping). The identification and localization of rotors provides a particularly interesting application of entropy within the AF mapping space, as it has been demonstrated that the pivot zone of a rotor experiences greater spatial uncertainty of wavefront direction, resulting in less stable bipolar EGM morphologies that can be quantified by entropy [17,83,84]. Other wave propagation dynamics are less well explored in relation to entropy, though additional mechanisms of interest (such as complex wavelet interaction regions) may also yield useful entropy characteristics. If statistical information theoretic approaches such as entropy can be used to pinpoint such potentially important AF landmarks, a targeted ablation strategy may become possible in the future.

In some ways, the concept of entropy shares some conceptual overlap with the notion of fractionation. Broadly speaking, the term fractionation is used to describe EGMs that possess multiple deflections and are prolonged, although no precise consensus definition currently exists [24, 166]. As such, like entropy, CFAE essentially aims to provide some definition to describe the complexity of an electrogram. A number of sources are said to be responsible for fractionation, with the local collision of multiple wavelets, local re-entry and zones of slow conduction said to result in EGM fractionation during AF [66, 254]. Consequently, it is thought that there is some relationship between CFAE and the maintenance of AF, thus CFAE mapping and CFAE guided ablation have

previously been explored [29, 47, 106, 166]. Though both CFAE and entropy aim to capture the qualitative property of signal fractionation to some degree, entropy is differentiated from CFAE by having a quantitative definition rooted in signal processing and mathematics, and does not use empirically derived definitions.

Outside of fractionation, entropy-based analysis of the EGM also has the potential to provide insights about the complex wave propagation dynamics underlying AF. For example, transfer entropy may possess the ability to determine information flow during AF and in turn, uncover causality and electrophysiological pathways between various regions of the heart that may be involved during AF propagation. Consequently, analysis of information flow may be useful for identifying the atrial regions central to maintaining AF [132].

3.7 Current studies using information theoretic approaches in atrial fibrillation

Though information theoretic and entropy-based approaches remain relatively limited within atrial fibrillation research, a handful of studies have explored their use. Broadly speaking, the use of entropy in AF can be categorized into three groups, namely: i) entropy for AF detection, ii) entropy for AF characteristic determination, and lastly iii) entropy for AF mapping. Some of the approaches using entropy in the current literature will be broadly discussed in the following, with particular focus on the role of entropy in AF mapping.

3.7.1 Entropy for AF detection

Presently, with respect to the study of atrial fibrillation (AF), entropy is most widely used for the detection of AF in ECG recordings and Holter monitors. As AF episodes occur paroxysmally in the majority of patients, human-based diagnosis of AF can oftentimes be difficult and time consuming, hence automated and computerized methods of AF detection have become a lucrative diagnostic application of entropy [63, 209].

Many algorithms have been developed to detect AF, which can often be broadly categorized as being based on either i) P-wave detection or ii) RR interval (RRI) variability [144]. Of these two methods, AF detection using the temporal variability of the RR interval has become a much more common approach in literature as analysis of the P-wave morphology is often difficult, as ECGs can be noisy and are prone to motion artefact. In addition, the determination of a P-wave fiducial point is challenging due to its low amplitude during AF which makes it more susceptible to corruption through noise, in turn lowering the signal-to-noise ratio [64, 143, 209].

Various studies have used Shannon entropy (ShEn) in conjunction with various other measures

of complexity such as the Turning Points Ratio (TPR) [64], Root Mean Square (RMS) of successive RR differences [64], symbolic dynamics [278] and time-varying coherence functions (TVCF) [144], among others, to better capture the randomness in the signal and detect variability of the RRI time series. As ShEn can be used to measure the level of uncertainty and information size in the signal, it can reflect whether the ECG morphology exhibits irregularities, and hence variability in the RRI time series. Results using these methods demonstrate high rates of sensitivity and specificity upwards of 95% [64, 144, 278], indicating the feasibility of entropy for detecting RRI variability.

Although the RRI time series approach is frequently used, widely available and capable of providing adequate AF detection in a number of cases, entropy-based approaches have also been used independently to detect AF [45, 140]. Sample Entropy (SampEn) algorithms have been used to detect the probability that runs of AF will match with others within the time series [140, 204]. A benefit of SampEn is its ability to use short runs or bursts of AF as a template for matching, hence avoiding issues relating to short AF episode durations that are common with RRI variability-based methods. These studies showed that SampEn provided a high degree of accuracy in distinguishing AF from sinus rhythm (5%), but encountered errors when atrial or ventricular ectopy were present, as this increased the entropy of the signal [45, 140].

The use of wavelet entropy (WE) for AF detection has also been explored in single lead electrograms [209]. This method was used under the premise that using entropy and wavelet decomposition in conjunction increases the robustness of the detection algorithm to noise, artifacts and non-stationarities. Ródenas et al. use this method to calculate the WE on a TQ interval to identify the presence and absence of the P-wave in each beat of the ECG, which in turn determines the presence of AF. Results demonstrated a discriminant ability of approximately 95% [209], which is comparable to results from other studies [45, 140].

3.7.2 Entropy for AF prediction and characteristic determination

To effectively treat atrial fibrillation, an understanding of the arrhythmia itself is also crucial. As such, another application of entropy is its use in determining the various characteristics of AF. One such area that has been studied are the changes in the RR interval dynamics preceding the onset of postoperative AF, as studying these characteristics may enable prediction of postoperative AF episodes. It has been hypothesized that heart rate variability (HRV), which can be used as an indicator of cardiac sympathovagal balance, would alter before the onset of postoperative AF and could be measured using entropy algorithms. Findings on this have been conflicting, however, with Hogue et al. showing a decrease in ApEn upon the onset of AF [109], whilst other studies show entropy and HRV analyses provide little predictive value when studying the onset of postoperative AF [15, 46].

Adding to this, it is argued that the ability to predict the spontaneous onset of AF for non-

postoperative patients is also important as it may allow prevention using electrical stabilization and various pacing techniques [235]. A number of studies have used ApEn and SampEn to predict the onset of paroxysmal AF (PAF), as these measures have the ability to measure the regularity of the time series signal, and hence quantify the heart rate variability (HRV) [253] [15] [222]. Findings showed that ApEn and SampEn could predict the onset of AF as entropy of the HRV reduced significantly in ECG preceding AF, in comparison to those distant from an AF episode [222, 235, 253].

In the same breath, predicting the termination of PAF may also have clinical implications, as it may in turn help improve management of the arrhythmia and avoid unnecessary treatments. Specifically, SampEn has been used to study the atrial activity (AA) organization from surface electrocardiograms (ECG) and predict the spontaneous termination of AF. It has been shown that SampEn of terminating AF episodes are lower in in comparison to non-terminating episodes [9–11].

Lastly, analysis of the HRV complexity using SampEn have also been used to evaluate the characteristics of both PAF and persistent AF. The study conducted by Sungnoon et al. aimed to test the hypothesis that impairment of cardiac autonomic control relates to increased irregularity in the AF signal. It was found that increased atrial signal irregularity as reflected by SampEn was consistent with an impairment of cardiac autonomic function in both PAF and persistent patients [229].

3.7.3 Entropy for AF mapping

AF mapping is pivotal to catheter ablation, as this helps locate AF triggers and substrates to guide the selection of ablation targets [25]. Currently, optimal ablation targets for persistent AF are still debated, as the mechanisms underlying this AF type are not yet well understood [117]. As a consequence of this, many approaches to AF mapping have been explored.

Masè et al. explore the use of entropy for quantifying synchronization during atrial fibrillation [159]. In this study, a synchronization index (Sy) was developed using Shannon entropy (ShEn) [219] to quantify the degree of synchronization during AF. Although AF is often described as being desynchronized, a certain amount of synchronized electrical activity is in fact present, and quantifying this was thought to facilitate the identification of various propagation patterns that may be associated with AF, and hence improve understanding on AF mechanisms and treatment. Sy was defined by quantifying the complexity of the distribution of the time delays between sites using ShEn estimates. Findings from this study showed that a progressive and significant decrease in Sy correlated with increasing AF complexity, using definitions for complexity classes as defined by Wells et al. [258]. Sy was also calculated on the whole right atrial chamber, showing the existence of spatial heterogeneities [159].

Following this, a number of studies have also utilised entropy for the identification of rotors during AF [83, 84, 188, 236]. There exists various schools of thought about the mechanisms driving an AF episode, with the rotor theory suggesting that AF is maintained by sites of rotational activation referred to as spiral waves or rotors [171,214]. There is clinical and experimental evidence to support this theory, and as such, rotors are thought to be potentially effective targets for ablation [169, 217, 225, 244]. Building on this, Ganesan et al. hypothesized that rotors could be identified through regions of high Shannon entropy, as wavefronts encircling the rotor pivot should result in broadening of the amplitude distribution of bipolar electrograms (EGM) due to their direction-dependent nature [84]. Findings showed that maximum ShEn co-located with the rotor pivot in computer simulated spiral waves, rat and sheep models, and human AF. Ganesan et al. also further explored the characteristics of high ShEn regions at rotor pivot zones [83] to test the hypothesis that pivot points possess higher ShEn than electrograms recorded at the periphery. It was found that the rotor pivot not only coincided with higher ShEn than those found at the periphery of the spiral wave, but also that pivot zones consistently resulted in maximum ShEn, irrespective of bipolar electrode spacing, signal filtering and rotor meander.

In a following independent study, Arunachalam et al. supported the ability for ShEn to identify rotors in isolated rabbit hearts [17]. Specifically, ShEn-based mapping techniques were used to identify pivotal rotor points in optically mapped data acquired from the rabbit hearts, following which the mapping approach was applied to clinical intracardiac human data. Results demonstrated that ShEn could accurately identify the rotor pivot in optically mapped data with known pivot zones, supporting findings published by Ganesan et al.. In a more recent study, however, Annoni et al. report that the performance of ShEn is greatly affected by the presence of artifacts, suggesting that other techniques such as multiscale frequency (MSF), Kurtosis (Kt) and Multiscale Entropy (MSE) provide more accurate and robust detection of rotors [16]. In a similar vein, Orozco-Duque et al. utilize approximate entropy (ApEn) for localizing rotors, under the hypothesis that complex fractionated electrograms (CFAE) are generated by the pivot point of a rotor [188]. Findings suggest that regions of high ApEn also co-located with the rotor pivot. Ugarte et al. also study the relationships between CFAE and the rotor pivot using ApEn [236], under the argument that a non-linear dynamic measure will better capture the property of fractionation in comparison to the empirical definitions proposed in the original CFAE study [166]. After simulating AF in a 3D human atrial model, results showed a positive correlation between ApEn and levels of fractionation, suggesting the ability of high ApEn regions to co-locate areas of high fractionation, and in turn the rotor pivot [236]. Sample entropy (SampEn) based approaches have also been explored for this purpose, with Cirugeda-Roldán et al. using SampEn to characterize the degree of fractionation in atrial electrograms [55]. A specificity of 86% and a sensitivity of 77% was reported when discerning between CFAE and non-CFAE electrogram signals.

Investigating the mapping of rotors further, Hwang et al. examined ablation approaches based on Shannon entropy (ShEn) in both 2D and 3D models [110]. The study compared ShEn to

other rotor mapping approaches commonly used in literature, namely: phase singularities (PS), dominant frequency (DF) and CFAE cycle length (CFAE-CL). Results from virtual ablation showed that ShEn, PS and CFAE-CL guided approaches did not result in AF termination or modify the AF into slow atrial tachychardia, whilst virtual DF ablation successfully achieved these end-points. Additionally, in 2D and 3D in-silico models, ShEn was shown to overlap with 33.2% and 27.5% of the rotor tip trajectory respectively, which was outperformed by DF wherein a 71% and 39.7% overlap was seen in the 2D and 3D models respectively [110].

Outside of rotor mapping, entropy can also be used to study causality and information flow. Transfer entropy (TE), which determines the directed exchange of information between two systems [215], can be used to investigate the direction and degree of information flow between electrograms. In a study conducted by Kosna et al., TE was used to study information flow between electrograms recorded in the high right atrium (HRA), coronary sinus (CS) and left atrial appendage (LAA) [132]. Findings demonstrated that information flow in the heart is symmetric, and that the direction and amount of information flowing between neighboring sites in the atria could be quantified using TE [132]. This suggests that studying information flow between different areas of the atria may provide useful insights into the complex wave propagation dynamics during AF.

Recalling the connections between transfer entropy and Granger causality (GC) as discussed previously, work published by Alcaine et al. [8] uses Granger causality based definitions to develop a multi-variate predictability framework to study information flow and causal relationships between different cardiac sites during AF. Using GC, causal interactions were analyzed between different atrial sites during different rhythms, by considering EGM as stochastic processes that interacts with neighboring atrial sites through information exchange that is driven by atrial activity. Predictability measures were also obtained from the residual variances of linear predictions performed with multivariate autoregressive (MVAR) modelling of involved EGM signals. As such, Alcaine's framework provides a measure of regularity for individual EGMs, in addition to the connectivity between neighboring sites [8]. Using computational simulations and clinical basket catheter data acquired from patients in paroxysmal AF, the study showed that the framework not only allowed different rhythms to be identified (using the regularity measures), but also that the underlying cardiac activity, acquired from simultaneous multi-electrode basket recordings, could be tracked and mapped using GC-based definitions. Although GC is a statistical concept rather than an information theoretic approach, this study demonstrates its connection to transfer entropy and its ability to also study causal relationships.

3.8 Summary and research gaps

Unfortunately, although AF has been a long-standing topic of research, there remains continuing debate regarding the mechanisms underlying the dynamics of the heart rhythm disorder. Currently,

there is some consensus that AF is the result of an interplay between substrate and triggering mechanism, though it is agreed that this interaction is not yet completely understood, nor is the triggering mechanism responsible.

Due to the complexity in understanding the AF phenomenon, establishing effective mapping approaches have proven hugely difficult, especially for real-time methods that can be used for guided ablation. While direct wavefront mapping during clinical AF procedures would be extremely valuable, current challenges make this approach practically impossible. With this in mind, a logical substitute is to take advantage of the intracardiac electrogram (EGM), which is the primary recording modality currently employed in electrophysiology (EP) clinics. Quantitative analysis of the EGM signal properties using information theoretic approaches has the potential to provide not only a clinically interpretable direct translation to what is seen in practice, but also insights into the system dynamics underlying AF. Aiming to understand the AF dynamics indirectly through analysis of the signal properties is not a left-field approach, as other well studied methods such as CFAE and DF use similar principles. Unlike these techniques, however, information theoretic approaches have the benefit of being less reliant on empirically derived definitions.

However at this time, few information theoretic approaches have been explored in the context of atrial fibrillation, particularly in AF mapping applications. Further studies are required to explore the various characteristics of measures such as entropy during AF, and understand their relation to the AF physiology. For example, there is room for studies to observe the spatial and temporal stability of EGM entropy, as this is an area that has not been investigated thus far. Understanding the spatiotemporal characteristics of AF may determine the presence or absence of spatial and temporal stability, which is important for developing novel adjunctive or primary ablation strategies based on high entropy regions as targets.

In summary, while information theory has proved a useful tool for analysis of physiological signals in other fields, it remains underutilized and under-explored in AF studies. As the AF phenomena is far from being understood, understanding the arrhythmia from a signal property perspective and using new approaches may be key to determining effective ablation targets and strategies for the ever increasing AF population.

Chapter 4

Spatiotemporal stability and specificity of high bipolar electrogram entropy regions in sustained atrial fibrillation: implications for mapping

The material contained within this chapter has been published in Dharmaprani, D., et. al., 2019. ***Temporal stability and specificity of high bipolar electrogram entropy regions in sustained atrial fibrillation: Implications for mapping***. Journal of electrocardiology, 53, pp.18-27. The core theme of the chapter is to research the use of entropy-mapping for atrial fibrillation, and assess the spatiotemporal stability of high entropy regions to make inferences about underlying re-entrant activity. Dhani's contribution to the study was data collection, development of the codebase, signal processing and computational analyses, statistical analysis, writing the manuscript and providing input for the conception of the study.

4.1 Introduction

Ablation outcome in persistent atrial fibrillation (AF) is a key area requiring improvement, with studies reporting the maintenance of sinus rhythm in less than 50% of patients following a single ablation procedure [56]. From this, it is clear that new approaches to human AF mapping are required [43, 248].

To date, a limitation of many of the emerging mapping approaches is that they have utilised internal or company-specific proprietary technology algorithms [25]. The paucity of externally verifiable algorithms has had important consequences for reproducibility and independent validation, and has led to growing scepticism regarding the viability of individual patient-level mapping in the AF ablation field [40]. In multiple instances, initially promising single-centre ablation results using novel mapping strategies [166,169] have been unable to be replicated in independent mapping studies [27] or well-conducted randomized controlled trials [19,248]. In this context, there remains a compelling case for rigorously performed, mechanistically-based, open-source signal analysis and mapping studies to improve mechanistic understanding of AF dynamics, and in turn improve ablation outcomes.

To address this, the use of an information theoretic measure known as entropy has recently been explored in AF applications to map rotors and provide insights into bipolar electrogram (EGM) signal properties [68]. The reasoning behind this is: i) experimental studies have suggested rotors as a potential AF driver [13,118,155,225], ii) entropy is well established outside of cardiology and is commonly utilised to provide insights into the dynamics of biological systems, with uses such as anaesthesia monitoring [239] and for the detection of epilepsy [180], and iii) entropy algorithms are open source, which may resolve the issue of reproducibility. In addition, bipolar electrograms are the most commonly used recording modality in clinical electrophysiology, making these signals readily available for entropy analysis whilst also providing a direct and interpretable translation to what is seen clinically. Lastly, high bipolar electrogram Shannon entropy (ShEn) has been demonstrated by our group to be associated with the pivot of rotors [25,83,85], and subsequently entropy-based identification of the rotor pivot has been independently observed by multiple groups using a variety of entropy-based approaches, and in multiple model systems [17,146,188,236].

Although the association of high entropy to the rotor pivot has undergone rigorous validation, application of entropy-based approaches to clinical ablation is reliant on two current gaps in literature: i) the spatiotemporal characteristics of entropy and ii) the specificity of high entropy. Specifically, spatial and temporal (referred to as spatiotemporal) stability determines whether high entropy regions are long standing and appearing consistently in the same regions over time, which would allow targeted ablation. On the other hand, specificity of high entropy determines whether these areas occur at only the pivot of rotors, or also other wave propagation patterns. The presence of both stability and specificity is critical to the feasibility of employing entropy for clinical AF ablation.

To address these gaps, the aim of this chapter was to explore the spatiotemporal characteristics and specificity of entropy using three studies: i) a medium-duration human basket catheter AF study, ii) a long-duration tachypaced sheep basket study, and iii) a computational AF study. These studies investigate the spatiotemporal stability of bipolar EGM entropy using three entropy-based measures of information content, Approximate Entropy (ApEn), Sample Entropy (SampEn), and

Shannon entropy (ShEn), applied to bipolar electrograms in prolonged recordings ($\geq$ 5 minutes) in human and ($\geq$ 20 minutes) animal experimental AF. To provide further insights into the potential AF mechanism responsible for the temporal characteristics seen in human and sheep models, a computer simulation study was performed to observe stability patterns in varying wave propagation scenarios.

4.2 Methods

4.2.1 Data Acquisition

Human AF Recordings

The vast majority of mapping studies available presently explore EGM properties using sequential AF mapping. However, a limitation of this approach is that it is limited by the inherent spatiotemporal stability of AF. Stable basket recordings can overcome this issue, and provides a means to assess the medium to long term temporal characteristics of electrograms [100]. Patients (n = 12) undergoing ablation for AF were recruited. Patients provided written informed consent with study approval by the Southern Adelaide Local Health Network Human Research Ethics Committee. 64-electrode basket catheters (Constellation, Boston Scientific, MA, 48mm (4mm spacing), 60mm (5mm spacing)) were utilized, based on pre-procedural computed tomographic scan atrial dimensions. Bipolar electrogram recordings [231] were obtained in spontaneous or induced AF lasting at least 5 minutes, similar to the protocol of Habel et al. [100]. For cases of induced AF, fibrillation was induced through rapid atrial pacing from the coronary sinus. 5-minute recordings were taken in the anterior left atrium (LA), posterior LA and right atrium (RA). Anatomical stability was verified by regular fluoroscopic visualization, and in NavX (Abbott, IL, USA). Signals were filtered from 30 Hz to 500 Hz with a sampling frequency of 1000 Hz using the Bard EP system (Laboratory System Pro, Boston Scientific, MA). Patient baseline characteristics are detailed in Supplementary Results A.

Sheep AF Recordings

To cross-validate findings in a secondary model system and allow for prolonged recordings of AF, an ovine model of sustained AF was also studied. To achieve AF, pacemakers were implanted in sheep and a rapid pacing protocol was carried out for $\sim$16 weeks. To perform pacemaker implantation, sheep were anaesthetised with sodium thiopentane 1g/sheep and 2-4% isofluorane in O_2. A customised single chamber permanent pacemaker (Medtronic, Dub, IE) was implanted within a subcutaneous pocket in each sheep's neck, and a pacing lead (Abbott, IL, USA) was introduced via the right internal jugular vein and screwed into the right atrial appendage guided by

periodic fluoroscopy and pacing lead signals. To prevent against infection, intramuscular injections of Noracillin (2mg/50Kg) was administered immediately prior to and for the following 5 days after the pacemaker implant procedure. An anaesthetic and anti-inflammatory agent (Rimidyl, 1ml/12.5Kg) was also administered during surgery and for the two days following. Following one week of recovery, the rapid pacing protocol was carried out. Pacemakers were set at an initial pacing rate of 200 beats per minute (bmp) or, if this rate could not be achieved, as high as possible while still maintaining capture. Pacing continued at this rate for 1-2 weeks to abbreviate the atrial tissue's effective refractory period and once achieved, the pacing rate was incrementally increased to allow for development of atrial fibrillation substrate over an 8 week period. The final rate of pacing (400 bpm) was maintained for 6 weeks to develop appropriate fibrillation substrate to promote sustained AF. Packemakers were interrogated weekly.

After successful induction of sustained AF, an electrophysiology study was undertaken under general anaesthesia using a 64-electrode constellation catheter (48mm). Bipolar electrograms were filtered from 30 Hz to 500 Hz, and sampled at 1000 Hz. For each sheep, $\geq$ 20 minutes of intracardiac data were obtained in both the left and right atrium. Anatomical stability was verified by regular fluoroscopic visualization, and in NavX (Abbott, IL, USA).

Computer Simulations

To provide further insight into the AF mechanisms underlying the human and animal entropy temporal characteristics, experimental results were compared to computational simulations demonstrating varying wave propagation patterns during fibrillation. This was particularly helpful as entropy mapping does not visualise the underlying wave propagation. Specifically, this study investigated simulations of: i) a single planar wave, ii) a single stable spiral, iii) colliding planar waves, iv) a stable spiral surrounded by moderately disorganised wave break-up, v) a stable spiral surrounded by highly disorganised wave break-up and vi) multiple wavelet re-entry without stable spirals (Figure 4.10 - 4.12).

Computer simulations were carried out on two-dimensional, isotropic, square grids based on the Tusscher-Panfilov model [232]. The rectangular grid used 80x80 diffusively coupled simulation nodes with a diffusion coefficient set to 0.02, which governs how the action potential is transmitted between coupled cells. If the diffusion coefficient is small, then propagation is slow and vice versa [86]. The system was integrated using a forward Euler scheme with no-flux boundary conditions, which causes an action potential propagating towards the edge of the 2D simulation to annihilate. This boundary condition is often used in simulations as it is thought to provide a realistic representation of a sheet of tissue being sliced out of the myocardium [198]. To achieve annihilation, the no-flux boundary condition causes the incoming wavefront to encounter a mirror image wave upon reaching a boundary.

In order to vary the degree of dynamical instability (e.g. the amount of wave break-up) and in turn the complexity of the dynamics of wave propagation, the value of the action potential recovery variable $\mu 1$ was varied between 0.02 and 0.2. This simplified model was used only to illustrate the link between different wave propagation dynamics and the resultant entropy characteristics. There are several mechanisms thought to play an important role in the maintenance of fibrillation (e.g. fibrosis, automaticity, heterogeneity of effective refractory period etc.), however, exploration of all potential factors is beyond the scope of this work and hence the study decided to simply focus on the spatiotemporal stability and specificity of entropy in relation to various wave propagation patterns. Since it was not the aim to model the detailed electrophysiology of the atria but rather show specific mechanisms, arbitrary units were used. Further details about the mathematical modelling of fibrillatory activity used for this analysis is provided in Supplement B.

Using the simulated square grid and parameterisation as specified, bipolar electrograms (EGM) were generated to calculate entropy using the same methodology as described for human and animal methods. To simulate bipolar EGM, extracellular unipolar EGM were first computed at each node of the isotropic grid as previously described [154] using equation 9.1:

$$u_{i,j}(t) = c \sum_{k,l=0}^{k,l=N} \frac{\vec{r}_{k,l} \nabla \upsilon_{k,l}(t)}{r_{k,l}^3} \tag{4.1}$$

where $u_{i,j}$ is the unipolar voltage at node (i, j), $\upsilon_{k,l}$ the transmembrane voltage at node (k, l) and $\vec{r}_{k,l}$ the distance between those nodes. A scaling coefficient is represented by c, which is assumed to equal 1 for simplicity.

Following this, bipolar EGM were computed as a difference of unipolar electrograms taken at a fixed spatial distance (equation 4.2):

$$w_{i,j} = u_{i,j} - u_{i+s,j}(t) \tag{4.2}$$

where $w_{i,j}$ is the bipolar voltage at node (i, j) and s represents the inter-electrode spacing (set to 3 in out study).

To determine the specificity of high entropy, additional AF-type scenarios demonstrating regions of repetitive wave cross propagation were simulated and analysed to test their association to high entropy. Specifically, these regions were defined as areas where waves pass from a multitude of directions, causing bipoles to experience an uncertainty in wavefront activation direction similar to what would be seen at the pivot of a rotor (Figure 4.13).

4.2.2 Signal processing

Export and Segmenting

Bipolar EGM were cleaned for low amplitude and noisy signals using an algorithm based on Welch's power spectral density [257] to ensure low contact and artifactual signals were not used in analyses. Specifically, this method estimates the power of a signal across various frequencies using a windowed discrete Fourier Transform (DFT):

$$S_k(v) = \frac{1}{K}\sum_{k=1}^{K} P_k(v) \tag{4.3}$$

where $S_k(v)$ is Welch's power spectral density (PSD), K the number of segments the data is partitioned into and $p_k(v)$ periodograms from the discrete Fourier transform. Signal power was used to identify poor contact signals as these tend to possess characteristically low amplitudes, as well as highly noise contaminated signals as these possess characteristically high amplitudes. To ensure accurate removal of bad channels, automatic removal was cross-validated using manual annotation. The remaining signals were then windowed into 5 second (5000 ms) segments; a temporal resolution used in previous literature to study spatiotemporal stability of EGM signal properties [100].

4.2.3 Entropy and Dominant Frequency Analysis

Entropy is an information theoretic approach that measures information content. In applications of signal analysis, this broadly speaking translates to measuring the complexity of a signal [68,219] (Figure 4.1). AF mapping of rotors provides an interesting application of entropy, as several studies have demonstrated that the pivot of rotors experience spatial uncertainty in wavefront direction. This in turn generates bipolar EGM morphologies that are less predictable and more complex, which can be identified using entropy [17,83,84,188].

In this study, entropy analysis was performed using three information theoretic measures: ShEn [219], ApEn [194] and SampEn [203], allowing for cross-validation of our findings. ShEn, ApEn and SampEn were estimated in 5 second windows for each bipolar electrode. For ShEn, samples were binned depending on their amplitude using a voltage histogram, with bin sizes dependent on the standard deviation (SD) of the signal ($binsize = 0.125 * SD$), as used in previous literature [83]. For ApEn and SampEn, we set an epoch length of $N = 5000$ (the window length at which to segment the data), a vector length $m = 2$ (finds matches of the same m voltage values within the sequence N) and a tolerance $r = 0.2{*}SD$ (determines how often the following point $m{+}1$

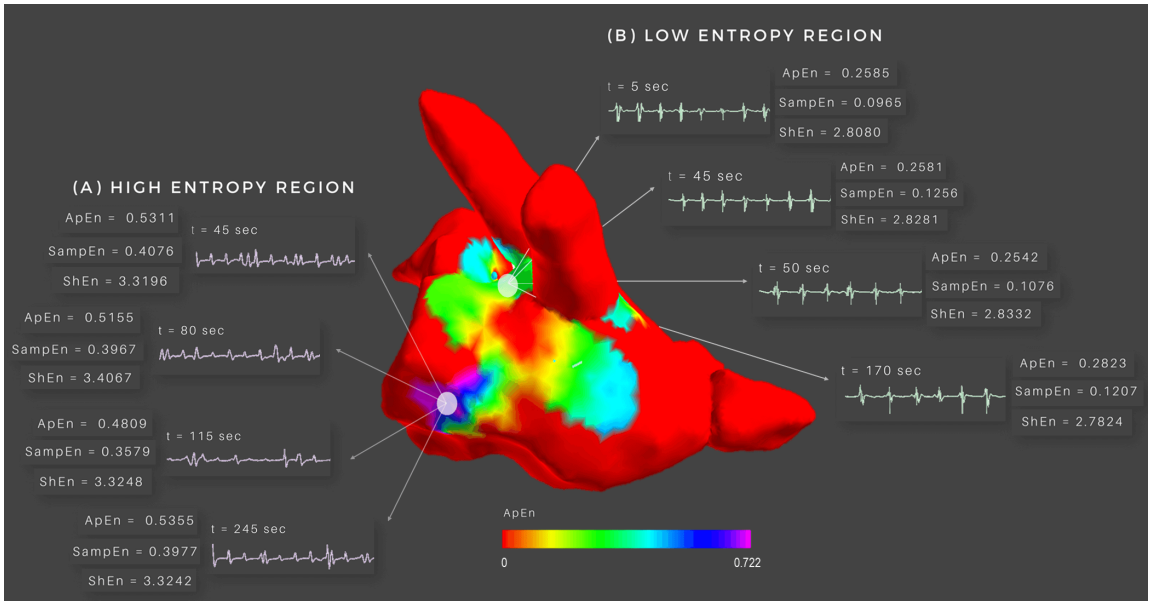

Figure 4.1: Schematic showing high entropy vs low entropy regions

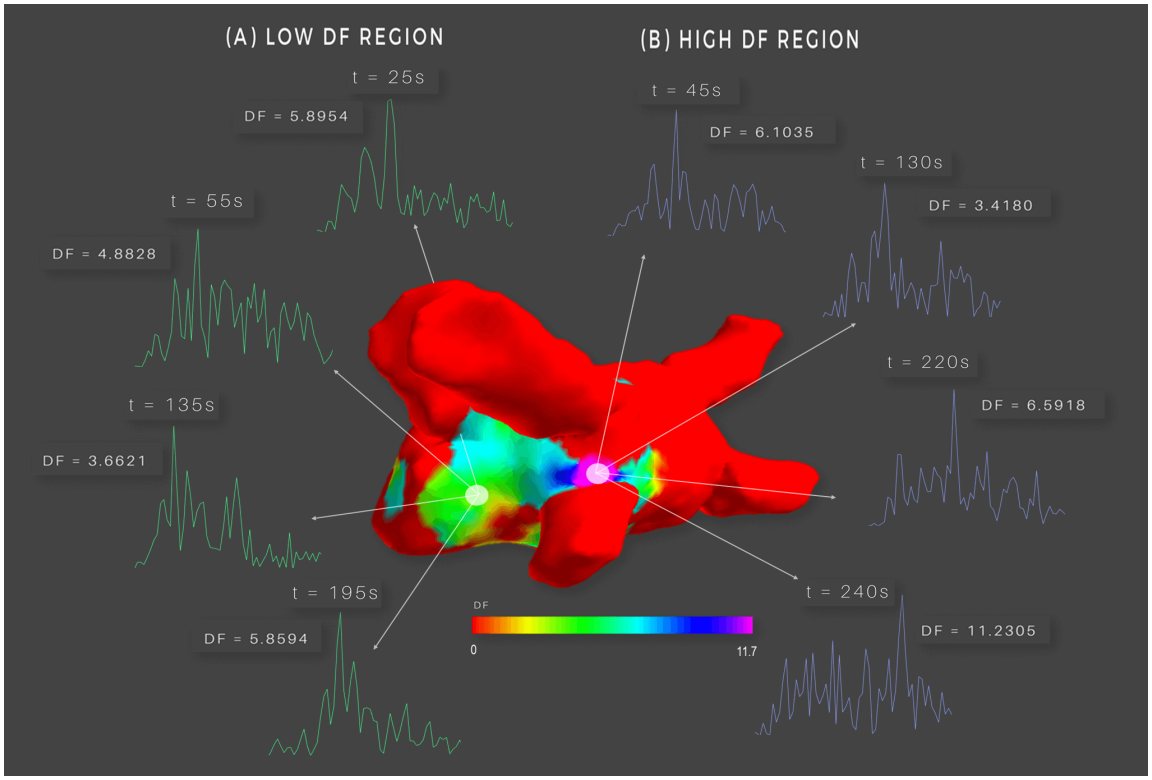

Figure 4.2: Schematic showing high vs low DF regions

lies within tolerance r of matched vectors). Details of these entropy algorithms are provided in Supplement C.

To compare entropy to a more established mapping approach with previously explored temporal characteristics published in literature, dominant frequency (DF) analysis was performed as previously described by Sanders et al. [211]. The rationale behind dominant frequency mapping is

that high-frequency activity is thought to be responsible for AF. It has been suggested that these regions can be identified using spectral analysis as they will correspond to the frequency with highest spectral power (referred to as the spectral peak) (Figure 4.2). To compute the DF, the edges of the signal were tapered using a Hanning window, followed by signal rectification and filtering with a non-biased 3 – 15 Hz band pass filter to minimise the double counting of bipolar double potentials. A fast Fourier transform (FFT) was then used to obtain the power spectrum of the electrogram at each recorded site (the anterior LA, posterior LA and RA), and assign the spectral peak as the dominant frequency (DF). However it can be seen in Figure 4.2 that the computed frequency transformation often produces many peaks close in amplitude. Therefore, to ensure that the DF selected reliably corresponds only to a distinct spectral peak, the regularity index (RI) of each DF was calculated. The RI is defined as the ratio of the power at the DF and its adjacent frequencies (∼0.75-Hz band) to the power of the 3 to 15 Hz band. Only points demonstrating RI $>$ 0.2 were included in subsequent analysis to control for ambiguity in DF detection related to poor signal-to-noise ratio.

4.2.4 Spatial Coregistration

In order to map entropy and DF spatially, ApEn, SampEn, ShEn and DF values were superimposed onto the respective 3D electroanatomical map (exported from NavX). To achieve this, custom C++ developed software (Valve Digital Health, Warsaw Poland) was used to project the three-dimensional (x,y,z) co-ordinates of each electrode onto the surface of the 3D map. The entropy and DF value at each electrode was then interpolated across the surface of the geometry in order to obtain maps as shown in Figure 4.3. This process was repeated for each 5 second segment, allowing the spatial location of entropy and DF to be assessed over time.

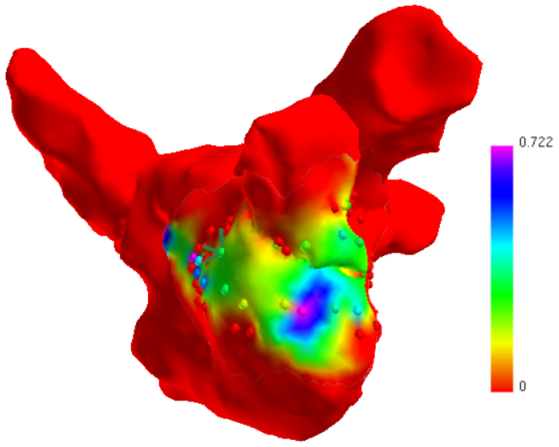

Figure 4.3: An example entropy map showing approximate entropy (ApEn) values spatially coregistered onto a 3D electroanatomical map exported from the NavX mapping system

4.2.5 Statistical Analysis

To study the temporal stability of entropy, the study utilised similar statistical analyses as previously published by Jarman [119] and Habel [100] to provide a multi-faceted approach to determine both the global stability of entropy and DF, as well as the relative stability of the highest entropy and DF regions.

First, the Friedman test was used to examine the global temporal stability of entropy and DF by ranking values in each 5 second window and looking at the differences in patterning across all segments [100]. The Friedman test is a non-parametric test that looks at differences between groups, with smaller p-values indicating significant differences. In this study, it was used to measure the global temporal stability of entropy and DF regions in each anatomical location, calculated using custom code developed in Matlab. Specifically, differences in patterning across all segments were observed (Figure 4.4) by ranking entropy and DF in each 5 second segment (stored in single-dimensional vectors) in ascending order using Matlab. Consistent ranking of entropy and DF values across the segments would suggest global temporal stability. A $P < 0.05$ was used to infer significant differences in patterning, and in turn global temporal stability of entropy and DF (Figure 4.4).

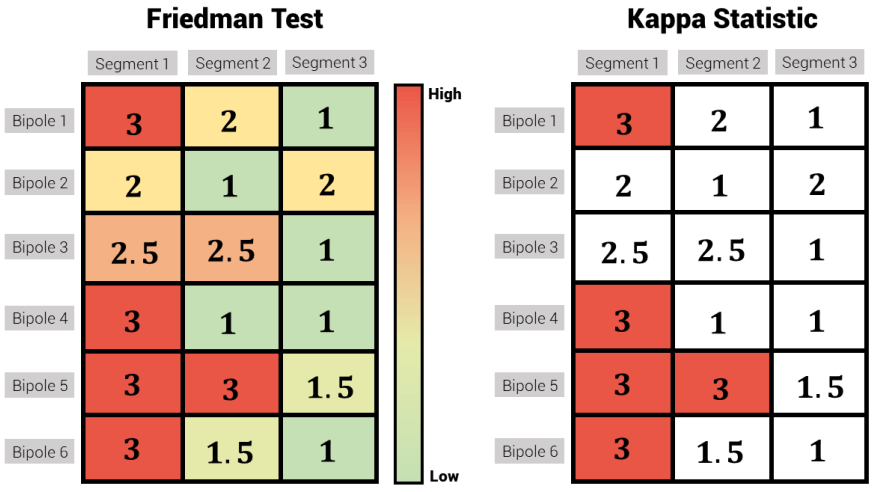

Figure 4.4: A schematic illustrating Friedman test and Kappa statistic computation
Left: Entropy and DF values in each segment are given a ranking, with the example showing highest values given a 3 (red) and lowest 1 (green). Using the Friedman test, the differences in ranking across each segment was analysed, providing a measure of global temporal stability **Right:** The top 10% of entropy and DF values were given a ranking of 3 (in red). Using the Kappa statistic, the agreement in the location and presence of only these top 10% values was analysed

As a secondary analysis of global pattern stability, bootstrapping was implemented. In statistics, bootstrapping allows inferences to be made about the sample distribution (or population) using only a small subset of samples. This is achieved by randomly re-sampling from the sample data with replacement to create a sampling distribution, which allows further inferences to be

made about the data. For example, if we want to draw conclusions about the mean height of a population but only have measurements from 1000 individuals, we can re-sample these heights with replacement n times to get a total of n means. A sample distribution of means can then be created to infer statistical properties such as the standard error and confidence interval of the estimated mean. This study made use of the assumed independence of values in each time segment, and therefore bootstrapped were created by randomly re-sampling the observed entropy and DF values by temporal segments (Figure 4.5). In turn, this obtained 10,000 randomly sampled versions of the original data matrix. The bootstrapped matrices were used to find an estimated sample distribution of Friedman test p-values. This in turn determined whether the observed experimental Friedman test p-value fell within the 95% confidence interval (CI) of the estimated sample distribution, allowing for validation of the experimental Friedman test p-value.

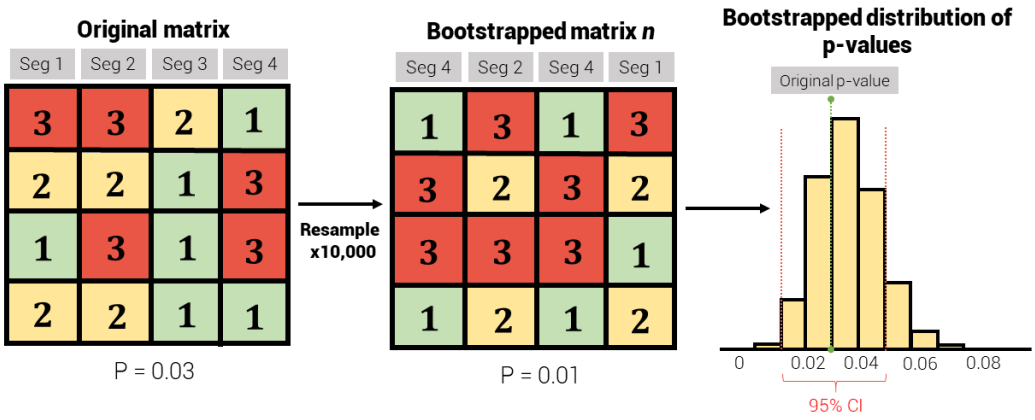

Figure 4.5: Process of running bootstrapping to validate Friedman test statistic
(The original matrix is randomly resampled to obtain bootstrapped matrix n). Bootstrapped matrices are used to create sample distribution and determine if experimental observed Friedman test p-value is within the 95%CI

The relative stability of high entropy regions were studied using the kappa coefficient, which analysed the temporal stability of only high entropy and DF regions [119]. In this study, the kappa statistic (a non-parametric test) was used specifically to measure the relative temporal stability of the top 10% of entropy and DF regions in each anatomical location. Kappa scores were obtained by ranking entropy and DF in each 5 second segment (stored in single-dimensional vectors) in ascending order using Matlab (Figure 4.4). We then categorized these rankings as high for the top 10% of values in each vector (given a score of 3), middle for the mid 45% of values (scored a 2) and low for the bottom 45% of values (scored a 1) as shown in Figure 4.4. The scored data matrix was then imported into Stata, and the 'kappa' function used to compare the position of the highest ranked values in each vector. Consequently, kappa values quantified the agreement of peak entropy across consecutive temporal segments. Consistent ranking of peak values in any given bipole would suggest relative temporal stability of the top 10% entropy or DF regions. Interpretations for the kappa statistic are detailed in Supplement D. Consistent ranking of the top 10% of values in any given bipole was suggestive of relative temporal stability. A threshold of kappa > 0.6 was used as

a cut-off of stability, as used by Jarman [119].

The coefficient of variation (CV) was also used to quantify the temporal variability of entropy and DF [100]. CV was calculated as a ratio of the standard deviation to the mean (SD/mean).

4.3 Results

Baseline characteristics of included patients are shown in Supplement A (Table A). Multiple episodes of AF were analysed in humans (H: 26 epochs, duration: 6,040 secs) and sheep (S: 15 epochs, duration: 4,160 seconds).

4.3.1 Global temporal instability of entropy

Entropy was found to change dynamically over time in medium to long-duration AF recordings, demonstrating global temporal instability. This was seen in both human and sheep models, and across all three entropy algorithms (ApEn, SampEn and ShEn). This dynamic change in entropy is clearly demonstrated in movie 1 (Supplement C), where the overall pattern of entropy is seen to exhibit flux and is not completely stable.

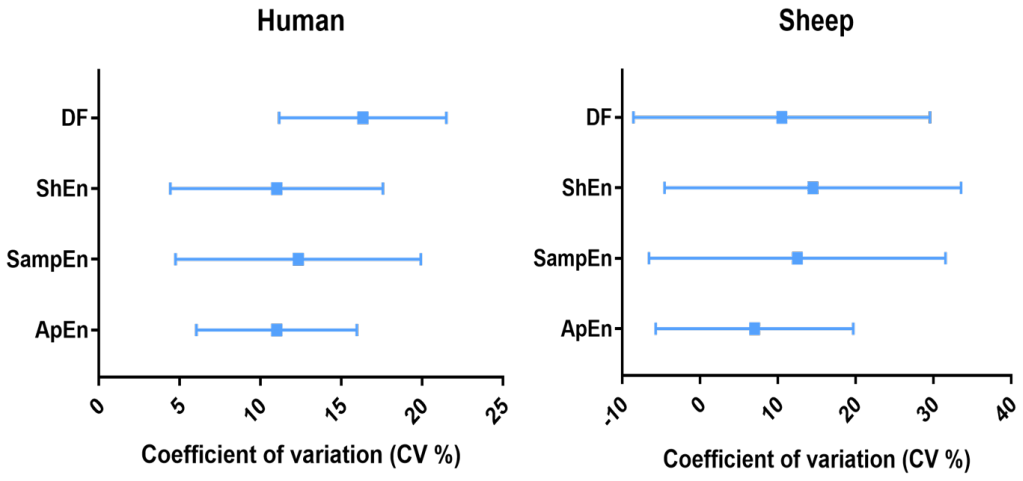

Figure 4.6: Coefficient of variation for ApEn, SampEn and ShEn in all cases of human and sheep tachypaced AF

CV for human and sheep cases. Center square indicates mean CV over all sites, and the line SD.

Statistically, these findings were supported by the small Friedman test p-values. In the human cohort specifically, analysis demonstrated inconsistent global entropy patterns for ApEn, SampEn and ShEn over time in the posterior LA (ApEn: $p < 0.001$; SampEn: $p < 0.001$; ShEn: $p < 0.01$), Anterior LA (ApEn: $p < 0.01$; SampEn: $p < 0.001$; ShEn: $p < 0.001$) and RA (ApEn: $p < 0.001$; SampEn: $p < 0.001$; $p < 0.01$). Additionally, the mean observed p-value ($P_{observed}$) fell within

the 95% confidence interval (CI) of bootstrapped p-values ($P_{bootsrapped}$), supporting the presence of global temporal instability.

In sheep, Friedman test analysis results aligned with human findings, obtaining statistically significant p-values in the LA (ApEn: $p < 0.001$; SampEn: $p < 0.001$; ShEn: $p < 0.001$) and RA (ApEn: $p < 0.001$; SampEn: $p < 0.001$; ShEn: $p < 0.001$). This indicates inconsistent global patterning of entropy over time, and global temporal instability of ApEn, SampEn and ShEn. Observed p-values also fell within the 95% CI of bootsrapped p-values.

The CV also confirms the global temporal instability of entropy. ApEn, SampEn and ShEn in humans showed a clear variability in entropy values over time in the posterior LA and Anterior LA (Figure 4.6). Similar values of coefficients of variation were seen in the RA (Table 4.1). Similar findings were seen for sheep in both the LA and RA (Table 4.2).

	Posterior LA	**Anterior LA**	**RA**
ApEn	11.5%	2.1%	2.1%
SampEn	15.7%	13.3%	18.3%
ShEn	10.2%	8.5%	14.2%

Table 4.1: Human CV by chamber

	LA	**RA**
ApEn	13.2%	13.8%
SampEn	18.3%	19.0%
ShEn	14.2%	14.2%

Table 4.2: Sheep CV by chamber

4.3.2 Relative temporal stability of the 10% of entropy

Despite the pattern of global flux, regions of highest entropy seemed to occur repetitively in the same location and exhibit modest stability. This was demonstrated in both human and sheep models, and across all three entropy algorithms (ApEn, SampEn and ShEn) as demonstrated in movie 1 (Supplement E) and Figure 4.7 and Figure 4.8, where the regions of highest entropy (in blue and purple) occur consistently in the same anatomical location, but transiently appear and disappear throughout the AF episode.

Kappa coefficients support this relative stability of highest entropy regions, with analysis of the top 10% of entropy in humans meeting the kappa stability cut-off of > 0.6 in the posterior LA for ApEn (0.61 ± 0.32 (Median$\pm$IQR)) and SampEn (0.65 ± 0.02). ShEn was just below the cut-off (0.58 ± 0.35). In the anterior LA, kappa met the cut-off for all three algorithms (ApEn: 0.70 ± 0.38;

SampEn: 0.61±0.23; ShEn: 0.60±0.39), as did kappa in the RA (ApEn: 0.66±0.17; SampEn: 0.66±0.16; ShEn: 0.65±0.19). Findings were similar for sheep, with kappa above 0.6 in the LA for ApEn (0.73±0.22) and SampEn (0.68±0.10), while ShEn yielded kappa just below the cut-off (0.59±0.15). In the RA, all kappa met the 0.6 threshold (ApEn: 0.76±0.22; SampEn: 0.74±0.18; ShEn: 0.61±0.27). Kappa values for human and sheep studies are summarized in Figure 4.9.

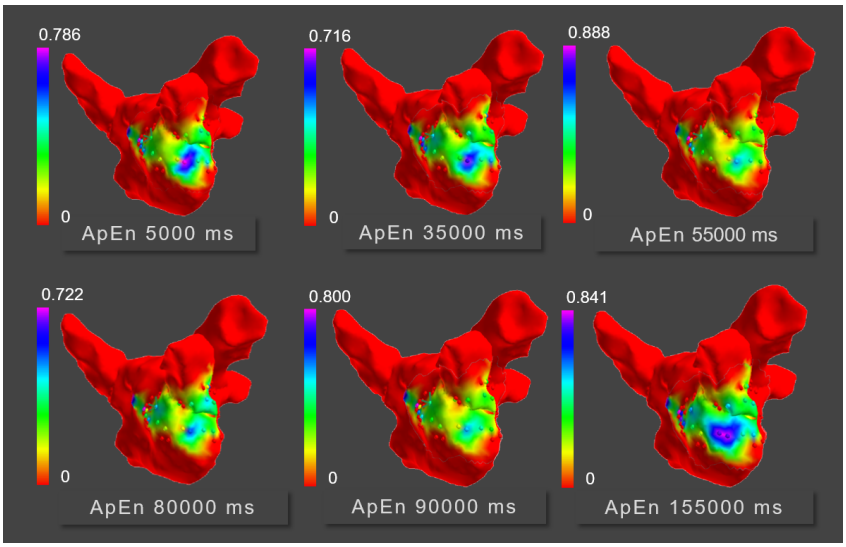

Figure 4.7: Relative temporal stability of 10% entropy regions for human AF

An example human anterior LA case. Each snapshot is representative of a 5 sec segment of recording, with ApEn plotted by color. Within the pattern of global flux and temporal instability, the top 10% of ApEn (in blue and purple) transiently recur at the same anatomical region

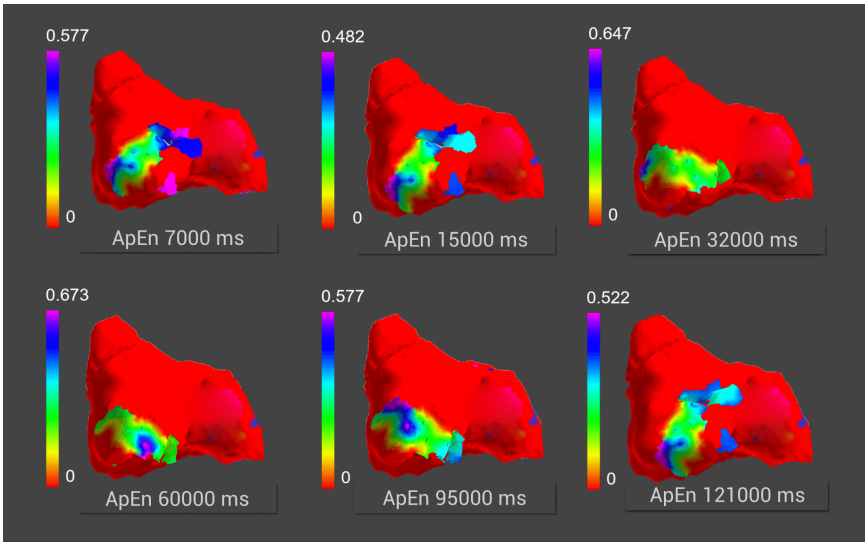

Figure 4.8: Relative temporal stability of 10% entropy regions for sheep AF

An example sheep LA case. Each snapshot is representative of a 5 sec segment of recording, with ApEn plotted by colour. The top 10% of ApEn (in blue and purple) exhibits modest temporal stability.

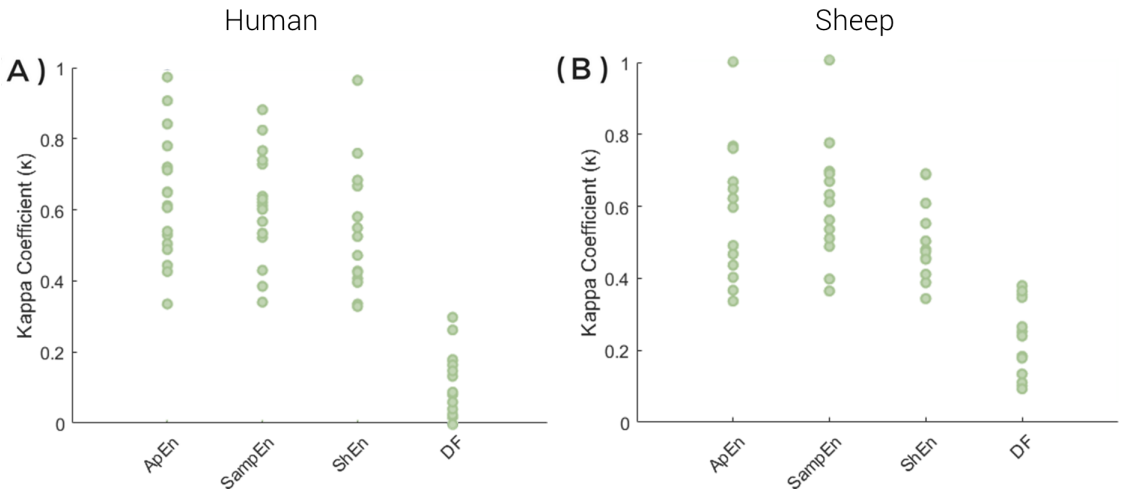

Figure 4.9: Summary of kappa values in humans and sheep

Scatter plot illustrating the distribution of Kappa across patients. For both species, DF did not demonstrate a relative stability of the top 10% of DF. Kappa across all entropy algorithms were consistently higher than for DF

4.3.3 Comparison of entropy temporal characteristics with DF

In both human and sheep models, DF demonstrated global temporal instability as reflected by the low p-values computed using the Friedman test (H: $p < 0.01$; S: $p < 0.01$). In addition, DF did not demonstrate a relative stability of the top 10% of DF in humans and yielded low kappa values (anterior LA: 0.09±0.15; posterior LA: 0.18±0.42; RA: 0.06±0.11). The same was seen in the long-term sheep study (LA: 0.22±0.22; RA 0.39±0.30). Kappa values were also found to be similar to those previously published by Jarman [119]. When compared to entropy, DF consistently yielded lower Kappa across all entropy algorithms and across the two species, with one way Anova testing reflecting these significant differences (H: $p = 0.003$; S: $p = 0.001$) (4.9).

4.3.4 Comparison of entropy temporal characteristics with computational simulations

To provide mechanistic insights into the potential AF mechanism responsible for the human and sheep temporal characteristics, findings were compared to various wave propagation scenarios.

Planar Wave Conduction

For planar waves (Figure 4.10), bipolar EGM morphologies were uniform throughout the mapped region, producing homogeneous ApEn, SampEn, ShEn and DF maps and high temporal stability (Entropy- Kappa: 0.921; Friedman test: $p > 0.01$; DF- Kappa: 1.00. Friedman test: $p > 0.01$).

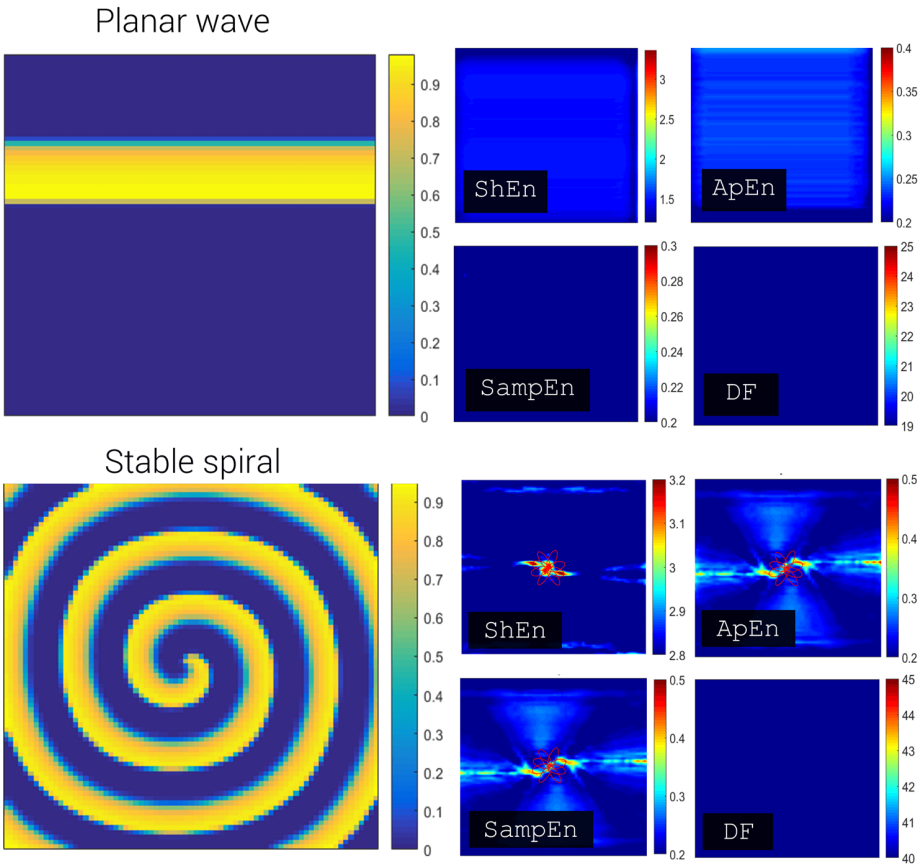

Figure 4.10: Stable spiral

Pivot point of spiral is marked with a red rosette

Stable spiral wave (rotor)

Bipolar EGM exhibited deflections with less regular morphologies at the centre of the rotor, producing a stable region of high entropy at the pivot (Figure 4.10). As maximum entropy is consistently localized at the pivot, high relative temporal stability of the 10% En (Kappa: 0.908) and global temporal stability ($p > 0.01$) of entropy was observed. Contrastingly, DF showed no association with the rotor pivot and was uniform across the mapped region (Kappa: 1.00; Friedman test: $p > 0.01$).

Planar Wave Collision

In simulations depicting the head-on collision of waves (Figure 4.11), low ApEn, ShEn and SampEn were associated with the collision zone. The difference between the collision zone and surrounding areas was ApEn: 0.08 bits; ShEn: 0.08 bits; SampEn: 0.03 bits. DF was uniform across the mapped region (18.4 Hz). High relative temporal stability (Kappa: 0.824) and global stability ($p > 0.01$) of entropy was observed

Relatively stable spiral surrounded by highly disorganised spiral wave break-up

Cases emulating a spiral surrounded by highly disorganised wave breakup (Figure 4.11) demonstrated low relative temporal stability of the top 10% of entropy and DF (Kappa: 0.319) and high global instability ($p < 0.0001$).

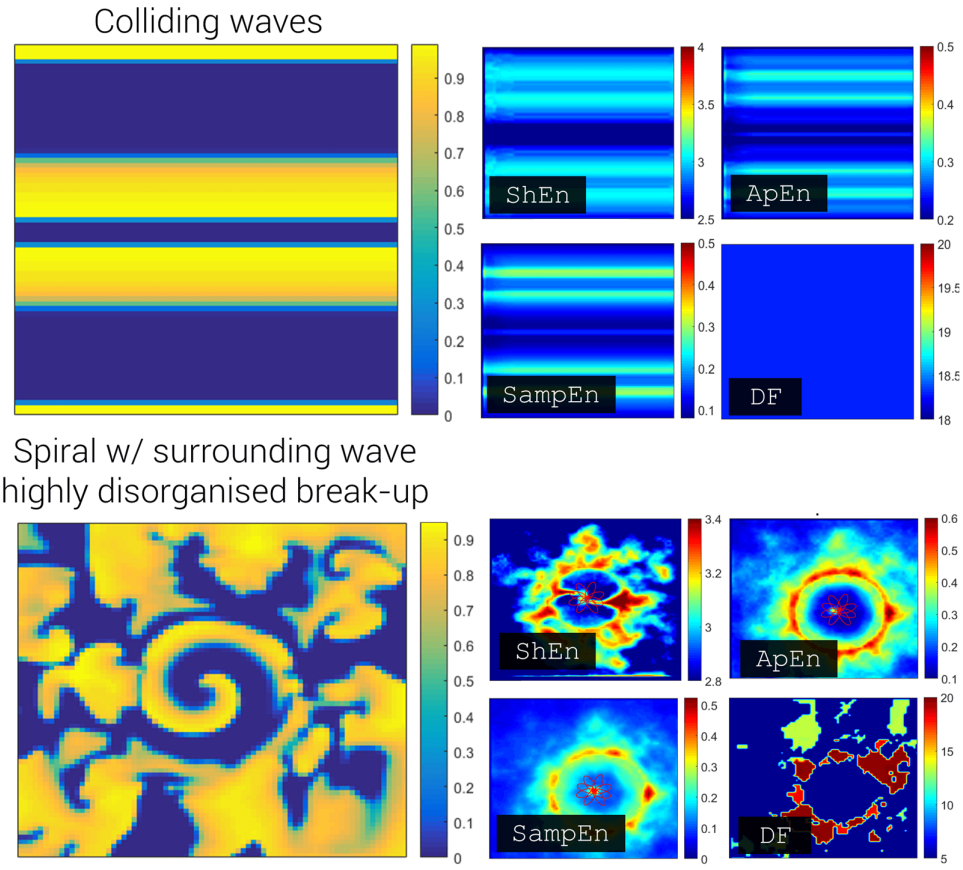

Figure 4.11: Relatively stable spiral surrounded by highly disorganised spiral wave break-up
Pivot points are marked with a red rosette

Relatively stable spiral surrounded by moderately disorganised spiral wave break-up

Contrastingly, a spiral surrounded by moderately disorganised wave breakup (Figure 4.12) reproduced human and animal results best, showing relative stability of the top 10% of entropy (Kappa: 0.610) but low global stability ($p < 0.001$). Like human and animal models, this model also produced top 10% DF regions with low stability (Kappa: 0.276; $p > 0.0001$). High entropy regions in these cases were associated with both the pivot and regions of repetitive cross propagation.

Multiple Wavelet Re-entry without locally stable spirals

Disorganised wavelet re-entry (Figure 4.12) demonstrated low spatiotemporal stability of the top 10% of entropy and DF (Kappa: 0.137) and high global instability ($p < 0.0001$).

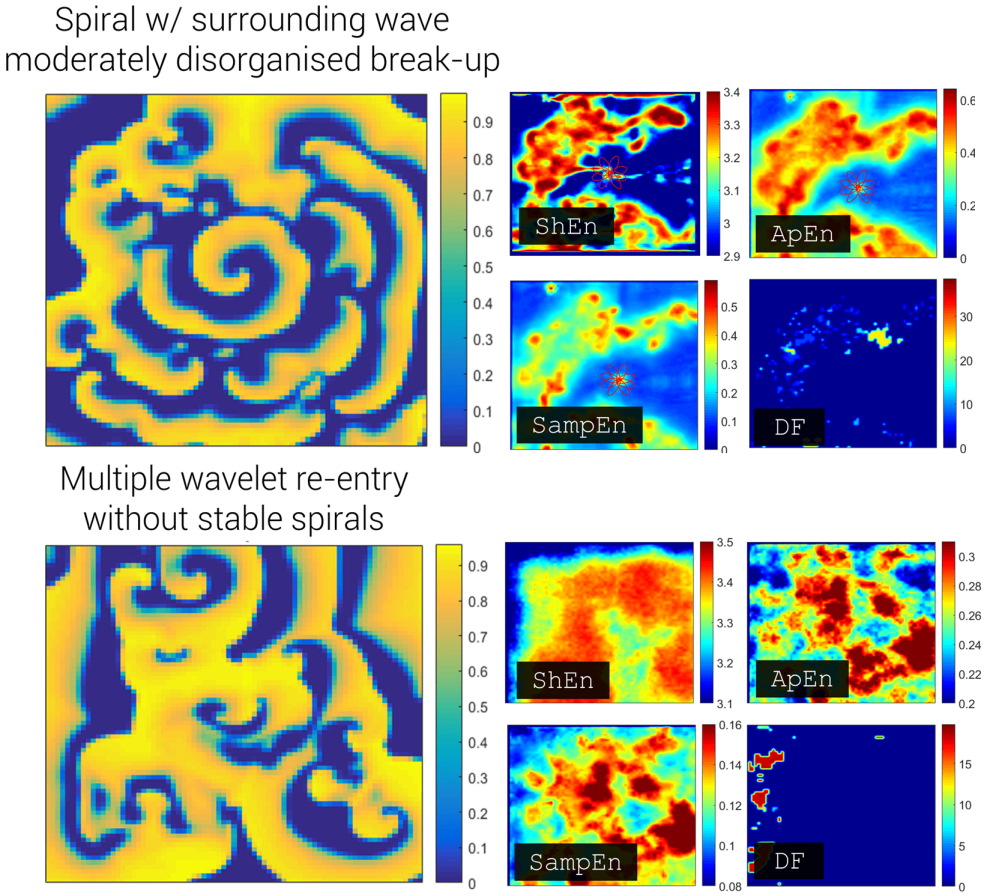

Figure 4.12: Multiple Wavelet Re-entry without locally stable spirals

4.3.5 Specificity analysis of high entropy

High entropy was not specific to only rotors, with regions of repetitive wave cross propagation also associated with high entropy (Figure 4.13). The entropy at the cross propagation zone was compared to surrounding planar propagation, with the difference equal to (ApEn: 1.75 ± 0.9, $P<0.01$; ShEn: 0.75 ± 0.3, $P<0.01$; SampEn: 2.5 ± 0.3, $P<0.01$).

Qualitatively, high entropy regions were associated with interaction zones where waves repeatedly arrive from different directions, whilst high DF regions did not show association to such behaviour (Figure 4.13).

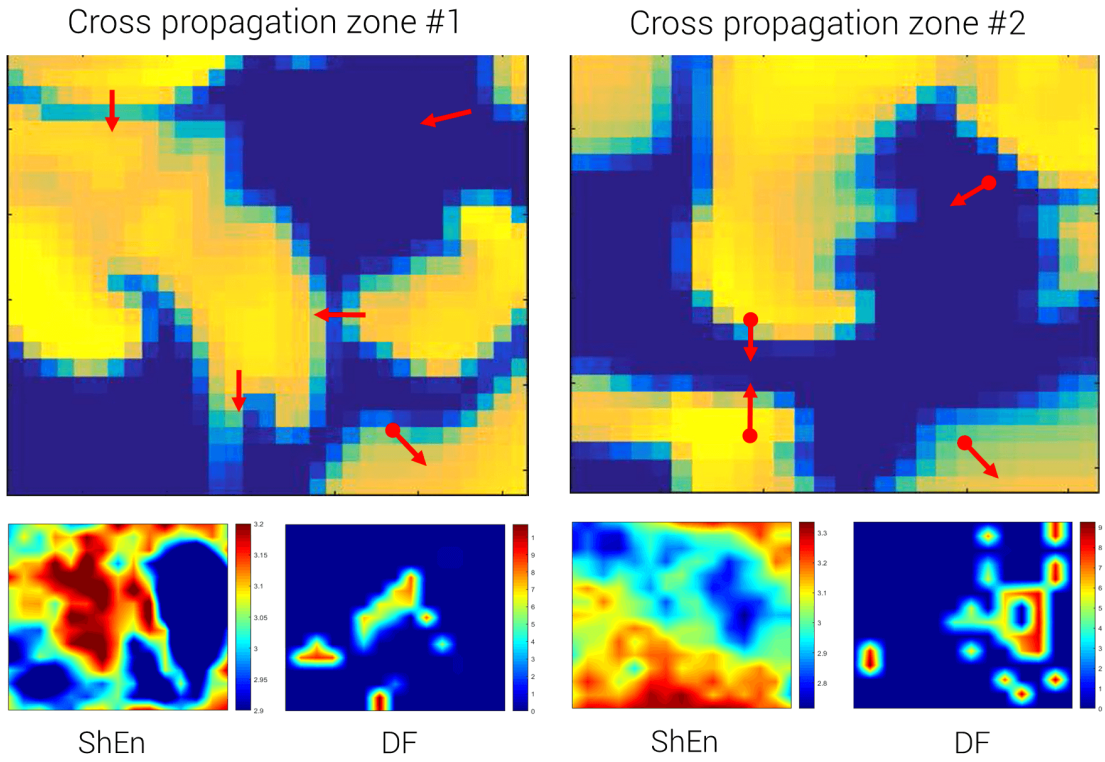

Figure 4.13: High entropy is not specific to rotors, occurring also at sites of repetitive wave cross propagation

Computer simulation demonstrated an association between high En and cross propagation regions. At such sites, waves arrive from different directions (indicated by arrow), creating spatial uncertainty in activation direction similar to what is seen for rotors.

4.4 Discussion

To date, the vast majority of electrogram stability studies have used sequential electroanatomic mapping, which is limited by the inherent spatiotemporal instability of AF. The use of stable basket recordings overcomes this, however, relatively few studies currently utilise this approach. One study, by Habel et al. [100], demonstrated high spatiotemporal variability in complex fractionated atrial electrograms (CFAE) in human AF using a contact basket over 5 minutes. Another by Jarman et al. [119] used a non-contact basket catheter to assess high-density DF spatiotemporal stability over prolonged recording periods, whilst Child et al. [50] used simultaneous panoramic recordings to assess the temporal stability of phase singularities (PS). Together, these studies have suggested a high degree of temporal instability of electrogram properties in sustained AF when mapped using DF, CFAE and PS, suggesting these regions are constantly migrating, making them potentially challenging to target for ablation. Although entropy provides an appealing new approach to targeted ablation, it remained unknown whether such approaches to mapping would exhibit similar characteristics of temporal instability, which would hinder clinical application. In addition, the specificity of entropy was also unknown, which is influential to the application of entropy clinically.

To address these potentially important knowledge gaps, this chapter investigated the temporal characteristics and specificity of entropy using three studies: (i) a medium-duration human AF basket study, (i) a long-duration tachypaced sheep AF basket study, and (iii) a computer simulation study. The principal findings of these studies were:

- Global temporal instability of entropy and partial stability of the top highest entropy regions
- The temporal characteristics of entropy seen in humans and sheep were best modelled by a relatively stable spiral surrounded by moderate wave breakup
- Entropy was not specific to only rotors, however, occurring also at sites of repetitive wave cross propagation

A major strength of this study is that findings have been cross validated, not only across species, but also across multiple entropy algorithms, with comparison to DF, and with follow up analyses of computational simulations. Further, to counter issues of reproducibility that are common with many current AF mapping studies in the field, the entropy algorithms used for mapping in this study are open source, allowing study findings to be reproduced by others.

An important consideration in this study is the relationship of entropy to previous studies of CFAE and DF. The concept of CFAE ablation was introduced by Nademanee [166, 167], and consisted of ablation of multi-component fractionated deflections with a voltage cut-off ≤ 0.15 mV. Using a systematic approach, high-rates of AF termination were achieved in the original study, and favorable clinical outcomes by some others. Conversely, other studies failed to reproduce the promising outcomes [186]. The entropy findings in this study potentially provide a unifying explanation for the divergent findings of CFAE literature. While high entropy is demonstrated to be an intrinsic property of the pivoting regions of rotors, it also occurs at regions of repetitive wave cross propagation. This dual explanation for electrogram entropy is consistent with previous qualitative studies of fractionation in optically mapped atrial monolayers [237]. It may also provide an explanation of the divergent clinical results of CFAE ablation, with AF termination a repeatable observation at sites of fractionation (presumably driver regions with high entropy), but clearly lacking specificity (perhaps regions of wave cross propagation, also high entropy).

In regards to DF, this study closely reproduced previous findings suggesting spatiotemporal instability of bipolar EGMs in AF [100]. The seminal original studies of DF were carried out with analysis of optically mapped action potentials in cholinergically stimulated sheep AF [225]. The repetitive wave-like morphology of these signals is ideal for phase and spectral analysis, in contrast to the multi-component complex morphology of bipolar EGMs in AF [258]. When studied clinically, it has been difficult to demonstrate that DF based ablation leads to AF termination [249] or improved clinical outcomes [19]. The temporal instability of bipolar EGM-based measures of DF encountered in our study and others [100, 119], is consistent with clinical data presented thus far.

4.4.1 Implications for Future Studies and Clinical AF mapping

These results suggest that there appears to be overarching instability of entropy during AF, suggesting unstable underlying wave behaviour. However, within this instability regions of high entropy tend to recur in the same anatomical location, but are transient. While these high entropy zones may seem a potentially appealing avenue for targeted ablation strategies in the future, this at present may prove difficult due to the evanescent nature of these regions.

Further, methods of delineating rotors and regions of cross propagation will be needed before clinical application is possible. This may be achieved in future via the use of machine learning algorithms that utilize other electrogram features, in addition to entropy, to differentiate between these two modes of wave propagation.

These findings lay the foundation for future studies exploring the statistical properties of bipolar electrograms in human AF. The approach taken in this study, with primary analysis of AF EGM properties followed by exposition with computer simulations to provide inference, is rare thus far in the field.

4.4.2 Study limitations

Using the bipolar electrogram-based approach in the current study, direct inferences about wave propagation were unable to be made. There is no consensus fiducial point for myocardial electrical activation with the bipolar EGM [32], with its complex nature precluding direct annotation of activation timing. The study as such, does not provide an overall comprehensive explanation of the AF mechanism, with the links to potential wave propagation mechanisms being inferred instead. Nonetheless, the nuanced findings will be reproducible by others, and suggest a potential future direction to AF statistical signal processing studies.

4.5 Conclusion

This study demonstrates the presence of global temporal instability of entropy, which suggests underlying instability of wave dynamics. Within this instability, partial stability of the top 10% of entropy was demonstrated, with these regions recurring transiently in the same anatomical locations over time. However, as wave propagation was not analysed in this study it is difficult to discern whether these regions arise due to spiral waves or with regions of repetitive wave cross propagation. Collectively, these findings raise questions about the ability to use entropy-based mapping in a 'point-and-shoot' ablation method. The overarching temporal instability observed also raises fundamental questions about the origins of this chaotic behaviour, and whether it is key to the underlying AF mechanism.

To summarise, this study adds important insights to the current literature by:

- Cross-validating the spatiotemporal stability and specificity of entropy using three model systems: (i) human, (ii) sheep and (iii) computer simulated AF
- The study findings show that there is global temporal instability of entropy, which suggests an underlying instability of re-entrant activity
- Within this global flux, there was a partial stability of the top 10% of entropy, though this was only moderate
- Entropy was not specific to only rotors, also occurring at sites of repetitive wave cross propagation. This highlights a potential limitation for the application of entropy-based mapping for therapeutic targeted ablation
- Computationally, the temporal characteristics of entropy seen in humans and sheep were best modelled by a relatively stable spiral surrounded by moderately disorganised wave break-up
- This study also establishes statistical approaches as a means to study AF electrogram properties

Part II

Understanding the instability underlying re-entrant circuits

Chapter 5

Part II foundations and literature review

5.1 Introduction

Findings of the entropy study detailed in ***Part I*** points towards a mechanism of AF that includes re-entrant circuits that are dynamic and unstable in time and space. This finding aligns with observations from several studies published by independent groups [118, 163, 262]. In fact, the presence of unstable re-entrant circuits has been a consistent finding for over 100 years. In 1914, Garrey [89] was the first to note the presence of "... a series of ring-like circuits of shifting location and multiple complexity". Later, the computational models of Moe and Abildskov also described a similar phenomenon, describing the "...numerous vortices, shifting in position and direction like eddies in a turbulent pool" [165]. Similar results have been in subsequent more physiological computational models [199, 200], and a feature of multiple epicardial mapping studies, in both experimental models and in humans [129, 143].

Given the intrinsic instability of re-entrant circuits collectively implied by the findings of Part I and this published literature, the focus of the PhD moved towards understanding the origin of this instability. It was reasoned, given the random or *'stochastic'* nature of electrical wave propagation in fibrillation, that the destruction and regeneration of re-entrant circuits may be modelled using stochastic process theory. Specifically stochastic process theory is a sub-branch of probability theory, an area of mathematics concerned with the analysis of models that involve randomness, uncertainty or chance [202]. Probability theory can also be used to model complex and dynamical systems such as the weather or the stock exchange. While these systems are not purely random, they are sufficiently complex that it would be easier and more useful to summarise them using stochastic models rather than using deterministic models (whereby a deterministic

process describes a process where the output is fully determined by given initial conditions and parameter values).

Further motivating this research is the fact that although an enormous amount of scientific and clinical effort has gone into the development of strategies to map rotational circuits during fibrillation [97,101,169], a universal quantitative framework to understand and model the processes underlying their formation and destruction is lacking [193]. Understanding the generative processes involved in giving rise to these reentrant phenomena may provide critical insights into why they appear during fibrillation, and how they help sustain fibrillation.

Under this rationale, ***Part II*** of this thesis had the following general aims:

- To develop a probability theoretic framework using stochastic process theory to understand and model the formation and destruction of re-entrant circuits
- To investigate whether probability theory can provide inferences about the underlying mechanisms relating to the maintenance of fibrillation
- To investigate whether probability theory can provide new insights for mapping and future therapeutic strategies

An overview of probability theory and its application in cardiac electrophysiology

5.2 What is probability theory?

In general terms, probability theory is a branch of mathematics that concerns itself with analysing the outcome of a given *'experiment'*, whereby an experiment defines any procedure or process that can be repeated and possesses well-defined possible outcomes. If an experiment has only one possible outcome, it is referred to as *'deterministic'*. The strength of probability theory, however, is its ability to gain insights into seemingly random phenomena. These situations, whereby the outcome is unknown, are referred to as *'random experiments'*. Examples of random experiments include tossing a coin and rolling dice, but also more complex examples such as gene inheritance [78]. Because the outcome of a random experiment cannot be determined with certainty before it occurs, we instead predict the likelihood or probability of several possible outcomes (hence the name probability theory).

To understand how probability theory can be applied in the context of cardiac electrophysiology, the following section aims to provide a simple explanation of what probability theory is using standard axioms and examples.

Defining the sample space and events

The set of all possible outcomes of a given experiment is known as a *'sample space'*, denoted by Ω. For example, if we want to observe the outcome of a single coin toss, we have a sample space with two possible outcomes: *'heads'* and *'tails'*. In mathematical notation, the sample space of this coin toss is therefore given by [78, 233]:

$$\Omega = \{Head, Tail\} \tag{5.1}$$

Each individual outcome in the sample space is known as a *'sample point'*. If the sample set contains an infinite number of sample points, then it is a *'continuous sample set'*. Conversely if it contains a finite number of sample points, it is referred to as a *'discrete sample set'* [233].

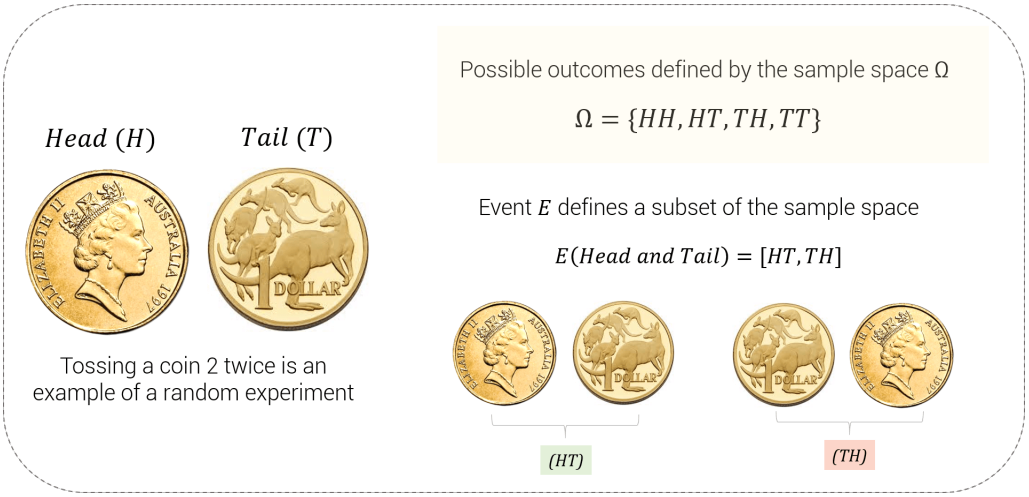

Figure 5.1: Illustration demonstrating the sample space and an example event for a random coin toss experiment

Within a sample space, it is important for each outcome to be distinguishable, hence we can denote a subset of the sample space Ω as an event E (e.g. E gives a set of sample points). For example, tossing a coin twice will result in a sample space of 4 possible outcomes (where H denotes heads and T denotes tails):

$$\Omega = \{HH, HT, TH, TT\} \tag{5.2}$$

In this instance, we must therefore be able to differentiate between landing on a head on the first toss and on tail for the second toss (H,T), and conversely landing on a tail on the first toss and on head for the second toss (T,H). By defining E as the event that we land on both heads and tails, we therefore can include both outcomes or sample points (H,T) and (T,H) (Figure 5.2).

Probabilities, random variables and the probability distribution

We can estimate the likelihood of a given event E occurring by taking the probability $P(E)$, which can assume any value between 0 and 1 (5.3) [206]:

$$0 \leq P(E) \leq 1 \tag{5.3}$$

If an event has no chance of occurring, it is called an *'impossible event'* and will equal 0. If an event is certain to occur, it is known as a *'certain event'* and will equal 1 [72]. It should be noted the sum of all the probabilities in the sample space is equal to 1. For the coin toss example, the

probability of landing on head will therefore be (equation. 5.4):

$$\begin{aligned} P(Head) &= \frac{n(E)}{n(\Omega)} \\ &= \frac{3}{4} \\ &= 0.5 \ (50\%) \end{aligned} \tag{5.4}$$

where $n(E)$ gives the number of outcomes defined by the event E and $n(\Omega)$ the total number of outcomes in the sample space.

In most cases, the outcome of experiments will be numerical values although this is not always the case. In some instances where the outcome may be *'yes'* or *'no'*, we may have to assign numerical values (e.g. 0 and 1) to each outcome. Assigning numerical values to outcomes in this way is useful because it allows identification of an outcome or event through the value of a function known as a *'random variable'*. A random variable, denoted by X, is a function that maps events within the sample space Ω on the real line R. In other words, the random variable assigns a real number to all possible outcomes of a random experiment. If the sample space is continous, the random variable X will be a continuous random variable, else if the sample space is discrete X will be a discrete random variable. To emphasise the fact that X is defined as a function of the sample space Ω, it is often written as [233]:

$$X : \Omega \rightarrow R \tag{5.5}$$

Therefore, for the random experiment of a single coin toss the discrete random variable X can be defined as:

$$X \begin{cases} 1, & \text{if Head} \\ 0, & \text{if Tail} \end{cases} \tag{5.6}$$

Defining outcomes using a random variable is useful as this allows us to describe the probabilities associated with all events and possible outcomes, rather than just a singular event as shown in equation 5.4. This is done using the *'probability distribution'*, which is a mathematical function that maps all possible outcomes of the random experiment depending on the random variable X. If X is a discrete random variable, then the discrete probability distribution $p(x)$ is given by the *probability mass function (PMF)* [53]:

$$p_x(x) = P(X = x) \tag{5.7}$$

where X is the random variable and x the value of the random variable. As all probabilities in the sample space should add to 1, the sum of P(x) over all possible values of x is therefore also equal to 1 [127]:

$$\sum_{i=1}^{n} p_x(x) = 1 \tag{5.8}$$

For a continuous random variable X, the probability of a specific value x cannot be defined and instead, the sample space is discretised such that we find the probability of X over a given interval, given by the *probability density function* [53]:

$$\int_{-\infty}^{\infty} f(x)dx = 1 \tag{5.9}$$

Much like the probability mass function, the integral given by the probability density function should equal 1.

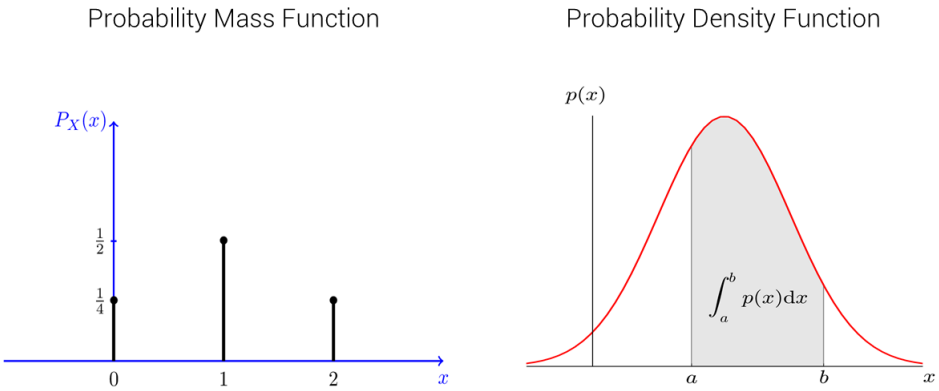

Figure 5.2: Probability mass function and probability density function

A worked example for the probability distribution of a discrete random variable

To elaborate on the concept of the probability distribution further, take for example a coin toss in which we flip a fair coin 3 times. This random process (experiment) will produce a total of 8 possible outcomes in the discrete sample space (with head denoted by H, and tail denoted by T):

$$\Omega = \{THH, THT, TTH, TTT, HHH, HTH, HHT, HTT\} \tag{5.10}$$

We can assign a random variable X to map the number of tails we obtain using numeric

variables such that:

$$X \begin{cases} 1, & \text{if 0 tails} \\ 0, & \text{if 1 tail} \\ 2, & \text{if 2 tails} \\ 3, & \text{if 3 tails} \end{cases} \tag{5.11}$$

Using the random variable X, we can then estimate the probability associated with each possible outcome:

$$\begin{aligned} P(X=0) &= \frac{1}{8}\ [HHH] \\ P(X=1) &= \frac{3}{8}\ [THH, HTH, HHT] \\ P(X=2) &= \frac{3}{8}\ [TTH, THT, HTT] \\ P(X=3) &= \frac{1}{8}\ [TTT] \end{aligned} \tag{5.12}$$

These probabilities define the PMF for this random process, whereby the PMF is a function $f(X)$ that describes the probability of the discrete variable X taking a particular value of x. If we take all possible values in the sample space and consider their associated probabilities, then this PMF also gives the discrete probability distribution. This can also be expressed as a normalised histogram as shown in Figure 5.3.

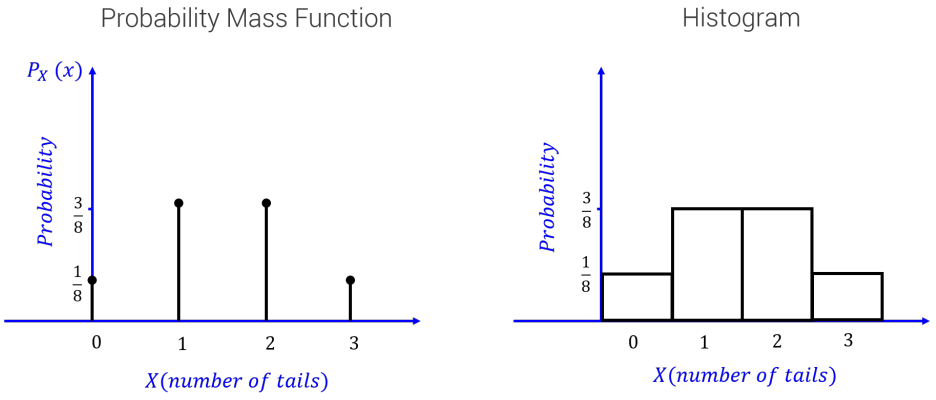

Figure 5.3: Probability mass function and histogram

5.2.1 Stochastic processes

Relating to probability theory is the concept of stochastic processes. In general terms, a stochastic process describes a random process that evolves over a common probability space. More accurately, it describes a collection or family of random variables [202]:

$$\{X(t) : t \in T\} \tag{5.13}$$

where t typically denotes time. In other words, for every time t in the set T, a random value of $X(t)$ is observed. Therefore, while a random variable can be thought of a single random element for a given point in time, a stochastic process is a collection of many random variables (one for *every* point in time). Examples of common stochastic processes include photon emission and the occurrence of earthquakes.

If T is a set of finite or countable integers that represent specific points in time (e.g. $t = 0, 1, 2.., n$), then the stochastic process is in discrete time. Otherwise, if the set T is not finite and definition 5.13 has a random value of $X(t)$ associated with all points in time, then the stochastic process is continuous [123].

Although we have discussed stochastic processes that evolve over time, the set T can also represent other domains like space, whereby the process will have a random value $X(t)$ for different spatial locations. Stochastic processes can also evolve in both time and space, known as *'spatio-temporal processes'*.

An important point to note as put forward by Karlin and Taylor [123], is that even though a process mat not be inherently or purely stochastic, it is often useful to model them as stochastic processes if they arise through deterministic chaos.

Poisson renewal processes

A special type of stochastic process is known as the *'arrival process'* [206]. Typically, an arrival process models the arrivals in a system as illustrated in Figure 5.4. Arrivals are denoted by S_n, which represent the time at which an event occurs. The times between individual events are referred to as the *'interarrival times'*, denoted by X_n [81]. Although we use the term arrival, this process can also refer to the departures in a system.

Within the class of arrival processes itself, a unique sub-type is known as the *'renewal process'*. A renewal process is an arrival process whereby interarrival times X_n are non-negative, and are mutually independent and possess the same probability distribution (this is a property referred to as *'independent and identically distributed'* (IID)) [81].

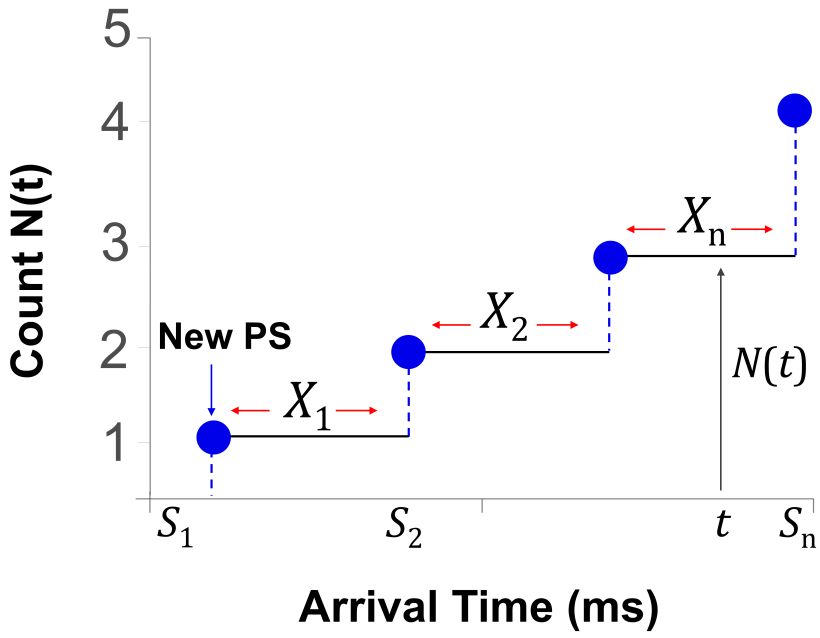

Figure 5.4: An arrival process of events S_n and its counting process ($\{N(t); t > 0\}$). $X(t)$ are random variables (rvs), and N(t) is sum of all rvs up to time t

The *'Poisson process'* is the archetypal example of such a renewal process, and has the following unique properties:

- Events are *independent* of one another. In other words, the occurrence of one event does not affect the probability of another event (a property known as *'memorylessness'*)
- The average rate of events (e.g. the events that occur per unit of time) is constant
- Two events cannot occur at the exact same time

To exemplify this, take for example the observed arrivals of passing cars. If we are sitting on the side of the road, we may observe cars passing as shown in Figure 5.5, whereby the arrival S_n of each car is completely random (stochastic). In other words, arrivals occur independently of one another and seeing a car arrive at time t doesn't mean we can predict when the next car will arrive. This is a property known as *'memorylessness'*, as the history of prior events has no effect on the outcome of future events. The memoryless property is what makes the Poisson process unique among other stochastic processes.

However, although individual arrivals are random, we are able to measure the average time between arrivals, which is a constant. The reasoning behind this is somewhat counter-intuitive, but rigorous mathematical proofs exist to explain this further [81, 206]. A constant long-term average rate of arrivals arises because the instantaneous probability is constant, as the probability of observing a car after 1 minute is the same as after 10 hours (and in fact after any time t), given that arrival times are completely random and independent. This instantenous probability is given

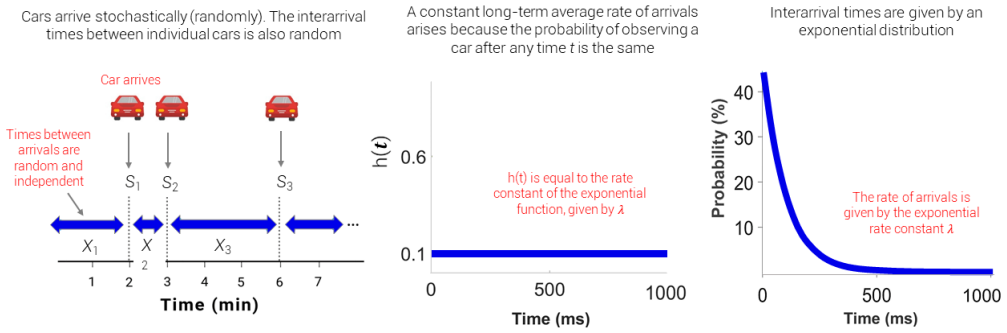

Figure 5.5: An example arrival process of passing cars

(Left) The arrival and interarrival times of individual cars is random. (Middle) as the probability of a car passing is the same for any time t, the instantaneous probability and hence hazard rate is constant. (Right) these properties give rise to an exponential distribution of interarrival times, where the average rate of arrivals is given by λ

by the *'hazard rate'* $h(t)$, a function that describes the probability of an event occuring per unit time (Figure 5.5). This constant hazard rate gives rise to interarrival times that are exponentially distributed, a key feature of the Poisson process:

$$f_X(x) = \lambda e^{-\lambda x} \quad for\ x \geq 0 \tag{5.14}$$

where the parameter λ gives the average rate of the Poisson process, which in this case is the average rate of cars passing.

5.2.2 Markov chains

Markov chains are mathematical systems used to model stochastic processes. Specifically, a Markov chain models transitions from one state to another according to probabilistic rules. These states may be a set of values or a situation [81].

The process begins at one of these states and moves from one state to another, with each move referred to as a *'step'*. If the chain is currently at state s_i, it will move to state s_j with a probability $p_{i,j}$. This probability is referred to as a *'transition probability'*, and will only depend on the current state and not any of the previously occupied states (this is known as the *'Markovian property'*). The process can also remain in its current state, which occurs with a probability $p_{i,i}$. The probability distribution of these state transitions can be given by the Markov chain's *'transition matrix'*. The transition matrix will be NxN in dimension, whereby N is equal to all possible states. The rows of this matrix must also sum to 1, as each row represents a unique probability distribution [206] [202].

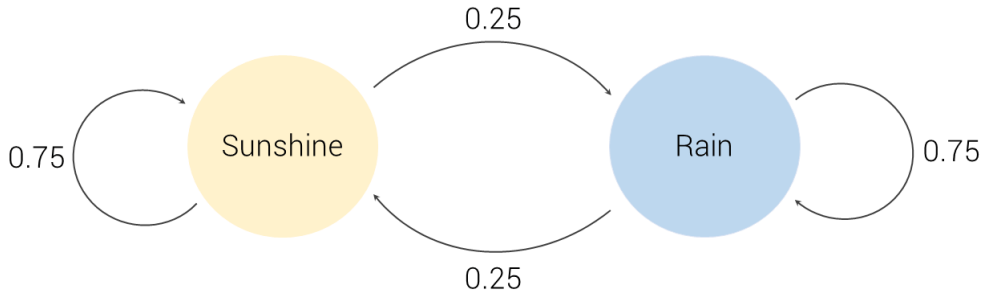

Figure 5.6: An example Markov chain state transition diagram for the weather in Adelaide

To define an example Markov chain, let's look at the weather in Adelaide. For simplicity, the weather can assume only one of two states: sunshine or rain. Hence, the state space is defined as:

$$\Omega = \{Sunshine, Rain\} \tag{5.15}$$

If we assume that tomorrow's weather will be the same as today, and this assumption is correct 75% of the time (irrespective of whether the weather today is sunshine or rain), then the transition matrix is given by:

$$\begin{vmatrix} 0.75 & 0.25 \\ 0.25 & 0.25 \end{vmatrix}$$

and hence the state transition diagram for this Markov chain will thus be as shown in Figure 5.6.

The Markov chain birth-death process

A birth-death process (BDP) is a continuous-time Markov chain that can be used to represent population growth [123, 126]. As the name implies, there are only two types of state transitions: i) *'births'*, which increase the population size by one, and ii) *'deaths'* that reduce the population size by one. When a birth occurs, the process transitions from state k to state $k+1$, whereby k represents the size of the population. Similarly, a death will cause the process to transition from state k to state $k-1$ [178]. This is illustrated in the state transition diagram shown in Figure 5.7.

In such a process, birth and death events are independent of each other, and thus the times between events (interarrival times) are modelled by Poisson processes given by an exponential probability distribution function (PDF). For births, the (PDF) is given by:

$$f(t) = \lambda e^{-\lambda t} \tag{5.16}$$

where λ is the birth rate and t time. For deaths, the PDF is given by:

$$f(t) = \mu e^{-\mu t} \tag{5.17}$$

where μ is the death rate and t time.

The BDP can also be described using queuing theory. Queuing theory is the mathematical study of waiting in a line (for example customers waiting to be served at a supermarket), and as such models the arrivals and departures for a queue in much the same way a BDP Markov process models births and deaths in a system. In queuing theory notation, the birth rate λ is referred to as the arrival rate to reflect how quickly customers arrive, and the rate of deaths μ referred to as the service rate to reflect how quickly customers are being served [126]. If the distribution between births and the times of deaths are given by exponential distributions (e.g. are Poisson processes), then they can be modelled using a class of queues known as $M/M/\sim$ queues, where M stands for Markovian or memoryless. $\sim$ represents the 'number of servers', which can be 1 for the simplest form of queue in which deaths occur one at a time, or by an $M/M/c$ queue if there are c servers. If an infinite number of deaths can occur at any one time, then the process can be modelled using an $M/M/\infty$ queue.

Birth-death processes are commonly used to study various aspects of population growth in biology [178]. In many applications, it is used to study how a theoretical population size changes in response to variations in the genetic makeup of a species (e.g. mutations) [153, 182]. It has also been used to study horizontal gene transfer [71] [130] and somatic evolution of cancer cells [128, 179].

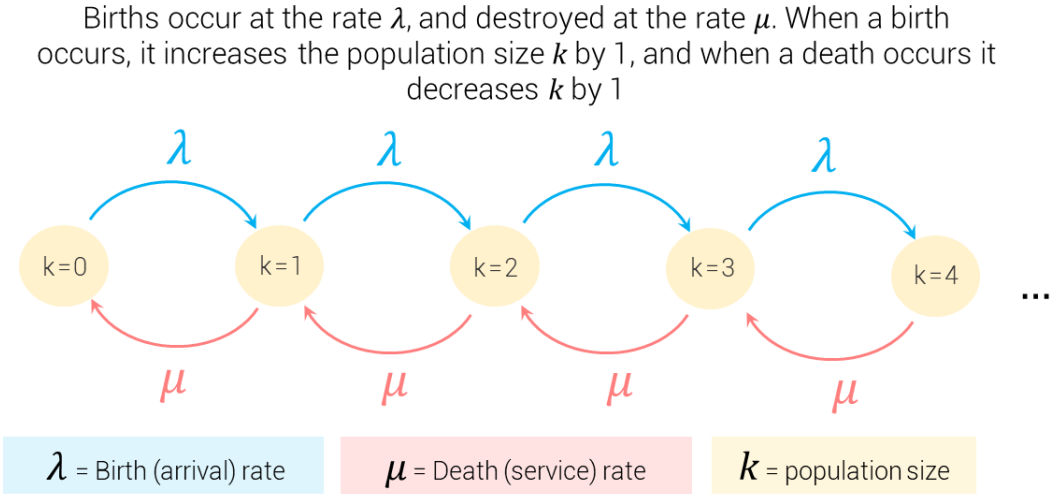

Figure 5.7: The birth-death process illustrated by a state transition diagram

5.3 Why use probability theory to study cardiac fibrillation?

As discussed in section 5.2, probability theory provides a framework to understand the nature of random (stochastic) phenomena. Although there is likely underlying determinism that contributes to cardiac fibrillation at the micro-scale (e.g. the influence of individual ion channels, remodelling of individual cardiomyocytes etc.), the interaction amongst these components is highly nonlinear and sensitive to initial conditions. The net effect of this is that even though the properties of the individual micro-components may be deterministic, their interaction as a dynamical system evolves over time to become effectively random. An analogy here is the coin toss. In tossing a coin, the precise outcome could in theory be characterised if all the physical parameters were known (e.g. the launch speed and trajectory, air resistance and friction etc.). However, in practice each of these components interact in a complex and dynamic way such that the outcome is effectively random, and therefore the system behaviour can be accurately modelled as stochastic process. In a similar way, electrical wave propagation dynamics during fibrillation at the macro-scale are sufficiently complex such that they can be accurately modelled as stochastic.

The complex, stochastic-like nature of electrical wave propagation during cardiac fibrillation is exemplified by the presence of random, transiently occurring, unstable re-entrant events, which have been reported by several studies throughout the history of the field. The earliest observation traces back to Garrey [89], who first reported that re-entrant circuits would shift in location and vary in complexity during episodes of fibrillation. Following this, Moe and Abildskov's computer model described the presence of numerous re-entrant circuits that could co-exist and shift in position and direction [165]. Using a slightly different approach, Winfree studied the behaviour of re-entrant-like vortex rings in a generic excitable media (a medium similar to mammalian cells and muscles). He reports that these vortex rings or filaments form 'organising centres', however, the nature of these are unstable as they continually change in shape [262]. Although these seminal studies helped to establish the notion of chaotic and randomly behaving re-entrant circuits in fibrillation, technology during much of this time limited the ability of these forefathers to definitively prove instability as being key to the perpetuation of fibrillation.

Since then, advancements in technology have allowed us to obtain greater insights into the complex wave dynamics during fibrillation. Using a canine sterile pericarditis model of paroxysmal atrial fibrillation, Kumagai et al. [137] were able to map the atria by placing electrode arrays on both the free atrial walls and along the atrial septum. Their experimental findings reported the presence of unstable re-entrant circuits of very short duration, principally present in the atrial septum. They further suggest that because re-entrant circuits are continuously generating multiple wave fronts, which in turn re-form re-entrant circuits with short cycle lengths, this is what maintains AF.

In a following study, Witkowski et al. [266] study re-entrant waves during ventricular fibril-

lation in an isolated perfused dog heart using optical mapping techniques. Similar findings were reported, with transiently erupting rotors being captured by the mapping system. Frequent wavefront collisions and wavebreak generation was also reported as a dominant feature of fibrillation.

Mapping studies have also been conducted in humans with similar observations. Konings et al. [129] utilise high-density mapping of electrically induced AF in patients undergoing surgery for interruption of the accessory pathway. They found that during pacing induced AF, the RA was activated by one or more random wavelets arising from different directions.

Even in studies in which stable re-entrant activity was observed, unstable reentry was also often reported. Schuessler et al. [217] use a 256 bipolar electrode mapping system to record epicardial sites during fibrillation and control conditions (no fibrillation). These recordings enabled computation of activation maps that visualise the propagation of electrical activity over the recorded site. Specifically, the study used choligernic agonists (acetylcholine) and vagal stimulation to induce atrial fibrillation in an isolated canine right atrium. Activation sequence maps revealed that as fibrillation sustained the reentry seemed to stabilise, however, during initiation and non-sustained episodes of fibrillation multiple re-entrant circuits were present.

A similar finding was seen in an isolated sheep heart model of AF. Chen et al. [48] used phase mapping to visualise fibrillatory conduction in a perfused isolated sheep heart. Results showed that the lifespans of re-entrant circuits (detected by their phase singularity) were short, and usually occurred during episodes of non-sustained arrhythmias.

Nash et al. [170] also found evidence for multiple wavelets co-existing with a mother rotor-type mechanism of VF in humans. This study mapped VF using a 256 electrode epicardial sock, fitted to the heart in 10 patients undergoing cardiac surgery. They found that although stable re-entrant waves were seen in some cases, in many others multiple, unstable wavelets were observed.

The observation of unstable re-entrant circuits reported by these studies seem to echo the observations of the entropy study as discussed in Part I. Collectively, this perhaps points towards a mechanism of fibrillation whereby instability of re-entrant sources may play, at least in part, a role in the initiation and/or perpetuation of both AF and VF. This rationale therefore warrants the investigation of this stochastic behaviour using probability theoretic principles from stochastic process theory.

Further motivating the application of stochastic process theory in cardiac fibrillation is the fact that although the instability of re-entrant activity has been reported by multiple studies, little scientific effort has thus far been made to understand and quantify the origins of this instability. Insights into this underlying stochasticity may help provide inferences about the physiological mechanisms relating to the maintenance of fibrillation, and insights for mapping and treatment.

5.4 Current studies using probability theory in cardiac electrophysiology

Even though probability theory is widely used in other fields such as computer science [275], biology [178] and finance [160], there currently exists very little literature on the application of probability and stochastic theory in cardiac electrophysiology.

In one study, Suzuki et al. [230] investigate the stochastic dynamics of phase singularities in a 2D model of ventricular fibrillation, under the rationale that the dynamical and stochastic nature of sustained VF remains unclear. Specifically, the authors study statistical characteristics of various fluctuations related to the phase singularity, including lifetime, velocity, rates of birth and death, and the probability density function of PS lifetimes. This was performed in simulations developed using i) normal and ii) modified ionic current. From this study, the authors conclude that the statistical properties studied were independent of tissue size. Further, the hyper-Gamma distribution was shown to reproduce the probability distribution for the number of PS in various tissue sizes and in both normal and diseased simulated tissue. Although the authors propose that these insights may provide new information for understanding the stochastic nature of VF, a connection between these statistical observations and the underlying mechanisms responsible for sustaining fibrillation was not provided.

In another study, Clayton and Holden [57] develop a method for the identification and tracking of filaments (areas around which re-entrant waves rotate during VF) in a computational model of ventricular fibrillation. Using this method, the authors aimed to calculate birth, death, amalgamation and bifurcation of these filaments, and use a directed graph to summarise these statistical characteristics. In doing so, this approach aims to provide a means to quantify the complex stochastic patterns of electrical activity prevalent in VF. However, again even though this method allowed for the dynamical behaviour and interaction of these filaments to be studied, a link between the observed stochastic behaviour to any potential underlying mechanisms was not discussed.

Studying yet another aspect of VF, Albrecht et al. [7] aimed to study ventricular ectopic beats (VEB) and characterise VEB-generating mechanisms based on timing information and beat-type. The approach characterises VEB-generating mechanisms using a multi-dimensional conditional probability distribution, under the rationale that each mechanism will produce and different distribution. Hence, these distributions can be considered a 'fingerprint' for a unique VEB-generating mechanism. By analysing a database of half-hour ECG tapes, the study concluded that VEB generation often demonstrated consistent distributions that can be characterized.

Applications of probability and stochastic process theory in AF are even more limited, but one study carried out by Zeng and Glass [276] investigates the statistical properties of heartbeat intervals during AF to develop a theoretical framework to model ventricular response during the

arrhythmia. The rationale behind this is that atrial activation travels to the AV node, and then causes conduction of the ventricles, and understanding and being able to predict this ventricular response during AF may be useful clinically. Because the AV node is subjected to irregular inputs arising from irregular activity in the atria, it was reasoned that a stochastic difference equation would be appropriate for modelling this random conduction. Using a stochastic map, the authors develop a method to model the ventricular response to atrial fibrillation, based on trying to construct a probability density function representing ventricular interbeat intervals given a random atrial activation such that the ventricular response can be predicted, assuming that the conduction properties of the atrioventricular node can be accurately modelled. Although the method worked well in some cases where the stochastic map was linear, clinical data often corresponded to nonlinear maps, thus casting doubt on the application of this method in practice.

In summary, probability and stochastic process theory remains under-explored in applications relating to cardiac fibrillation, despite being widely used in other fields. Additionally, the few studies conducted to date have been unable to relate the observed statistical properties of fibrillation to the underlying physiology and mechanism. Further investigation of these arrhythmia using probability theoretic principles may provide new and potentially key insights into the initiation and maintenance of AF/VF.

Chapter 6

Renewal theory as a universal quantitative framework to characterise phase singularity regeneration in mammalian cardiac fibrillation

The material contained within this chapter has been published in Dharmaprani, D., et. al., 2019. ***Renewal theory as a universal quantitative framework to characterise phase singularity regeneration in mammalian cardiac fibrillation***. Circulation Arrhythmia and Electrophysiology (in press). The core theme of the chapter is to develop a renewal framework based on stochastic process theory to model the formation and destruction of re-entrant activity during cardiac fibrillation. Dhani's contribution to the study was data collection, development of the codebase, signal processing and computational analyses, statistical analysis, writing the manuscript and providing input for the conception of the study.

6.1 Introduction

Cardiac fibrillation is characterised by aperiodic turbulence of wave propagation [96, 214]. This can occur in the atria, known as atrial fibrillation (AF), or the ventricles, constituting ventricular fibrillation (VF). The mechanisms by which these arrhythmias are maintained remain incompletely understood, but are of great significance as AF is the most common cardiac arrhythmia in humans,

and VF the leading cause of sudden death [12].

Although the atria and ventricles possess vastly different geometries, ionic mechanisms and global structures, they share similar electrical wave propagation dynamics [192]. A defining characteristic of both AF and VF is the presence of unstable re-entrant circuits that stochastically disappear and spontaneously regenerate during ongoing fibrillation [48, 90, 97, 101, 118, 129, 137, 155, 164, 165, 217, 262, 266]. A key feature of such re-entrant circuits is the presence of a phase singularity (PS) at their pivoting region [172]. Although an enormous amount of scientific and clinical effort has gone into the development of strategies to map rotational circuits during fibrillation [97, 101, 169], a universal quantitative framework to model the processes underlying their formation and destruction is lacking [193].

Given the stochastic nature of electrical wave propagation in fibrillation, it was reasoned that the destruction and regeneration of re-entrant circuits may be modelled using renewal theory. Renewal processes are a class of stochastic processes for which the timing of intervals between events can be approximated as statistically independent, identically distributed random variables [202].

The study hypothesises that if PS formation and destruction processes are stochastic renewal processes, then the time intervals between phase singularity formation and destruction events should follow exponential distributions, implying that these occur via memoryless Poisson point processes with constant rate-parameters. To test this hypothesis and gain insight into the processes by which AF and VF are sustained, the statistical distributions of waiting-times for PS formation and destruction was studied using a multi-modality,multi-species investigation using basket and optical mapping in human, ovine, rat and computer simulated atrial and ventricular fibrillation

6.2 Methods

6.2.1 Data acquisition

A multi-modality, multi species study was performed to analyse basket and optical mapping in: i) human persistent AF, ii) tachypaced sheep AF, iii) rat AF, iv) rat VF and v) computer simulated fibrillation. Patients provided written informed consent with study approval by the institutional ethics committee. All animal studies were also approved by the institutional ethics committee. To cross validate findings with source data from the literature, a systematic review was also conducted. The data acquisition for each of the model systems are as described below.

Human AF

The human AF study was a multicentre observational design analysing electrograms acquired prior to ablation, as previously described in chapter 4.2.1. The inclusion criterion was persistent AF undergoing clinically indicated ablation. Patient participation was by informed consent, with recruitment from two centres (Flinders University, Australia), and Hamburg University (Germany). Patient characteristics are provided in the Supplementary Results and Materials section F.

Basket catheter recordings were performed as previously described in chapter 4.2.1. 64-electrode basket catheters (Constellation, Boston Scientific, MA, 48mm(4mm spacing), 60mm(5mm spacing)) were utilized, based on computed tomographic scan. Unipolar electrogram recordings (1-500 Hz, 2000Hz sampling frequency) were obtained in spontaneous or induced AF lasting ≥ 5 minutes in the left and right atria. Catheter stability was verified fluoroscopically, and in Velocity (Abbott, IL, USA).

Sheep AF

Ovine persistent AF was induced via atrial tachypacing for 16 weeks at ≥ 300 bpm per minute as described in chapter 4.2.1. Unipolar electrograms were obtained during an electrophysiology study, using 64-electrode Constellation catheters (48mm). Electrograms were filtered from 1 Hz to 500 Hz, sampled at 2 kHz on NavX (Abbott, IL, USA). ≥ 5 minutes LA and RA recordings were obtained.

Rat AF

Optical mapping in a rat AF model was performed as previously described by Aguilar et. al. and Nattel et. al. [4, 172]. Male Wistar rats weighing 200-275 g were injected subcutaneously (SC) with preoperative buprenorphine (0.03 mg/kg) and anaesthetized with 2% isoflurane. Under endotracheal intubation and assisted ventilation, a left thoracotomy was performed, followed by ligation of the left anterior descending coronary artery with 6-0 silk. The thorax was sutured using a 3-0 silk and the skin was stapled using metal clips. Buprenorphine (0.03 mg/kg) was injected SC 6 and 12 hours postoperatively. Echocardiography was performed at baseline 1 day before the surgery, then 2 weeks later, to assess successful MI, and followed by final echocardiography 3 weeks following surgery. The same day, rats underwent transesophageal electrophysiological study (EPS). The heart was excised and perfused in Langendorff mode with Krebs solution at 30 ml/min and 37degC. After 30 min for stabilization and electrical/mechanical decoupling with blebbistatin (15 M), the heart was loaded with di-4-ANEPPS (Biotium, Inc., Hayward, California). A charge-coupled device (CardioCCD, RedShirtImaging, LLC, Decatur, Georgia) was used to record RA free wall fluorescence at 1 kHz. Optical maps were obtained during AF induced by 1.5 $\times$ threshold

current 2 ms stimulation at a reducing cycle length from 150 ms to 20 ms.

Rat VF

Optical mapping in a rat VF model was performed as previously described by Ilkan et. al. [112]. Rat hearts were excised and transferred to a Langendorff apparatus, and retrogradedly perfused through the aorta with oxygenated Tyrodes solution. Perfusion pressure was maintained at ∼60 mm Hg by adjusting perfusion flow. Hearts were regulated at 37deg C. Volume conducted electrocardiograms (EGMs) were recorded. Background fluorescence intensity was measured periodically in 1 minute intervals, using a 6400 pixel charge coupled device.

Computer Simulated Fibrillation

Computer simulations were based on transmembrane voltages generated using the Ten Tusscher-Panfilov model on 2-D, isotropic square grids (80 x 80) as previously described in chapter 4.2.1. Model calculations are in Supplement B. Three fibrillation-type scenarios were generated: i) continuous fibrillation with uniform electrophysiological properties, ii) stable spiral with uniform surrounding electrophysiological properties and iii) stable spiral surrounded by non-uniform surrounding electrophysiological properties. These scenarios were generated by varying the recovery variable $\lambda_d 1$ as described in Supplement B, and were selected to understand the effect of spiral breakup on PS destruction and formation.

6.2.2 Cleaning, Filtering and Sinusoidal Recomposition

Unipolar signals, surface ECG, and 3D data were exported from NavX, and signal processing of AF electrogram signals was performed similarly to previously published studies [50]. As unipolar electrograms often pick up far field ventricular artifact, QRS subtraction was performed to remove the ventricular component of the signal, allowing only atrial activity to be analysed. Specifically, QRS subtraction was performed using a template matching method as described by Shkurovich [223]. The template subtraction method uses a detection algorithm by Pan and Tompkins [191] to detect QRS complexes in the signal. Using these complexes, a 'median' ventricular complex is constructed by aligning the detected QRS segments at their respective fiducial points, and performing a median operation of the matching points. Subtracting the median complex from each ventricular complex results in signals free from QRS complexes and hence ventricular activity (Figure 6.1). QRS subtracted signals were filtered using a 4th order Butterworth fitted with a 1 to 30 Hz band pass filter applied in forward and reverse mode [50].

Following this, sinusoidal recomposition of the signal was applied to transform the AF electrogram signal into a sum of sinusoidal wavelets (Figure 6.2). Doing so increases the accuracy of

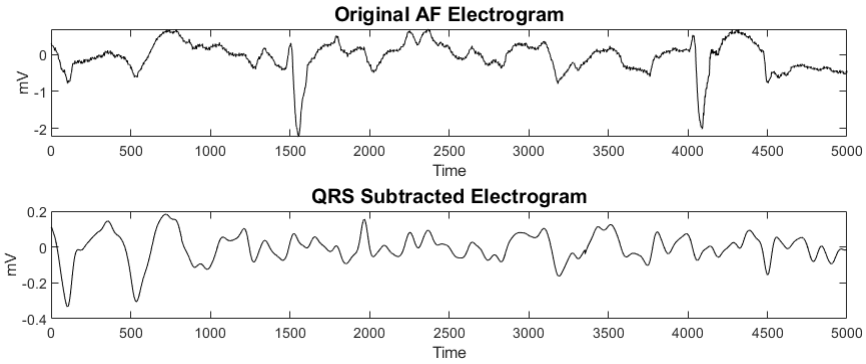

Figure 6.1: Schematic showing QRS subtraction from an AF electrogram. Fiducial points are indicated by red dot

the phase reconstruction using the Hilbert transform, as mathematically this transformation works best on signals with a sinusoidal morphology (e.g. ventricular signals). As atrial signals are characterised by long iso-electric intervals between consecutive deflections, these can result in artifacts in the reconstructed phase [135]. The sinusoidal recomposition transforms AF electrograms into sinusoidal wavelets which only exist when there is a negative derivative in the original signal (as a negative slope in a unipolar electrogram corresponds to the passing of a wavefront). The amplitude of the wavelet is proportional to the slope of the signal, and has a period equal to the mean cycle length of the electrogram (which was derived from the dominant frequency of the electrogram). These properties result in more accurate phase reconstruction for subsequent PS analyses, which is given by the 'sawtooth' wave in 6.2.

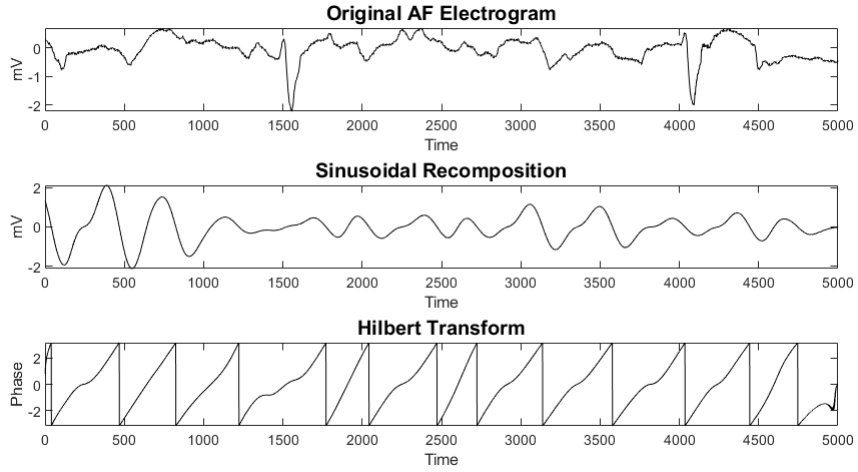

Figure 6.2: Schematic showing sinusoidal recomposition in paroxysmal and persistent AF

Original AF electrogram is shown above, and negative slope or derivative of this signal is used to construct a sinusoidal wavelet transform (middle). The sinusoidal morphology helps construct a Hilbert transformed phase signal (bottom), whereby one phase cycle is represented by a single 'sawtooth' complex traversing from -pi to +pi

For optical mapping data, a Gaussian smoothing filter was applied to the transmembrane voltage (fluoresced signal) to improve the signal to noise ratio and phase reconstruction. This step is

crucial for accurate PS detection as shown in Figure 6.3, where it can be seen that no single point exists in which all phase values (denoted by all colours from blue to red) meet. Consequently, no PS will be detected in the un-smoothed signal. The Gaussian smoothing filter is a 2-D convolution operator that uses a smoothing kernel to average data points in an image with its neighbouring points, which has the effect of blurring sharp edges and smoothing the data [21]. Computationally, the smoothing kernel used is a Gaussian function that expresses the Gaussian or 'normal' distribution [265]. The amount of smoothing achieved is determined by the standard deviation of the distribution σ, as shown in equation 6.1:

$$G(x, y) = \frac{1}{2\pi\sigma^2} e^{-} \frac{x^2 + y^2}{2\sigma^2} \tag{6.1}$$

where x and y give the distance from the origin in the horizontal and vertical directions respectively [265].

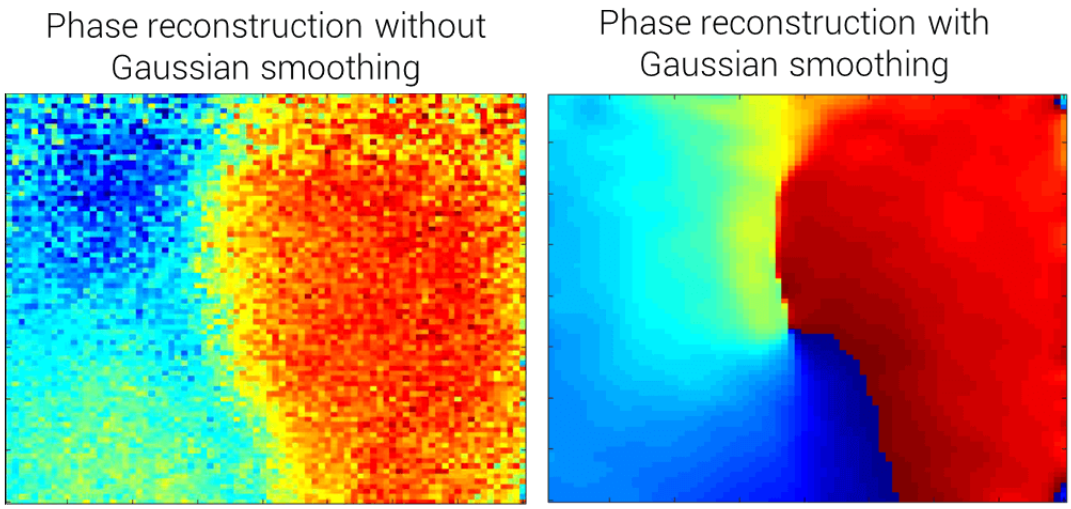

Figure 6.3: Optical mapping phase reconstruction before and after Gaussian smoothing
In the un-smoothed phase reconstruction, the phase singularity cannot be determined as no clear point exists where all phase values (blue to red) meet. In the smoothed phase reconstruction, the phase singularity point can clearly be seen in the centre of the rotor

Hilbert Phase Mapping and Phase Singularity Detection

Instantaneous phase for each electrogram was computed by applying the Hilbert transform on cleaned and sinusoidally reconstructed signals. Mathematically, the Hilbert trasnform can be given as follows:

$$\phi(t) = \arctan \frac{(-u(t) - u*)}{H(u)(t) - u*} \tag{6.2}$$

where $u*$ sets the origin of the phase plane with respect to the phase that is computed.

To detect PS, two approaches were used to allow for cross validation: i) the line integral [113] and ii) the double ring extended topological charge approach [136]. The classical line integral approach is based on the line integral of the phase gradient:

$$\oint_c \nabla\phi dl \tag{6.3}$$

where ∇ is the spatial derivative, c is a closed loop surrounding a given point and ϕ is a phase map [113]. Because the integral has to be discretized and approximated, c becomes the ring of electrode that encircles a point being tested for the presence of a PS. Theoretically, the integral should result in $\pm 2\pi$ only at phase singularity points. To implement this in the study, a the PS detection algorithm was employed as first described by Iyer and Gray [113], whereby a path length of eight pixels was used to compute the line-integral or phase change around a site. A PS is said to exist at the intersection of the four pixels identified by the PS-finding algorithm (2.3.5).

PS detection was also performed using the double-ring extended topological charge method to avoid noise-related issues [136]. The double ring method is a modification of the line integral method shown in equation 6.3, and consists of an inner 2 x 2 grid, enclosed by an outer 4 x 4 ring of electrodes. In a small 2 x 2 ring, PS detection translates to the presence of just a single phase difference greater than pi, which is half of the full 2π cycle. The PS is said to exist at the intersection of the four pixels constituting the inner 2 x 2 ring. As using a single 2 x 2 ring may encompass more than one wave and cause artificial phase transitions, the second ring is added to ensure a PS is only identified if it is simultaneously detected by both the inner and outer ring. This results in greater noise insensitivity (2.3.5. Given the increased robustness of the extended topological charge method, the results presented throughout this chapter are calculated using this approach, with the line-integral results presented in section 6.3.4 for cross-comparison.

6.2.3 PS look-up table

To determine PS lifetime and PS inter-formation event times, a look-up table indexing onset time, offset time and electrode location for each new PS detection was created. A new PS detection event was defined as the detection of a PS at an electrode and its surrounding 1-electrode neighbourhood for geq 20 consecutive frames, corresponding to a duration of 10 ms. The look-up table enabled computation of histograms for: (i) PS lifetimes and (ii) inter-formation event times.

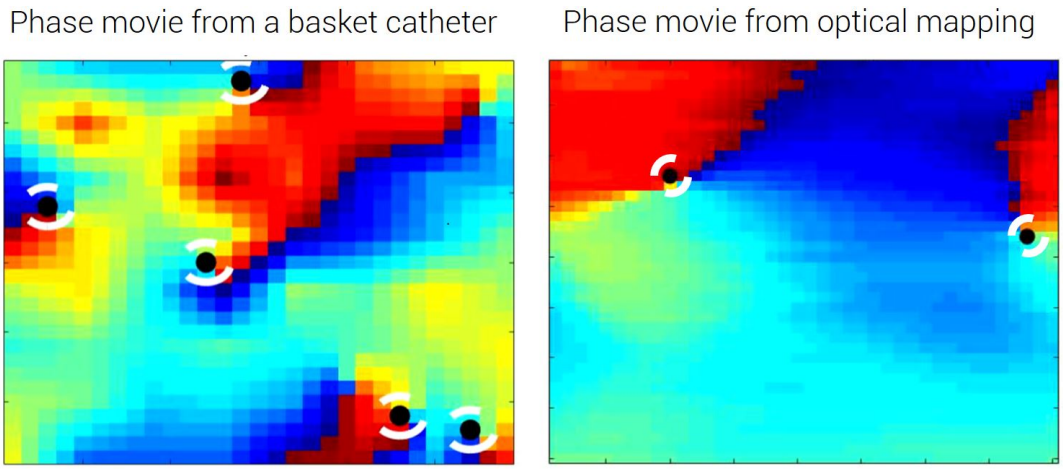

Figure 6.4: Example phase maps from basket catheter (left) and optical mapping (right).
Two example phase maps showing basket catheter data (left) versus optical mapping data (right). Phase singularities (PS) are indicated by the black dot, surrounded by white ring. A larger number of PS are detected in basket data due to the larger mapped field.

6.2.4 Modelling PS formation and destruction using a stochastic renewal theory framework

To gain insights about the underlying data generating mechanisms responsible for the formation and destruction of phase singularities during atrial and ventricular fibrillation, data from the 5 model systems was analysed using a stochastic renewal theory framework. Specifically, the study hypothesised that PS lifetimes and formation times would occur due to a Poisson renewal process.

A Poisson renewal process is a special type of stochastic or random process (chapter 5.2.1). It is characterised by an arrival process in which the times between events are independent, but events occur at a long-term constant rate (Figure 6.5 i and 6.5 ii). In the discrete case, the probability distribution function (PDF) of the Poisson process takes the form of a geometric distribution, which converges to an exponential distribution when large numbers of of events are considered (Figure 6.5 iii). A proof of this convergence is provided in Supplement G.

If data possesses these properties, it implies the generating process is a Poisson renewal process and therefore should produce an exponential distribution of inter-event times. Under this rationale, the study investigates whether PS lifetimes and inter-formation event times produce exponential distributions. This would suggest that although the behaviour of individual PS are random, the long-term average rate of formation and destruction will be stable.

Examples of Poisson processes in other scientific disciplines include the timing of radioactive decay events [206], and in simple models of survival analysis [233].

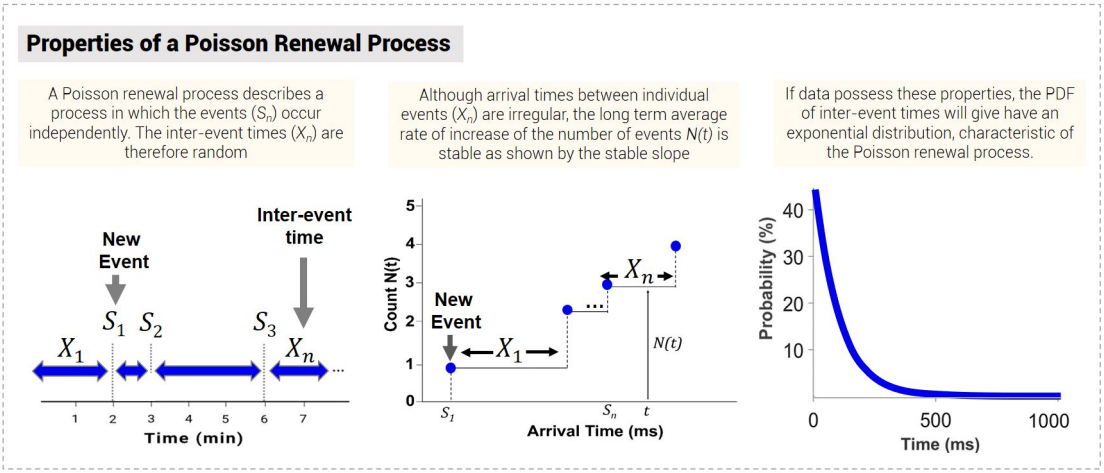

Figure 6.5: Properties of a Poisson Process

Probability distribution function of PS lifetimes and as an index of PS destruction

For each epoch, observed experimental PS lifetime data was fitted with an exponential distribution given by the probability distribution function (PDF):

$$f(t) = \lambda_d e^{-\lambda_d t} \tag{6.4}$$

where λ_d gives the rate of PS destruction, and t denotes the PS lifetime. Specifically, data was fitted using non-linear least-squares regression, and the adequacy of fit determined using the R-squared value (R^2). To validate, PS data was fitted using maximum likelihood and adequacy of fit evaluated using the chi-squared (χ^2) goodness of fit test.

Probability distribution function of PS formation times and as an index of PS formation

To evaluate the contribution of stochastic processes to PS formation, we also calculated R^2 of the probability distribution function (PDF) given by equation 6.5:

$$f(t) = \lambda_f e^{-\lambda_f t} \tag{6.5}$$

where λ_f gives the rate of PS formation, and t denotes the time between consecutive between PS formations. Like PS lifetimes, formation time data was fitted to an exponential distribution using non-linear least squares regression.

For interpretability, the cumulative density function (CDF) was also calculated to show the probability that a new PS has formed after an inter-formation event time of t (Figure 6.10). The

exponential CDF can be given by:

$$f(t) = 1 - e^{\lambda_f t} \tag{6.6}$$

where λ_f is the formation rate parameter, and t the time between formation events. Maximum likelihood was used for cross-comparison.

Non-linear Least Squares Data Fitting

Parameter fitting to the exponential distribution was first completed using non-linear least squares on the probability distribution function (PDF) for each case. PDFs were generated by binning PS lifetime and inter-formation time data to form normalized histograms. Data fitting was performed in Matlab, and the fitting options selected include the Trust-Region Algorithm, with minimum difference change $1.0^{-}8$, and maximum iterations set to 400. The r-squared (R^2) value was used to determine the adequacy of fit.

Maximum Likelihood Fitting

As a comparison to an alternative data fitting approach, PS data was also fitted using maximum likelihood. For continuous data, a histogram can throw away information and fitting is also dependent on the choice of bin edges and bin widths. Maximum likelihood does not suffer from these problems, and as such was used as a comparative approach. Data fitting was performed in Matlab, using the probability density function (PDF) of each case. The chi-squared (χ^2) goodness of fit test was used to assess the adequacy of fit, which uses the null hypothesis that the data evaluated comes from an exponential distribution ($p < 0.05$ for non-exponential data).

Sensitivity analyses

To cross-validate, a number of sensitivity analyses were conducted. First, electrode permutation was performed to destroy spatial correlations and assess the sensitivity of PS detection. This was done to determine whether the rates of PS formation and destruction from the experimental observed data would be the same as from pure noise. To perform electrode permutation, the 64 electrodes of the basket catheter were randomly shuffled spatially prior to phase reconstruction (Figure 6.6), and PS detected on the randomly permuted grid. This allowed permuted rate constants to be determined and compared with experimental λ_f and λ_d.

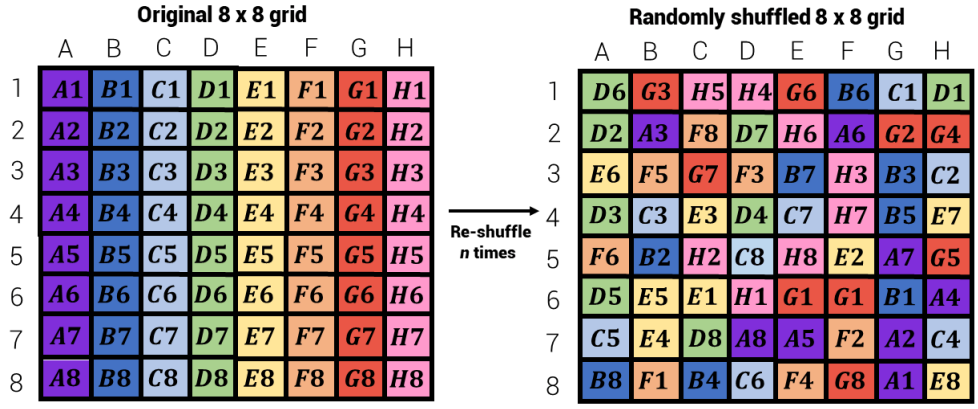

Figure 6.6: Electrode permutation of 8x8 basket catheter grid

As an additional sensitivity analysis to ensure results do not arise from pure noise, rate estimates after single electrode elimination were also computed. In this instance, all phase values corresponding with the electrode to be deleted were set to 0 in order to maintain a symmetrical 8 x 8 grid, but break spatial correlations associated with the electrode.

To validate the computation of rate constants, λ_f calculated from inter-event time distributions were compared to λ_f directly calculated from the slope of the cumulative PS count data (Figure 6.7). Mathematically calculation of the rate constant from these two methods should be equivalent (5.4), however, for validation this extra calculation step was performed.

Although no two events (PS) can occur simultaneously in a Poisson renewal process, the limited temporal resolution of experimental data means some PS may appear to arrive simultaneously. This is because experimental conditions do not permit data to be sampled at an infinitely small time interval (or in other words at an infinitely large sampling frequency). To ensure these 'simultaneous arrivals' did not effect calculations, rate constants λ_f and λ_d were calculated using the raw data, as well as data after omitting concurrent PS events. Concurrent PS events were defined as PS that either formed or died within the sample time step/sample.

Given that long lasting rotors have been put forward as drivers of AF, the consistency of the exponential distribution was also calculated for only longer-lasting PS to determine whether rotors of greater stability also follow Poisson renewal processes. To calculate this, PSs > 150 ms across patients were pooled and the distributions for λ_f and λ_d examined.

Lastly, as the PS tracking and partitioning algorithm for creation of the PS look-up table requires input parameters to set the tracking window length, the impact of changing this tracking threshold on the computed rate constants was assessed. Computationally, varying this window alters the number of time steps that the algorithm searches for a PS existing within the same x, y location. If another PS is not located in the vicinity of this x, y location within the tracking window, it will subsequently be labelled as a new PS.

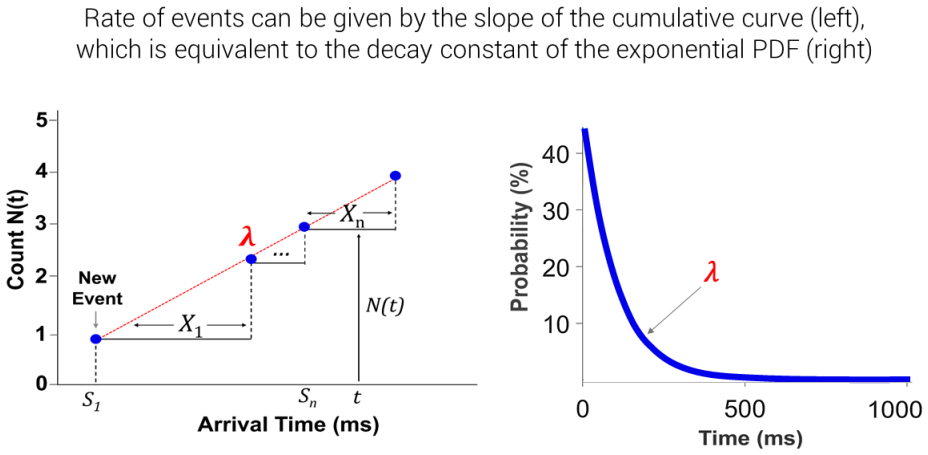

Figure 6.7: Calculation of rate constants from cumulative count slope and exponential PDF

6.2.5 Comparison with Maximum Entropy (MaxEnt) Predicted Distribution

Maximum Entropy (MaxEnt) is a rigorously proven principle of statistical inference allowing prediction of the least-biased (most purely random) underlying probability distribution, given prior constraints. MaxEnt has been applied in physics [224], neuroscience [213], and ecology [105]. A mathematical step-by-step guide for calculating the MaxEnt distribution is provided in Supplement H.

If the observed experimental data distribution matches that predicted by MaxEnt, it implies the generating process can be accurately modelled as purely stochastic and random, except for the constraint of the mean rate. This study compares the distributions of observed waiting-times for PS formation and destruction to those predicted by MaxEnt to further validate whether these processes can be accurately modelled as stochastic Poisson renewal processes.

6.2.6 Comparison with PS Data in Other Studies

For further cross-validation with published source data, a systematic review of the PubMed English language medical literature was conducted to study the distribution of PS inter-event time data.

The search criteria was: 'atrial fibrillation OR ventricular fibrillation AND rotor* OR phase singularit* OR spiral wave*.' Ventricular fibrillation was also included as it was reasoned that a similar stochastic process could apply in VF, and a subgroup analysis was performed for these data. The criteria for inclusion were studies in humans or experimental model systems reporting histogram or probability distribution data for phase singularity inter-event distributions. Studies were excluded if they were reviews, editorials, or commentary. Candidate full-text studies were retrieved for secondary review, with final inclusion determined by consensus (Figure 6.8). It can

be noted that in the identified studies, only PS lifetime data was provided, hence no existing PS inter-formation event distributions could be analysed.

For each study, histograms of PS lifetime were digitized, with probabilities measured with digital calipers (DigitizeIt, Koln, Germany). λ_d observed was computed from the exponential decay constant of the digitized PDF. To cross validate, the λ_d MaxEnt was computed using the principle of Maximum entropy and Langrangian multipliers.

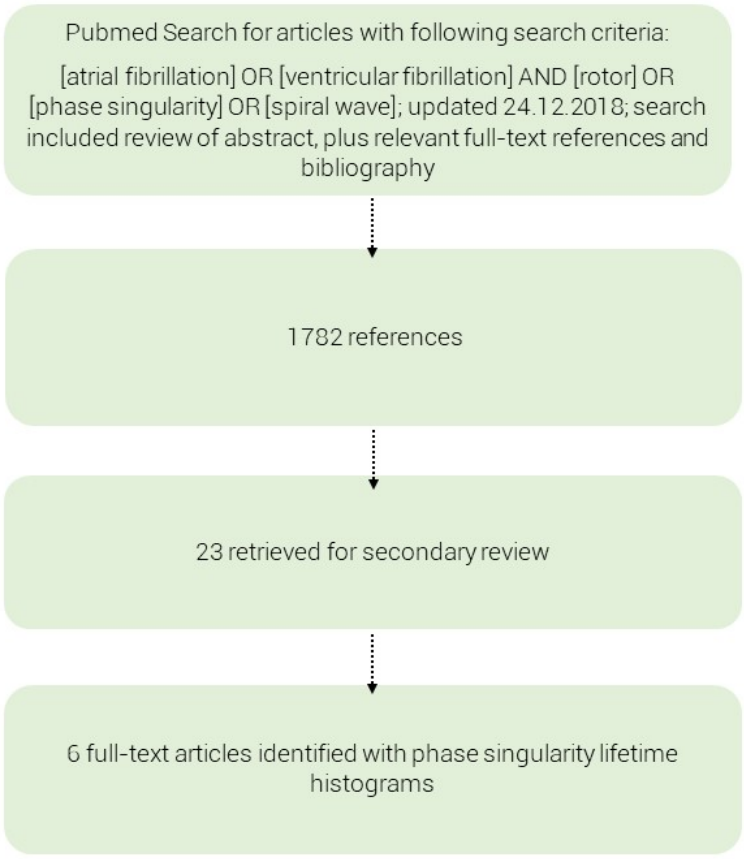

Figure 6.8: Search and inclusion criteria for systematic review of current literature

6.3 Results

6.3.1 PS Destruction in Human and Animal Cardiac Fibrillation

PS lifetime distributions for all human AF cases (19/23 persistent AF, Supplement F) showed an exponential distribution (Figure 6.9), with R-squared values (R^2) $\geq$ 0.90. A summary of data fitting results is shown in Table I.1 (Supplement I). The mean PS destruction rate (λ_d) was 4.6%/ms$\pm$1.5 (95%CI, 4.3, 4.9), translating to a PS half-life (t1/2) of 15 ms (95%CI, 14, 16). There were no statistically significant differences (P=0.18) in PS destruction λ_d between the LA

(4.5%/ms (95%CI, 4.1, 4.8)) and RA (4.9%/ms (95%CI, 4.3, 5.4).

PS destruction in sheep tachypaced sustained AF was similar to humans, with PS lifetime distributions showing good fits to the exponential distribution ($R^2 \geq 0.90$, Table I.2) Supplement I). In sheep, the mean was 4.6%/ms±1.4 (95%CI, 4.3, 4.8) and t1/2 equal to 15 ms (95%CI, 14, 16). Mean λ_d sheep did not differ significantly between LA (4.5%/ms (95%CI, 4.02, 5.1)) and RA (4.22%/ms (95%CI, 3.8, 4.6)) (P=0.20).

Rat AF data demonstrated PS lifetime distributions that were well fitted by an exponential distribution ($R^2 \geq 0.90$)(Table I.3, Supplement I), with a mean λ_d of 38%/ms±6.6 (95%CI, 22, 55). (t1/2) was 1.8 ms (95%CI, 1.2, 3.1). Faster λ_d may be accounted for by the differences in action potential dynamics of the rat in comparison to larger mammals.

In rat ventricular fibrillation, PS lifetime curves also showed good fits to an exponential distribution ($R^2 \geq 0.92$)(Table I.4, Supplement I). Similarly to rat AF, faster λ_d was observed (λ_d = 46%/ms±21 (95%CI, 31, 60), (t1/2) was 1.5 ms±3.3 (95%CI, 2.2, 5.7)).

6.3.2 PS Formation in Human and Animal Cardiac Fibrillation

Similarly to PS destruction, PS formation probability density functions (6.10) showed exponential distributions ($R^2 \geq 0.90$ (Table I.5, Supplement I)). Mean λ_f was 4.2%/ms±1.1 (95%CI, 4.0, 5.0), translating to a t1/2 of 16 ms (95%CI, 13, 17). For interpretability, the cumulative density function (CDF) is also provided to show the probability that a new PS has formed after an inter-formation event time of t. λ_f in the LA (4.9%/ms (95%CI, 4.5, 5.4)) was not different to the RA (4.1%/ms (95%CI, 3.6, 4.6) (P=0.28)).

Tachypaced sheep curves also showed good fits with exponential distributions in all cases (R2 $\geq$ 0.90 (Table I.6 Supplement I). Mean λ_f was 4.4%/ms±1.4 (95%CI, 4.1, 4.7), corresponding to a PS half-life (t1/2) of 16 ms (95%CI, 15, 18). λ_f for PS formation in the LA (LA: 4.5%ms/s (95%CI, 5.1, 6.7) was not different to the RA (4.6%ms/s (95%CI, 5.3, 6.9))(P = 0.79).

Rat AF also showed good fits with an exponential distribution for all cases (R2 $\geq$ 0.90). Mean λ_f was 33%/ms±8.8 (95%CI, 11, 55) and t1/2 equal to 2.1 ms (95%CI, 12, 6.3). Again, λ_f was faster in comparison to human and sheep (Table I.7, Supplement I).

In rat VF, mean λ_f was 38%/ms±24 (95%CI, 22, 55) and t1/2 equal to 1.8 ms (95%CI, 1.3, 3.2). All cases showed good fits with an exponential distribution ($R^2 \geq 0.91$) (Table I.8, Supplement I).

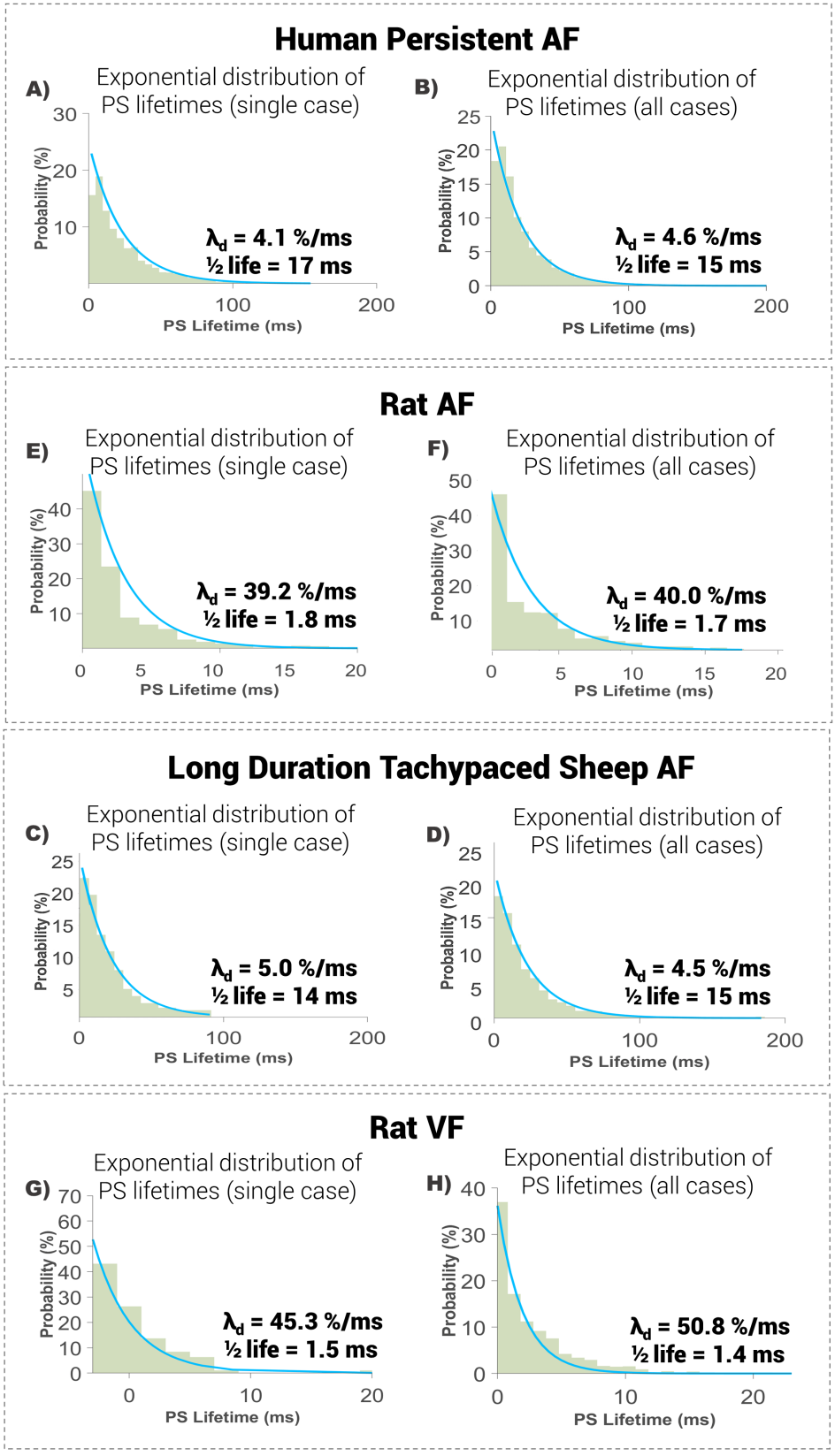

Figure 6.9: PS destruction occurs via a Poisson renewal process

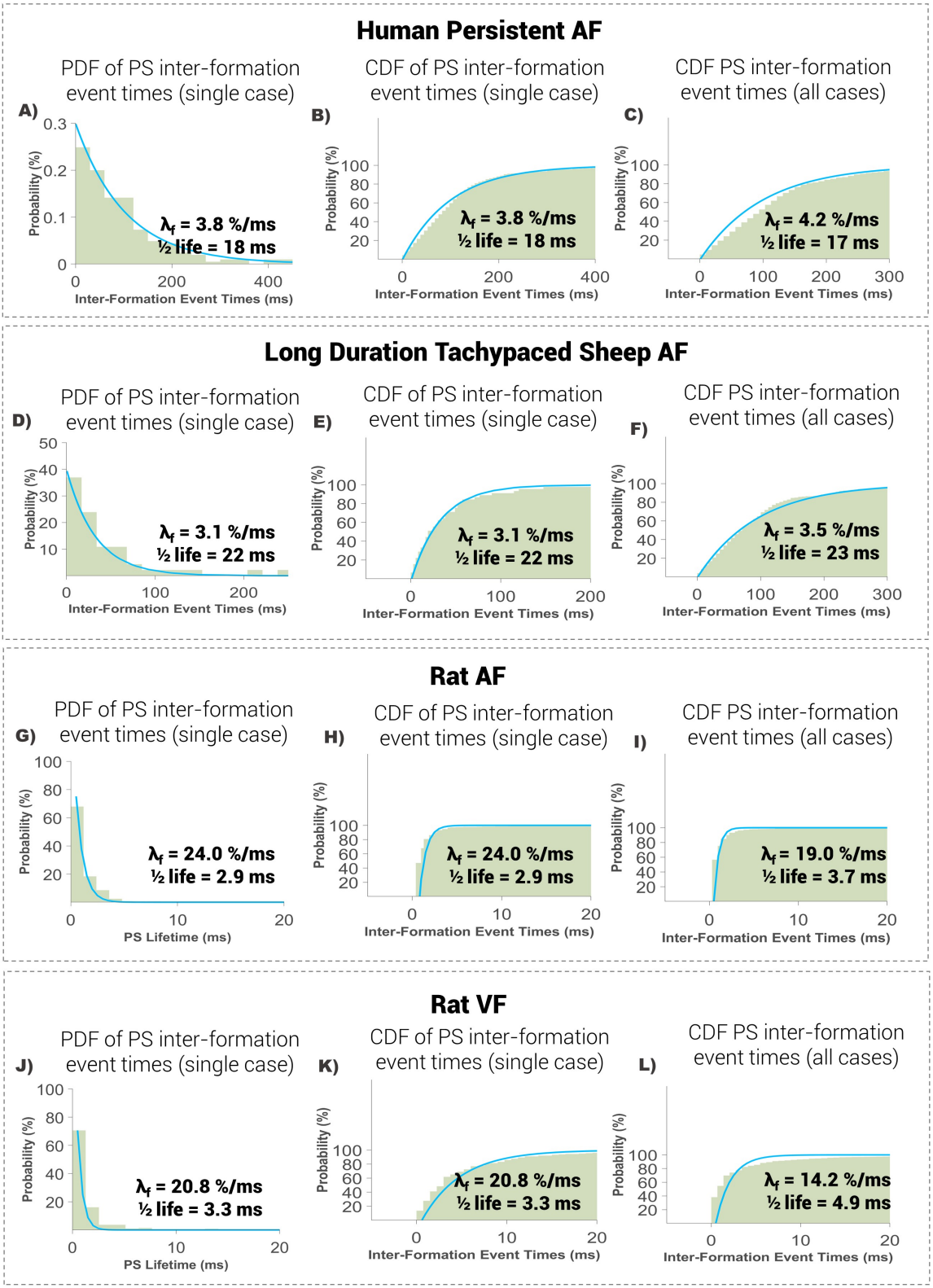

Figure 6.10: PS formation occurs via a Poisson renewal process

6.3.3 PS Lifetimes in Computer Simulated Fibrillation

Figure 4 shows the distribution of PS lifetimes in the Ten-Tusscher Panfilov model of fibrillation in 3 different scenarios. Figure 6.11A shows fibrillation in the case of uniform electrophysiological properties. It can be seen that the distribution of PS lifetimes follows an exponential distribution consistent with a Poisson renewal process (R^2=0.99; λ_d = 8.97%/ms). Figure 46.11B shows the impact of introducing a stable spiral into this model. In this case, the distribution of PS lifetimes remains exponential consistent with a Poisson renewal process (R^2=0.99), with a slight reduction in the rate constant of destruction potentially accounted for by the area controlled by the stable spiral (λ_d = 8.42%/ms). Figure 6.11C shows the impact of introducing electrophysiological non-uniformity of the $\mu 1$ recovery variable in the presence of a stable spiral. It can be seen that this also shows an exponential distribution (R^2=0.97) consistent with a Poisson renewal process, but the rate constant of PS destruction is decreased compared to the earlier cases with uniform values of the $\mu 1$ recovery variable (λ_d = 6.60%/ms).

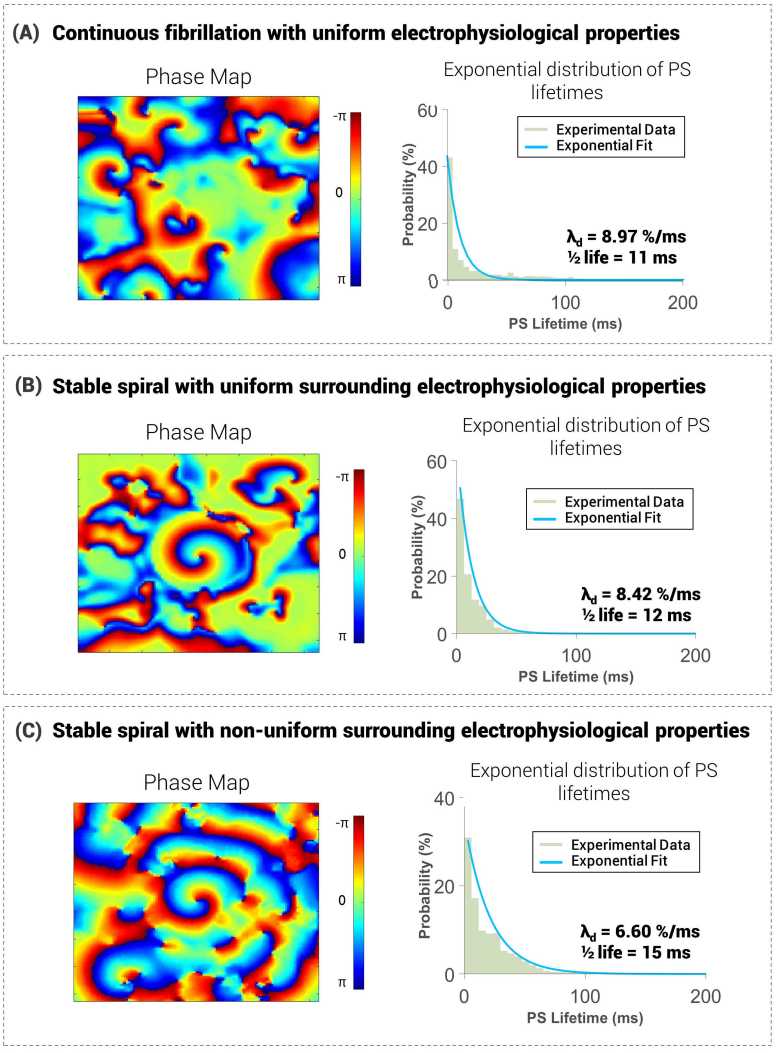

Figure 6.11: PS lifetime distributions under different scenarios of fibrillation

6.3.4 Results from sensitivity analyses

For sensitivity analysis, datasets were subjected to repeat analyses using the line integral topological charge PS detection method [113]. PS lifetime and inter-formation event time curves showed exponential distributions, consistent with findings using the double-ring extended topological charge method. In humans λ_d was equal to 4.5%/ms (95%CI, 3.8, 4.3; t1/2: 15ms (95%CI, 16, 18)). In sheep AF, λ_d was 3.7%/ms (95%CI, 3.4, 4.0; t1/2: 19ms (95%CI, 17, 20)). PS formation was similar, with λ_d in humans equal to 4.8%/ms (95%CI, 4.6, 5.1) and in sheep, 4.4%/ms (95%CI, 4.2, 4.7).

Electrode permutation resulted in an increased number of PS detections using the line integral approach (un-permuted count: 330±6.4 PS; permuted count: 415±4.7 PS). Contrastingly, the double ring approach decreased the number of PS detections (un-permuted count: 261±1.9 PS; permuted count: 257±2.0 PS), confirming its noise insensitivity. Permuted data consistently yielded lower λ_d for both PS detection methods, with mean λ_d equalling 2.8 %/ms for unshuffled data, and dropping to 1.2 %s PS/s for shuffled data using the line integral approach approach. Results were similar for the double ring approach (un-permuted- λ_d: 4.4 %m/s; permuted λ_d: 2.3 %/ms). A one sample t-test verified consistent statistical significance between permuted and un-permuted λ_d ($p < 0.001$ for all cases).

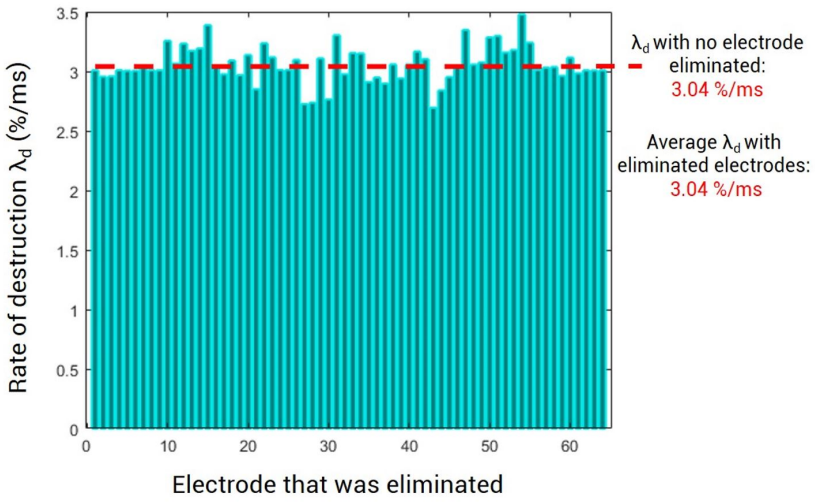

Figure 6.12: Effect of single electrode deletion in a single example case

As an additional sensitivity analysis, λ_d estimates after single electrode elimination were also computed. An example case is shown below in Figure 6.12. λ_d estimates were very comparable to those calculated without the removal of any electrodes, and that the average of this was equal to λ_d computed without eliminating any electrodes. Further, λ_d with and without single electrode deletion was not statistically different ($P = 0.386$). The range of $\lambda_d$values are shown in Figure 6.12, which plots the electrode (1-64) that was eliminated on the x-axis, vs. the computed rate of destruction on the y-axis.

To verify the validity of calculating rate constants from the inter-event time distribution, λ_f was computed independently from the time series of the events. To do this, the hazard function was directly calculated from the slope of the cumulative arrival count data (the time series) as illustrated by A in Figure 6.13. This was compared to the rate constant of PS formation derived from the distribution of inter-event times (as illustrated by Figure 6.13B). The rate of formation for both methods was strongly correlated (R = 0.956) (Figure 6.13C).

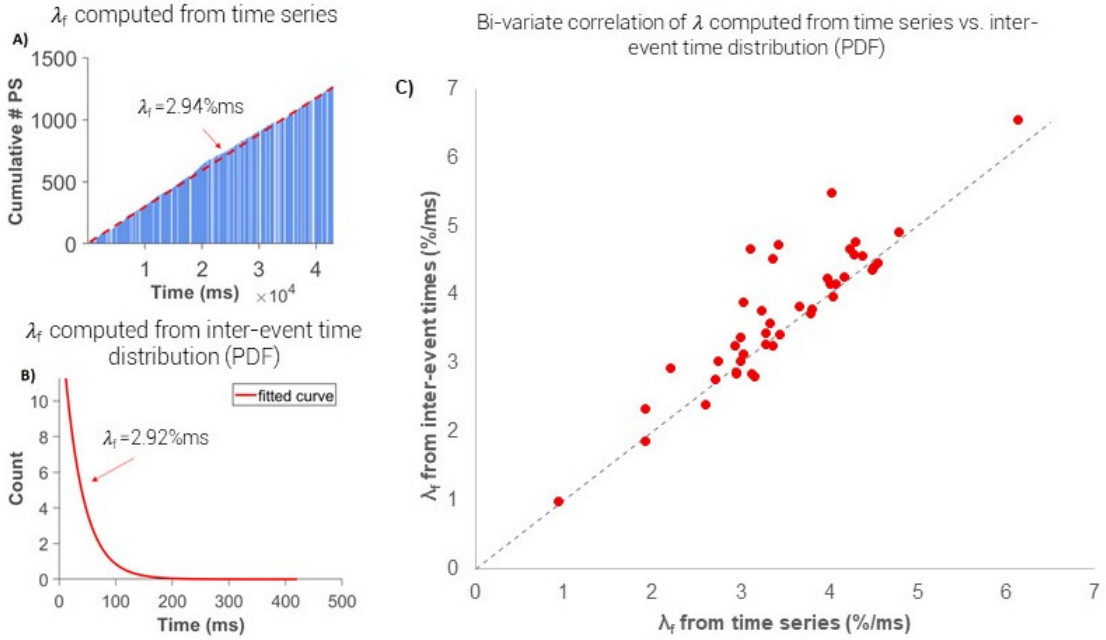

Figure 6.13: Correlation between *lambda* computed from the cumulative slope (time series) vs. inter-event times (exponential PDF)

To assess the incidence of simultaneous arrivals and whether they significantly impact experimental measurements of λ_f and λ_d, an additional sensitivity test was conducted. Simultaneous arrivals only occurred in 0.5% of PS events, and removal of these events from the analysis were not shown to significantly alter computed λ_f and λ_d (Figure 5).

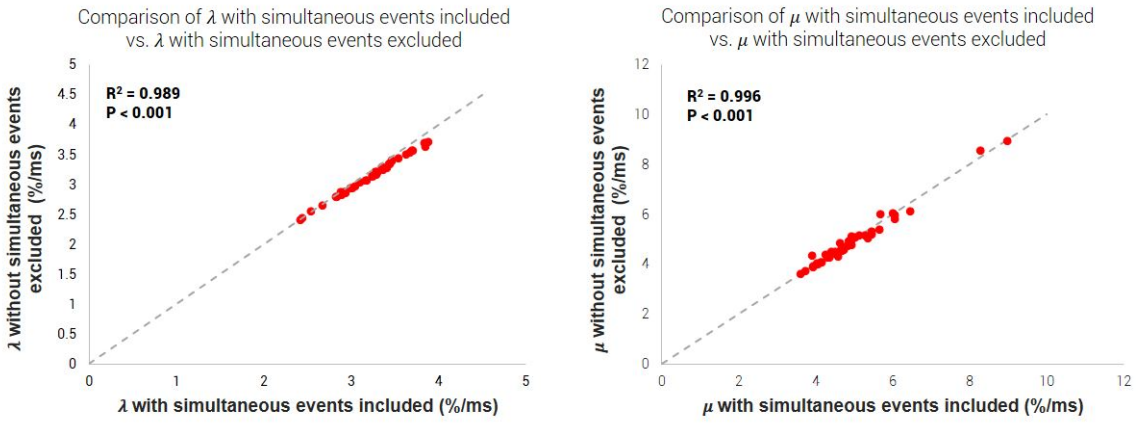

Figure 6.14: Effect of simultaneous events

To evaluate whether long lasting PS would also follow a Poisson renewal process, the consistency of the exponential distribution in PS $>$ 150ms (pooled across patients) was examined. As shown in the Figure 6.15, longer lasting PS also produced an exponential distribution for both PS lifetimes and inter-formation times. The exponential distribution of PS time-to-event data supports the notion that a Poisson renewal parameter determines the instantaneous and random probability of formation and destruction of individual PS.

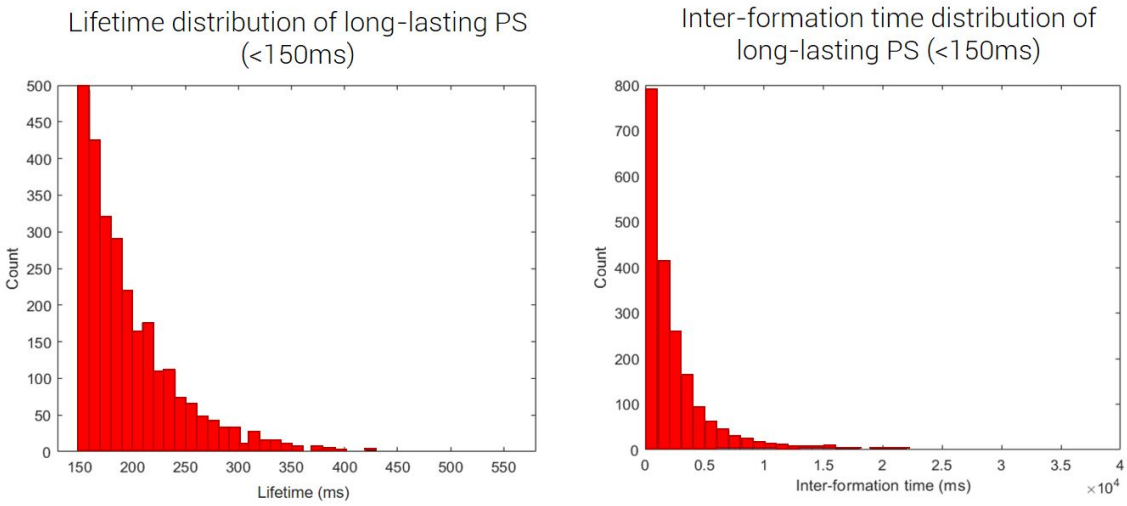

Figure 6.15: Analysis of long lasting PS

As a final sensitivity analysis, analyses were repeated after varying the parameter sensitivity of the PS partitioning algorithm such that a PS were required to be present for $\geq$ 10, 20, 30, 40 and 80 consecutive frames (corresponding to durations of 5ms, 15ms, 20ms and 40ms respectively at a 2000 Hz sampling frequency). As shown below in Figure 6.16, increasing the length of thr tracking window did not significantly alter computed λ_d, with estimates shown to be strongly correlated by points lying on the line of identity. Computed λ_d also began to converge after increasing the number of frames $\geq$ 30.

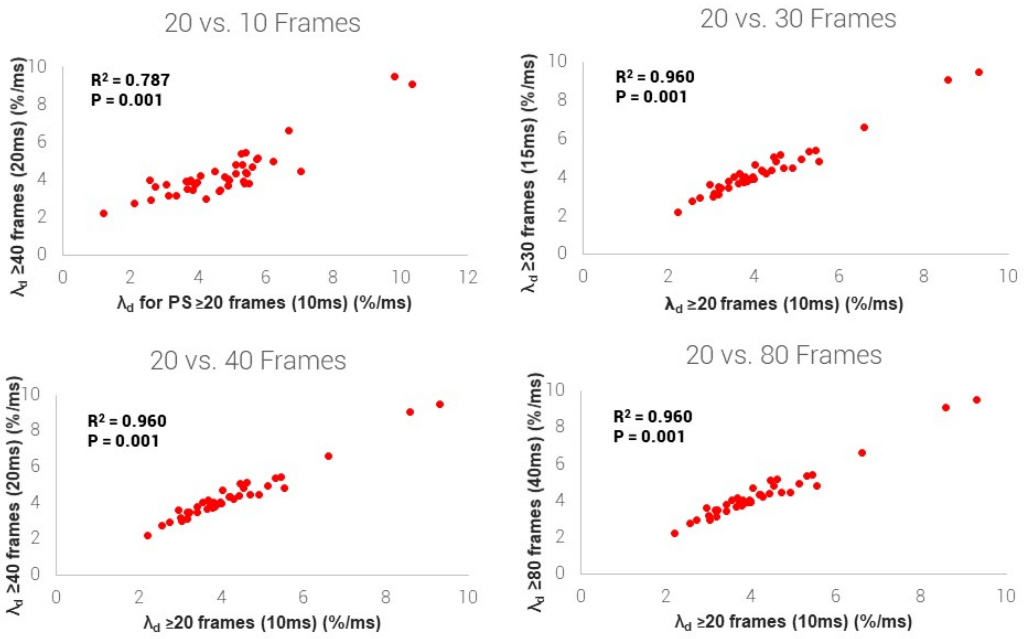

Figure 6.16: Effect of varying tracking window length

6.3.5 Comparison with Maximum Entropy Predicted Distribution

PS lifetime distributions for PS destruction returned similar experimental λ_f and MaxEnt derived λ_f in both humans and sheep (Human: 4.9%/ms (95%CI, 4.6, 5.3); Sheep: 4.6%/ms (95%CI, 4.2, 5.0)) (S16), which were strongly correlated (Human R2: 0.99; Sheep R2: 0.99). PS formation demonstrated similar results (Human: 4.3%/ms (95%CI, 4.0, 4.5); Sheep: 3.7%/ms (95%CI, 3.3).

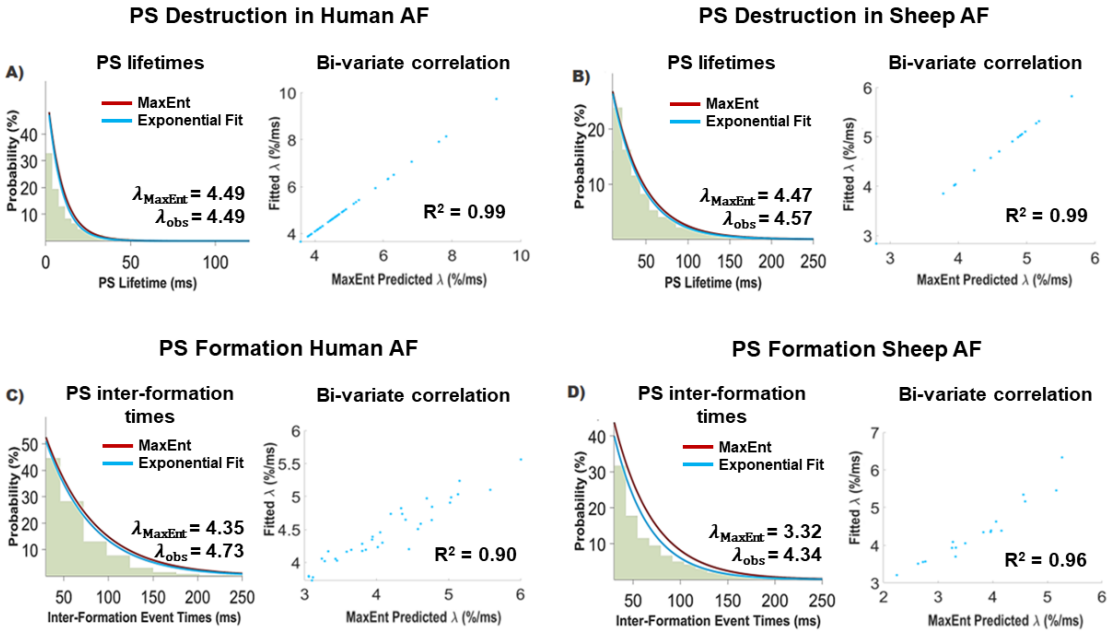

Figure 6.17: MaxEnt Predicted and Fitted λ_f are Highly Correlated

6.3.6 Comparison with Experimental Observations from Previously Published Studies

In the systematic literature search 1782 references were identified, with 23 retrieved for full-text review. A further 6 articles were identified that produced a phase singularity distribution histogram. The the search criteria is outlined in Figure 6.8. PS lifetime histograms from published papers are reproduced in Figure 6.18, showing that these distributions were consistent with an exponential form (Table 6.1). Rate constants for $\lambda_{dm}axEnt$ and $\lambda_{do}bserved$ were comparable in all cases, and also produce similar values to the observed experimental λ_d from this study.

YEAR	**AUTHOR**	**AF/VF**	**MODEL**	$\lambda_{dMaxEnt}$ **(%/ms)**+	$\lambda_{dobserved}$ **(%/ms)**++
2000	Chen	VF	Sheep, optical mapping	6.8%/ms	6.1%/ms
2000	Chen	AF	Sheep, optical mapping	5.1%/ms	5.2%/ms
2006	Kay	VF	Porcine optical mapping	*	2.7 %/ms
2017	Kuklik	AF	Contact plaque	**	1.6%/ms
2018	Child	AF	Human basket catheter	2.7%/ms	3.4%/ms
2018	Christoph	VF	Optical mapping, electromechanical mapping	2.1%/ms	2.9%/ms

Table 6.1: Systematic Review Results - Studies showing histogram or probability distribution for phase singularity lifetime in AF and VF 2000-2018

+ Predicted λ is derived from expectation of PS lifetime using Lagrangian multipliers as shown in Methods
++ Observed λ is determined from nonlinear least squares fitted coefficient for the probability distribution for PS lifetime

*Estimated based on text that 0.996 of PS were <200ms, MaxEnt prediction unable be calculated as sample mean for PS lifetime because binning was too wide (200ms). PS –observed based on curve fit.

** MaxEnt prediction unable to calculate sample mean for PS lifetime as binning too wide (by rotation number) to allow estimation of sample mean lifetime; λ -observed based on fitting curve to histogram with estimated PS lifetime for 1 rotation of 160ms.

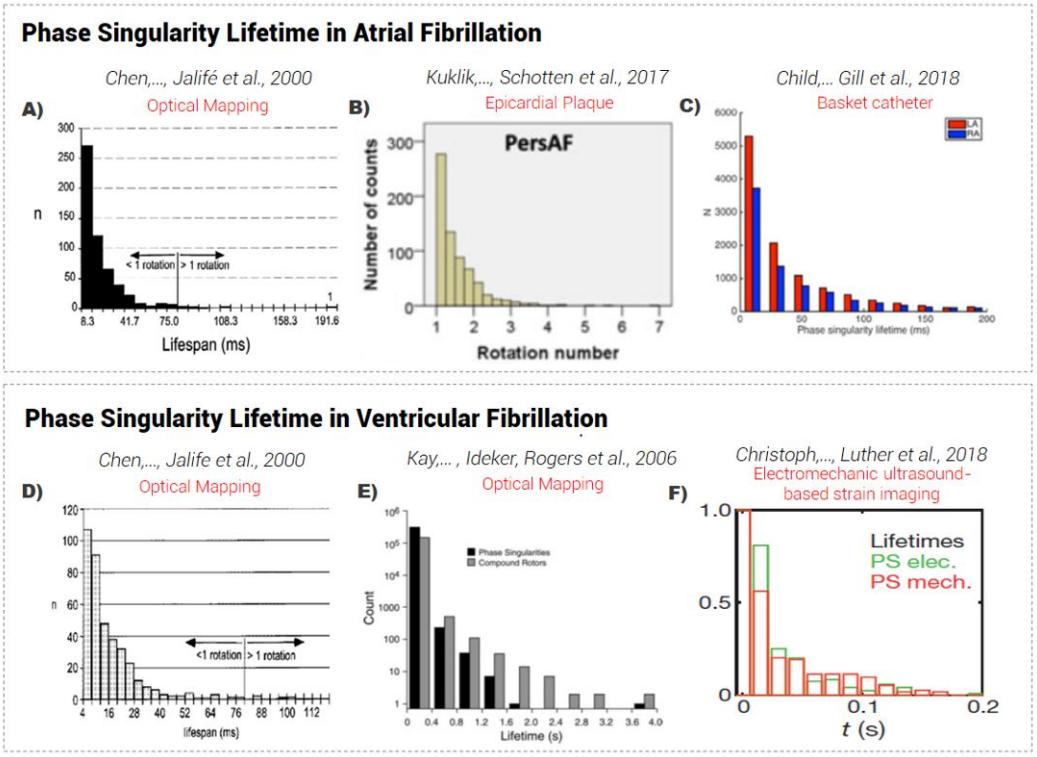

Figure 6.18: Phase Singularity lifetime histograms from previously published studies consistently demonstrate exponential distributions irrespective of mapping modality. Reprinted with permissions.

6.4 Discussion

The continuous appearance and disappearance of unstable re-entrant circuits is a distinguishing feature of cardiac fibrillation. This study shows that PS lifetimes and inter-formation event times during AF and VF show exponential distributions, consistent with the notion that PS disappear and are regenerated by Poisson point processes. The results provide a universal quantitative framework to characterise the formation and destruction of PS in cardiac fibrillation, and indicate that paradoxically during periods of sustained AF and VF, the system dynamics are conserved, despite the aperiodic turbulence of wave propagation.

6.5 Unstable re-entrant circuits - a historical context

The observation of unstable re-entrant circuits in cardiac fibrillation has been a consistent finding throughout the history of the field [89, 129, 143] (chapter 5.3), but thus far, the characterization of these processes has predominantly been qualitative. Indeed, the absence of quantifiable predictions based on the multiple wavelet theory has been a criticism levelled at Moe's original conceptualisation [193]. Although multiple reports have observed the stochastic nature of the formation and

disappearance of re-entrant circuits, the statistical processes underlying these events have not been well studied.

An interesting feature of the previous literature is that exponential distributions of PS lifetimes are observable in many published data from AF [48, 50, 136] and VF [48, 51, 124]. However, in these studies the connection of the distribution to the underlying data generating process was not explored. Collectively, however, this provides support for results of the current study.

6.5.1 AF and VF as renewal processes

Poisson point processes are the archetypal example of a renewal process, in which the inter-event waiting times are independent, but the long-term rate is constant. Mechanistically, the results may perhaps provide a bridge between the multiple wavelet and rotor theories of fibrillation, by suggesting that continuous generation and destruction of PS (e.g. wavebreaks in Moe's theory), can be conceptualized as a memoryless, stochastic processes, strictly governed by measurable rate parameters, but that long lasting rotors can also co-exist though are a rare phenomena. As PS have a fixed rate of being destroyed at any given time, long lasting rotors are less likely to occur. This is further supported by the exponential distribution of PS lifetimes, which shows a decrease in the number of PS observed the longer the lifetime becomes.

6.5.2 Origins of the exponential limiting distribution - applying the principle of maximum entropy

An important question is the origin of the exponential distribution of PS formation and destruction. The phenomenon of microscopic uncorrelated stochastic processes adding to macroscopically stable limiting distributions is a constant motif repeated throughout nature [80,105]. This occurs because if the system is averaged over long periods of time, then fluctuations in dynamics of natural systems tend to summate towards recognisable distributions. The principle of MaxEnt [120] has been used in a variety of fields including neuroscience and ecology [23] to enable prediction of the least biased (most stochastic) distribution of a sample. Demonstration that the observed data fits the MaxEnt predicted distribution shows that lifetime processes of PS formation and destruction can be accurately modelled as stochastic processes.

6.5.3 Implications for overall cardiac fibrillation system dynamics

The switch from sinus rhythm into fibrillation has been considered a form of chaos [87, 88]. Such systems may have the property of being dissipative, in the sense that the long-term trajectory through the system phase space is unstable, or conservative, so that the long-term behaviour of

the system dynamics in phase space is conserved [73]. By demonstrating that the processes of PS destruction and formation are regenerative renewal processes, it suggests that this aspect of sustained AF and VF is a conservative, rather than dissipative, nonlinear system [73]. This is consistent with the clinical behaviour of AF, which in persistent forms can last for decades. The nature of how AF becomes more persistent, and how terminations in AF and VF occur, remain questions that will be objectives of future studies.

Computer simulations were performed to evaluate the impact of introducing stable spirals and electrophysiological inhomogeneities into cardiac fibrillation. Fibrillation in the absence of stable spirals showed an underlying PS lifetime distribution that was consistent with an underlying Poisson renewal process. The addition of a single stable spiral into the continuous fibrillation model led to a small reduction in λ_d, perhaps by supressing spiral breakup in the local area of the stable rotor. Adding inhomogeneities to the recovery variable $\mu 1$ led to significant decrease in λ_d, perhaps by leading to a more global suppression of spiral breakup [232].

6.5.4 Implications for candidate biological mechanisms in cardiac fibrillation

A number of potential mechanisms have been proposed for the maintenance of atrial and ventricular fibrillation including multiple wavelet re-entry [165], discrete local rotors [96, 225], repetitive focal activation [143] and endocardial to epicardial dissociation. This study finds support for a mechanism of fibrillation based on formation and destruction of phase singularities, which most closely relates to the notion of rotors. However, rather than individual discrete local rotors autonomously driving fibrillation, the study suggests that it is in fact the continuous generation and annihilation of PS that leads to the perpetuation of AF and VF.

The reason why this occurs lies in the topological constraints on phase singularity dynamics [262]. Every PS formed by a rotor is, at least for an instant, surrounded by the complete phase cycle and therefore provides the opportunity for incoming waves to break, thereby forming a new PS. Further, every PS is at a continuous fixed incoming risk of annihilation by an incoming wave arising from a counter-chiral PS. Collectively, this suggests that a cycle of continuous formation and destruction of PS leads to the perpetuation of fibrillation.

6.5.5 Interpretation for the clinical context

The key point of the current study that PS formation and destruction are continuous Poisson processes has potentially significant implications for treatment. It implies that despite the irregularity of electrical wave propagation in AF and VF, PS formation and destruction, essential to the perpetuation of fibrillation, occur via stable mechanisms. The findings explain why temporal

instability is an essential property of individual rotors. Rotor temporal instability is a unifying finding in most AF mapping studies that has presented a practical barrier to the reproducible ablation of AF driving rotors. Potential future clinical applications could be to use the rates of PS formation and destruction for monitoring clinical AF progression, and intraprocedural monitoring of the effectiveness of catheter ablation strategies. Ongoing investigations are underway into these possibilities.

6.5.6 Limitations

A key question at the heart of fibrillatory dynamics is the relative contribution of a casually deterministic role for rotors versus stochastic mechanisms in sustaining AF and VF. The current study assumes the latter approach, and is consistent with a role for rotors in sustaining fibrillation via continuous PS formation and annihilation. As such, it does not necessarily exclude a deterministic role for stable rotors in experimental and clinical contexts seen outside the arrhythmias studied. Additionally, as the study focused on PS dynamics, it is unable to address the relative contribution of other potentially adjunctive mechanisms such as repetitive focal discharges [143] or endo-epicardial dissociation.

6.5.7 Future directions

By recasting the formation and destruction of rotational events as renewal processes, the results provide a universal theoretical basis for the modelling of rates of PS destruction and formation, which may be related to the persistence and termination of the arrhythmia. These rate constants are easily measurable statistical parameters that allow the fibrillatory process to be characterised. Future research efforts should be directed to understand how AF and VF terminate, and to determine the effects of autonomic nervous system regulation, substrate modification, pharmacological therapy and ablation strategies on renewal process parameters in relationship to successful termination or prevention of fibrillation, in order to obtain new mechanistic insights.

6.6 Conclusion

This study demonstrates that PS destruction and formation in cardiac fibrillation are renewal processes. These results provide a potentially powerful universal quantitative framework to explain the formation and destruction of rotational events in mammalian cardiac fibrillation.

To summarise, this study adds important insights to the current literature by:

- Providing the first universal framework to quantify the rate of formation and destruction of rotational events in cardiac fibrillation

- Showing that the formation and destruction of re-entrant activity occurs due to a stochastic Poisson renewal process, whereby even individual PS behave randomly, but the aggregate rate of formation and destruction is stable
- The study provides a comprehensive investigation that cross-validates findings in 5 model systems, using multiple mapping modalities in both atrial and ventricular fibrillation, as well comparison with current literature using a systematic review
- This study is also the first to establish stochastic and renewal process theoretical approaches as a means to study the behaviour of re-entrant activity in fibrillation

Chapter 7

Renewal rate constants of phase singularity formation and destruction in atrial fibrillation are temporally stable: implications for AF mechanism

7.1 Introduction

As discussed in chapter 6, a recurring pattern in studies of cardiac fibrillation is that PS lifespans follow exponential distributions [49, 70, 136]. The insight that PS lifetimes produce an exponential distribution is important because it is the hallmark of an underlying Poisson renewal process. In chapter 6, the formation and destruction of phase singularities (PS) was studied, demonstrating that these could be modelled as Poisson renewal processes [70]. It was found that PS formation and destruction processes followed exponential distributions of inter-event times, which can be characterized by the formation rate (λ_f) and destruction rate (λ_d).

A characteristic of Poisson renewal processes is that although the timings of individual events are statistically independent, the underlying Poisson rate is stable over time [81]. In the context of AF, paradoxically this would mean that the arrhythmia generating mechanism is temporally stable, despite the superficial appearance of uncoordinated or random electrical wave propagation. This is important, because it would recast the disorder of AF as the product of an underlying

stable stochastic process. It would also have the practical implication that measuring the rate constants λ_f and λ_d would be a simple, reliable way to characterize AF in individual patients, compared to other measures of AF electrogram properties that are spatiotemporally variable over time [69, 100, 119, 211].

Here, it is hypothesised that if PS formation and destruction processes are stable, then the rate constants λ_f and λ_d should be consistent over time. To investigate the temporal stability of λ_f and λ_d this study systematically tested for the statistical property of stationarity. A stationary process is one that conserves its statistical parameters over time [104]. To establish the property of wide-sense stationarity, two key properties were investigated:

- consistency of the mean over time
- a time invariant autocorrelation function

To investigate whether the stationarity hypothesis applies to PS formation and destruction processes, this chapter studies the statistical distributions of PS lifetimes, and the time taken between the formation of new PS (referred to as formation times), in basket-catheter mapped AF in humans and sheep. Specifically, it was evaluated whether estimates of λ_f and λ_d derived using short-duration random time windows approach the long-term time domain average, hence demonstrating conservation of the mean. The study also assessed whether the autocorrelation of PS lifetime and formation times are independent of time. As a practical application of this stationarity, this chapter concludes by estimating the minimum sampling time required to accurately determine PS formation and destruction rates λ_f and λ_d.

7.2 Methods

7.2.1 Human Study Design and Data Acquisition

The human AF study was a multi-center observational design analyzing electrograms acquired prior to ablation, as previously detailed in chapter 4.2.1. Details of this dataset are detailed in Supplement F. The inclusion criterion was persistent AF undergoing clinically indicated ablation. Patient participation was by informed consent, with recruitment from two centers (Flinders University, Australia), and Hamburg University (Germany). Patient characteristics are provided in Supplement F.

Basket catheter recordings were performed as previously described in chapter 4.2.1. 64-electrode basket catheters (Constellation, Boston Scientific, MA, 48mm (4mm spacing), 60mm (5mm spacing)) were utilized, based on computed tomographic scan. Unipolar electrogram recordings (1-500 Hz, 2000Hz sampling frequency) were obtained in spontaneous or induced AF lasting at least 5

minutes in the left and right atria. Catheter stability was verified fluoroscopically, and in Velocity (Abbott, IL, USA).

7.2.2 Ovine Study Design and Data Acquisition

The ovine study was performed in a rapid atrial pacing model in sheep, involving right atrial tachypacing for 16 weeks ($\geq$300 bpm) to obtain persistent AF. The details of the model are as reported previously in chapter 4.2.1.

Ovine persistent AF was induced in sheep via atrial tachypacing for 16 weeks at $\geq$ 300 bpm per minute as described in chapter 4.2.1. Unipolar electrograms were obtained during electrophysiology study, using 64-electrode Constellation catheters(48mm). Electrograms were filtered from 1 Hz to 500 Hz, sampled at 2000 Hz on NavX (Abbott, IL, USA). $\geq$5 minutes LA and RA recordings were performed.

7.2.3 Cleaning, Filtering and Sinusoidal Recomposition

Signal processing was performed similarly the previous study outlined in chapter 6. Unipolar electrograms, surface ECG, and 3D data were exported from Velocity (St Jude Medical, MN, USA) in humans, and NavX (St Jude Medical, MN, USA) in sheep. QRS subtraction was performed [223]. Signals were filtered using a 4th order Butterworth fitted with a 1 to 30 Hz band pass filter applied in forward and reverse mode17. A Hanning window was applied for edge tapering, and the Welch power spectral method applied. The Fourier dominant frequency was used as the wavelet period for sinusoidal wavelet recomposition [135].

7.2.4 Hilbert Phase Mapping and Phase Singularity Detection, PS look-up table

The instantaneous phase for each electrogram was constructed by applying the Hilbert transform as detailed in chapter 6.2.2. A PS appears when the phase around a given point progresses through from $-\pi$ to $+\pi$. PS detection was performed using the double-ring extended topological charge method (chapter 6.2.2). To determine PS lifetime and PS inter-formation event times, a look-up table indexing onset time, offset time and electrode location for each new PS detection was created as previously described (chapter 6.2.2). A new PS detection event was defined as the detection of a PS at an electrode and its surrounding 1-electrode neighborhood for at least 20 consecutive frames (10 ms). The look-up table enabled computation of histograms for: (i) PS lifetimes and (ii) inter-formation event times.

7.2.5 Computation of PS rates of formation λ_f and destruction λ_d

A schematic providing an overview of PS formation and destruction times is shown in Figure 7.1. PS occur at the pivot of spiral waves, but also due to topological considerations at the end of free wavelets (Figure 7.1A, 7.1B) [264, 266]. The PS lifetime is the interval from the start to the end of each PS, shown in red in Figure 7.1C. The PS formation interval defines the interval between the creation of a new PS until the creation of the next consecutive PS, shown in blue in Figure7.1C.

For each epoch, observed experimental PS lifetime data was fitted with an exponential distribution using maximum likelihood as previously described (chapter 6.2.4). The adequacy of fit was assessed using the chi-squared (χ^2) goodness-of-fit test. The exponential decay constant (λ_d) from of the probability distribution function (PDF) of PS lifetimes yields the average rate of PS destruction. The exponential decay constant (λ_f from the probability distribution function of inter-formation event times yields the average rate of PS formation.

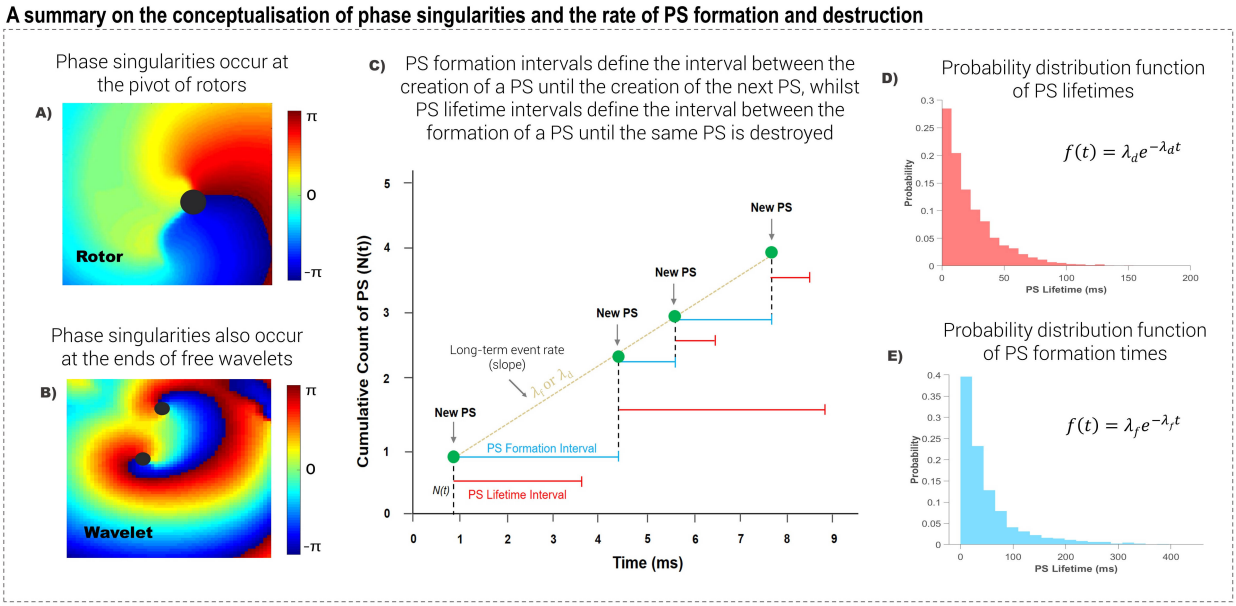

Figure 7.1: A summary schematic to describe phase singularities, and the rate of PS formation and destruction

7.2.6 Approaches to Establish Stationarity

A stationary process is one whose statistical properties are constant over time. To assess whether PS formation and destruction processes are stationarity, the study tested for i) conservation of the mean rate of PS formation (λ_f) and destruction (λ_d) over time, and ii) a time invariant autocorrelation function for PS lifetime and formation times. That is, the study sought to establish

that:

$$\mu_X(t) = \mu_X \tag{7.1}$$

where μ_X represents the mean value and t time. In addition, the autocorrelation function should only depend on the time difference τ (and thus independent of time t) such that:

$$R_X(t, t+\tau) = R_X(\tau) \tag{7.2}$$

where R_X is the autocorrelation function of $\{X(t)\}$, t time and τ the time shift [183].

7.2.7 Conservation of the mean

Random ensembles were constructed using randomly selected windows of consecutive PS to investigate whether the PS rate of formation and destruction (λ_f and λ_d) were conserved. Specifically, λ_f and λ_d were estimated for each ensemble, and compared to the long-term average λ_f and λ_d.

Randomly windowed ensembles

To create random windows of size n, a random PS was selected as the starting index from the look-up table of a 5-minute AF epoch, along with respective inter-formation event time. To ensure windows remained of size n the starting index was selected such that it fell between the total number of PS minus the window size n For each ensemble size, at least 1000 random ensembles were created. PS data were fitted with an exponential distribution using maximum likelihood for each random window, and the rate constants λ_f and λ_d were estimated. A schematic outlining the creation of random ensembles is shown in Figure 7.3.

Autocorrelation

The autocorrelation for PS formation and destruction was assessed using the sample autocorrelation function of the univariate time series of PS lifetimes or PS formation times respectively. Specifically, the autocorrelation function of a stochastic process is given by measuring the correlation between the time series y_t and y_{t+k} (e.g. a time shifted or 'lagged' version of the time series). The sample autocorrelation function r_k for lag k is given by [34]:

$$r_k = \frac{c_k}{c_o} \tag{7.3}$$

where c_o is the sample variance of the time series, and c_k the estimate of the autocovariance $\hat{\gamma}_k$ given by:

$$c_k = \hat{\gamma}_k = \frac{1}{T}\sum_{t=1}^{T-k}(y_t - \overline{y})(y_{t+k} - \overline{y}) \tag{7.4}$$

where $\overline{y}$ is the sample mean of the time series, and T the number of observations [34].

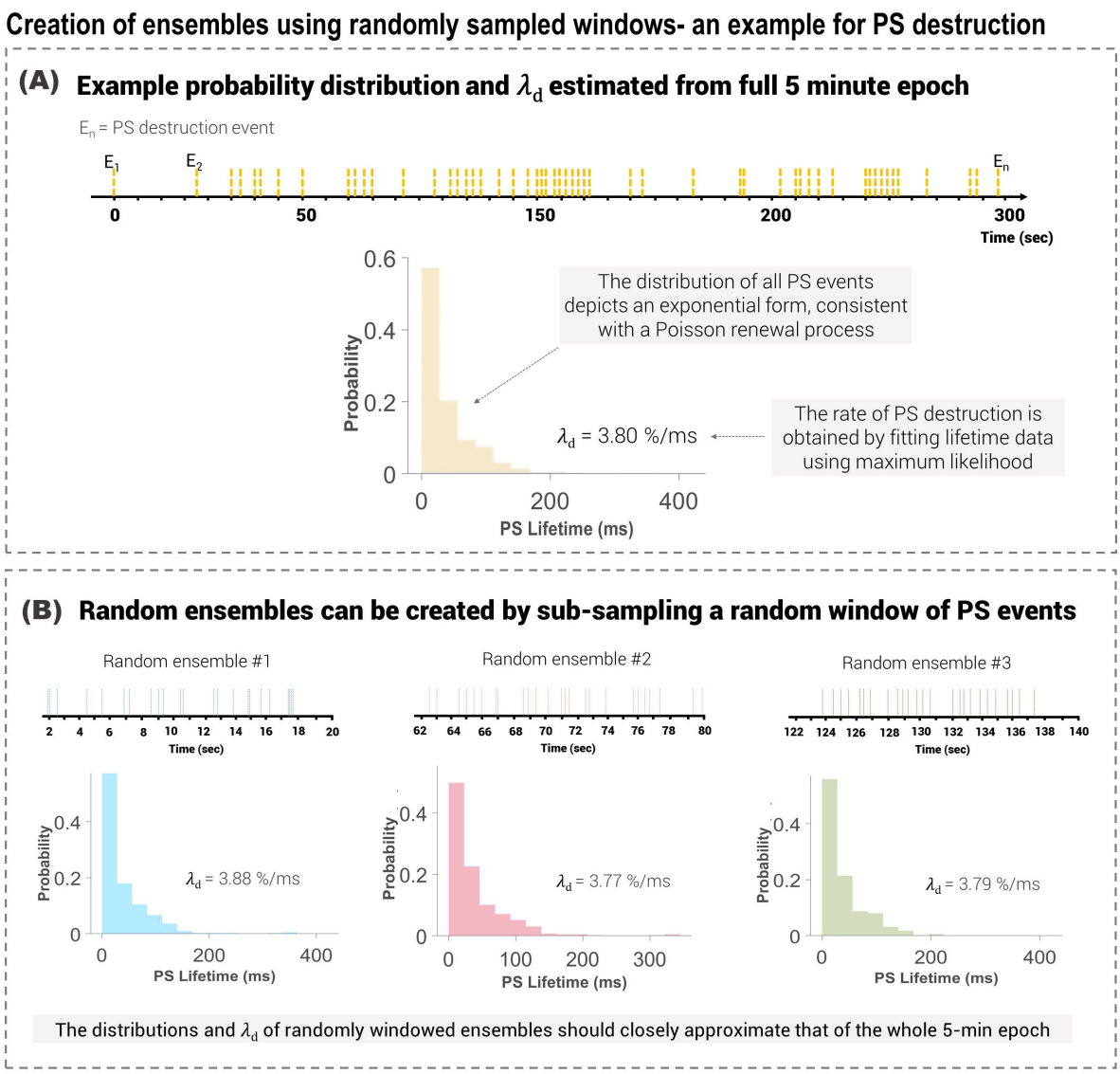

Figure 7.2: Creation of ensembles using randomly sampled windows- an example for PS destruction

A: Example probability distribution and λ_d estimated from full 5-minute epoch- PS destruction events denote the time at which PS are destroyed. **B**: A random window is created by sub-sampling a random segment of continuous PS events (shown here for a window length of 20 seconds). If the distribution and rate estimates closely approximate those from the whole epoch, this suggests that the statistical properties are conserved and the process is stationary.

7.2.8 Minimum Sampling Calculation

To determine the minimum length of recording needed to accurately estimate λ_f and λ_d, the long-term average λ_f and λ_d was first from each full 5-minute epoch. Upper and lower error bounds for 1-20% error from the true λ_f and λ_d were then calculated (Figure 7.3). The number of PS to be sampled from the look-up table (the sample size, n) was iteratively increased from 2 to the total number of PS to simulate the effect of recording at different lengths. For each sample size n, 1000 random ensembles were created by randomly sampling a window of n consecutive PS. λ_f and λ_d was estimated for each random ensemble. The percentage of ensemble estimates out of 1000 that fell within the 10% error of the true λ_f and λ_d was recorded, which allowed identification the minimum sample size needed, and in turn length of recording. In this study specifically, the minimum length of recording needed to obtain 95% and 90% of λ_f and λ_d estimates within 10% error of the true λ_f and λ_d was calculated.

Using the PS formation look-up table, which records the cumulative count of new PS and the respective times at which they appear, the time needed to achieve the minimum sample size was determined by identifying the time at which the required number of PS have formed.

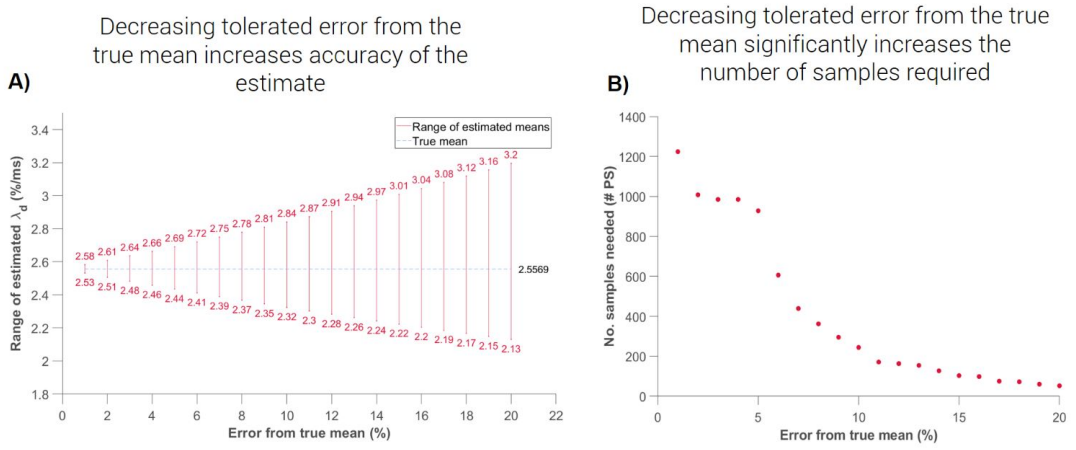

Figure 7.3: Example calculation for minimum sampling

7.3 Results

7.3.1 Conservation of the mean rate of PS destruction λ_d

The first condition to establish temporal stability of the rate of PS destruction λ_d is to verify that the mean λ_d is conserved over time. Figure 7.4 A and B illustrate the creation of two example ensembles using random 20 sec duration windows sampled from a 5-minute AF basket recording from a patient in persistent AF. It can be seen that the distributions and λ_d computed from

each random ensemble show good correspondence to the distribution and λ_d computed from the complete 5-minute AF recording (Figure 7.4A and B). Figure 7.4C shows the estimated λ_d for all 1000 ensembles, each created using random a 20 second window.

Ensemble estimates of λ_d show good correspondence to the long-term mean λ_d of 3.56 %/ms, with a low coefficient of variation (CV) of 1.52%. Very close approximation to the long-term mean λ_d is consistently observed for ensembles created using various window lengths, shown in Figure 3D for window lengths of 20 seconds to 5 minutes (CV = 0.34%). When compared in all cases, λ_d computed from 20 sec windows showed a strong correlation with λ_d computed from the respective 5-minute recording ($R^2 = 0.996$; P < 0.001), and lie along the line of identity (Figure 7.4E).

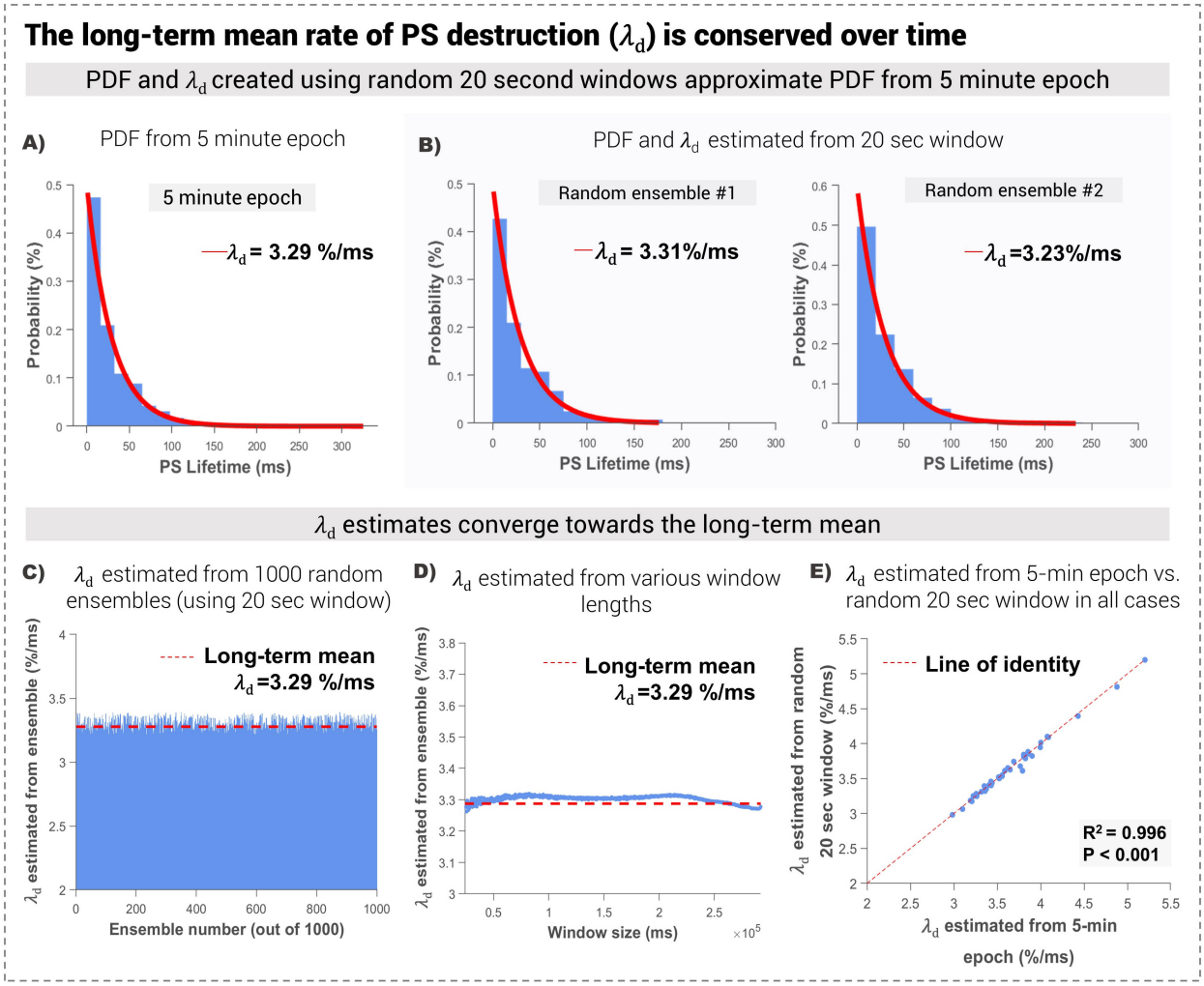

Figure 7.4: PS destruction is a stationary process that is stable in the time domain

7.3.2 Time invariant autocorrelation function for PS destruction

The second condition to establish stationarity is to establish the absence of a temporal dependence on the autocorrelation function. To study the autocorrelation function over time, individual PS

lifetimes were considered as an ordered time series, and correlograms constructed. Example plots for human persistent AF in the LA and RA are shown in Figure 7.5. It can be seen in this case that the autocorrelation function approaches zero for all non-zero lags, indicating that PS lifetime is independent of time. Correlograms for all cases are shown in Supplement J.

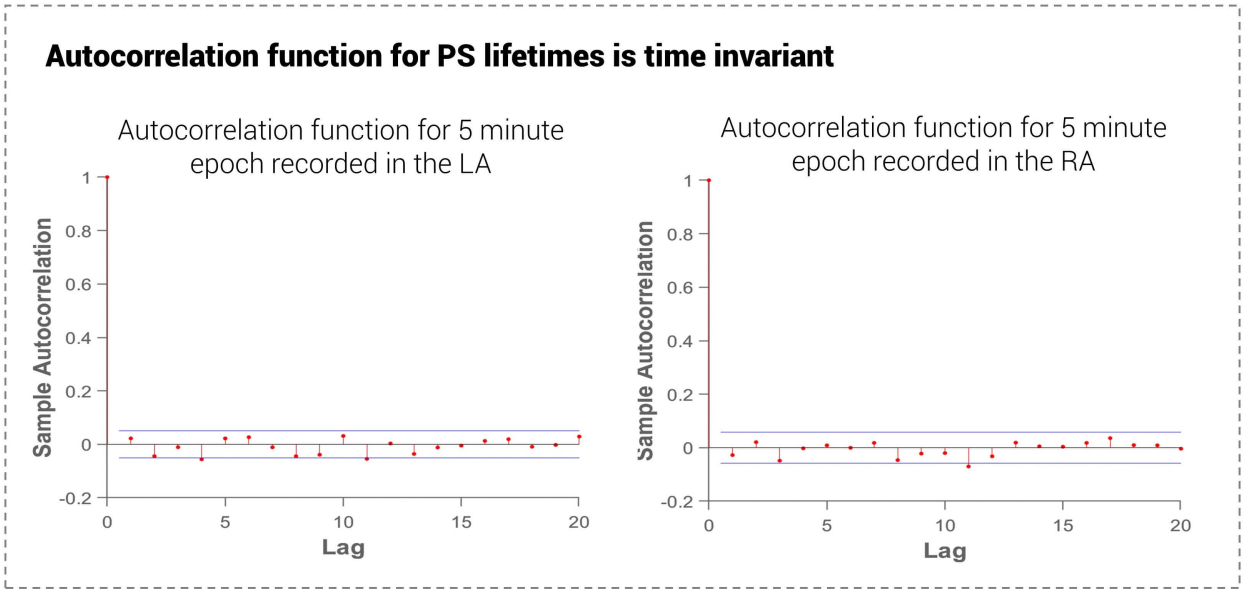

Figure 7.5: PS destruction is time invariant

7.3.3 Conservation of the mean rate of PS formation λ_f

Similar to λ_d, the study sought to establish whether the mean rate of PS formation λ_f approached the long-term rate of formation over time. Figure 7.6A and 7.6B provides an overview of the creation of random ensemble windows of 20 seconds. Distributions and λ_f computed from random 20-second windows show good correspondence to the distribution and λ_f computed from the complete 5-minute AF recording. Figure 7.6C shows the estimated λ_f for all 1000 ensembles, each created using a random 20-second window. Ensemble estimates of λ_f show closely approximate to the long-term mean λ_f of 2.63 %/ms, with a low coefficient of variation (CV) of 3.85%. Very close approximation to the long-term mean λ_f is again consistently observed for ensembles created using various window lengths (CV = 0.40%) (Figure 4D). λ_f computed from 20-second windows showed a strong correlation with λ_f computed from the respective 5-minute recording in all cases ($R^2 = 0.999$; $P < 0.001$), and lie along the line of identity (Figure 7.6E).

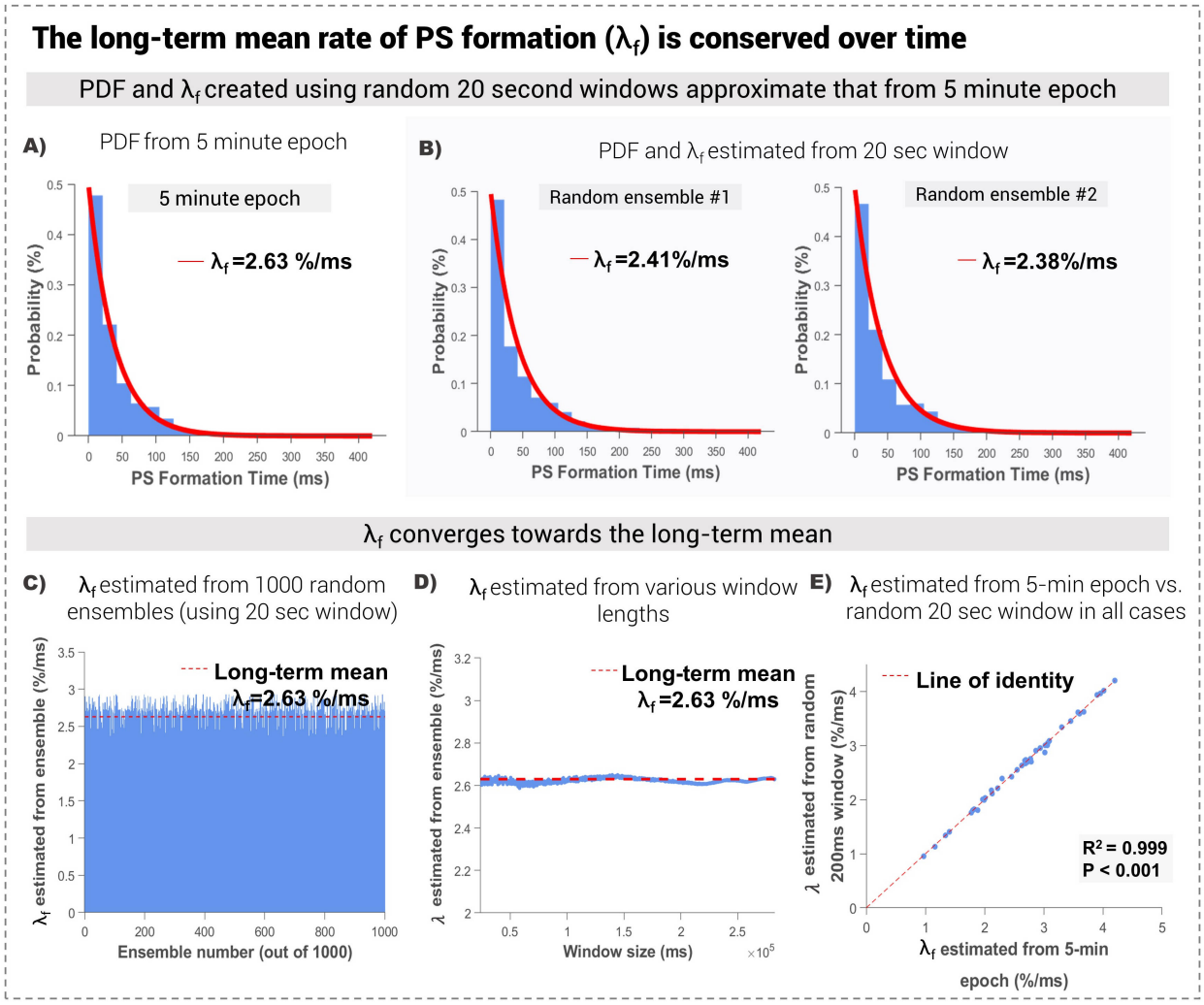

Figure 7.6: PS formation is a stationary process that is stable in the time domain

7.3.4 Time invariant autocorrelation function for PS formation

To study the autocorrelation function for PS formation, PS formation times were considered as an ordered time series, and correlograms constructed. Example plots for human persistent AF in the LA and RA are shown in Figure 7.7. It can be seen in this case that the autocorrelation function approaches zero for all non-zero lags, indicating that PS lifetime is independent of time. Correlograms for all cases are shown in Supplement J.

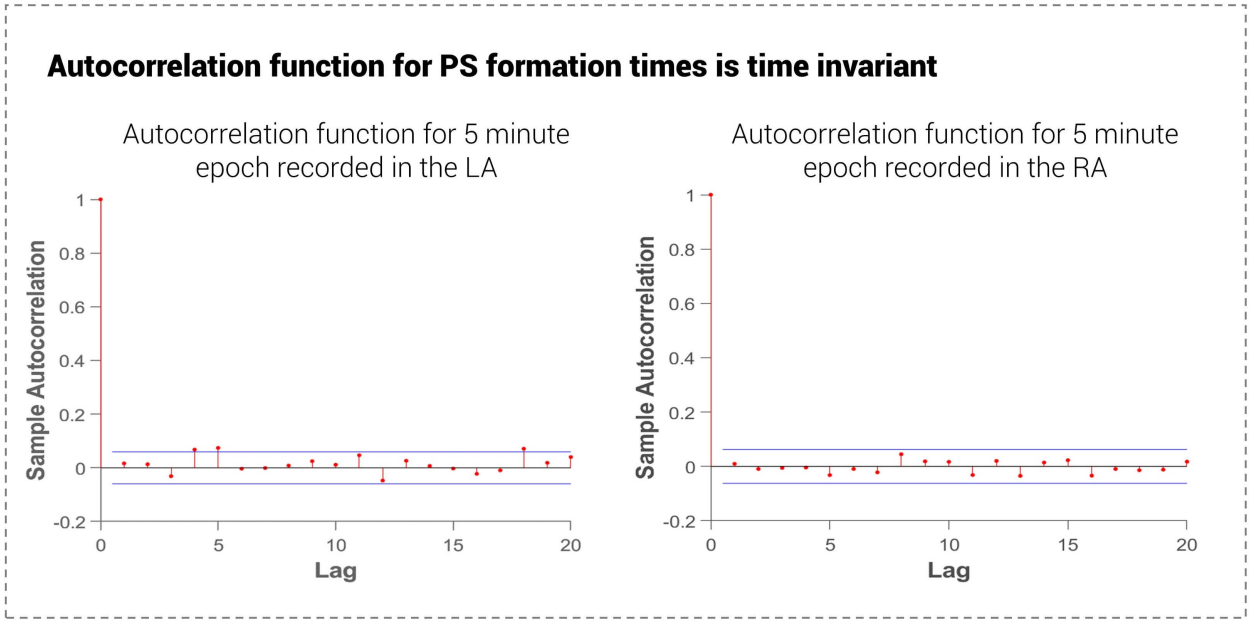

Figure 7.7: PS destruction is time invariant

7.3.5 Minimum Sampling for Rate of PS Destruction λ_d

Minimum sampling required for λ_d estimation in human persistent AF

Figure 7.8A and B show the calculation of the minimum sampling required for a single human AF case. The percentage of λ_d estimates from random short duration windows that fell within a specified error percentage of the long-term mean λ_d was calculated (Figure 7.8A), and it can be seen that with increasing error tolerance, a higher percentage of ensemble estimates of λ_d fall within the error bound. Figure 7.8B shows the length of recording required to get 90% of ensemble averages within 10% of λ_d in the same example case. A greater number of PS samples, and in turn recording length, is required to estimate λ_d with higher accuracy. In this example epoch, 16 seconds of recording was needed to achieve an accuracy of 90% (Figure 7.8B).

For an accuracy of 90%, an average of 342 PS (95%CI, 289, 395) and a minimum recording time of 14.64 sec (95%CI, 12.86, 16.42) was required (Figure 7.8C) and for 95% accuracy, an average of 403 PS (95%CI, 348, 458) was needed (Figure 7.8D). This translates to a minimum recording time of 15.00 sec (95%CI, 13.22, 16.77).

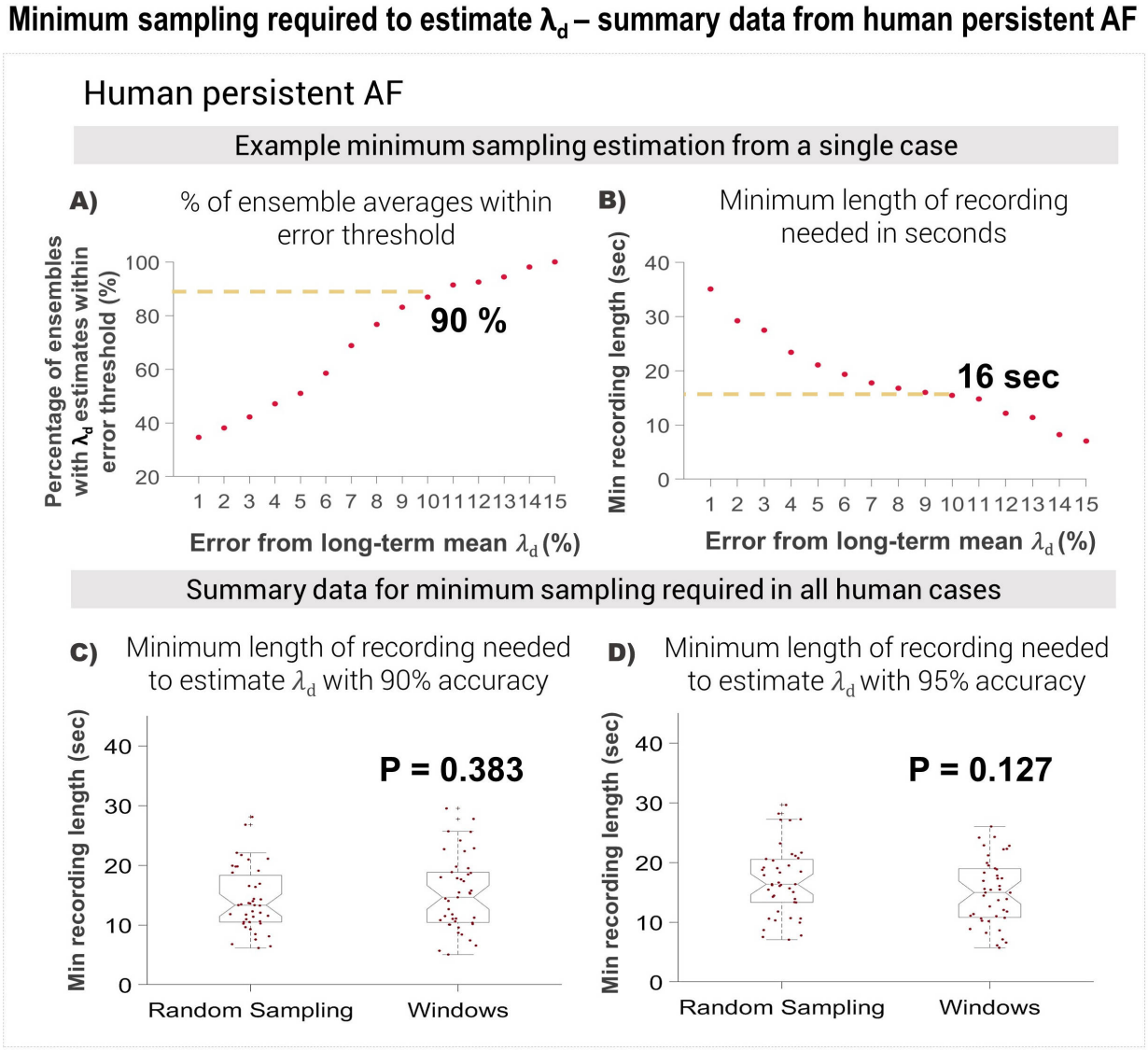

Figure 7.8: Minimum sampling required to estimate λ_d summary data from human persistent AF

Minimum sampling required for λ_d estimation in ovine sustained AF

Figure 7.9 shows an example of calculation of the minimum sampling required for a single ovine sustained AF case. The percentage of randomly windowed ensemble averages within a specified error percentage of the λ_d is shown in Figure 7.9A. Figure 7.9B shows that the minimum recording duration to get 90% accuracy of the long-term mean $\lambda_d$is 9 seconds in the same example case.

Figure 7.9C shows that an average of 389 PS (95%CI, 363, 414) and minimum recording time of 11.96 sec (95%CI, 8.57, 15.33) was required to achieve an accuracy of 90%. For an accuracy of 95%, the minimum sampling increases to 401 PS (95%CI, 373, 429), translating to a minimum recording time of 13.17 sec (95%CI, 9.73, 16.60) (Figure 7.9D).

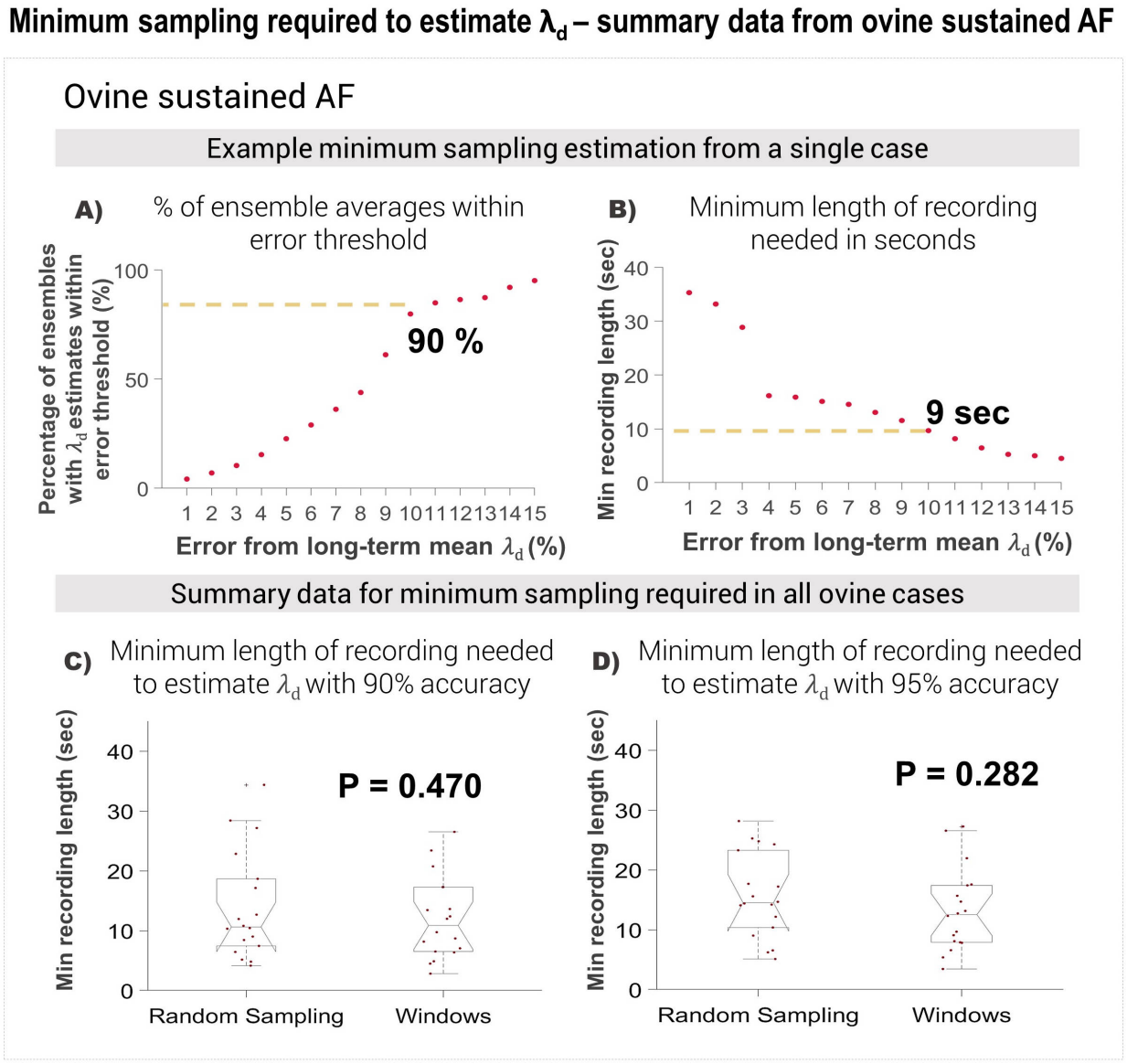

Figure 7.9: Minimum sampling required to estimate λ_d summary data from ovine sustained AF

7.3.6 Minimum Sampling for Rate of PS Formation λ_f

Minimum sampling required for λf estimation in human persistent AF

Figure 7.10A shows the number of PS required to get 90% of the randomly windowed ensemble averages within 10% error of the long-term mean λ_f in a single example case of human persistent AF. Figure 7.10B shows the same example, and it can be seen that the minimum recording duration required to achieve 90% accuracy of λ_f is 16 seconds.

Figure 7.10C shows that an average of 418 PS (95%CI, 367, 467) and a minimum recording time of 15.21 sec (95%CI, 13.30, 17.11) was needed to achieve an accuracy of 90% for λ_f estimates. An average of 472 PS (95%CI, 407, 538) and a minimum recording time of 16.67 sec (95%CI, 13.60,

17.23) was needed to obtain an accuracy of 95% (Figure 7.10D).

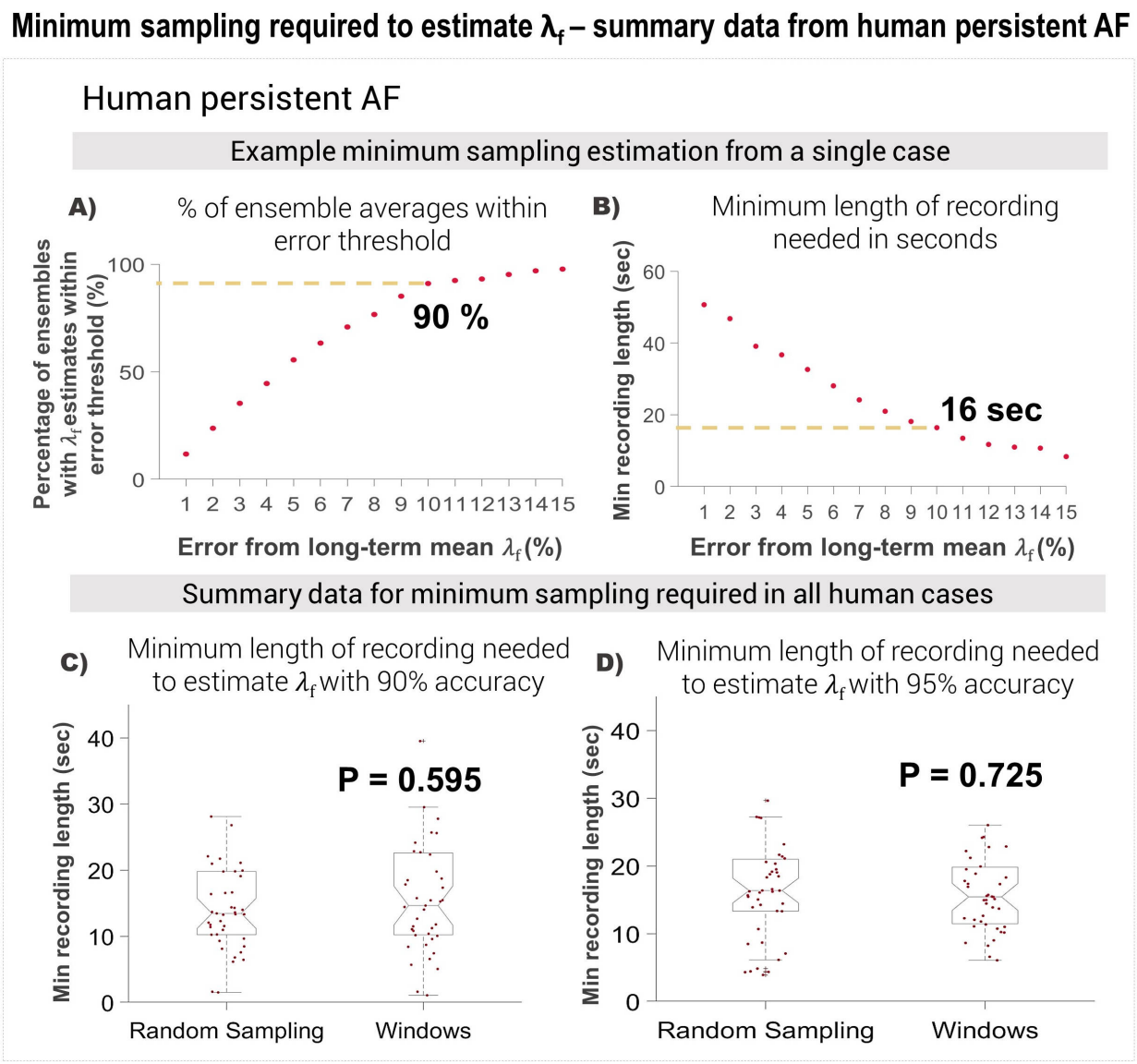

Figure 7.10: Minimum sampling required to estimate λ_f summary data from human persistent AF

Minimum sampling required for λ_f estimation in ovine sustained AF

Figure 7.11A shows the percentage of randomly windowed ensemble averages within a specified error percentage of the $\lambda_f$in a single example case of sustained ovine AF. Figure 7.11B shows the minimum length of recording required to get $\lambda_f$estimates with 90% accuracy in the same example, which in this case is 10 seconds.

Figure 7.11C shows that a minimum of 411 PS (95%CI, 334, 489) and a recording length of 11.22 sec (95%CI, 8.81, 13.63) is needed to estimate λ_f with 90% accuracy. For 95% accuracy, an

average of 550 (95%CI, 453, 647) and a minimum of 12.33 sec (95%CI, 9.94, 14.71) of recording was needed (Figure 7.11D).

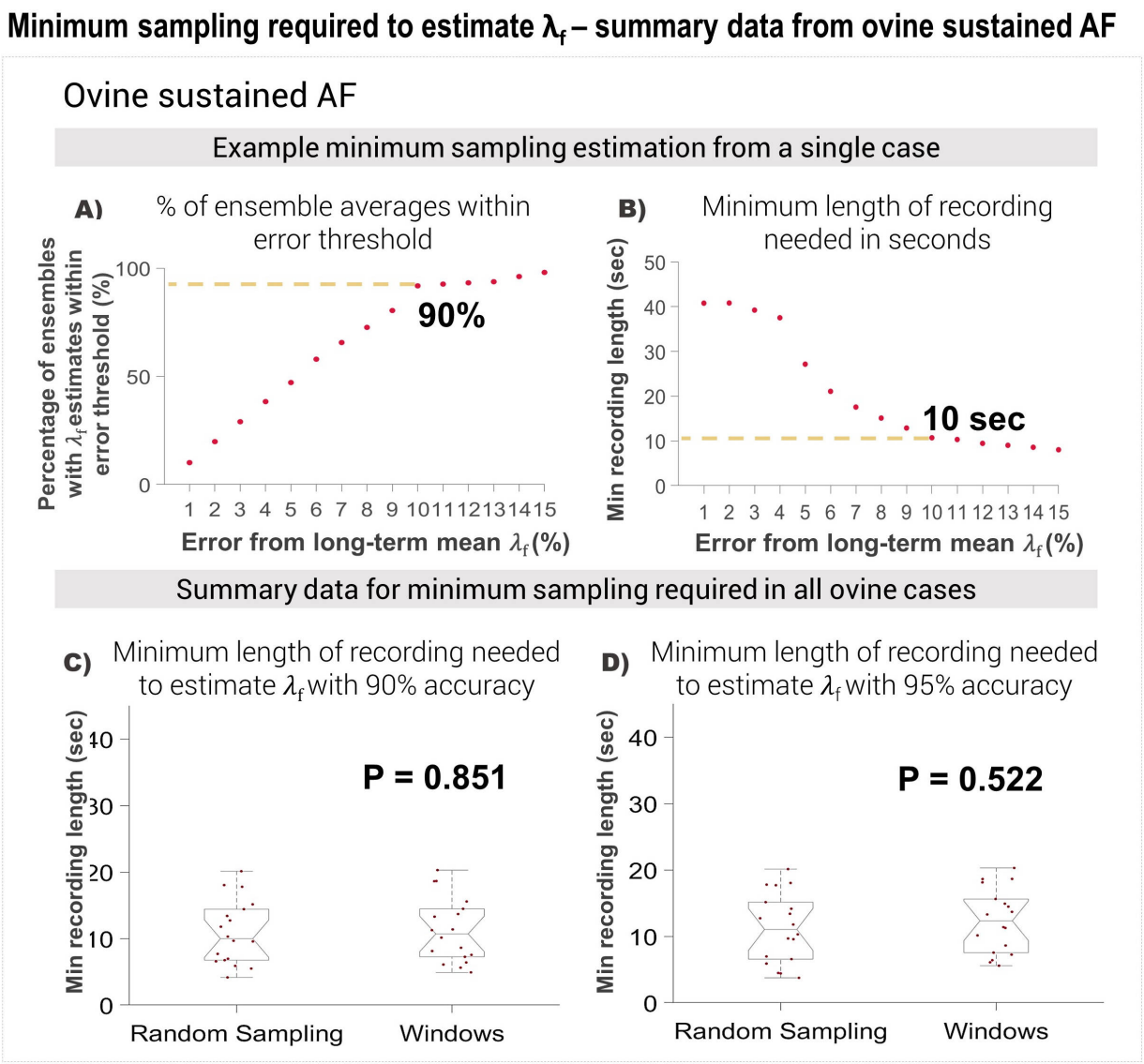

Figure 7.11: Minimum sampling required to estimate λ_f summary data from ovine sustained AF

7.4 Discussion

Atrial fibrillation is characterized by complex, aperiodic wave dynamics, with rotors believed to play a key role in sustaining AF [116,118,172]. In the previous chapter (6), it was shown that rotors are destroyed and formed by Poisson point processes, yielding exponential distributions of PS lifetimes and PS formation times. Here, the convergence of ensemble estimates obtained from randomly created short duration time windows converge to the long-term time domain average suggesting that in aggregate, λ_f and λ_d are consistent over time. Further, autocorrelation analyses showed an absence of time dependence in PS time series data. Collectively, these data are consistent with the concept that the limiting distributions of λ_f and λ_d are quite temporally stable. By demonstrating the temporal stability of these underlying rate constants, the findings fundamentally reformulate the prevailing notion that AF is incoordinate and chaotic. Instead, the aggregate stability of these rate constants suggests a model of AF in which the underlying arrhythmia generating process is temporally stable, despite the superficial appearance of randomness or incoordinate electrical wave behavior.

7.4.1 Implications for the AF mechanism

These findings are of potential significance to contemporary understanding of AF mechanisms. The typical textbook characterization of AF is an arrhythmia that is disorganized and irregular, as a reflection of the underlying spatiotemporal instability of wave propagation in AF [37]. The results of the study stand in marked contrast to this understanding of the underlying nature of the arrhythmia, by suggesting that despite the apparent random nature of wave propagation, the underlying limiting distributions of PS formation and destruction are wide-sense stationary. This suggests that, counter-intuitively, the underlying generating mechanism for fibrillation is in fact stable over the time.

The temporal stability of λ_f and λ_d is of relevance to the century-old debate regarding the underlying AF mechanism, for which multiple mechanisms have been proposed including rotors, multiple wavelet reentry, repetitive focal discharges and endocardial to epicardial dissociation [172]. The consistent finding of temporal stability of rotor formation and destruction rates in the current study are consistent with a notion in which the fundamental nature of AF is based on being an essentially temporally stable process, involving stochastic dynamical process based on repetitive formation and destruction of re-entrant events.

In this regard, the findings of the study assist in the reconciliation of the rotor mechanism with more stochastic theories of AF. An important strength of the renewal theory approach, however, is that it provides quantitative understanding about the nature of AF. This is in contrast to earlier formulations of fibrillation which qualitatively describe random aspects of electrical wave behavior,

without providing a universal quantitative architecture [12, 48, 67, 89, 129, 165, 193]

7.4.2 Clinical Implications of temporal stability of λ_f and λ_d

Conceptualisation of AF as stochastic process based on repetitive regeneration and destruction of new PS has important clinical implications. It would provide a mechanistic explanation for the temporal instability of PS and rotors seen in the majority of clinical studies, and would suggest that directed ablation of PS may be difficult or potentially impossible clinical target. At a practical level, the demonstration of λ_f and λ_d as temporally stable measures of underlying fibrillatory dynamics has the potential for clinical applications. Potential use cases include utilisation of λ_f and λ_d as an objective physiological marker for the persistence or progression of AF, or intraprocedural measurement of λ_f and λ_d as a marker for the likelihood of spontaneous AF termination.

7.4.3 Minimum sampling time to determine λ_f and λ_d

In essence, stationary properties in PS formation and destruction processes means the system dynamics do not change over time. This has a number of practical implications: (i) it implies that these rates can be estimated accurately irrespective of the start point at which data is sampled; (ii) PS destruction and formation rates can be estimated from short duration AF recordings, amounting to around 15 seconds in basket catheter mapped AF. This has potential for practical application as a reliable marker of AF dynamics.

7.4.4 Comparison to spatiotemporal stability of other markers of AF dynamics

In the clinical domain, a number of markers have been utilized to capture dynamic properties of cardiac fibrillation including dominant frequency (DF), complex fractionated electrograms (CFAE) and AF cycle length. Of these, spatiotemporal instability constrains the usefulness of DF [76,119], and CFAE [100]. AF cycle length, which is based on the average distribution of AF cycles, is potentially a marker of overall AF dynamics, has a higher coefficient of variation [90], and suffers from the limitation that it is an indirect marker of the AF process, rather than quantifying the mechanistic process underlying the perpetuation of the arrhythmia. In contrast to the above measures, λ_f and λ_d has a number of potential advantages: (i) it is connected to the underlying fibrillatory dynamics; (ii) the robustness of the Poisson renewal pattern in our data but also in the data presented by others points to this as a fundamental component of the fibrillatory process; (iii) it is a temporally stable measure, with clearly definable, objective criteria derived with a substantial theoretical basis in stochastic process theory.

7.5 Conclusion

Atrial fibrillation phase singularity formation and destruction processes follow stationary dynamics. it can be concluded that PS formation and destruction rates are therefore stable in the time domain, and can be accurately estimated from short-duration AF recordings, providing a mechanistic tool to measure overall AF dynamics, directly connected to rotor regeneration as the underlying mechanism of the perpetuation of AF.

To summarise, this study adds important insights to the current literature by:

- Demonstrating that PS formation and destruction processes in atrial fibrillation are robustly temporally stable
- As they are stable in the time domain, these processes can be accurately estimated from short-duration AF recordings, providing a mechanistic tool to measure overall AF dynamics, which is directly connected to rotor regeneration as the underlying mechanism of the perpetuation of AF
- The study also identifies the minimum sampling time required to accurately estimate the rate of PS formation and destruction (only $\sim$15 seconds)

Chapter 8

Self-regeneration of atrial fibrillation can be summarised and predicted using a Markov birth-death framework

8.1 Introduction

As we know, the electrophysiological mechanism by which AF perpetuates remains unresolved. The principal classical theories of wave propagation during fibrillation have included: (i) localized rapidly circulating rotors, with downstream fibrillatory conduction [155], (ii) multiple wavelets precessing irregularly through the myocardium [163]; (iii) rapidly firing foci [145]; and more recently (iv) endocardial-to-epicardial dissociation of conduction [241]. The failure to resolve the mechanistic basis of electrical wave propagation has had important consequences for clinical treatment, where the role and nature of further interventions beyond pulmonary vein isolation in persistent AF remains unclear at the present time.

A potential weakness of existing theories of cardiac fibrillation is that they are essentially qualitative and descriptive in character. Although experimental evidence exists to support each of the classical theories in human AF, none of the theories have the necessary quantitative architecture to provide specific predictions about overall wave propagation behavior in clinical recordings. From a scientific point of view, the lack of a quantitative predictive capability is a limitation, because it means that it is difficult to validate any of the classical theories of fibrillation. In the clinical context, the lack of predictive capability is also a major problem, because it has made it difficult to

prove if potential therapeutic interventions have had an effect on underlying fibrillatory dynamics.

In chapters 6 and 7, the statistical properties of phase singularity formation and destruction processes were studied. These chapters demonstrate that the distributions of PS inter-formation event times and lifetimes can be modelled as stochastic Poisson processes, and that PS formation and destruction processes are essentially stationary. These findings are critically important, as they collectively point towards a robustly stable underlying process of formation and destruction, despite the apparently chaotic nature of electrical wave propagation.

In this chapter, the following study aims to further use these insights to develop a comprehensive quantitative Markov birth-death framework to understand, summarise and even predict fibrillatory dynamics in human persistent AF, which could be applicable in both mechanistic studies and in clinical settings. Based on the fact that PS formation and destruction in AF occur as memoryless Poisson processes, it was hypothesised that the interplay between PS formation and destruction could be modelled as a Markov birth-death process.

The Markov birth-death process is considered a foundational element of stochastic process and queueing theory [126]. In a Markov birth-death process, Poisson renewal rate constants of formation and destruction stochastically interact to determine the quantity and lifetime of particles in the system (Figure 9.3). Markov birth-death processes have been used to model a variety of biological processes and have been extensively used in cardiac electrophysiology, where they are the default quantitative framework to understand how a single ion channel gating gives rise to aggregate membrane currents [210].

Here, I explore the utilisation of a Markov birth-death process framework to summarise, explain and predict the number and duration of phase singularities in: i) basket catheter recordings of human AF and ii) HD-grid recordings of human AF. This study hopes to provide the first quantitative explanation of how these circuits regenerate and thereby contribute to the perpetuation of fibrillation.

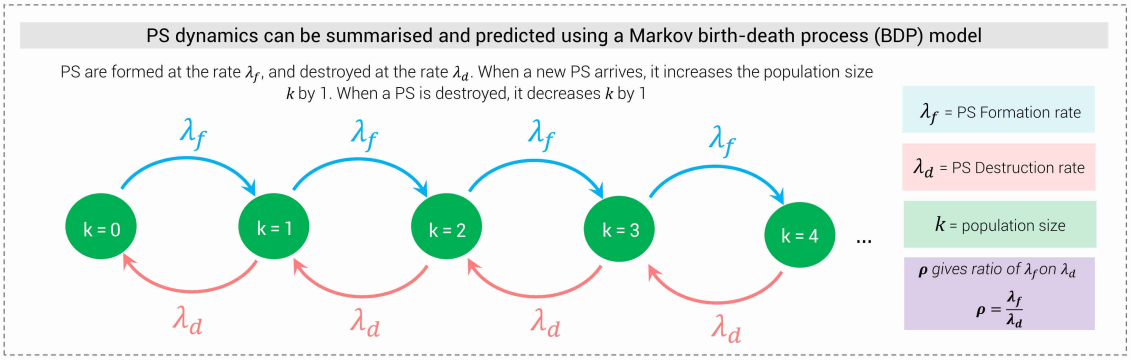

Figure 8.1: Conceptualisation of the Markov Birth-Death Process (BDP)

8.2 Methods

8.2.1 Human Study Design

The human AF study is as reported in chapters 6 and 7. The study was a multi-center observational design analyzing electrograms acquired prior to ablation. The inclusion criterion was persistent AF undergoing clinically indicated ablation. Patient participation was by informed consent, with recruitment from two centers (Flinders University, Australia), and Hamburg University (Germany). Details of this dataset are provided in Supplement F.

8.2.2 Data Acquisition

Basket Catheter Recordings of Human Persistent Atrial Fibrillation

Basket catheter recordings (n = 43 epochs) were performed as previously described in chapter 6. 64-electrode basket catheters (Constellation, Boston Scientific, MA, 48mm (4mm spacing), 60mm (5mm spacing) were utilized, based on computed tomographic scan. Unipolar electrogram and surface electrocardiogram recordings (1-500 Hz, 2000 Hz sampling frequency) were obtained in spontaneous or induced AF lasting at least 5 minutes in the left and right atria. Catheter stability was verified fluoroscopically, and in Velocity (Abbott, IL, USA).

HD Grid Recordings of Human Persistent AF

In a subset of patients, simultaneous basket catheter and HD-grid catheter recordings were obtained. The HD-grid catheter (Abbott, IL, USA) is a 3-3-3 mm catheter with 16 electrodes. During these recordings, the HD grid catheter was placed alternately on the anterior left atrial surface, and then on the posterior surface, whilst leaving the basket catheter in situ.

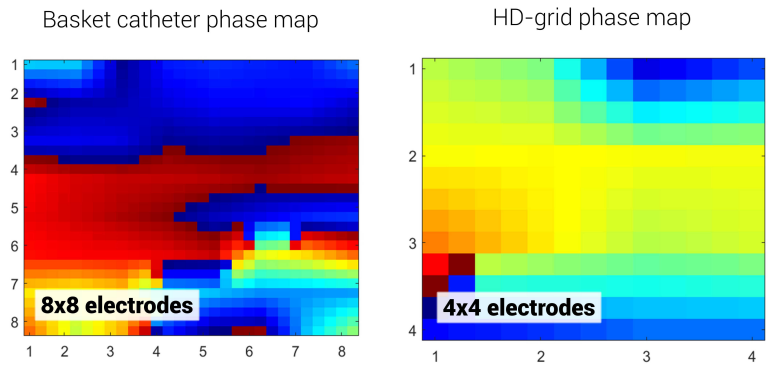

Figure 8.2: Basket catheter phase map (8x8 electrodes) vs. HD-grid catheter phase map (4x4 electrodes)

8.2.3 Cleaning, Filtering and Signal Processing

Pre-processing of AF unipolar signals

Signal processing was performed similarly to previous studies (chapter 6 and 7). Unipolar electrograms, surface ECG, and 3D data were exported from NavX. QRS subtraction was performed [223]. Signals were filtered using a 4th order Butterworth fitted with a 1 to 30 Hz band pass filter applied in forward and reverse mode. A Hanning window was applied for edge tapering, and the Welch power spectral method applied. The Fourier dominant frequency was used as the wavelet period for sinusoidal wavelet recomposition [135].

8.2.4 Hilbert Phase Mapping and Phase Singularity Detection, PS look-up table

In human AF data, the instantaneous phase for each electrogram was constructed by applying sinusoidal recomposition and the Hilbert transform as described in chapters 6 and 7. PS detection was performed using the double-ring extended topological charge method [136].

To determine PS lifetime and PS formation times, a look-up table indexing onset time, offset time and electrode location for each new PS detection was used as previously described (chapter 6). A new PS detection event was defined as the detection of a PS at an electrode and its surrounding 1-electrode neighborhood for at least 20 consecutive frames (10 ms). The look-up table enabled computation of histograms for: (i) PS lifetimes and (ii) inter-formation event times.

8.2.5 Modelling persistent atrial fibrillation as a Markov birth-death process

A birth-death process (BDP) is a continuous-time Markov chain that can be used to represent the number of particles in a stochastic system. As the name implies, there are only two types of state transitions: i) 'births', which increase the population size by one, and ii) 'deaths' that reduce the population size by one (Figure 9.3).

In such a process, birth and death events are independent of each other, and thus the times between events are modelled by Poisson processes given by an exponential probability distribution function (PDF). For PS births, the (PDF) of inter-formation events is given by:

$$f(t) = \lambda_f e^{-\lambda_f t} \tag{8.1}$$

where λ_f is the rate of PS formation, also referred to as the arrival rate often denoted by the

symbol λ, and t time. For PS deaths (lifetimes), the PDF is given by:

$$f(t) = \lambda_d e^{-\lambda_d t} \tag{8.2}$$

where λ_d is the rate of PS destruction, also referred to as the service rate ofen denoted by the symbol μ, and t time.

It can be noted that the birth-death process is the most fundamental example of a Markovian queuing model, whereby births and deaths in a system are analogous to the arrivals and departures in a queue [126]. Much in the same way that births increase the population k by 1 and deaths decrease the population by 1, arrivals and departures in a queue also govern the size of a queue. Because of this equivalence, queuing theory principles can be used to estimate the system's properties. In queuing theory nomenclature, different types of birth-death processes can be expressed using *'Kendall's notation'* [126]:

$$A/S/c \tag{8.3}$$

whereby A represents the time between arrivals (births) to the queue, S the distribution of service times (lifetimes), and c the number of servers. As PS inter-formation event times and PS lifetimes are both given by Poisson processes with an exponential distribution (chapter 6), PS formation and destruction processes can be modelled by $M/M/\sim$ birth-death queues, where M represents a random (Poisson) process that has Markovian or memoryless properties [126].

The simplest Markov birth-death process is an $M/M/1$ birth-death process. For an $M/M/1$ BDP, the average number of phase singularities can be summarised and predicted using:

$$N = \frac{\lambda_f^2}{\lambda_d(\lambda_f - \lambda_d)} \tag{8.4}$$

where λ_f gives the rate of PS formation, and λ_d the rate of PS destruction. The average PS duration can be summarised by:

$$W = \frac{\lambda_f}{\lambda_d(\lambda_f - \lambda_d)} \tag{8.5}$$

To test hypothesis that peristent atrial fibrillation could be modelled as an $M/M/1$ BDP, the observed experimental number (N_{obs}) and duration (W_{obs}) of PS from basket and HD-grid mapped was compared to the computed PS number (N) and duration (W) predicted from the $M/M/1$ BDP model. N_{obs} was calculated by taking a running count of the PS at each time-step, and finding the mean. To calculate W_{obs}, the mean of the time taken for each PS to be destroyed was calculated.

Predicting phase singularity population dynamics in future AF epochs

It was reasoned that if the paired Poisson process of PS formation and destruction is central to the self-perpetuation of atrial fibrillation, then birth-death models can be used to predict the future average number and duration of PS. To assess this, 5 minute epochs of basket human AF data were divided into two 2.5 minute halves epochs ($Epoch_{1st-half}$ and $Epoch_{2nd-half}$). The number and duration of active PS in $Epoch_{2nd-half}$ was predicted using λ_f and λ_d obtained from $Epoch_{1st-half}$. Predictions were compared to the observed experimental number and duration of active PS in the second half of the epoch, given by the mean of the running count of the number of PS present, and the mean of the time taken for each PS to be destroyed respectively.

8.2.6 Association of spontaneous termination to renewal rate constants of PS formation and destruction

It was also hypothesised that if the paired Poisson process of PS formation and destruction is central to the self-perpetuation of atrial fibrillation, λ_f and λ_d should alter for cases in which fibrillation will terminate. To test this hypothesis, λ_f and λ_d were estimated from cases exhibiting spontaneous AF termination and compared to rate constants calculated from epochs exhibiting sustained AF. Sustained AF was defined as any episode lasting more than 5 minutes. Epochs were analysed using only segments of recordings capturing fibrillation, and any recorded activity capturing termination of AF into sinus or other forms of organised arrhythmia was removed prior to analysis. Phase analysis was performed as described in section 8.2.4, and the rate of PS formation and destruction calculated from the probability distribution function (PDF) of PS formation times and lifetimes (equation 8.1 and 8.2).

8.2.7 Statistical Analysis

To determine the rate constants of PS destruction (λ_f) and PS formation (λ_d), exponential distributions were fitted using a maximum likelihood based approach (described in Supplement I). Data fitting was performed in Matlab, using the probability density function (PDF) of each epoch. The chi-squared (χ^2) goodness of fit test was used to assess the adequacy of fit, which uses the null hypothesis that the data evaluated comes from an exponential distribution ($P > 0.05$). Comparison of predicted vs. directly observed was performed using bivariate Pearon's correlation. Comparison of λ_f and λ_d values in which spontaneous termination occurred was performed using a paired t-test. Two-tailed p-values < 0.05 were considered significant.

8.3 Results

8.3.1 Markov birth-death model summarises PS population dynamics in basket mapped human persistent AF

Figure 9.11A shows the probability distribution function (PDF) of PS inter-formation times for a single basket-mapped human persistent AF case, corresponding to a PS formation rate of λ_f = 0.0243 PS/ms (2.43 %/ms), given by an exponential distribution (χ^2 goodness of fit P-value = 0.143, indicating a good fit). In Figure 9.11B, the PDF of PS lifetimes for the same example case is also given by an exponential distribution, with a PS destruction rate of λ_d = 0.0367 PS/ms (3.67 %/ms). These are consistent with a Poisson birth-death process (χ^2 P-value = 0.748). A worked example showing the calculation for the computed average number of PS (N) for this example case is shown in Figure 9.11C. In Figure 9.11D, the computed average number of PS is plotted against a running count of the observed number of PS throughout the recorded epoch, demonstrating that the Markov birth-death model summarises the observed PS number throughout the recording. Figure 9.11E plots the computed and observed average number of PS for all n = 43 human AF epochs. It can be seen that N and $N_{observed}$ were highly correlated (R^2 = 0.96; P < 0.001), with points lying along the line of identity.

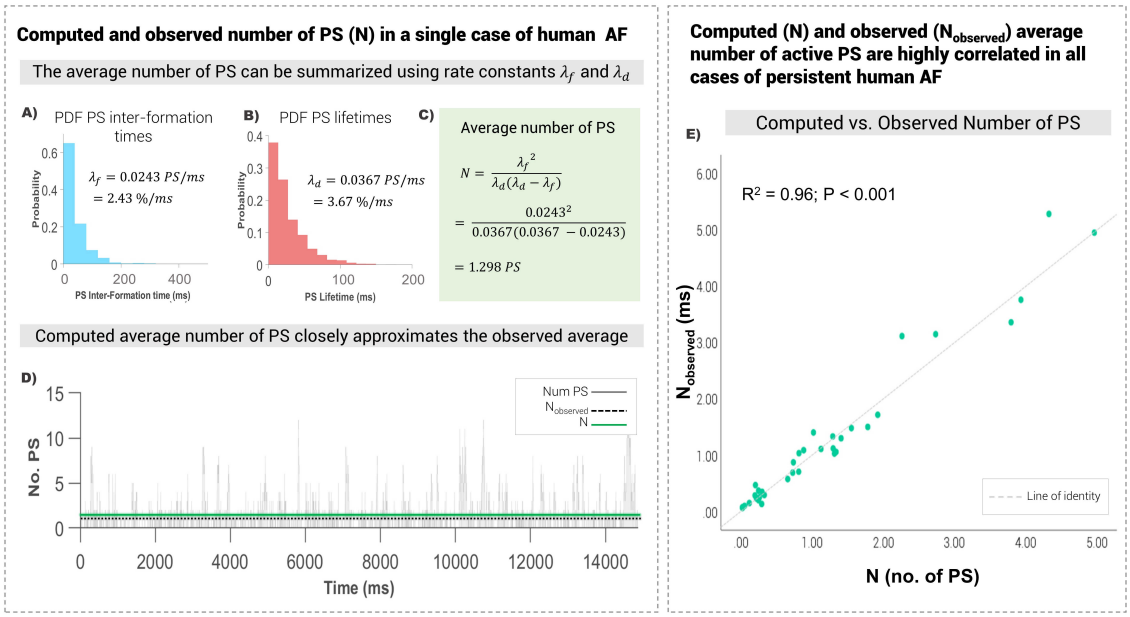

Figure 8.3: Computed average number of PS in basket catheter mapped human persistent AF

Similar results were seen for PS duration. The exponential distribution of PS inter-formation times and lifetimes is shown in Figure 9.12A. A worked example of the calculations for W and $W_{observed}$ for this same example case is shown in Figure 9.12B. The computed average duration of PS is plotted against the average time taken for each PS to be destroyed for this example epoch, which is shown in Figure 9.12C. W and $W_{observed}$ were highly correlated ($R^2 = 0.94$; $P < 0.001$) in all n = 43 epochs, with points lying along the line of identity.

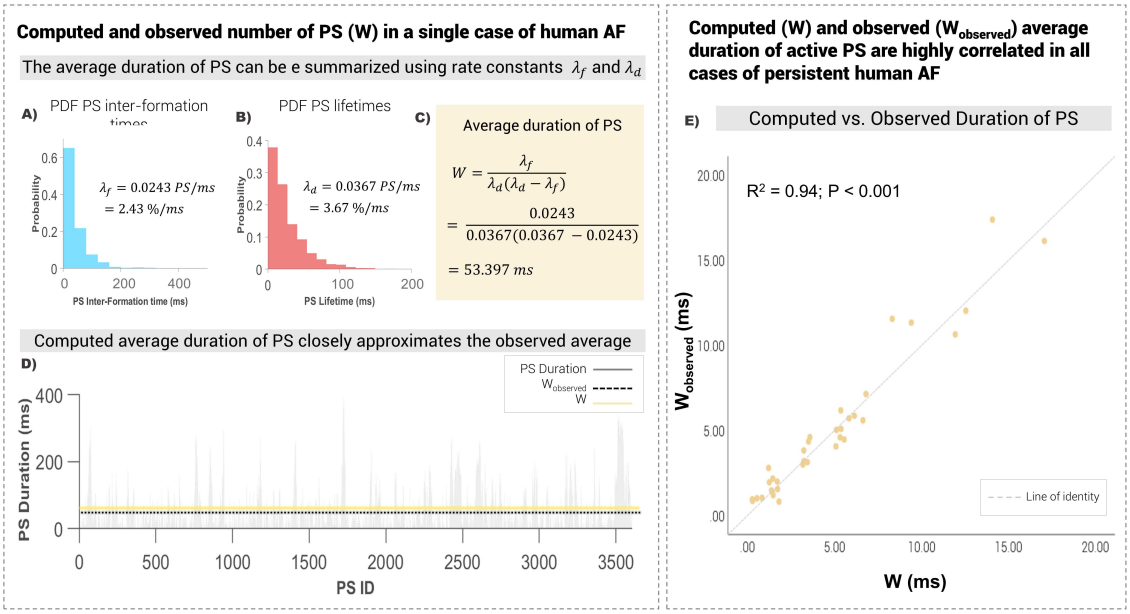

Figure 8.4: Computed average duration of PS in basket catheter mapped human persistent AF

8.3.2 Markov birth-death model summarises PS population dynamics in HD-grid mapped human persistent AF

Figure 9.13A shows the exponential probability distribution function (PDF) for PS inter-formation times from an example HD-grid mapped human persistent AF case, corresponding to a PS formation rate of $\lambda_f = 0.015$ PS/ms (0.15 %/ms). The PDF of PS lifetimes for the same example case yields a PS destruction rate of $\lambda_d = 0.0673$ PS/ms (6.73 %/ms) and is also given by an exponential distribution (Figure 9.13B). Figure 9.13C plots the computed and observed average number of active PS for all n = 23 HD grid epochs. N and N_{obs} demonstrated strong linear correlation ($R^2 = 0.97$; $P < 0.001$), with points lying along the line of identity.

Similarly, Figure 9.13D plots the computed and observed average duration of PS for all n = 23 HD-grid epochs. W and W_{obs} demonstrated strong linear correlation ($R^2 = 0.95$; $P < 0.001$), with points lying along the line of identity.

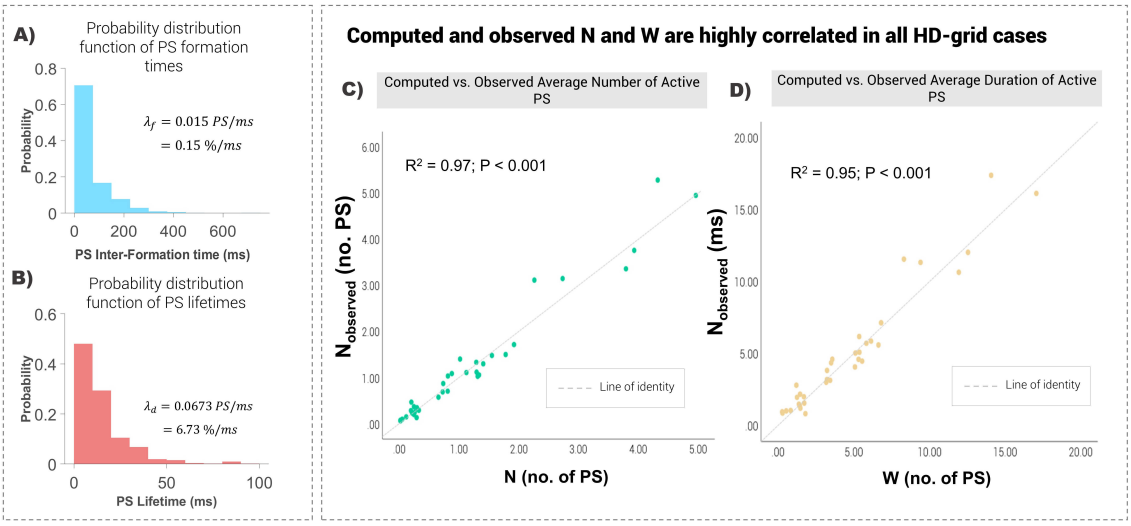

Figure 8.5: Computed average number and duration of PS in HD-grid mapped human persistent AF

8.3.3 Markov birth-death model predicts phase singularity population dynamics

PS population dynamics predictions were calculated in n = 43 human basket AF epochs. Figure 8.6A shows the predicted average number of PS, N, in $Epoch_{2nd-half}$ calculated using λ_f and λ_d obtained from $Epoch_{1st-half}$, plotted against the observed experimental average number ($N_{observed}$) of PS in $Epoch_{2nd-half}$. In all cases, N and $N_{observed}$ are highly correlated ($R^2 = 0.95$; $P < 0.001$), with points lying along the line of identity.

Figure 8.6B shows the predicted average duration of PS, W, in $Epoch_{2nd-half}$ calculated using λ_f and λ_d obtained from $Epoch_{1st-half}$, plotted against the observed experimental average duration ($W_{observed}$) of PS in $Epoch_{2nd-half}$. W and $W_{observed}$ are correlated ($R^2 = 0.82$; $P < 0.001$), with points lying along the line of identity.

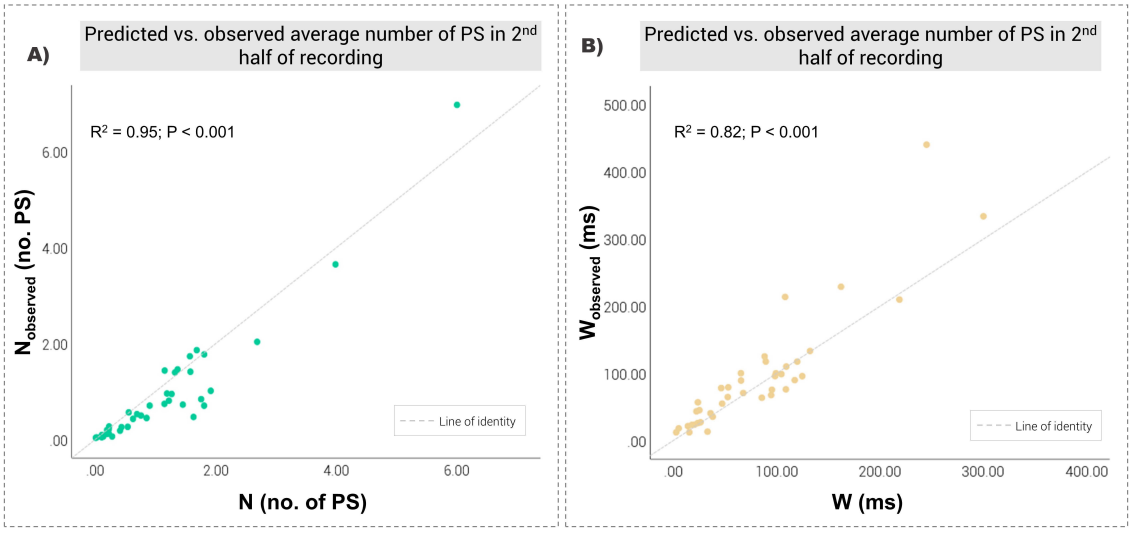

Figure 8.6: Predicting PS population dynamics in human persistent AF

8.3.4 Association of changes in λ_f and λ_d with spontaneous AF termination

Figure 8.7A shows phase maps for a segment of an epoch during of AF termination. Figure 8.7B illustrates a cumulative count of PS for the same segment of recording, and Figure 8.7C the corresponding unipolar electrograms illustrating termination of AF into sinus rhythm.

In all n = 20 epochs of spontaneous human AF termination, λ_f showed a statistically significant difference in comparison to λ_f calculated from n = 48 epochs of sustained human AF ($P < 0.001$) (Figure 8.7D). The median λ_f was 0.124 PS/ms (IQR 0.101, 0.137) for epochs showing spontaneous termination, and 0.041 (IQR 0.018, 0.036) in cases of sustained human AF.

A statistically significant difference was also seen in all epochs for λ_d ($P < 0.001$). For epochs showing spontaneous termination, median λ_d was 0.079 (IQR 0.071, 0.095). For cases of sustained human AF, median λ_d was 0.037 (IQR 0.036, 0.043) (Figure 8.7E).

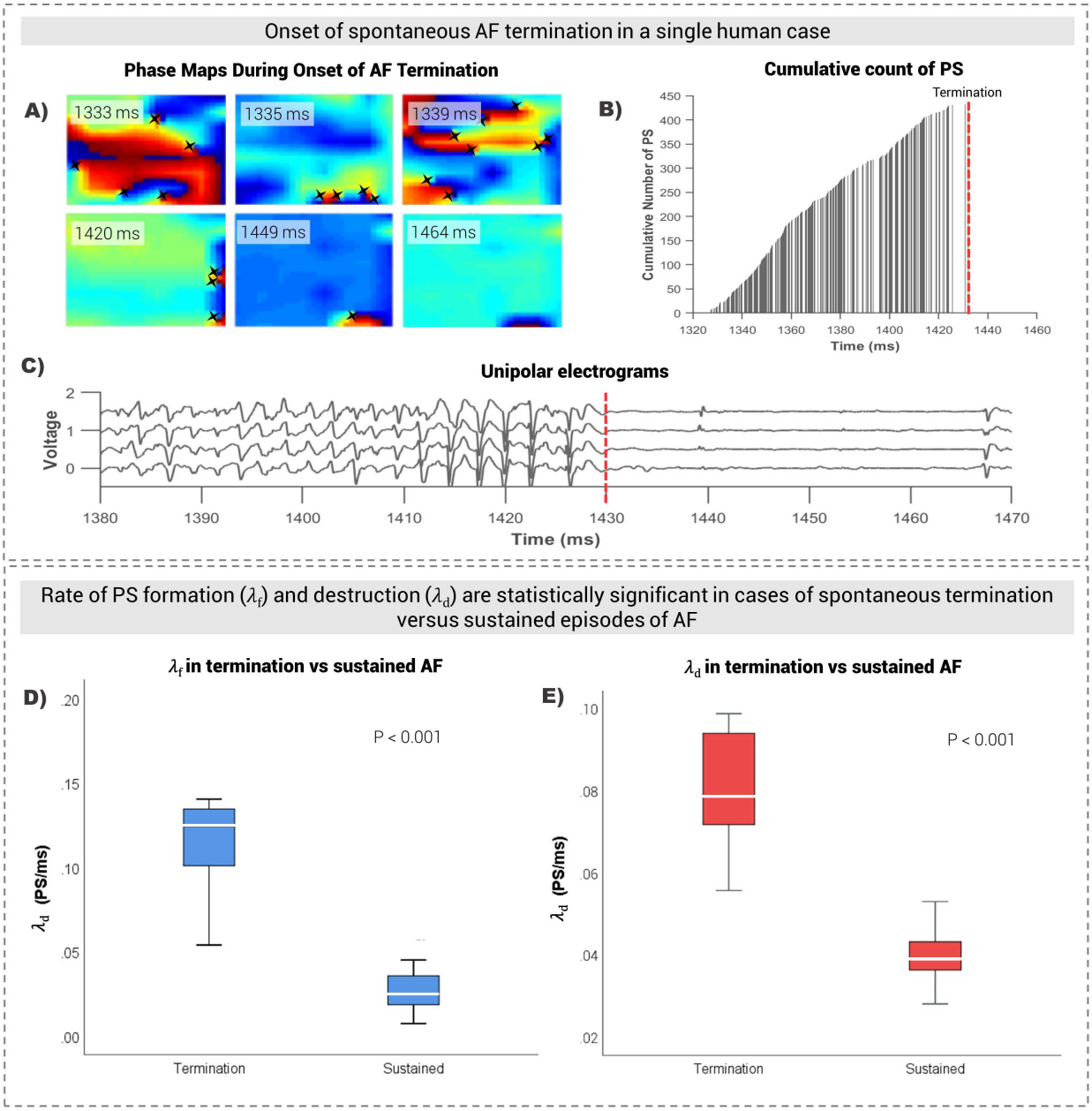

Figure 8.7: Association of changes in λ_f and λ_d with spontaneous AF termination

8.4 Discussion

Unstable reentrant circuits have been a consistent observation since the very earliest investigations of cardiac fibrillation. Through studying phase singularities, the pivot points of reentrant circuits, this study presents a number of important new observations regarding the formation and destruction of this rotational activity. The Markov birth-death process provides a natural and logical framework to understand the cycle of PS formation and destruction that has been a universal observation in cardiac fibrillation research. Birth-death processes arise in many natural systems, where stochastic renewal processes govern the transitions between states [178], and have previously been utilized to understand a wide array of biological processes including biology, population genetics, ecology and epidemiology [178]. In the context of cardiology specifically, Markov chains are widely used to study ion channel gating [210]. In this way, the Markov birth-death process also provides a theoretical framework that connects wave conduction during cardiac fibrillation to similar stochastic processes in other biological and physical systems in nature.

Although fibrillatory dynamics are not purely stochastic, the findings presented in this study demonstrate that the PS formation and destruction in AF can be modelled by an essentially stochastic, Markov birth-death process. This provides a compact way to summarise and explain the continuous regeneration of unstable reentrant circuits; a fundamental feature of the perpetuation of cardiac fibrillation that has been seen by nearly all investigators in the past 100 years of the field.

A standout finding of this study is that the Markov birth-death framework also allows forward prediction of phase singularity properties. This suggests that despite the random appearance of fibrillation, underlying wave propagation dynamics can be forward forecast. This predictive capability may be useful for better understanding the fibrillatory mechanism, and whether this has been modulated by therapeutic interventions.

In addition, the study provides new evidence to support that PS formation and destruction are associated with clinical arrhythmia behaviour, with the renewal rate constants λ_f and λ_d predicting spontaneous termination of AF. This relationship suggests the use of λ_f and λ_d as potential markers of termination, and points to potentially new avenues in research to understand the causal role of this rate change in AF termination. If alteration to λ_f and λ_d is the final common pathway to termination, then this would also open new avenues for potential treatments based on rate parameter modulation.

8.4.1 Theorized mechanisms of fibrillation – A historical context

The underlying electrophysiological mechanism responsible for AF remain incompletely understood, leading to important consequences for the development of optimal interventions. Several

theories of wave propagation during fibrillation have been put forward, including: (i) localized rapidly circulating rotors [155]; (ii) multiple wavelets [163]; (iii) rapidly firing foci [145]; and (iv) endocardial-to-epicardial dissociation of conduction [241]. However, a key limitation of these theories is that they provide primarily qualitative descriptions of electrical wave propagation, making it difficult to validate the contributions of any of these mechanisms to arrhythmia perpetuation.

In contrast, the Markov birth-death framework presented in this study provides a quantitative, compact approach to summarise and explain the continuous regeneration of unstable reentrant circuits. The results also indicate that paradoxically during periods of sustained AF, the system dynamics are conserved and can be summarised and forward predicted, despite the superficially chaotic and aperiodic turbulence of wave propagation.

8.4.2 Significance to the understanding of the fibrillatory mechanism

The current study reconciles a number of important theories of AF. For several decades, the debate regarding fibrillatory mechanisms has been principally framed as a contest between stochastic multiple wavelet propagation, versus a more hierarchical mechanism in which rotors have more agency as arrhythmia drivers.

The accurate characterization of PS formation and destruction via Markov birth-death processes reconciles these two competing frameworks. Due to topological considerations, phase singularities are an important component of both theories of fibrillation. PS have long been recognized as the crucial core of re-entrant spiral waves, but less well understood is the fact that PS must topologically occur at what Winfree called the "dangling free ends" of wavelets in the atrium. The current is consistent with the notion of stochastic generation that the multiple wavelets proposed to be generated by Moe and Abildskov, as the generation of new PS inevitably for the topological reasons outlined earlier leads to the generation of new wavelets.

However, the study provides several important new concepts not outlined by Moe's original conceptualization. The Markov birth-death model explains wavelet regeneration as the natural consequence of repetitive PS regeneration. Central to the model is the concept of phase singularities existing on a topological continuum between those PS that sustain as the cores of spiral waves, and those attached to wavelets. Importantly, the Markov renewal model outlined here provides a quantitative framework to understand the maintenance of AF via regeneration of unstable reentrant circuits whose number and duration are determined by the dynamic interaction of Poisson processes of PS formation and destruction. None of these ideas were recognized in Moe's model.

On the other hand, the study provides an important reconciling role for the role of spiral waves and phase singularities, which have played a critical role in contemporary understanding of fibrillation since the time of Winfree. The proposed mechanism places stochastic regeneration of PS

via Poisson renewal processes as the most fundamental component of the fibrillatory mechanism. The proposed mechanism explains the existence of spiral waves as the consequence of locally sustained phase singularities, but also provides an explanation of why sustained spiral waves are both transient and rare, a point that has consistently been observed, but has never fully been explained.

Additionally, the Markov birth-death model provides a quantitative framework to characterize and predict PS number and duration, which will be the foundation for new investigations into mechanism, and potentially the basis for improved clinical understanding of AF.

Finally, the association of rate constant changes with the spontaneous self-termination of AF episodes is of significance, as it implies that the rate of PS regeneration is related to arrhythmia behaviour. This suggest a potential paradigm shift from defining atrial fibrillation as a completely chaotic arrhythmia, to one that is perpetuated by the stable cycle of formation and destruction. Further, the results open the possibility for a number of clinical applications. It is potentially possible that rate constants of PS formation and destruction evolve over time with the evolution of AF from paroxysmal to persistent AF, and could be used as a clinical marker to detect the likelihood of progression.

8.4.3 Clinical implications

One of the most significant implications of this study is that for the first time, the Markov birth-death framework provides a quantitative framework to measure the regeneration rate of phase singularities during fibrillation, which may be useful in measuring the effect of therapeutic interventions. This may be of particular importance in the context of catheter ablation. For the past decade, the field has used a variety of approaches including complex fractionated electrograms [166], dominant frequency [225], substrate-directed [103], and rotor ablation in seeking to terminate AF via catheter ablation [169], with a particular focus on searching for particular local drivers or key regions responsible for sustaining fibrillation. Although a number of these approaches have reported acute effectiveness in achieving AF termination, to date none of these approaches have not demonstrated consistent long-term clinical benefit. With this in mind a potential use case is to use the Markov birth-death framework to develop more effective ablation strategies, by using λ_f and λ_d as a quantitative measure of the effect of ablation on the underlying arrhythmia dynamics.

Furthermore, although a number of the aforementioned approaches have reported acute effectiveness in achieving termination, to date none of these approaches have demonstrated consistent long-term clinical benefit, suggesting that termination is not a reliable marker of outcome. Recent findings suggesting that termination in many cases occurs at a distance from mapped drivers is consistent with the notion that termination may in fact be independent of any local effect on particular PS, but instead in changes being made to the regeneration rate of these PS. Stochas-

tic regeneration of PS would suggest that potentially such driver-based approaches might not be achievable, and that future research efforts could be focused on substrate modification that would seek to modulate the rates of PS formation and destruction with the goal of inducing spontaneous termination.

Other potentially useful applications include the use of λ_f and λ_d to assist the stratification of patients suitable for ablation, and those in whom ablation is unlikely to improve clinical outcomes. In the context of monitoring, λ_f and λ_d could also potentially be useful for monitoring clinical AF progression, and intraprocedural monitoring of the effectiveness of catheter ablation strategies. The predictive capability presented by the Markov birth-death framework may also allow effective interventions to be forecast, as well as the future progression of the arrhythmia to be projected ahead of time. Ongoing investigations are underway into these possibilities.

8.5 Conclusion

This study demonstrates that phase singularity dynamics during human persistent atrial fibrillation can be modelled using a Markov birth-death framework, providing a compact theoretical approach to summarise, explain and predict the repetitive regeneration of unstable reentrant circuits that is a defining characteristic of cardiac fibrillation. Additionally, findings suggest that the cycle of continuous PS birth and death plays a role in the perpetuation of atrial fibrillation. These findings may have potentially significant implications for future research and therapeutic strategies.

To summarise, this study adds important insights to the current literature by:

- Establishing the Markov birth-death framework as a compact theoretical approach to summarise and explain phase singularity regeneration
- Showing that despite the superficial randomness of AF, the Markov birth-death allows phase singularity dynamics to be predicted in future epochs of AF
- Demonstrating that PS formation and destruction as paired Poisson processes influence the self-regeneration of fibrillation, supported by the association of changes in rate constant with the spontaneous termination of AF. This suggests that PS renewal rates may be related to arrhythmia behaviour, and may provide new novel avenues for monitoring and treatment

Chapter 9

Phase singularity formation and destruction processes in cardiac fibrillation are scale-dependent

As discussed previously throughout this dissertation, one motif that has been an essentially universal observation throughout the history of AF and VF research has been the presence of unstable re-entrant circuits [172]. Unstable reentry has not only been noted by proponents of the rotor theory [155], but has also been consistently observed by supporters of focal [145], multiple wavelet [163] and endocardial-to-epicardial dissociation [241]. The consistent and essentially universal observation of unstable re-entry in AF and VF dynamics in the past century would suggest this is a fundamental property of mammalian cardiac fibrillation, with a deep connection to the underlying biology of the arrhythmia.

A defining feature of these re-entrant circuits are phase singularities (PS), which occur at their pivoting region. In the previous chapter (chapter 8), a Markov birth-death framework was introduced, which allowed the population dynamics of these phase singularities to be modelled, summarised and predicted. Using this framework, it was also shown that the continual cycle of phase singularity births and deaths plays a role in the perpetuation of fibrillation. These insights point to potential mechanistic and clinical applications, whereby the rate constants λ_f and λ_d can be used as markers of the underlying fibrillatory activity, with use case scenarios including monitoring the likelihood of termination, monitoring arrhythmia progression, or development of more effective ablation strategies. Furthermore, PS population dynamics as predicted by the Markov birth-death model may help prove if potential therapeutic interventions have had any effect on underlying fibrillatory dynamics.

However, before these applications can be realised, it is important to understand how to most

optimally model phase singularity dynamics given that there are several types of Markov birth-death models. In chapter 8, the $M/M/1$ model was used given that it is the simplest birth-death model, however, a key unanswered question is whether this is universally the optimal model to apply. Another knowledge gap relates to understanding the baseline rates of PS formation and destruction, as this has direct consequences on how these processes are interpreted.

Along this line of thought, we hypothesised that PS formation and destruction processes would be scale-dependent, in that both the measured rates of PS renewal and the Markov birth-death model would be governed by the size of the mapped field. The reason for this is that the size of the mapped area should influence the number of PS formation and destruction events captured, which would in turn effect the calculated rate of PS formation (λ_f) and destruction (λ_d), as well as the Markov birth-death model that can be used to characterise the system.

Identifying this scale dependence would present practical value, as it extends the findings in chapter 8 to allow fibrillatory wave dynamics to be most accurately summarised, understood and predicted using the optimal Markov birth-death framework. Second, demonstrating that PS population dynamics can be modelled by Markov birth-death processes determined by the field of view would provide a bridge between various mapping modalities, by potentially presenting evidence to suggest that less invasive local mapping techniques with a small field of view are essentially interchangeable with those possessing a large field of view for the context of measuring underlying wave dynamics.

To test this hypothesis of scale dependence, we investigated PS renewal rates and different types of Markov birth-death models in: i) computer simulated fibrillation, ii) epicardial sock recordings of early human VF, iii) basket catheter recordings of human persistent AF, and iv) HD-grid recordings of human persistent AF.

9.1 Methods

9.1.1 Data acquisition

Human study design

The human AF study is as previously described. The study was a multi-center observational design analyzing electrograms acquired prior to ablation. The inclusion criterion was persistent AF undergoing clinically indicated ablation. Patient participation was by informed consent, with recruitment from two centers (Flinders University, Australia), and Hamburg University (Germany). Details of this dataset are provided in Supplement F.

The Human VF study is as described by Nash et al. [170] and Bradley et al. [36]. The

study recruited ten patients aged 53 to 87 years undergoing routine cardiac surgery. Six of the ten patients (all men) underwent graft procedures for coronary artery disease, while the remaining four patients underwent aortic valve replacement. Individual patient details are given in Table K.1, Supplement K.

Basket atheter recordings of human persistent AF

Basket catheter recordings (n = 43 epochs) were performed as previously described in chapter 6. 64-electrode basket catheters (Constellation, Boston Scientific, MA, 48mm (4mm spacing), 60mm (5mm spacing)) were utilized, based on computed tomographic scan. Unipolar electrogram and surface electrocardiogram recordings (1-500 Hz, 2000Hz sampling frequency) were obtained in spontaneous or induced AF lasting at least 5 minutes in the left and right atria. Catheter stability was verified fluoroscopically, and in Velocity (Abbott, IL, USA).

HD-Grid catheter recordings of human persistent atrial fibrillation

In a subset of patients, simultaneous basket catheter and grid catheter (AdvisorTM-HD grid, Abbott, IL) recordings were obtained. The HD-grid catheter is a 3-3-3 mm catheter with 16 electrodes. During these recordings, the HD grid catheter was placed alternately on the anterior left atrial surface, and then on the posterior surface, whilst leaving the basket catheter in situ.

Epicardial sock recordings of human ventricular fibrillation

Epicardial sock recordings were performed as described by Nash et al. and Bradley et al. [36,170], using an epicardial sock with 256 electrodes (with interelectrode spacing of 10 mm) fitted over the left and right ventricles. Unipolar epicardial electrograms were sampled at 1 Hz (UnEmap system, Uniservices Ltd, New Zealand) with the reference channel connected to chest retractors. VF was induced using 50 Hz burst pacing, during which continuous recordings were made during the first 20-40 seconds of VF.

To obtain 3D locations of the epicardial electrodes, the epicardial sock was placed over a phantom heart model prior to the commencement of the experiments. 3D locations of the epicardial electrodes were digitized.

Computer simulated fibrillation

To provide further insights about the underlying scale depence, PS formation and destruction was modelled using a Markov birth-death process in computer simulated fibrillation. Specifically, computer simulations were carried out on two-dimensional, isotropic, square grids based on the

Tusscher-Panfilov model Ten Tusscher, 2006 90 The square grid used 80x80 diffusively coupled simulation nodes with a diffusion coefficient set to 0.02, which governs how the action potential is transmitted between coupled cells. If the diffusion coefficient is small, then propagation is slow and vice-versa. The system was integrated using a forward Euler scheme with no-flux boundary conditions, which causes an action potential propagating towards the edge of the 2D simulation to annihilate. This boundary condition is often used in simulations as it is thought to provide a realistic representation of a sheet of tissue being sliced out of the myocardium Puwal2009. To achieve annihilation, the no-flux boundary condition causes the incoming wavefront to encounter a mirror image wave upon reaching a boundary.

Using the simulated square grid and parameterization as specified, unipolar electrograms (EGM) were generated using:

$$u_{i,j}(t) = c \sum_{k,l=0}^{k,l=N} \frac{\vec{r}_{k,l} \nabla v_{k,l}(t)}{r_{k,l}^3} \tag{9.1}$$

where $u_{i,j}$ is the unipolar voltage at node (i, j), $v_{k,l}$ the transmembrane voltage at node (k, l) and $\vec{r}_{k,l}$ the distance between those nodes. A scaling coefficient is represented by c, which is assumed to equal 1 for simplicity. Further details about the computational modelling used is provided in Supplement B.

9.1.2 Cleaning, filtering and signal processing

Pre-processing of unipolar AF signals

Signal processing was performed as previously described in chapter 6. Unipolar electrograms, surface ECG, and 3D data were exported from NavX. QRS subtraction was performed [223]. Signals were filtered using a 4th order Butterworth fitted with a 1 to 30 Hz band pass filter applied in forward and reverse mode. A Hanning window was applied for edge tapering, and the Welch power spectral method applied. The Fourier dominant frequency was used as the wavelet period for sinusoidal wavelet recomposition [135].

Pre-processing of unipolar VF signals

To allow for phase analysis, electrode coordinates were projected on a 2D plane (Figure 9.1). This transformation first required a 3D triangular mesh representation of the sock, which was constructed using Delaunay triangulation to connect neighboring electrodes. The three-dimensional co-ordinates of mesh vertices were mapped onto a planar surface using the methods as described by Roney et al [205]. Specifically, geodesic distances between all n vertices on the mesh were calculated

using a fast marching algorithm, and a multi-dimensional scaling technique applied to project the three-dimensional vertices onto a 2D plane in a way that best preserved the geodesic distances. This was achieved using spectral decomposition and Sammon's nonlinear mapping criterion. Using this 2D projection, electrode potentials were linearly interpolated from the electrodes onto a fine regular grid (100x100 grid points, Figure 9.1).

As a number of electrodes possessed poor signal-to-noise ratios, these electrograms were removed from the analyses prior to 2D projection of the mesh using a method based on the Fast Fourier Transform. Specifically, as the main source of noise was a combination of baseline movement and electrical mains interference, only signals with a dominant frequency within the 1.5 to 45 Hz band were selected for analyses [170]. A number of EGMs near the stimulus electrode also demonstrated an exponential artifact, as well as respiration artifacts. To remove this, a mode was fitted with a constant offset of the signal mean, an exponential term, as well as a sinusoidal term. This fitted signal was subtracted from the raw signal to improve signal to noise ratio.

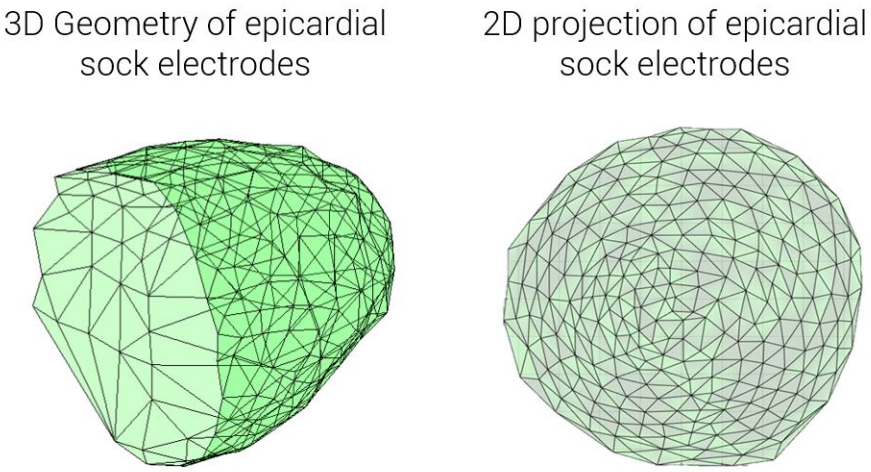

Figure 9.1: 3D and 2D projections of epicardial sock electrodes (pictured here on 80 x 80 grid)

9.1.3 Phase mapping, phase singularity detection and PS look-up table

In human AF data, the instantaneous phase for each electrogram was constructed by applying sinusoidal recomposition and the Hilbert transform as described in chapters 6 and 7. PS detection was performed using the double-ring extended topological charge method [136].

In human VF data, phase singularities were also identified by a method based on topological charge but using a convolution kernel method [36, 38]. Specifically, this method approximates the gradient of phase from the discretised phase map using a finite difference operation in the x and y

directions given by:

$$k_x[m,n] = \nabla\phi_x[m,n] = \phi[m+1,n] - \phi[m,n] \tag{9.2a}$$

$$k_y[m,n] = \nabla\phi_y[m,n] = \phi[m,n+1] - \phi[m,n] \tag{9.2b}$$

where ϕ is phase, and $[m,n]$ the pixel coordinates. The line integral at $[m,n]$ can therefore be approximated using the convolution equation:

$$(\nabla X\vec{k}) \cdot \hat{z} \propto \nabla_x \otimes k_y + \nabla_y \otimes k_x \tag{9.3}$$

where $\otimes$ is the convolution operator, and the convolution kernels ∇_x and ∇_y given by 9.4 and 9.5 respectively:

$$\nabla_x = \begin{vmatrix} -1/2 & 0 & +1/2 \\ -1 & 0 & +1 \\ -1/2 & -1 & -1/2 \end{vmatrix} \tag{9.4}$$

$$\nabla_y = \begin{vmatrix} +1/2 & +1 & +1/2 \\ 0 & 0 & 0 \\ -1/2 & -1 & -1/2 \end{vmatrix} \tag{9.5}$$

To avoid detection of spurious PS, a wavefront detection method was also implemented as previously described by Bradley et al. [36], such that any PS not attached to a wavefront is discarded (9.2). Wavefronts were identfied as lines of zero phase (green areas in Figure 9.2), and wavefront lengths calculated by the summation of the distance between pixels located along the wavefront [36].

To determine PS lifetime and PS formation times, a look-up table indexing onset time, offset time and electrode location for each new PS detection was used as previously described (chapter 6). A new PS detection event was defined as the detection of a PS at an electrode and its surrounding 1-electrode neighborhood for at least 20 consecutive frames (10 ms). The look-up table enabled computation of histograms for: (i) PS lifetimes and (ii) inter-formation event times.

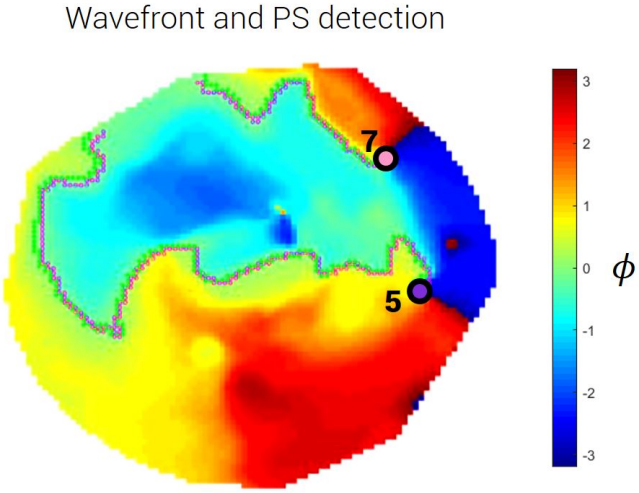

Figure 9.2: Wavefront (shown in magenta line) and PS detection (coded by colour and number to represent PS ID)

9.1.4 Investigating the effect of mapping field of view on PS formation and destruction

It was hypothesized that PS population dynamics in cardiac fibrillation could be modelled by Markov birth-death processes determined by the field of view of mapping, as the size of the mapped area would influence the number of PS formation and destruction events captured. Therefore, it was reasoned that this would in turn effect the calculated rate of PS formation (λ_f) and destruction (λ_d), as well as the Markov BDP that can be used to model the system. Mathematically speaking, the shift from a single-server ($M/M/1$) birth-death model to a multi-server model ($/M/M/\infty$) is hypothesised to occur due to a larger number of servers required to stabilize the system when the ratio of PS formation to destruction rate, ρ, becomes > 1 (Figure 9.3) [126] (Figure 9.3).

To test this hypothesis of scale dependence, PS renewal rates and Markov birth-death models were investigated in: i) wide-area computer simulations; ii) wide-area recordings of early human ventricular fibrillation; iii) constrained local basket catheter recordings of human persistent AF; and iv) constrained local HD-grid recordings of human persistent AF.

Although AF basket recordings should theoretically capture the whole chamber, practically they are only able to sample a limited portion of the chamber, hence are regarded here as constrained recordings.

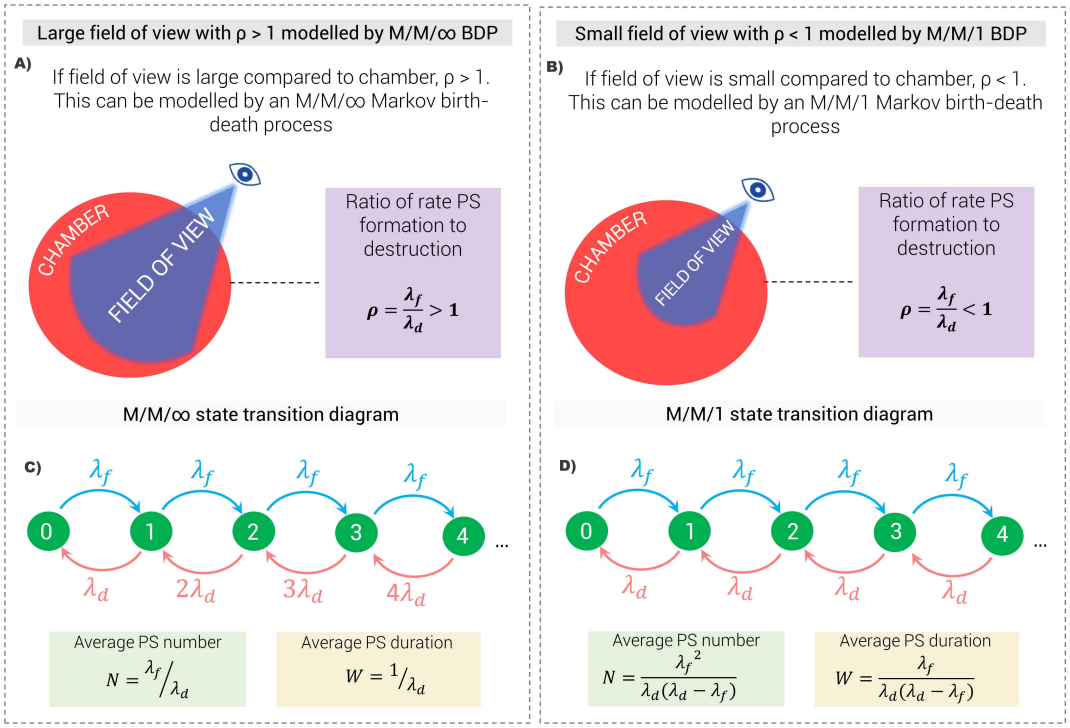

Figure 9.3: Conceptualization of the Markov birth-death process for varying fields of view

Wide-area global recordings with large field of view

It was reasoned that global recordings with a large field of view would capture a greater number of PS formation and destruction events. It therefore hypothesised that:

- the larger number of events captured should cause the timings between PS formation events to decrease, resulting in a higher rate of PS generation (λ_f)
- a larger mapped area is likely to capture rare long-lasting PS, hence resulting in a slight decrease in the rate of PS destruction (λ_d)
- global recordings with a larger number of PS events could be modelled using an $M/M/\infty$ birth-death process

An $M/M/\infty$ BDP is a Markov birth-death process used to describe a stochastic process in which arrivals and departures in a system occur at infinite possible locations (e.g. at infinite servers). We reasoned this would approximate electrical wave dynamics in global recordings, whereby PS formation and destruction events can be observed at infinite possible locations within the chamber. For an $M/M/\infty$ BDP, the average number of phase singularities present in the system can be summarized and predicted using:

$$N = \frac{\lambda_f}{\lambda_d} \tag{9.6}$$

where N gives the number of PS, λ_f the rate of PS formation and λ_d the rate of PS destruction. Another descriptor of the PS population dynamics is the average duration (or wait in the system) of phase singularities, which can be summarized and predicted using:

$$W = \frac{1}{\lambda_d} \tag{9.7}$$

where W gives the duration of PS, and λ_d the rate of PS destruction.

To test the hypothesis of whether globally mapped fibrillation could be accurately modelled as an $M/M/\infty$ BDP, the observed experimental number ($N_{observed}$) and duration ($W_{observed}$) from global epicardial sock recordings of human ventricular fibrillation and computer simulated fibrillation was compared to N and W computed from the $M/M/\infty$ BDP model using equations 9.6 and 9.7. $N_{observed}$ was calculated by taking a running count of the PS at each time-step, and finding the mean. To calculate $W_{observed}$, the mean of the time taken for each PS to be destroyed was calculated.

Constrained local recordings with small field of view

As the whole chamber is not able to be mapped in most clinical or mechanistic arrhythmia recordings, we reasoned that it was clinically and practically useful to investigate local recordings with a constrained field of view. Specifically, we postulated that a smaller, more localized mapping field would result in a decreased number of PS events being captured by the mapped field, and therefore hypothesized that:

- the smaller number of events captured should cause the timings between PS formation events to increase, resulting in a slower rate of PS generation (λ_f)
- a smaller mapped area is less likely to capture rare long-lasting PS, hence resulting in an increased rate of PS destruction (λ_d)
- in the constrained recording case, where the mapped area is small compared to the chamber of interest, that the destruction process could be effectively modelled as a single source of annihilating waves, suggesting an $M/M/1$ birth-death process might be optimally suited to this scenario.

For an $M/M/1$ BDP, the average number of phase singularities can be summarized and predicted using (as previously described in chapter 8):

$$N = \frac{\lambda_f^2}{\lambda_d(\lambda_f - \lambda_d)} \tag{9.8}$$

where λ_f gives the rate of PS formation, and λ_d the rate of PS destruction. The average PS duration can be summarised by:

$$W = \frac{\lambda_f}{\lambda_d(\lambda_f - \lambda_d)} \tag{9.9}$$

The hypothesis that locally mapped fibrillation could be modelled as an $M/M/1$ BDP was studied by comparing the observed experimental number ($N_{observed}$) and duration ($W_{observed}$) from local basket catheter and HD-grid recordings of human persistent atrial fibrillation to N and W computed from the $M/M/1$ BDP model using equations 9.8 and 9.9 . $N_{observed}$ and $W_{observed}$ were calculated as described for global wide-area recordings.

9.1.5 Statistical analysis

To determine the rate constants of PS destruction (λ_f) and PS formation (λ_d), exponential distributions were fitted using a maximum likelihood based approach (described in Supplement I). Data fitting was performed in Matlab, using the probability density function (PDF) of each epoch. The chi-squared (χ^2) goodness of fit test was used to assess the adequacy of fit, which uses the null hypothesis that the data evaluated comes from an exponential distribution ($P > 0.05$). Comparison of predicted vs. directly observed was performed using bivariate Pearon's correlation. Comparison of λ_f and λ_d values in which spontaneous termination occurred was performed using a paired t-test. Two-tailed p-values < 0.05 were considered significant.

9.2 Results

9.2.1 Computer simulated fibrillation

Scale dependence of λ_f and λ_d in computer simulated fibrillation

Figure 9.4 Ashows phase maps for various grid-sizes in computer simulated fibrillation to represent recordings with variously sized fields of view. For each grid size, the corresponding exponential probability distribution function (PDF) of PS inter-formation times and lifetimes is shown, demonstrating consistency of PS formation and destruction to a Poisson renewal process at each scale.

As the size of the mapped field is increased in computer simulations (which reflects the number of pixels in the simulated grid), the number of PS formation and destruction events captured also increases as shown in Figure 9.4B. The larger number of PS events captured by larger fields of view cause the timings between observed PS formation events to increase (Figure 9.4C). For smaller fields of view, the longer inter-formation event times result in a slower rate of new PS formations being captured, causing an aggregate decrease in the long-term average rate of PS formation λ_f in smaller grids (Figure 9.4D and 9.4E).

For PS destruction events, although the number of events similarly increases with grid size (Figure 9.4B), PS lifetimes slightly decrease for smaller fields of view (Figure 9.4C). Consequently, the long-term average rate of PS destruction is more constant across varying fields of view (mean λ_d = 24.2 %/ms (95%CI, 22.8, 25.8)) (Figure 9.4D), but still demonstrates an aggregate increase for smaller grid sizes (Figure 9.4E).

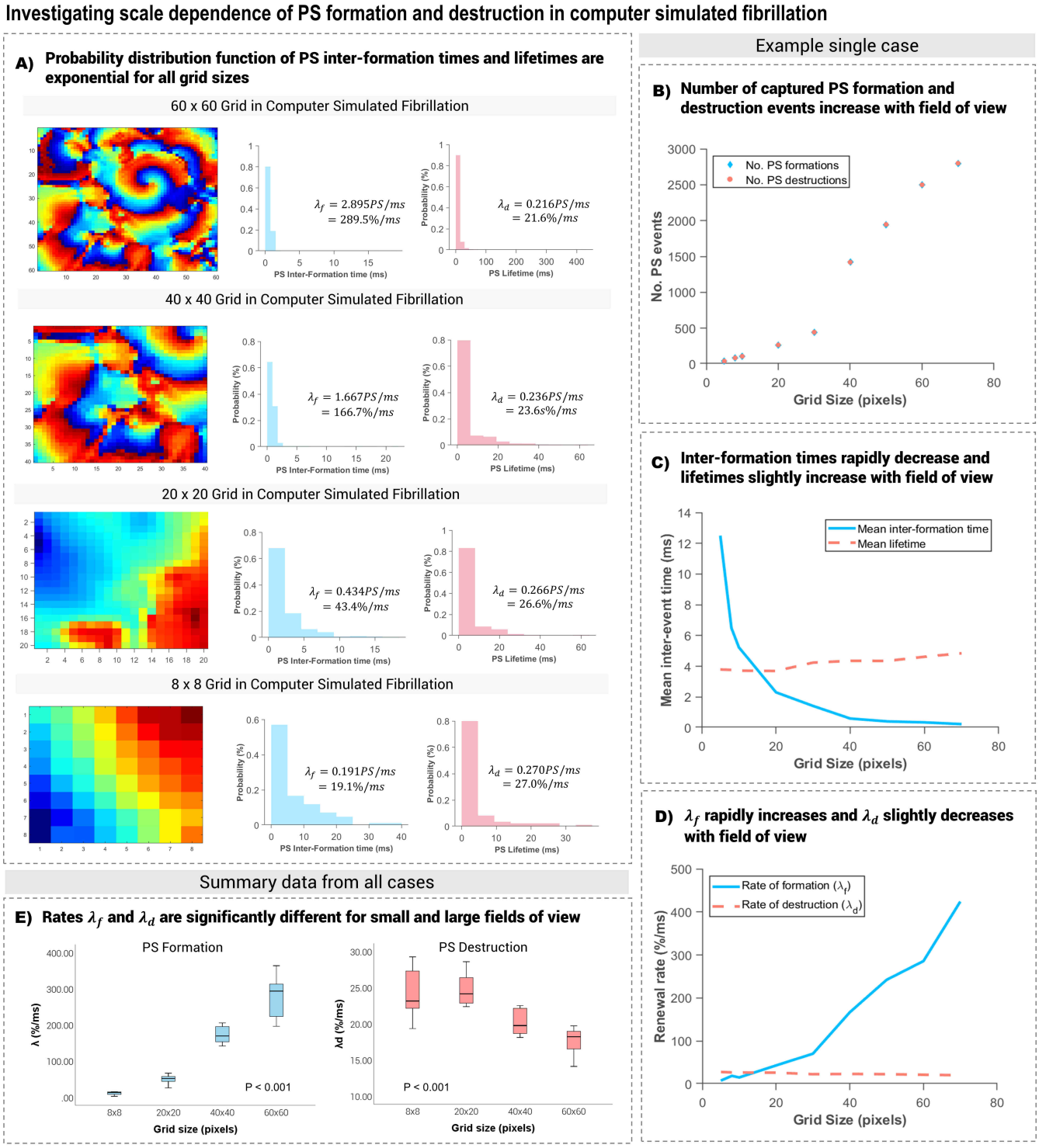

Figure 9.4: Scale dependence of PS renewal rates in computer simulated fibrillation

PDFs for all grid sizes are exponential (A). As the grid size increases, the number of PS events captured increases (B). Timings between PS formations decrease, but timings between PS destructions slightly increase (C). This cases λ_f to increase rapidly, and λ_d to decrease slightly (D).

Scale dependence of Markov birth-death process

Figure 9.5A demonstrates that as the field-of-view is increased, the single-server $M/M/1$ model is no longer able to accurately predict the number and duration of PS present. However, for larger mapped fields the $M/M/\infty$ model much better estimates the system parameters. As shown in Figure 9.5B, this shift is reflected by the change in ρ, which gives the ratio of λ_f on λ_d, which rapidly becomes > 1 as the field of view increases.

In Figure 9.6A and 9.6B, bivariate correlation plots are shown between the computed and observed average number and duration of PS for a 100x100 pixel grid. For this large field of view, the multi-server $M/M/\infty$ model summarizes the average number ($R^2 = 0.99$; $P < 0.001$) of PS present, with points lying along the line of identity. In this case, the utilization rate ρ, which gives the ratio of λ_f on λ_d, is > 1. For completeness, we also present the average PS duration computed from the $M/M/\infty$ equation (Figure 9.6B). It can be noted, however, that for a large field of view the computed average duration of PS by definition converges to the mean observed PS lifetime in the system given by $\frac{1}{\lambda_d}$, hence producing a bivariate correlation of $R^2 = 1.00$ ($P < 0.001$).

Similarly, Figures 9.6C and 9.6D show bivariate correlation plots between the computed and observed average PS number and duration in a small 8x8 pixel grid. As the field-of-view is decreased, ρ becomes < 1 due to the much slower measured λ_f. In this instance, the simple single-server $M/M/$ model can be used to summarize the average number of PS ($R^2 = 0.99$; $P < 0.001$) (Figure 9.6C). The computed average duration of PS is also linearly correlated with the observed average PS duration ($R^2 = 0.87$; $P < 0.001$), with points lying on the line of identity.

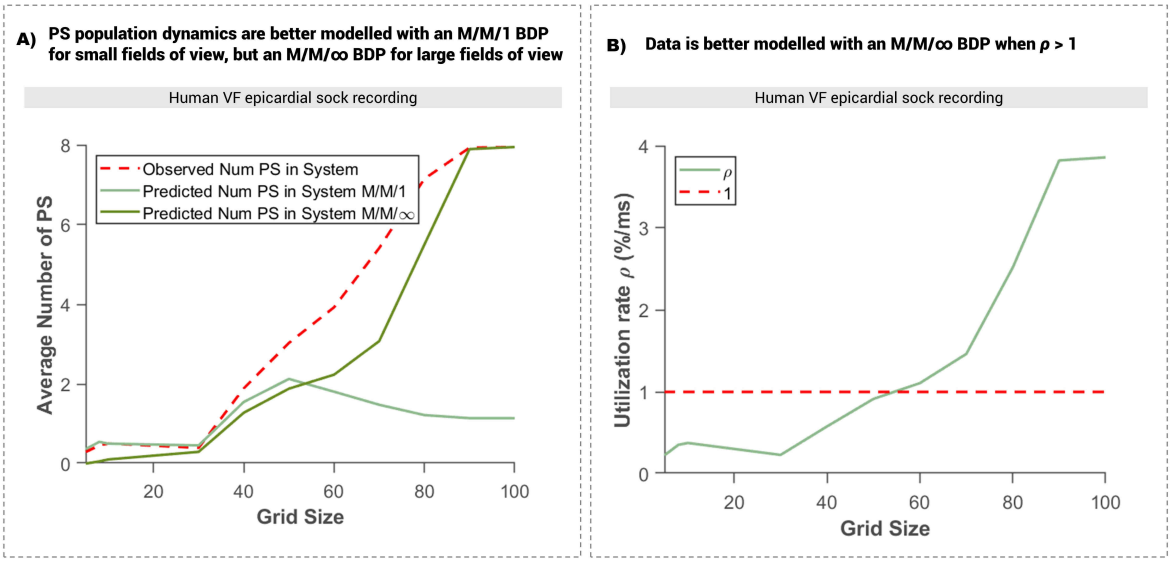

Figure 9.5: Modelling the phase singularity birth-death process using the $M/M/1$ vs. $M/M/\infty$ model in various grid sizes

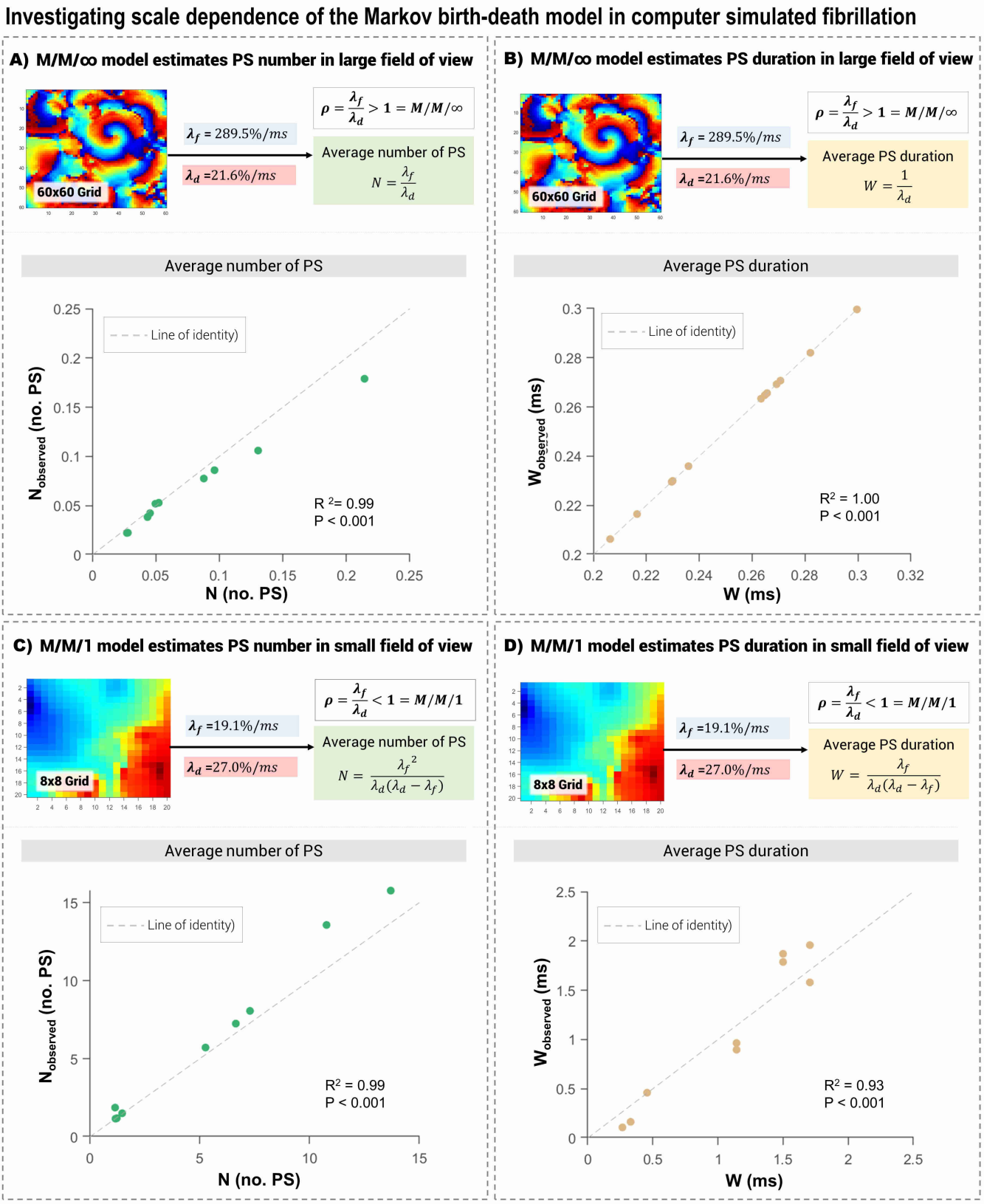

Figure 9.6: Scale dependence of the Markov birth-death model

In large grids with a big field of view, the $M/M\infty$ model summarises PS dynamics. Contrastingly, for small grids with a smaller field of vire the $M/M/1$ model can summarise PS dynamics

9.2.2 Human ventricular fibrillation

Scale dependence of λ_f and λ_d in early human VF

Figure 9.7A shows phase maps for various grid-sizes in epicardial sock recordings of human ventricular fibrillation to represent recordings with variously sized fields of view. For each grid size, the corresponding exponential probability distribution function (PDF) of PS inter-formation times and lifetimes is shown, demonstrating consistency of PS formation and destruction to a Poisson renewal process at each scale. Similarly to computer simulated data, the number of PS formation and destruction events captured increases with the size of the field of view (Figure 9.7B). The greater number of PS events captured by larger fields of view causes the timings between observed PS formation events to decrease (Figure 9.7C). In small grids, longer inter-formation event times result in a faster rate of PS formation λ_f (Figure 9.7D and 9.7E).

PS destruction events similarly increases with grid size (Figure 9.7B), causing PS lifetimes to slightly increase with the field of view (Figure 9.7C). Consequently, the long-term average rate of PS destruction is more constant across varying fields of view (mean λ_d = 3.02 %/ms (95%CI, 2.33, 3.71)) (Figure 9.7D), however, still demonstrates an aggregate increase for small fields of view (Figure 9.7E).

$M/M/\infty$ BDP model summarizes PS population dynamics in global recordings of early human VF

Given that epicardial sock recordings provide a global, large field of view with $\rho > 1$, we reasoned that PS population dynamics could be summarized with an $M/M/infty$ birth-death model. Figure 9.8A shows the probability distribution function (PDF) of PS inter-formation times for a single human VF case, corresponding to a PS formation rate of λ_f = 0.0158 PS/ms (1.58 %/ms), given by an exponential distribution (χ^2 goodness of fit P-value = 0.102, indicating a good fit). In Figure 9.8B, the PDF of PS lifetimes for the same example case is also given by an exponential distribution, with a PS destruction rate of λ_d = 0.0853 PS/ms (8.53 %/ms). These are consistent with a Poisson birth-death process (χ^2 P-value = 0.113). A worked example showing the calculation for the computed average number of active PS for this example case is shown in Figure 9.8C. In Figure 9.8D, the computed average number of PS is plotted against a running count of the observed number of active PS throughout the recorded epoch, demonstrating that the computed number of PS summarizes the observed PS number throughout the recording. Figure 5E shows the average number of active PS, given by N, plotted against the observed average number of active PS for all n = 8 epochs (given by $N_{bserved}$). N and $N_{observed}$ demonstrate strong linear correlation (R^2 = 0.87; P < 0.001), with points lying along the line of identity.

Figure 9.9C illustrates a worked example for calculating the average duration W of active

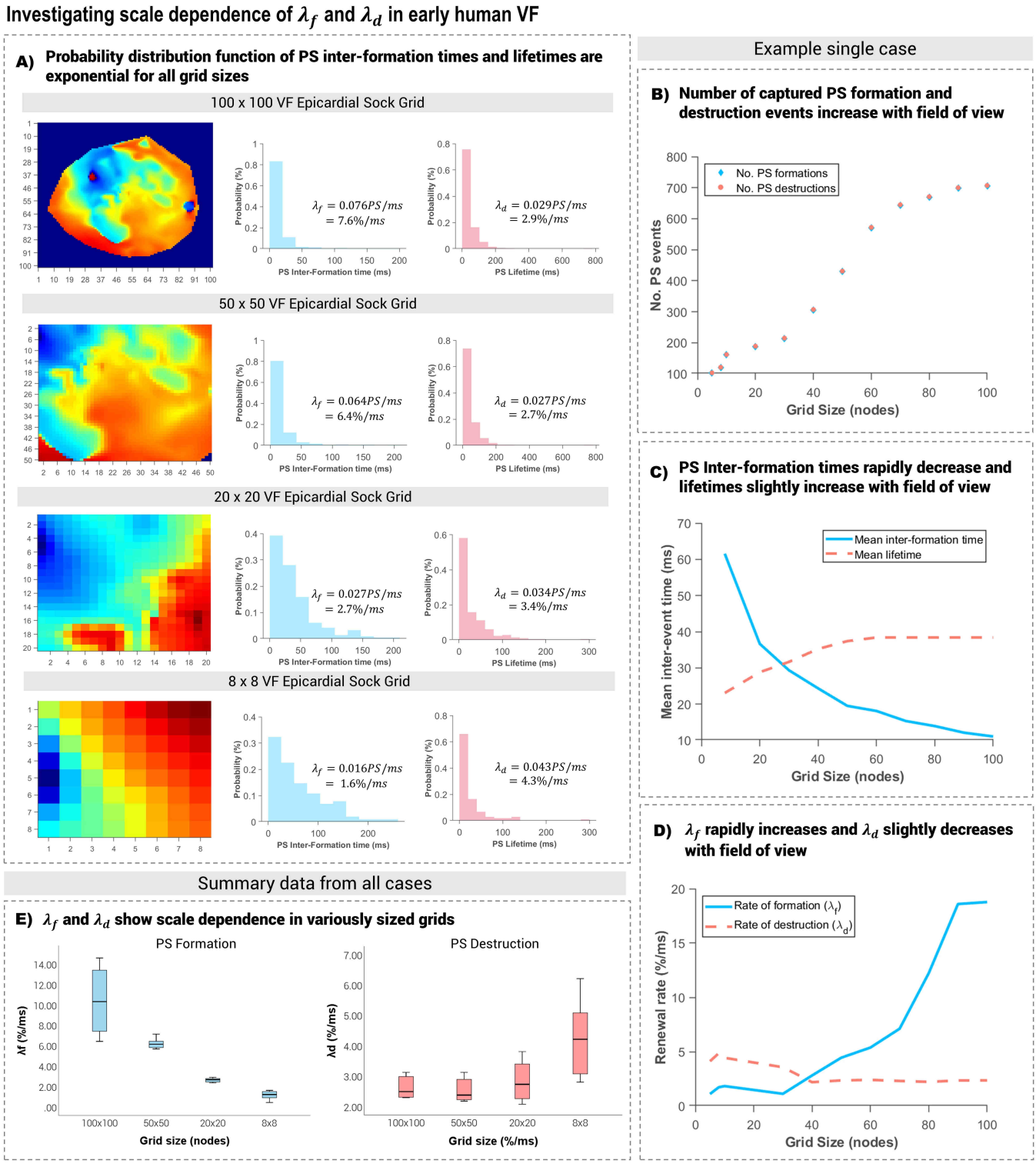

Figure 9.7: Scale dependence of PS renewal rates in computer epicardial sock recordings of early human VF

PDFs for all grid sizes are exponential (A). As the grid size increases, the number of PS events captured increases (B). Timings between PS formations decrease, but timings between PS destructions slightly increase (C). This cases λ_f to increase rapidly, and λ_d to decrease slightly (D).

phase singularities. As a large field of view results in the computed average duration of PS by definition converging to the mean observed PS lifetime, the computed and running average of the observed PS duration throughout the recorded epoch are equivalent (Figure 9.9D). In Figure 9.9E, the average duration of PS, W, is plotted against the observed average duration of active PS given by $W_{observed}$, which demonstrate this equivalence ($R^2 = 1.00$; $P < 0.001$).

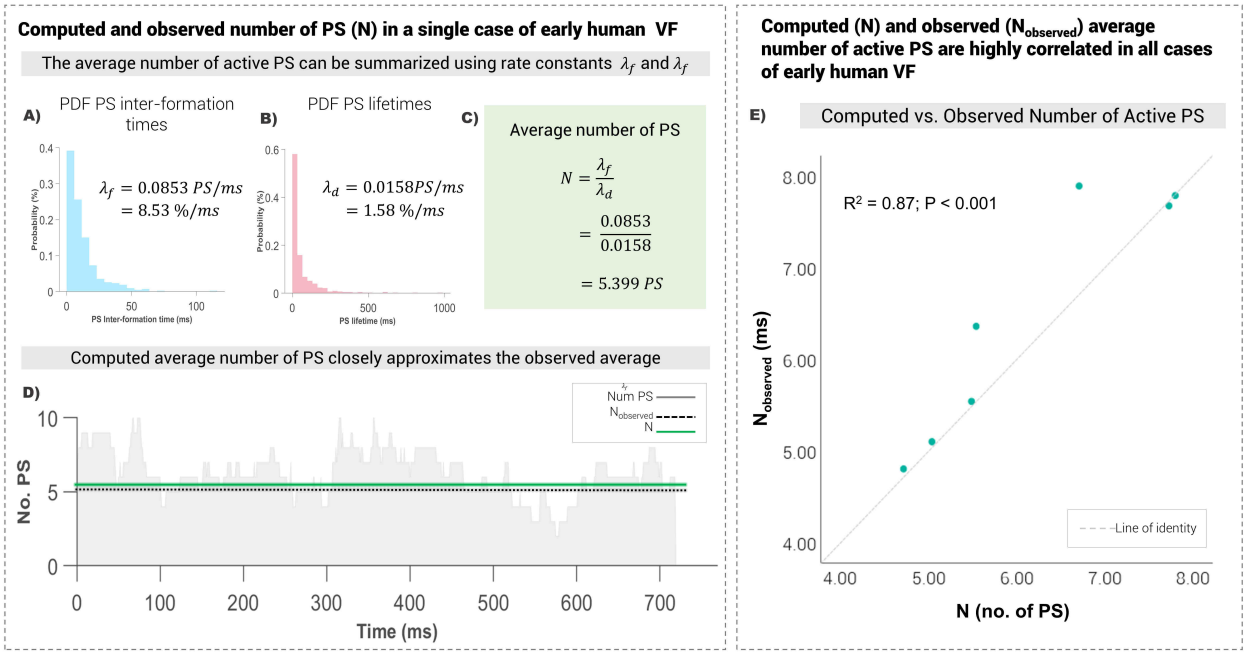

Figure 9.8: Computed average number of PS in epicardial sock recordings of early human VF

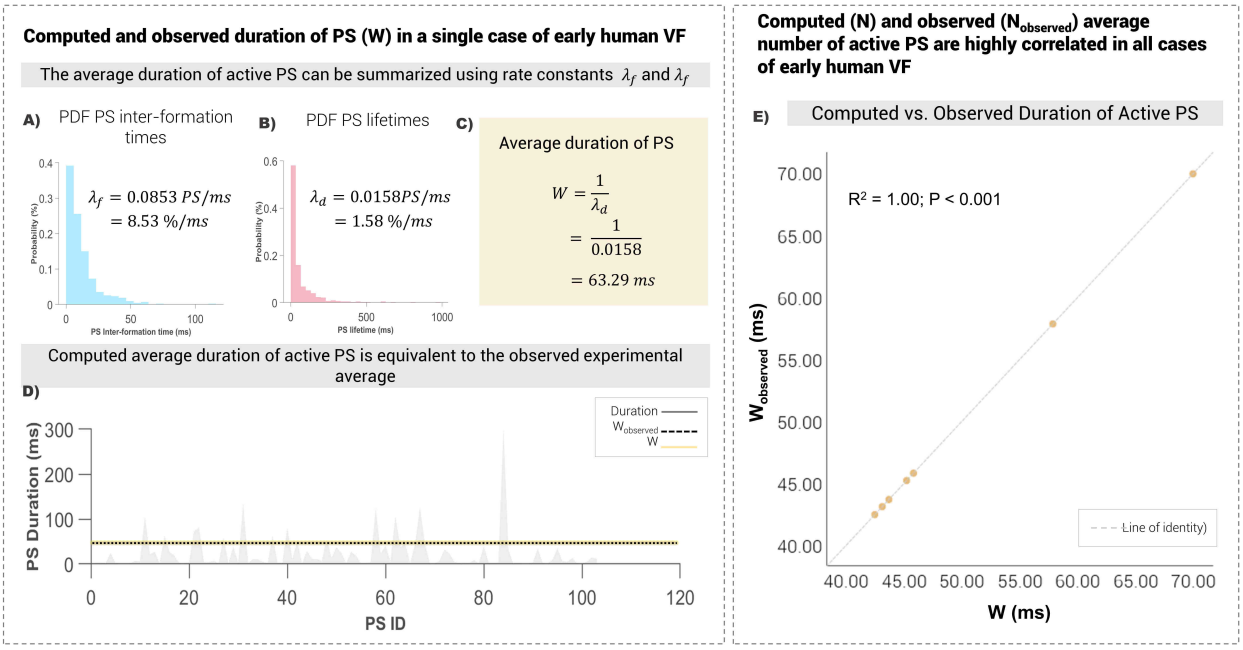

Figure 9.9: Computed average duration of PS in epicardial sock recordings of early human VF

9.2.3 Human persistent atrial fibrillation

Scale dependence of λ_f and λ_d in human persistent atrial fibrillation

To further validate the presence of scale dependence on PS formation and destruction rates, λ_f and λ_d were calculated for simultaneous basket catheter (8x8 electrodes) and HD-grid (4x4 electrodes) recordings taken during human persistent AF. Figure 9.10A shows example phase maps from the basket-catheter recording and the corresponding HD-grid recording of the same human persistent AF epoch, which clearly demonstrates the smaller field of view. PDFs are consistently exponential for both basket and HD-grid catheter recordings. Similarly to epicardial sock recordings and computer simulated fibrillation data, recordings with a smaller field of view (HD-grid) consistently produced significantly smaller λ_f ($P < 0.001$) (Figure 9.10B), representing a slower measured rate of PS formation. λ_d was also slightly faster, however, was not statistically different between the HD-grid and basket recordings ($P = 0.046$).

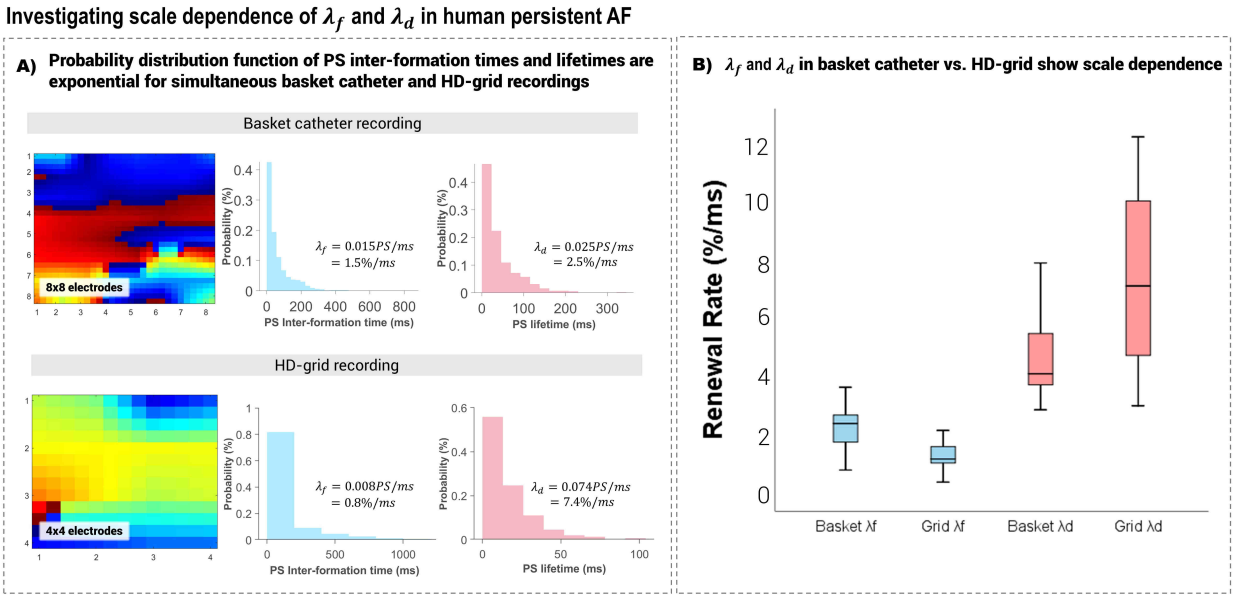

Figure 9.10: Investigating scale dependence of PS renewal rates in basket catheter and HD-grid mapped human persistent AF

M/M/1 BDP model summarizes PS population dynamics in local recordings of human AF

As shown previously in chapter 8, local basket catheter and HD grid mapped AF can be accurately summarised using the $M/M/1$ model. For completeness, these results are again provided here.

In Figure 9.11D, the computed average number of PS is plotted against a running count of the observed number of PS throughout the recorded epoch, demonstrating that the $M/M/1$ birth-

death model summarises the observed PS number throughout the recording. Figure 9.11E plots the computed and observed average number of PS for all n = 43 human AF epochs. It can be seen that N and $N_{observed}$ were highly correlated ($R^2 = 0.96$; $P < 0.001$), with points lying along the line of identity.

Similar results were seen for PS duration. The computed average duration of PS is plotted against the average time taken for each PS to be destroyed for this example epoch, which is shown in Figure 9.12C. W and $W_{observed}$ were highly correlated ($R^2 = 0.94$; $P < 0.001$) in all n = 43 epochs, with points lying along the line of identity.

Figure 9.13C plots the computed and observed average number of active PS for all n = 23 HD grid epochs. N and N_{obs} demonstrated strong linear correlation ($R^2 = 0.97$; $P < 0.001$), with points lying along the line of identity. Similarly, Figure 9.13D plots the computed and observed average duration of PS for all n = 23 HD-grid epochs. W and W_{obs} demonstrated strong linear correlation ($R^2 = 0.95$; $P < 0.001$), with points lying along the line of identity.

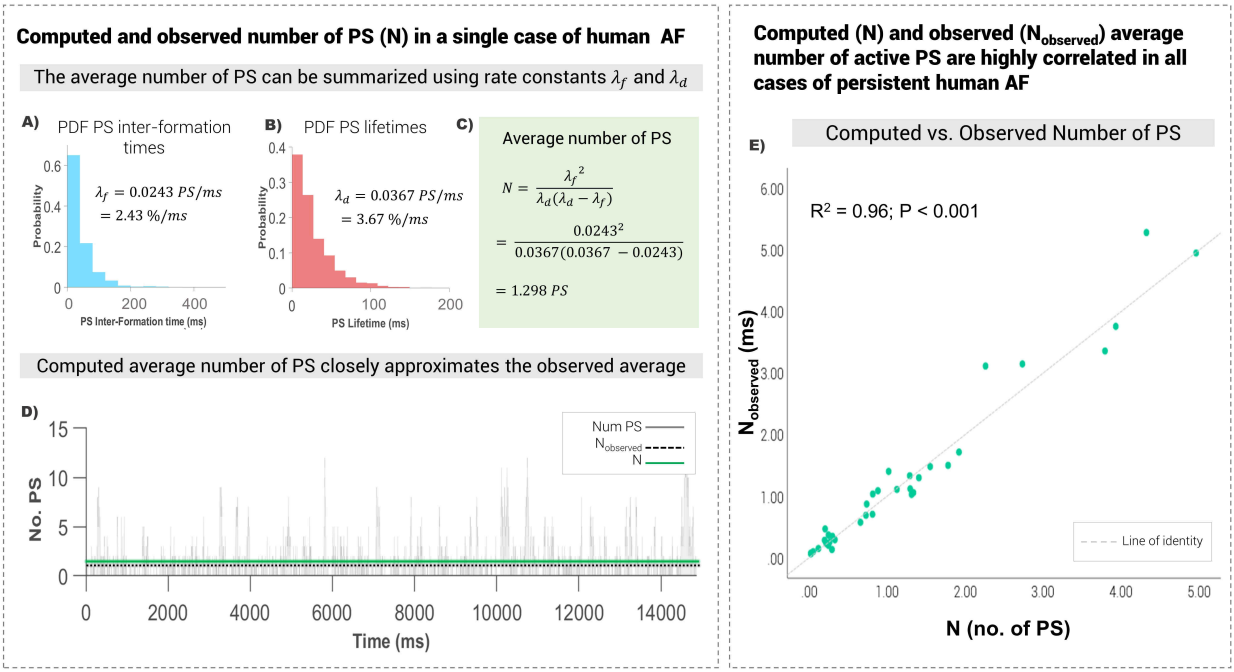

Figure 9.11: Computed average number of PS in basket catheter mapped human persistent AF

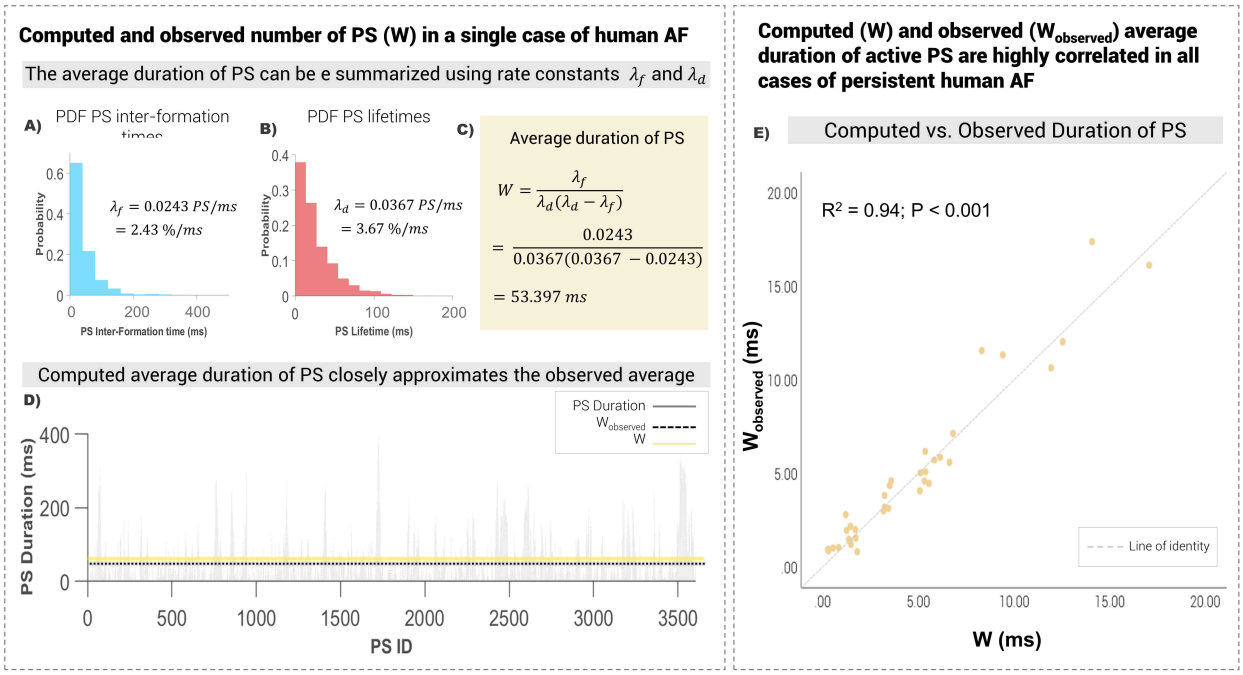

Figure 9.12: Computed average duration of PS in basket catheter mapped human persistent AF

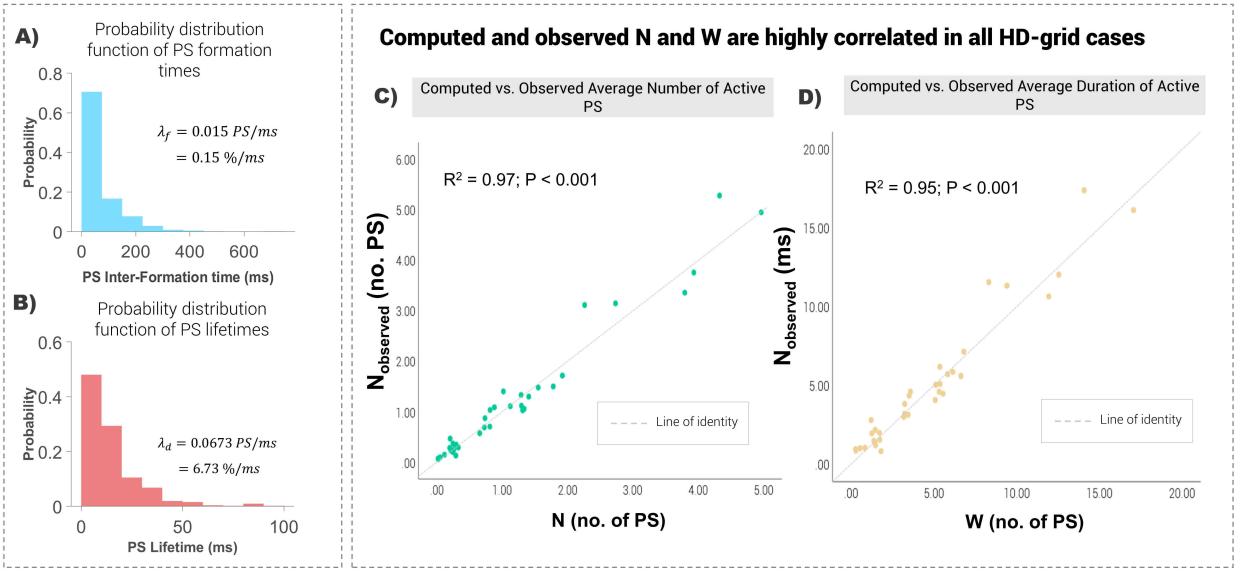

Figure 9.13: Computed average number and duration of PS in HD-grid mapped human persistent AF

9.3 Discussion

As discussed throughout ***Part II*** of this dissertation, unstable reentrant circuits feature in many of the notable mechanistic theories of cardiac fibrillation. Through studying the dynamics of phase singularities, which occur at the pivot points of reentrant circuits, this chapter extends on the findings presented in chapter 8 by providing a number of new insights regarding the formation and destruction of these circuits.

In the previous chapter (chapter 8), it was shown that arrhythmia dynamics can be summarised and predicted using a compact quantitative Markov birth-death framework. Here, it is demonstrated that the phase singularity birth-death process is in fact scale dependent and governed by the size of the mapped field. By demonstrating this scale dependence, this study provides useful practical insights about how these processes can be optimally quantified and modelled to characterise the underlying fibrillatory process. This ability may have very useful applications for monitoring the likelihood of termination, monitoring arrhythmia progression, or development of more effective ablation strategies. Furthermore, PS population dynamics as predicted by the Markov birth-death model may help determine the effect of therapeutic interventions on underlying fibrillatory dynamics.

9.3.1 Effect of scale on measured λ_f, λ_d and the Markov birth-death model

This study demonstrates a scale dependency of the observed phase singularity birth-death process. For a large field of view, PS population dynamics can be summarized and predicted using the $M/M/\infty$ birth-death model, whilst small fields of view can be modelled by an $M/M/1$ model. This is due to the destruction process effectively being modelled as a single source of annihilating waves for a constrained field, whilst a global field of view captures many sources and hence is more appropriately represented by the multi-server birth-death model. Mathematically speaking, the shift from the single-server to multi-server birth-death model is due to a larger number of servers required to stabilize the system when $\rho > 1$ [126], which is a central fact of queuing theory.

As the field of view is reduced, the measured PS formation rate (λ_f) is also shown to rapidly decrease due to the increased timings between consecutive PS formations captured by the mapped field. Contrastingly, the PS destruction rate (λ_d) demonstrates only a slight increase, which is due to the fact that the lifespan of any individual PS is not directly influenced by the number of PS observed, but instead, mapping a smaller area decreases the likelihood for rare long-lasting PS to be captured. This is demonstrated by probability distribution function of PS lifetimes seen for larger grids (Figure 9.4 and Figure 9.7).

9.3.2 Implications for the fibrillatory mechanism

These findings are of potential significance to the current understanding of fibrillation. By definition, both atrial and ventricular fibrillation are characterised by disorganised and irregular wave propagation [37], however, the results of this study find further support for a stable underlying limiting distribution of PS formation and destruction.

Evidence for this stability can be described by the thinning theorem. In stochastic process theory, thinning (otherwise referred to as splitting) a Poisson process refers to independently classifying each random point into different types. If these points are sampled from a Poisson process, then the random points of any given type should also form an independent Poisson process [81]. An analogy for this is measuring radioactive emission. In such a scenario, each particle can either be missed (type 1) or detected (type 2) by a counter. If we consider the random type 1 and 2 events independently, then these will form separate Poisson processes corresponding to a rate of $\lambda 1$ and $\lambda 2$ respectively [81]. The combined Poisson process of both type 1 and type 2 events subsequently has a rate of $\lambda 1 + \lambda 2$ [**?**].

This radioactive emission example is analogous to the small field of view case observed in this study, whereby small grids similarly classify PS formation and destruction events as either missed or detected. The probability distribution function of PS inter-formation times and lifetimes therefore effectively analyse only detected events captured by the mapped area. This is shown to consistently produce exponential probability distribution functions of PS inter-event times, which is consistent with a Poisson process.

These results suggest that PS formation and destruction observed at the small scale is effectively a thinned or split version of the overarching Poisson process, which provides support for wave propagation dynamics during fibrillation being accurately modelled as a stochastic Poisson process that gives rise to a robustly stable average rate of PS formation and destruction.

9.3.3 Clinical Implications

The finding that phase singularity formation and destruction in cardiac fibrillation can be modelled by a scale-dependent Markov birth-death process may have useful clinical implications. Potentially, it suggests that local catheters such as the HD-grid are interchangeable with more global mapping modalities for the purpose of analyzing underlying fibrillatory dynamics. This may be practical given the ease of use of local mapping modalities versus global recording methods. The property of Poisson thinning also adds validity to sub-sampling a constrained area of the chamber in this way, as capturing a small portion of PS events will still lead to a Poisson process reflective of the governing Poisson process at the whole chamber level. Furthermore, the Poisson thinning property may suggest that PS formation and destruction can effectively be sampled from anywhere within

the chamber, as this would similarly lead to an independent Poisson process.

Another useful finding of this study is that at baseline without any intervention, λ_f is consistently larger than λ_d for recordings with a large field of view, but reverses for small fields of view. This insight may be potentially useful in applications where fibrillatory dynamics are monitored, or for the development of future treatments based on rate parameter modulation.

The finding that λ_d is more consistent over various fields of view also suggests suggests that λ_d may be a more practically useful marker of underlying fibrillatory dynamics given its smaller coefficient of variation.

9.4 Conclusion

This study demonstrates that phase singularity dynamics during human persistent atrial fibrillation and early human ventricular fibrillation can be modelled using a scale-dependent Markov birth-death framework, providing a compact theoretical approach to summarise, explain and predict the repetitive regeneration of unstable reentrant circuits. Additionally, findings suggest that the Poisson processes of phase singularity births and deaths can be accurately characterised irrespective of the field of view of the mapping modality used and, potentially, irrespective of the location at which the recording is taken in the chamber.

To summarise, this study adds important insights to the current literature by:

- Establishing that the observed phase singularity birth-death process is scale dependent, governed by the field of view of mapping
- The magnitude of renewal rate constants λ_f and λ_d is consequently governed by the mapping field of view
- The optimal Markov birth-death model is also dependent on scale
- The phase singularity birth-death process can be accurately characterised irrespective of the field of view of the mapping modality used, meaning local catheters can be used in place of difficult global recording methods

Part III

Summary, concluding remarks and supplementary material

Chapter 10

Summary and Conclusions

Re-entrant circuits have been a key and consistent observation in the field, dating as far back as almost a century ago. However, the nature of this rotational activity and whether it plays a role in initiating and maintaining cardiac fibrillation has thus far remained a mystery. This has unfortunately lead to downstream consequences in treatment, as incomplete understanding of the underlying fibrillatory mechanism has hindered the development of effective therapeutic interventions, even though atrial and ventricular fibrillation are the most common and most deadly arrhythmia respectively. This served as the primary motivation of this thesis, in which I aimed to use computational and statistical approaches to provide insights into the mechanisms by which these re-entrant circuits promote the perpetuation of cardiac fibrillation.

10.1 *Study I*- Spatiotemporal stability and specificity of high bipolar electrogram entropy regions in sustained atrial fibrillation: implications for mapping (ch.4)

At the heart of our incomplete understanding of cardiac fibrillation is the debate about whether the arrhythmia arises from anarchical versus hierarchical mechanisms. Although anarchical mechanisms such as the multiple wavelet reentry hypothesis have been put forward, studies demonstrating the presence of localised, stable reentrant activity (e.g. rotors) have recently resulted in an enormous amount of effort, time and money being directed into mapping and targeting these sources. From a clinical perspective, localised stable drivers are appealing as they suggest that a 'point-and-shoot' approach may lead to long-term termination or modulation of the arrhythmia. Many independent research groups have investigated methods to map and ablate these 'driver' regions, but currently the success of these methods are either non-reproducible or require further investigation.

A major limitation of many of these mapping approaches is that they utilise internal company-specific or proprietary technologies that prevent studies from being reproduced and externally validated. In order to provide a solution to this, entropy has previously been presented as an open-source, non-proprietary method of rotor mapping. However, a fundamental knowledge gap was that the specificity of entropy remained unknown (e.g. whether it co-locates only with the pivot of rotors or also other wave propagation patterns). Further, in order for entropy-guided targeted ablation to be possible, stability is needed in both time and space in order for physical ablation lesions to be placed.

This was investigated in ***Part I*** of the thesis, using a study comprising of i) human medium-duration AF recordings, ii) sheep tachypaced long-duration AF recordings and iii) computer simulated fibrillation (ch.4). Findings from this first study demonstrated that although there was a relative stability of the highest top 10% of entropy regions, which recurred in the same spatial location over time, they were transient and surrounded by dynamic global spatial and temporal instability. Additionally, high entropy regions were shown to correlate not only with the pivot of rotors, but also with areas of repetitive cross propagation. These findings collectively suggest that entropy-based mapping requires further investigation before being used as part of a targeted ablation strategy.

However, an interesting finding of the study that echoes a number of reports throughout the history of the field is the the overarching temporal instability observed. Given unstable reentrant activity has been widely reported, it raises fundamental questions about the origins of this random behaviour, and whether it is key to the underlying fibrillatory mechanism.

10.2 *Study II*- Renewal theory as a universal quantitative framework to characterise phase singularity regeneration in mammalian cardiac fibrillation (ch.6)

Due to the intrinsic instability of re-entrant circuits implied by the findings of the entropy study, ***Part II*** of this thesis aimed to study the random, unstable behaviour of rotational activity in fibrillation using a stochastic renewal theory framework, which uses probability theoretic principles to study random phenomena. Specifically, in this study (chapter 6), a universal quantitative framework was developed to study the formation and destruction of reentrant circuits in both atrial and ventricular fibrillation.

Reentrant activity can be detected by the phase singularity (PS), which occurs due to the topology at the centre of a rotor as well as at the free ends of wavelets. It was reasoned that by studying the probability distribution functions of the inter-event times between PS formations

and PS lifetimes, insights could be made about the underlying data generating mechanism. It was discovered that PS inter-formation event times and lifetimes always followed exponential distributions, consistent with a Poisson renewal process. A defining feature of the Poisson renewal process is that although individual events occur at random, there is paradoxically a robustly stable underlying rate that governs the Poisson process. Mechanistically, this suggests for the first time that although individual PS behave at random, the long term rate of formation and destruction is robustly stable and able to be quantified using the Poisson rate constant.

This finding was rigorously validated in 5 model systems (i) human AF, ii) sheep AF, iii) rat AF, iv) rat VF and v) computer simulated fibrillation), as well as comparison with the most stochastic distribution as estimated using a Maximum Entropy approach, and cross-validation with current source literature. The contribution of these findings to literature is that they recast PS destruction and formation in cardiac fibrillation as Poisson renewal processes, which provides a powerful universal quantitative framework to explain the formation and destruction of rotational events in mammalian cardiac fibrillation.

10.3 *Study III*- Renewal rate constants of phase singularity formation and destruction in atrial fibrillation are temporally stable: implications for AF mechanism (ch.7)

Study III (chapter 7) investigates the Poisson processes of PS formation and destruction further by assessing their temporal stability. Characteristically, because the timings of individual events are statistically independent but the underlying Poisson rate is stable over time, the arrhythmia generating mechanism should be temporally stable, despite the superficial appearance of uncoordinated or random electrical wave propagation. This would recast fibrillation as the product of an underlying stable stochastic process and implies that measuring the rate constants would be a simple, reliable way to characterize fibrillatory dynamics.

To investigate this, the study assesses stationarity in i) human persistent and ii) sheep tachypaced AF. In both species findings consistently demonstrated stationary dynamics, thus validating that PS formation and destruction rates are stable in the time domain.

As a practical application of this temporal stability, the minimum sampling time required to accurately estimate rates of formation and destruction was calculated and shown to be 15 seconds. This suggests that these rate constants can also be accurately estimated from short-duration recordings, providing a novel mechanistic tool to measure overall fibrillatory dynamics, directly connected to rotor regeneration.

10.4 *Study IV*- Self-regeneration of atrial fibrillation can be summarised and predicted using a Markov birth-death framework (ch.8)

Due to the findings of study II and III consistently pointing towards PS formation and destruction occurring via Poisson renewal processes, study IV (chapter 8) aimed to answer the question of how these processes relate to the underlying fibrillatory mechanism. It was hypothesised that if PS formation and destruction act as paired Poisson processes to perpetuate atrial and ventricular fibrillation, then this dynamic relationship could be modelled using a Markov birth-death process, which would provide a compact quantitative framework to summarise, understand and even predict fibrillatory behaviour.

To explore this an $M/M/1$ model, the simplest Markov birth-death model, was used to characterise phase singularity dynamics in: i) basket catheter recordings of human AF and ii) HD-grid recordings of human AF. The $M/M/1$ Markov birth-death framework allowed system properties such as the average number and duration of PS to be accurately summarised, consistently close matching the observed experimental system properties. Importantly, the Markov birth-death framework also provided the necessary quantitative architecture for future prediction of phase singularity dynamics, which from a scientific point of view helps validate the contributions of PS formation and destruction processes to the maintenance of fibrillation. In the clinical context, the predictive capability may also prove if potential therapeutic interventions have had an effect on underlying fibrillatory dynamics.

To further investigate whether the paired Poisson process of PS birth and death plays a role in the fibrillatory mechanism, rate constants were compared between cases of sustained and spontaneously terminating AF. In all cases, a statistically significant difference in the rate of PS formation and destruction was seen for all cases in which fibrillation terminates.

Collectively, this study demonstrates that phase singularity dynamics can be modelled using a Markov birth-death framework, providing a compact theoretical approach to summarise, explain and predict the repetitive regeneration of unstable reentrant circuits. The cycle of continuous PS birth and death is shown to also play a role in the perpetuation of atrial fibrillation.

10.5 *Study V*- Phase singularity formation and destruction processes in cardiac fibrillation are scale-dependent (ch.9)

Extending on findings from the Markov birth-death framework introduced in 8, study V (chapter 9) aimed to understand how to most optimally model phase singularity dynamics, given that there

are several types of Markov birth-death models.

Although the $M/M/1$ model was used in study IV (as it is the simplest birth-death model) it remained unknown whether this was universally the optimal model to apply. Furthermore, baseline rates of PS formation and destruction were also not understood, which would be directly applicable to interpretation of PS formation and destruction processes.

To investigate this, PS renewal rates and different types of Markov birth-death models were studied in: i) computer simulated fibrillation, ii) epicardial sock recordings of early human VF, iii) basket catheter recordings of human persistent AF, and iv) HD-grid recordings of human persistent AF.

It was found that the observed phase singularity dynamics during human persistent atrial fibrillation and early human ventricular fibrillation were scale dependent and could be accurately modelled using a scale-dependent Markov birth-death framework. As a result of this scale, findings suggest that the Poisson processes of phase singularity births and deaths can be accurately characterised irrespective of the field of view of the mapping modality used, meaning local catheters can be used to analyse PS renewal in place of difficult global recording methods.

10.6 What this thesis adds to current literature

To summarise, the findings in this thesis presents potentially significant implications for future research and therapeutic strategies, and provides the following key contributions to literature:

- The study findings show that there is global temporal instability of entropy, which suggests an underlying instability of re-entrant activity. Within this global flux, there was a partial stability of the top 10% of entropy, though this was only moderate and occurs not at just rotors, but also at areas of repetitive wave cross propagation.

- Demonstration that PS destruction and formation in cardiac fibrillation are renewal processes. These results provide a potentially powerful universal quantitative framework to explain the formation and destruction of rotational events in mammalian cardiac fibrillation.

- Atrial fibrillation phase singularity formation and destruction processes follow stationary dynamics and stable in the time domain. This implies that rates of PS formation and destruction can be accurately estimated from short-duration AF recordings, providing a mechanistic tool to measure overall AF dynamics, directly connected to rotor regeneration as the underlying mechanism of the perpetuation of AF.

- Demonstration that phase singularity formation and destruction can be accurately summarised, understood and predicted using a compact quantitative Markov birth-death frame-

work. This framework also demonstrates how PS formation and destruction act as a paired Poisson process to promote self-regeneration of cardiac fibrillation.

- Demonstration that the observed phase singularity formation and destruction processes are scale-dependent and governed by the field of view of mapping. However, this can be accurately modelled by the Markov birth-death framework at all fields of view, suggesting that local and global recording modalities are potentially interchangeable.

10.7 Future directions

In regards to the entropy study in chapter 4, investigation is needed to define methods of delineating rotors and regions of cross propagation. This may be achieved in future via the use of machine learning algorithms that utilize other electrogram features, in addition to entropy, to differentiate between these two modes of wave propagation. In addition, cross validation with other mapping modalities such as phase mapping may be required in order to relate entropy patterns to the underlying wave propagation dynamics.

The finding that re-entrant circuits are unstable, mobile and change dynamically throughout time supports the notion that they are regenerated stochastically through Poisson renewal processes. As they are simply regenerated at random, this suggests that a 'point-and-shoot' approach targeted at singular circuits may be ineffective. Instead, therapeutic strategies may have to be designed such that they modulate the rate of PS regeneration, which in turn provides conducive conditions for spontaneous termination. Further investigation will have to be done in order to identify ablation strategies that most effectively modulate the rate of PS regeneration.

In addition, although a change in the rate of PS formation and destruction was seen in cases of spontaneous AF termination, the mechanisms behind this still remain unknown. In fact, there is currently limited data on how exactly AF and VF terminate. An area of study may be to assess whether changes in PS rate constants are a common pathway to termination, and to study how PS regeneration is altered in these cases.

Another area of study is to assess the ionic and tissue determinants of the PS rate constants. As it has long been postulated that episodes of fibrillation encourages 'remodelling', which alters cardiac substrate to promote the maintenance of re-entrant arrhythmia, ionic and structural remodelling may influence changes in the rate parameters of PS formation and destruction. Currently, it is unknown which of these substrates influence the rotor regeneration cycle, and how, although it could be reasoned that perhaps more advanced substrate remodelling will result in a rotor regeneration rate that promotes ongoing maintenance of AF/VF.

Although the findings outlined in this thesis suggest that that PS destruction and formation in

cardiac fibrillation can be characterised by renewal rate constants, measurement of these constants currently rely on invasive means of data collection. A potentially clinically useful application would be to derive the rate constants from surface ECG, enabling non-invasive measurement of the underlying AF dynamics. This could to be used as an objective marker of the AF phenotype, which would be clinically useful in stratifying which patients should be treated. Non-invasive renewal rate measurement may also provide a platform for longitudinally assessing the progression of a patient's AF over time.

10.8 Concluding remarks

The investigations and methods described in this dissertation find evidence for the presence of unstable reentrant circuits during atrial and ventricular fibrillation. In addition, the studies discussed support the notion that both atrial and ventricular fibrillation should be redefined as stochastic Poisson renewal processes, which perpetuate due to a continuous regeneration cycle of PS births and deaths. These findings have, for the first time, allowed for quantitative assessment of the rates of PS formation and destruction, as well as the number and duration of phase singularities. In addition, the Markov birth-death framework provides an accurate prediction of these system properties in future AF episodes. Collectively, these findings have potentially significant implications for research and the development of more effective treatments for atrial and ventricular fibrillation, which has remained elusive for the last century.

Supplementary Results and Material

Supplement A

Patient AF baseline characteristics - Part I

For the entropy study detailed in ***Part I*** of this dissertation, patient baseline characteristics are as shown below in Table A.1.

Characteristics (patients n = 10)	
Age	62 ± 9
Gender	
Male	80% (8)
Female	20% (2)
BMI	28.7 ± 3.8
CHA_2DS_2VaSC	1.6 ± 1
AF type	
Persistent	80% (8)
Paroxysmal	20% (2)
Echocardiographic parameters	
LVEF (%)	59 ± 7
LA area (cm^2)	25 ± 4
E/E'	8.4 ± 1.6

Table A.1: Patient Baseline Characteristics

Supplement B

Mathematical Model of Fibrillatory Activity

One of the mechanisms of wave conduction driving fibrillation is the presence of dynamically unstable areas (e.g. high degree of electrical alternans) causing continuous wave break and fibrillatory conduction. Dynamically unstable areas continuously disrupt wave conduction in the surrounding areas, generating short-lived pivoting waves. In order to model this scenario, a Panfilov-Tusscher model[232] was used, which due to its simple formulation, allows straightforward control of dynamical stability of the wave conduction.

A rectangular grid of 80x80 diffusively coupled simulation nodes (diffusion coefficient set to 0.2) was utilised. Space step was set to 0.6 and time step to 0.02. The system was integrated using a forward Euler scheme with no-flux boundary conditions. Based on the study by Ten-Tusscher and Panfilov [232], the following model parameters were used: $a = 0.1$, $k = 8$, $\epsilon = 0.01$, $b = 0.1$, $\mu 2 = 0.2$. In order to induce dynamical instability, the value of $\mu 1$ was varied between 0.02 and 0.2. By varying the recovery variable $\mu 1$ in this way, three various AF-type scenarios were developed. In the renewal process studies in Part II, these included: i) continuous spiral wave breakup with uniform electrophysiological properties, ii) stable spiral with uniform surrounding electrophysiological properties and iii) stable spiral surrounded by non-uniform surrounding electrophysiological properties. For cases with uniform electrophysiological properties, $\mu 1$ was set uniformly throughout the grid. For the stable spiral case with non-uniform surrounding electrophysiological properties, the parameter $\mu 1$ was varied in the model to influence the steepness of the restitution curve. A random distribution of $\mu 1$ was implemented, which led to the presence of localized areas of high dynamical instability (leading to spiral wave breakup) surrounded by dynamically stable areas.

This simplified model was used only to illustrate the link between dyssynchrony and regions maintaining fibrillation due to electrical instability. There are several mechanisms thought to play

an important role in the maintenance of fibrillation (e.g. fibrosis, automaticity, heterogeneity of effective refractory period). However, exploration of all potential factors is beyond the scope of this work and hence the study decided to focus on selected one (heterogeneity of electrical alternans) to demonstrate how dyssynchrony can point to regions critical to fibrillation maintenance. Since it was not the aim to model the detailed electrophysiology of the atria but rather show specific mechanisms, arbitrary units were used.

Supplement C

Entropy Algorithms

In information theory, entropy measures the information content of a signal and as such, can be used to quantify electrogram complexity. For example, an EGM in sinus rhythm contains more repetition and therefore less randomness than a fractionated EGM in AF. Entropy measures this 'randomness' to quantify the complexity of the EGM signal, and hence will return a higher entropy for more complex signals. The entropy algorithms used in this dissertation are further described in the following.

C.0.1 Shannon Entropy

In AF analysis, Shannon Entropy (ShEn) is often used to measure the information content of an ECG or EGM. ShEn typically measures this using the amplitude distribution within the signal histogram. Specifically, a voltage histogram can be acquired by binning signal samples according to its amplitude. Following this, the relative probability density $p(i)$ is obtained by dividing the sum of counts in each amplitude bin by the total number of counts. In effect, ECG or EGM with regular morphologies (i.e. signals that only possess a few states) will yield a narrow amplitude distribution2. Conversely, complex morphologies containing a number of dissimilar deflections, such signals in AF, will lead to more varying amplitudes and in turn a broader amplitude distribution (C.1). In effect, as ShEn is taken a sum of the probabilities, broader amplitude distributions will result in higher ShEn. In this study, we computed ShEn by binning samples depending on their amplitude using a voltage histogram, with bin sizes dependent on the standard deviation (SD) of the signal (bin size = 0.125 * SD). In mathematical notation, ShEn can be given by:

$$ShEn = \sum_{i=1}^{n} p(i) log_2 p(i) \tag{C.1}$$

where n is the number of discrete values the variable can take and p the probability of a

sample falling within a given amplitude bin. Previous studies published by Ganesan et al. [83] [85] showed that ShEn co-located with the rotor centre ($P < 0.001$) in both computer simulations and animal models of rotors and AF under the premise that EGMs in the pivot zone of a rotor experience greater spatial uncertainty of wavefront direction, which in turn results in less stable EGM morphologies due to the direction-dependent nature of the bipolar EGM signal. Results showed that more complex EGMs demonstrated various different deflections and comprise of more varying amplitudes, hence possessing a broader voltage distribution that coincides with higher ShEn (Figure C.1).

C.0.2 Approximate Entropy

Like ShEn, Approximate Entropy (ApEn) also measures the information content of a signal. In place of using an amplitude distribution, ApEn detects the presence of repetitive patterns of fluctuation, and measures the likelihood that runs of similar patterns will remain similar when incrementally compared. Specifically, the prevalence of repetitive patterns was identified by forming a sequence of vectors, S_N, using the time series data, and measuring the difference between them. If the relative difference between any pair of corresponding measurements is less than the length of the pattern m, the pattern is deemed similar. A simple example is shown in 3.2. In mathematical notation, this can be expressed using the equation:

$$ApEn(S_N, m, r) = ln\frac{Cm(r)}{Cm+1(r)} \tag{C.2}$$

where m is the pattern length, r is the similarity criterion or threshold, and *Cm(r)* the prevalence of patterns of length m in the sequence S_N [194]. In this study, we set an epoch of length $N = 5000$, due to the 5 second window length selected as used in previous literature. The tolerance or similarity criterion r was set to 0.2 multiplied by the standard deviation of the sequence. Lastly, the vector length m was set to 2. As a result, the algorithm searches through the sequence S_N and compares this with the vector of length m to find matches of the same 2 voltage values within the sequence (bipolar EGM). If there is a match, the algorithm will determine how often the following point $(m + 1)$ lies within the tolerance r of these matched vectors.

C.0.3 Sample Entropy

Sample Entropy (SampEn) is a modified rendition of ApEn that works in much the same fashion. Computationally, however, SampEn differs in that it does not include comparisons between a vector

and itself, hence avoiding biased regularity. SampEn is defined as:

$$SampEn = \tag{C.3}$$

$$SampEn = -log\frac{\sum A_i}{\sum B_i} = -log\frac{A}{B} \tag{C.4}$$

where A_i is the number of matches of length $m+1$ with the i^{th} template, B_i the number of matches of length m with the i^{th} template. A simple example is shown in Figure C.1. Like ApEn, we used an epoch of length $N = 5000$, a tolerance or similarity criterion $r = 0.2 * SD$ of the sequence, and a vector length $m = 2$.

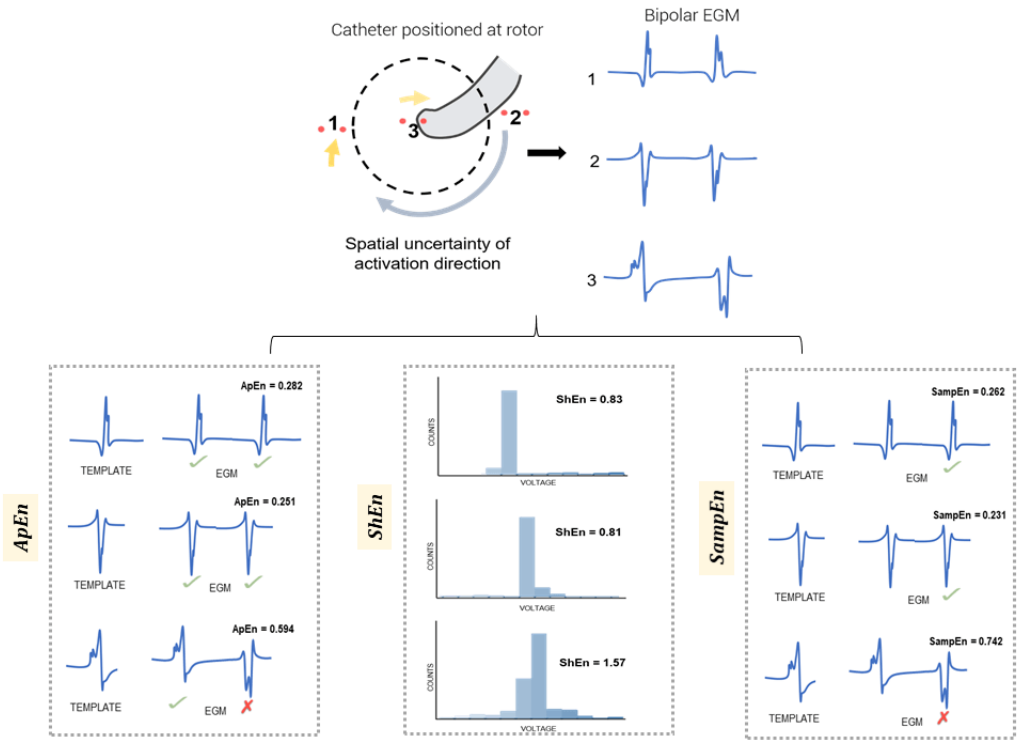

Figure C.1: Schematic showing high ApEn, ShEn and SampEn calculation. Adapted from [Dharmaprani, 2018]

Supplement D

Interpretation of Kappa statistic values

Kappa interpretations were taken from Landis and Koch, 1997 [141], as shown in Table D.1. In this study, kappa values were used to quantify the level of agreement between the presence and location of the top 10% of entropy and DF values between consecutive segments. If the top 10% of values were not consistently present in the same location over all segments, then the kappa statistic will return a *low* value. Conversely, if the top 10% of values wereconsistently present in the same location over all segments, then the kappa statistic will retun a *high* value.

Below 0	Poor agreement
0.00 - 0.20	Slight agreement
0.41 - 0.60	Moderate agreement
0.61 - 0.80	Substantial agreement
0.81 - 1.00	Alomst perfect agreement

Table D.1: Kappa Interpretations

Supplement E

Example entropy and DF movies

Movie 1: Entropy

For an example movie of entropy in a single human persistent AF case, see: `https://youtu.be/ohZOi8XdMBw`

Movie 2: Dominant Frequency

For an example movie of DF in a single human persistent AF case, see: `https://youtu.be/4gHZLNalFf4`

Supplement F

Patient AF baseline characteristics - Part II

For the renewal process studies detailed in ***Part II*** of this dissertation, patient baseline characteristics are as shown below in Table F.1 for the Australian cohort (Flinders University, South Australia), and in Table F.2 for the German cohort (University Medical Centre, Hamburg).

Characteristic (patients n = 12)	
Age	62 ± 9
Gender	
Male	83% (10)
Female	17% (2)
BMI	28.7 ± 3.8
CHA_2DS_2VaSC	1.6 ± 1
AF type	
Persistent	80% (10)
Paroxysmal	20% (2)
Echocardiographic parameters	
LVEF (%)	59 ± 7
LA area (cm^2)	25 ± 4
E/E'	8.4 ± 1.6

Table F.1: Patient Baseline Characteristics

Characteristic (patients n = 13)	
Age	62 ± 9
Gender	
Male	92% (13)
Female	0.07% (1)
BMI	29 ± 5
CHA_2DS_2VaSC	1.6 ± 1
AF type	
Persistent	100% (13)
Paroxysmal	0% (0)
Echocardiographic parameters	
Reduced LVEF (40-55%)	2/10
LA diameter (mm)	48 ± 6
Hypertension	3/10
Diabetes	0/10

Table F.2: Patient Baseline Characteristics, German cohort

Supplement G

A proof for the convergence of a geometric distribution to exponential distribution

In the case of PS formation and destruction times, we consider the 'time until the next event', which in the discrete case is a geometric distribution. The geometric distribution is a special case of the negative binomial distribution, which is the number of number of failures in a sequence of Bernoulli trials until the first success [206]. The probability mass function for the geometric distribution is shown below:

$$Pr(X = k) = p(1-p)^k, \forall k \geq 1 \tag{G.1}$$

Consider if p is small, then $\frac{n}{p} = \pi \ldots (*)$

Also, let $x = \frac{k}{n} \ldots (**)$

Then pmf of the geometric distribution is:

$$\sum_{k=0}^{\infty} Pr(X = k) \tag{G.2a}$$

$$= \sum_{k=0}^{\infty} p(1-p)^k \tag{G.2b}$$

$$= \sum_{k=0}^{\infty} \frac{\lambda}{n}(1 - \frac{\lambda}{n})^k \ldots using(*) \tag{G.2c}$$

$$= \sum_{k=0}^{\infty} \frac{\lambda}{n}(1 - \frac{\lambda}{n})^{n \cdot \frac{k}{n}} \ldots using(**) \tag{G.2d}$$

$$= \sum_{k=0}^{\infty} \frac{\lambda}{n}(1 - \frac{\lambda}{n})^{n.x\frac{1}{n}} \tag{G.2e}$$

$$= \sum_{k=0}^{\infty} \frac{\lambda}{n}(1 - \frac{\lambda}{n})^{n.x}\ \delta x\ (as\ n \xrightarrow{\infty},\ x \to \Delta x \tag{G.2f}$$

$$= \sum_{k=0}^{\infty} \lambda e^{-\lambda x}\ \Delta x\ (using\ characterisation\ of\ e^y = (1 + \frac{y}{n})^n,\ as\ n \to \infty \tag{G.2g}$$

$$= \int_0^{\infty} \lambda e^{-\lambda x} \tag{G.2h}$$

Supplement H

A step by step guide for λestimation using MaxEnt principles and Lagrange multipliers

The general principle behind MaxEnt is that the optimal choice for the predicted probability distribution of a given data set is one with the largest amount of uncertainty or 'entropy', e.g. the choice that is the most purely random containing the least number of assumptions, while still meeting the known constraints [80] [105]. To achieve this, we can maximize the entropy function subject to our constraints using the Lagrange multiplier method:

$$\frac{\partial f}{\partial x} = \sum_{i=1}^{N} \lambda i \frac{\partial g_x}{\partial x} \tag{H.1}$$

where N is the number of constraints, $g_x(x)$ are the constraints, λ_i the Lagrange multiplier, and $f(x)$ is the entropy function:

$$f(x) = -\sum_{x=0}^{\infty} (p_x) log(p_x) \tag{H.2}$$

In general terms, the Lagrange multiplier itself is a variable that allows the directions and gradients of $f(x)$ and $g(x)$ to be compared, despite their respective magnitudes not necessarily being equal. This allows the Lagrange multiplier method to find the minima and maxima of a function subject to constraints without having to explicitly solve the conditions.

For a waiting-time process, the lowest moment of the sample distribution, the sample mean, is applied as the constraint to achieve the most unbiased probability distribution (P_MaxEnt). In

this study specifically, the sample mean is equal to the mean of PS lifetimes or PS inter-formation event times for each AF epoch. As probabilities must always sum to 1, a normalization constraint must also be applied. Therefore, we must find P_MaxEnt such that:

- P_MaxEnt satisfies the constraint on the average sample mean
- P_MaxEnt satisfies the normalisation constraint
- P_MaxEnt has the maximum entropy

Mathematically, such a distribution can be found by setting the gradient of the function to equal a linear combination of the gradients of the constraints:

$$\frac{\partial f}{\partial p_x} = \lambda_1 \frac{\partial g_1}{\partial p_x} + \lambda_2 \frac{\partial g_2}{\partial p_x} \tag{H.3}$$

where $f(x)$ is the entropy function and $g_1(x)$ is the expectation of X (sample mean)

$$g_1(x) = E[X] \tag{H.4a}$$
$$= \sum x.p_x \tag{H.4b}$$
$$= \langle w \rangle \tag{H.4c}$$

Where $\langle w \rangle$ can be estimated by the sample mean. Further:

$$\frac{\partial g_1}{\partial p_x} = x \tag{H.5}$$

and $g_2(x)$ the normalization constraint:

$$g_2(x) = \sum p_x \tag{H.6a}$$
$$= 1 \tag{H.6b}$$
$$\frac{\partial g_2}{\partial p_x} = 1 \tag{H.6c}$$

Therefore, solving equation (1) gives the P_MaxEnt of PS lifetimes and PS inter-formation event times. This can be achieved by following the steps as outlined below. First, To find $\frac{\partial f}{\partial p_x}$, we use the chain rule:

$$f(x) = -\sum_{x=0}^{\infty} (p_x) log(p_x) \tag{H.7a}$$
$$\frac{\partial f}{\partial p_x} = -log(p_x) + p_x . \frac{1}{p_x} \tag{H.7b}$$

Substituting into equation 1

$$-log(p_x) + 1 = \lambda_1(x) + \lambda_2(1) \tag{H.8a}$$

$$-log(p_x) + 1 = \lambda_1(x) + \lambda_2 \tag{H.8b}$$

1. Solving for p_x

$$p_x = e^{-1-_1x-\lambda_2} \tag{H.9a}$$

$$= e^{-1-_1x}.e^{-\lambda_2+1} \tag{H.9b}$$

$$p_x = \frac{e^{-\lambda_1 x}}{Z} \tag{H.9c}$$

$$where\ Z = e^{1+\lambda_2} \tag{H.9d}$$

As we can see, the functional form of P_MaxEnt gives an exponential distribution. As a result, solving for λ_1 will give the predicted exponential decay constant of the distribution, and in turn the predicted PS destruction and formation rate. This was used to compare with the observed λ from the experimental data. To solve for λ, we must solve for Z:

2. Plugging in constraint g_2 (normalization constraint) into equation H.9d gives:

$$\frac{1}{Z}\sum_{0}^{\infty} e^{-\lambda_1 x} = 1 \tag{H.10a}$$

$$Z = \sum_{o}^{\infty} e^{-\lambda_1 x} \tag{H.10b}$$

Using geometric series expansion:

$$1 + e^{-\lambda_1} + e^{-2\lambda_1+\ldots} \tag{H.11a}$$

$$Z = \frac{1}{1 - e^{-\lambda_1}} \tag{H.11b}$$

$$\frac{\partial Z}{\partial \lambda_1} = \frac{e^{-\lambda_1}}{(1 - e^{-\lambda_1})^2} \tag{H.11c}$$

3. Plugging in constraint and g_1 (sample mean constraint) into equation H.9d gives:

$$g_1(x) = \sum x.p_x \tag{H.12a}$$
$$= \sum x \frac{e^{-\lambda_1 x}}{Z} \tag{H.12b}$$
$$= \frac{1}{Z} \sum_0^\infty x e^{-\lambda_1 x} \tag{H.12c}$$
$$= \langle w \rangle \tag{H.12d}$$

4. To help solve for equation H.12b, we take the derivative of Z (equation H.10b):

$$\frac{\partial_Z}{\partial \lambda_1} = \sum_0^\infty x e^{-\lambda_1 x} \tag{H.13}$$

5. Therefore we can re-write the first constraint equation H.12b as:

$$g_1(x) = \frac{1}{Z} \sum_0^\infty x e^{-\lambda_1 x} \tag{H.14a}$$
$$= \frac{1}{Z} * \frac{-\partial Z}{\partial \lambda_1} \tag{H.14b}$$
$$= \langle w \rangle \tag{H.14c}$$
$$\frac{1}{Z} \frac{\partial Z}{\partial \lambda_1} = \frac{(1 - e{-}^{\lambda_1})}{1} * \frac{e{-}^{\lambda)1}}{(1 - e^{-\lambda_1})^2} \tag{H.14d}$$
$$\frac{e^{-}\lambda_1}{1 - e^{-}\lambda_1} \tag{H.14e}$$
$$= \langle w \rangle \tag{H.14f}$$
$$\tag{H.14g}$$

Solving for equation H.14c will therefore give l_1 and in turn the PS destruction or formation rate.

Supplement I

Renewal Process Models

We model PS destruction and formation as renewal processes. For PS destruction, we measured the waiting times for an existing PS to be destroyed, and for PS formation, we studied the waiting times between the creation of new phase singularities. PS lifetime and inter-formation event times are random variables generated according to an exponential distribution, under the rate parameter λ. The probability density function for the all PS lifetimes or inter-formation times is thus given by:

$$f(t) = \lambda e^{\lambda t} \tag{I.1}$$

where t is time, and λ the PS destruction or formation rate, differentiated in this study using the terms λ_d and λ_f respectively.

I.1 Non-linear Least Squares Data Fitting

Parameter fitting to the exponential distribution was first completed using non-linear least squares on the probability distribution function (PDF) for each case. PDFs were generated by binning PS lifetime and inter-formation time data to form normalized histograms. Data fitting was performed in Matlab, and the fitting options selected include the Trust-Region Algorithm, with minimum difference change 1.0E-8, and maximum iterations set to 400. The r-squared (R2) value was used to determine the adequacy of fit.

I.2 Maximum Likelihood Data Fitting

As a comparison to an alternative data fitting approach, PS data was also fitted using maximum likelihood. For continuous data, a histogram can throw away information and fitting dependent on the choice of bin edges and bin widths. Maximum likelihood does not suffer from these problems, and as such was used as a comparative approach. Data fitting was performed in Matlab, using the probability density function (PDF) of each case. The chi-squared ($\chi 2$) good-ness of fit test was used to assess the adequacy of fit, which uses the null hypothesis that the data evaluated comes from an exponential distribution.

I.3 Data fitting results

To assess the adequacy of fit, we evaluated the R^2, sum of squares error (SSE), degrees of freedom error (DFE) and the standard error (RMSE) using non-linear least squares fitting. For the maximum likelihood approach, we determined the chi-squared (χ^2) goodness-of-fit p-value, with $p < 0.05$ indicating that the null hypothesis is rejected and the data does not fit with the tested distribution.

Table I.1: Destruction Process in Human Persistent AF

CASE	λ_d	$1/\lambda_d$	**R^2**	**SSE**	**DFE**	**RMSE**	χ^2 **p-value**
1	-0.0410	-24.3780	0.9794	0.0009	155	0.0024	0.14
2	-0.0358	-27.9177	0.9023	0.0013	167	0.0028	0.92
3	-0.0362	-27.6473	0.9284	0.0005	216	0.0015	0.21
4	-0.0448	-22.3211	0.9100	0.0007	186	0.0019	0.32
5	-0.0451	-22.1816	0.9180	0.0006	169	0.0019	0.08
6	-0.0511	-19.5678	0.9554	0.0004	171	0.0016	0.09
7	-0.0523	-19.1335	0.9215	0.0007	175	0.0019	0.31
8	-0.0369	-27.0865	0.9484	0.0004	214	0.0013	0.45
9	-0.0455	-21.9864	0.9663	0.0003	219	0.0011	0.24
10	-0.0753	-13.2727	0.9639	0.0013	129	0.0031	0.92
11	-0.0522	-19.1610	0.9878	0.0010	126	0.0028	0.27
12	-0.0681	-14.6820	0.9579	0.0014	142	0.0032	0.77
13	-0.0506	-19.7622	0.9438	0.0019	95	0.0045	0.19
14	-0.0388	-25.7533	0.9444	0.0017	132	0.0036	0.29
15	-0.0423	-23.6537	0.9689	0.0002	225	0.0011	0.09
16	-0.0370	-27.0051	0.9091	0.0006	186	0.0019	0.58
17	-0.0311	-32.1554	0.9977	0.0015	108	0.0037	0.68
18	-0.0322	-31.0795	0.9364	0.0011	110	0.0032	0.55
19	-0.0507	-19.7213	0.9373	0.0006	187	0.0017	0.43
20	-0.0381	-26.2146	0.9083	0.0006	177	0.0019	0.64
21	-0.0431	-23.2038	0.9900	0.0007	159	0.0022	0.65
22	-0.0595	-16.8024	0.9852	0.0015	121	0.0035	0.68
23	-0.0381	-26.2131	0.9822	0.0001	280	0.0007	0.64
24	-0.0390	-25.6334	0.9165	0.0006	181	0.0018	0.95
25	-0.0435	-23.0031	0.9196	0.0006	167	0.0019	0.21
26	-0.0316	-31.6781	0.9152	0.0005	225	0.0016	0.71
27	-0.0339	-29.4629	0.9839	0.0009	164	0.0024	0.24
28	-0.0436	-22.9554	0.8927	0.0012	112	0.0033	0.12
29	-0.0504	-19.8610	0.9335	0.0006	167	0.0019	0.61
30	-0.0556	-17.9914	0.9698	0.0012	119	0.0031	0.45
31	-0.0637	-15.7036	0.9166	0.0009	129	0.0026	0.46
32	-0.0497	-20.1090	0.9147	0.0008	160	0.0022	0.66
33	-0.0552	-18.1207	0.9096	0.0008	146	0.0024	0.77
34	-0.0429	-23.3163	0.9876	0.0008	159	0.0023	0.35
35	-0.0530	-18.8568	0.9190	0.0010	153	0.0025	0.66

Table I.2: Destruction Process Sheep AF

CASE	λ_d	$1/\lambda_d$	**R^2**	**SSE**	**DFE**	**RMSE**	χ^2 **p-value**
1	-0.0579	-17.2641	0.9768	0.0013	152	0.00288	0.77
2	-0.0432	-23.1674	0.9256	0.0006	173	0.00182	0.40
3	-0.0409	-24.4553	0.9899	0.0007	176	0.00204	0.81
4	-0.0438	-22.8181	0.9373	0.0005	184	0.00166	0.76
5	-0.0461	-21.6732	0.9067	0.0008	185	0.00205	0.38
6	-0.0448	-22.3027	0.9389	0.0005	183	0.00164	0.22
7	-0.0503	-19.8749	0.9169	0.0015	122	0.00346	0.79
8	-0.0515	-19.4243	0.9267	0.0016	137	0.00339	0.95
9	-0.0459	-21.7629	0.9053	0.0015	144	0.00324	0.33
10	-0.0497	-20.1324	0.9405	0.0013	164	0.00285	0.67
11	-0.0425	-23.5366	0.9556	0.0012	157	0.00271	0.44
12	-0.0454	-22.041	0.9375	0.0012	165	0.00271	0.83
13	-0.0419	-23.8595	0.9546	0.0011	183	0.00242	0.77
14	-0.0360	-27.8098	0.9551	0.0009	192	0.00218	0.17
15	-0.0411	-24.3285	0.9793	0.0014	200	0.00265	0.86
16	-0.0368	-27.1747	0.9763	0.0008	159	0.00227	0.99
17	-0.0368	-27.1681	0.9402	0.0011	156	0.00263	0.51
18	-0.0342	-29.229	0.9550	0.0009	165	0.00233	0.88

Table I.3: Destruction Process Rat AF

CASE	λ_d	$\mathbf{1}/\lambda_d$	**R^2**	**SSE**	**DFE**	**RSME**
1	0.39464	2.53397	0.920077	0.001655	19	0.015156
2	0.32009	3.12408	0.906601	0.001161	24	0.014547
3	0.45308	-2.2071	0.910141	0.001666	25	0.014645
4	NO PS					

Table I.4: Destruction Process in Rat VF

CASE	λ_d	$\mathbf{1}/\lambda_d$	**R^2**	**SSE**	**DFE**	**RSME**
1	-0.616976139	1.62081	0.925768	0.005767	16	0.018985
2	-0.762581075	1.31134	0.965581	0.003513	23	0.012359
3	-0.499943945	2.00022	0.935486	0.004449	27	0.012837
4	-0.392332499	2.54886	0.952071	0.025498	18	0.037637
5	-0.386703801	2.58596	0.915747	0.008958	17	0.022955
6	-0.393236373	-2.543	0.949446	0.007835	18	0.020863
7	-0.571397065	-1.7501	0.92278	0.020703	11	0.043383
8	-0.791982816	1.26265	0.938596	0.011686	12	0.031207
9	-0.099075603	10.0933	0.921393	0.021087	13	0.040275
10	-0.263687202	3.79237	0.965384	0.01155	18	0.025331
11	-0.251567598	3.97507	0.96888	0.009258	19	0.022075

Table I.5: Formation Process in Human AF

CASE	λ_f	$1/\lambda_f$	R^2	SSE	DFE	RMSE	^{2} P-VALUE
1	-0.0324	-23.601	0.9798	0.0009	260	0.0019	0.26
2	-0.0440	-18.526	0.9291	0.0011	187	0.0025	0.32
3	-0.0277	-26.529	0.9545	0.0007	343	0.0014	0.12
4	-0.0396	-20.145	0.9001	0.0006	226	0.0016	0.94
5	-0.0423	-19.116	0.9476	0.0010	273	0.0019	0.65
6	-0.0342	-22.615	0.9041	0.0005	378	0.0011	0.48
7	-0.0416	-19.381	0.9599	0.0009	227	0.0020	0.64
8	-0.0437	-18.623	0.9381	0.0005	260	0.0013	0.54
9	-0.0425	-19.040	0.9411	0.0004	307	0.0012	0.65
10	-0.0475	-17.405	0.9168	0.0009	374	0.0016	0.54
11	-0.0301	-24.912	0.9327	0.0011	292	0.0020	0.72
12	-0.0312	-24.285	0.9566	0.0010	310	0.0018	0.52
13	-0.0496	-16.784	0.9302	0.0017	203	0.0029	0.99
14	-0.0279	-26.377	0.9576	0.0010	195	0.0022	0.22
15	-0.0287	-25.856	0.9296	0.0003	361	0.0010	0.11
16	-0.0285	-26.004	0.9425	0.0005	274	0.0014	0.11
17	-0.0536	-15.735	0.6165	0.0017	338	0.0023	0.06
18	-0.0653	-13.279	0.9074	0.0011	367	0.0017	0.40
19	-0.0107	-48.242	0.9071	0.0039	20	0.0139	0.45
20	-0.0383	-20.690	0.9793	0.0007	246	0.0017	0.37
21	-0.0415	-19.431	0.9661	0.0008	266	0.0017	0.76
22	-0.0297	-25.165	0.9647	0.0012	333	0.0019	0.63
23	-0.0107	-48.265	0.9501	0.0057	50	0.0107	0.77
24	-0.0328	-23.362	0.9329	0.0006	269	0.0015	0.93
25	-0.0345	-22.487	0.9374	0.0006	267	0.0015	0.97
26	-0.0358	-21.812	0.9415	0.0006	223	0.0017	0.19
27	-0.0379	-20.872	0.9184	0.0011	205	0.0023	0.14
28	-0.0231	-30.232	0.9157	0.0019	216	0.0030	0.70
29	-0.0466	-17.676	0.9889	0.0007	306	0.0015	0.09
30	-0.0489	-16.974	0.9689	0.0019	196	0.0031	0.53
31	-0.0466	-17.675	0.9468	0.0009	281	0.0018	0.53
32	-0.0451	-18.140	0.9899	0.0007	284	0.0015	0.86
33	-0.0376	-21.004	0.9074	0.0010	323	0.0017	0.48
34	-0.0126	-44.284	0.9577	0.0008	310	0.0016	0.39
35	-0.0323	-23.613	0.9782	0.0009	319	0.0017	0.67

Table I.6: Formation Process in Sheep AF

CASE	λ_f	$1/\lambda_f$	**R^2**	**SSE**	**DFE**	**RMSE**	χ^2 **p-value**
-0.0473	-21.1452	0.9333	0.0010	233	0.0020	0.24	
2	-0.0487	-20.5526	0.9851	0.0007	197	0.0019	0.44
3	-0.0459	-21.7789	0.9662	0.0007	200	0.0019	0.69
4	-0.0552	-18.1025	0.9297	0.0005	176	0.0017	0.36
5	-0.0552	-18.1040	0.9135	0.0006	179	0.0019	0.74
6	-0.0550	-18.1693	0.9889	0.0008	167	0.0022	0.39
7	-0.0367	-27.2372	0.9264	0.0014	250	0.0024	0.68
8	-0.0491	-20.3860	0.9733	0.0012	257	0.0022	0.70
9	-0.0442	-22.6277	0.9121	0.0014	251	0.0023	0.44
10	-0.0456	-21.9182	0.9106	0.0010	237	0.0021	0.09
11	-0.0467	-21.4319	0.9203	0.0010	249	0.0020	0.33
12	-0.0407	-24.5926	0.9740	0.0010	250	0.0020	0.42
13	-0.0434	-23.0544	0.9788	0.0011	235	0.0022	0.27
14	-0.0458	-21.8345	0.9385	0.0008	247	0.0018	0.20
15	-0.0456	-21.9338	0.9455	0.0014	238	0.0024	0.82
16	-0.0400	-24.9770	0.9153	0.0009	228	0.0020	0.43
17	-0.0372	-26.8711	0.9783	0.0010	231	0.0020	0.89
18	-0.0381	-26.2718	0.9788	0.0010	233	0.0020	0.39

Table I.7: Formation Process in Rat AF

CASE	λ_f	$\mathbf{1}/\lambda_f$	**R^2**	**SSE**	**DFE**	**RSME**
1	0.419942	2.381283	0.942991	0.001655	17	0.005932
2	0.243807	4.101607	0.931647	0.001161	19	0.00598
3	0.315868	3.165879	0.94344	0.001666	8	0.00343
4			NO PS			

Table I.8: Formation Process in Rat VF

CASE	λ_f	$\mathbf{1}/\lambda_f$	$\mathbf{R}^2$	**SSE**	**DFE**	**RSME**
1	0.654083648	1.528856	0.911355	0.001497	30	0.007063
2	0.630159282	1.5869	0.970007	0.002665	26	0.010125
3	0.130750854	7.648134	0.939085	0.001106	20	0.007438
4	0.465554173	2.147978	0.960541	0.001834	39	0.006858
5	0.359369029	2.782655	0.904757	0.003788	30	0.011236
6	0.195596497	5.112566	0.95903	0.008241	33	0.015803
7	0.219044658	4.565279	0.986648	0.004465	29	0.012409
8	0.113454978	8.814069	0.995203	0.014203	22	0.025408
9	0.863465002	1.158125	0.917717	0.018902	20	0.030743
10	0.280973897	3.559049	0.987404	0.004937	33	0.012231
11	0.310418765	3.221455	0.911724	0.002504	37	0.008226

Supplement J

Correlogram plots

J.1 Correlogram of PS lifetimes

Correlograms for PS lifetimes in all human persistent AF epochs (n = 43) are provided on the following pages.

Correlograms provide a visual representation of the autocorrelation (the cross-correlation between a variable and itself) over various lags. The correlograms below are calculated from a lag of 0 to 20 for PS lifetimes treated as an ordered time series.

In all correlograms, the highest autocorrelation (of 1) was found at lag 0 as the variable will have perfect autocorrelation with itself. However, as the variable is shifted in time, the autocorrelation is close to 0 for all lags.

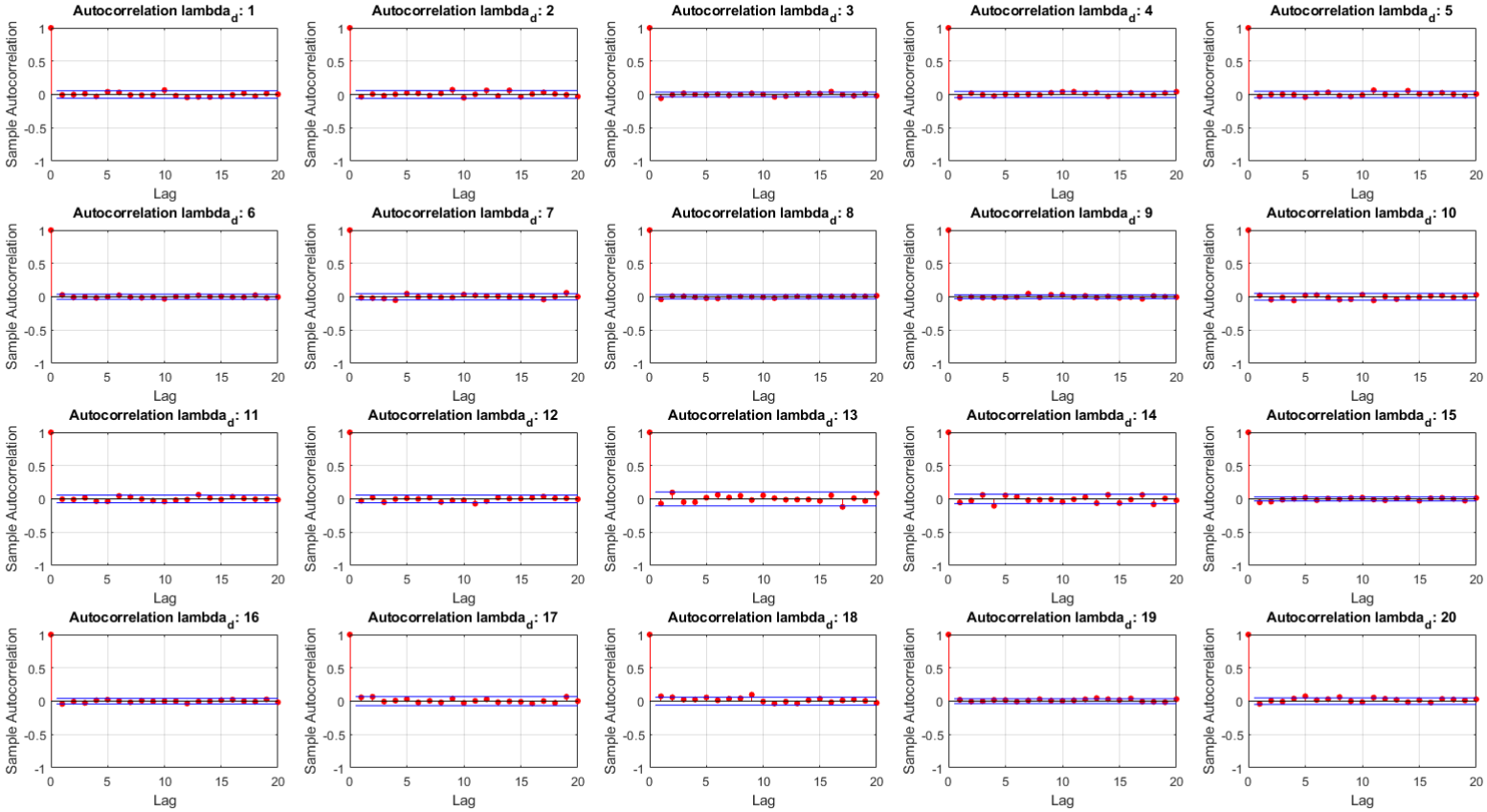
Autocorrelation lambda_d: 1
Autocorrelation lambda_d: 2
Autocorrelation lambda_d: 3
Autocorrelation lambda_d: 4
Autocorrelation lambda_d: 5
Autocorrelation lambda_d: 6
Autocorrelation lambda_d: 7
Autocorrelation lambda_d: 8
Autocorrelation lambda_d: 9
Autocorrelation lambda_d: 10
Autocorrelation lambda_d: 11
Autocorrelation lambda_d: 12
Autocorrelation lambda_d: 13
Autocorrelation lambda_d: 14
Autocorrelation lambda_d: 15
Autocorrelation lambda_d: 16
Autocorrelation lambda_d: 17
Autocorrelation lambda_d: 18
Autocorrelation lambda_d: 19
Autocorrelation lambda_d: 20
Sample Autocorrelation
Lag

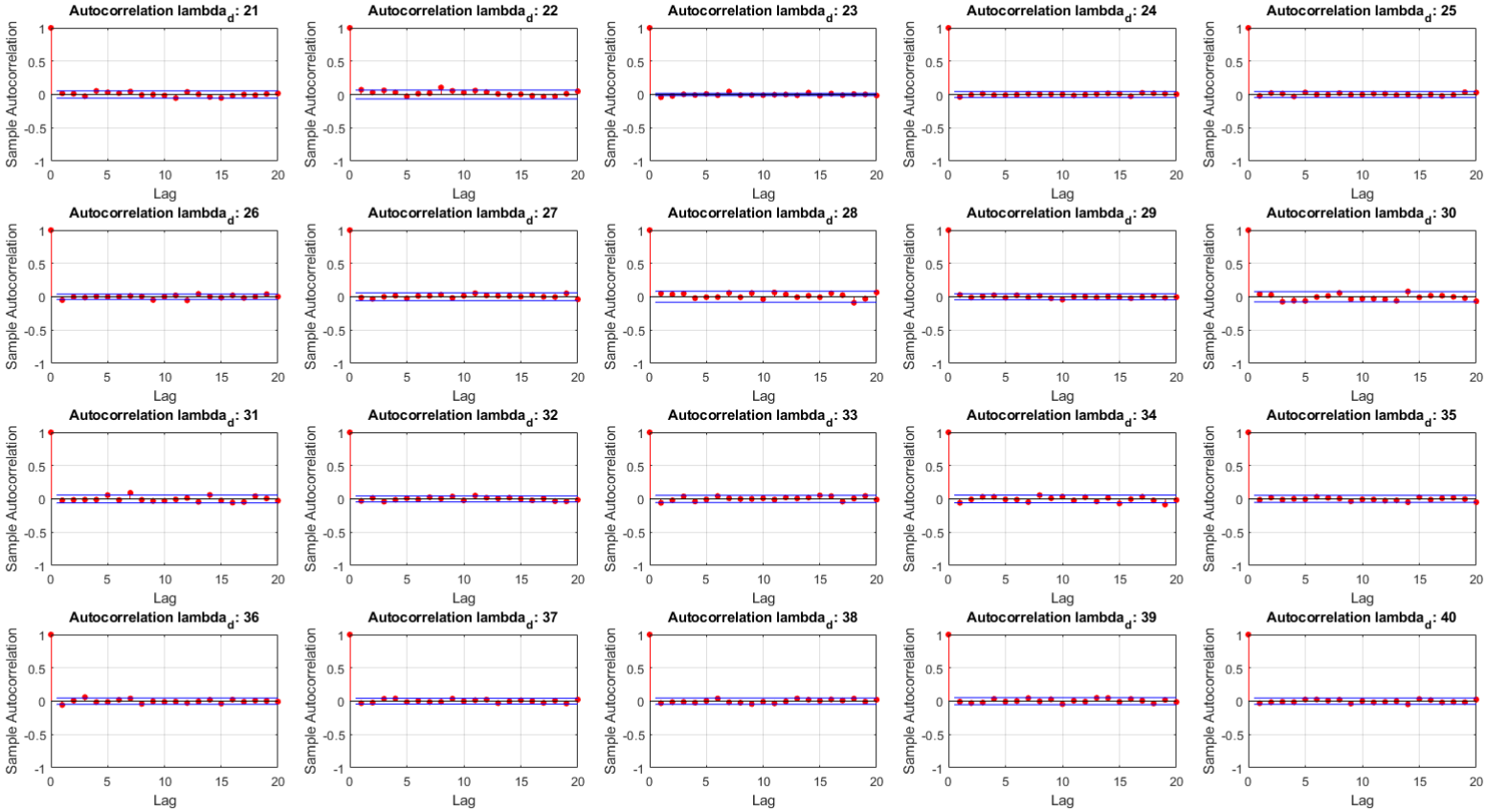
Autocorrelation lambda_d: 21
Autocorrelation lambda_d: 22
Autocorrelation lambda_d: 23
Autocorrelation lambda_d: 24
Autocorrelation lambda_d: 25
Autocorrelation lambda_d: 26
Autocorrelation lambda_d: 27
Autocorrelation lambda_d: 28
Autocorrelation lambda_d: 29
Autocorrelation lambda_d: 30
Autocorrelation lambda_d: 31
Autocorrelation lambda_d: 32
Autocorrelation lambda_d: 33
Autocorrelation lambda_d: 34
Autocorrelation lambda_d: 35
Autocorrelation lambda_d: 36
Autocorrelation lambda_d: 37
Autocorrelation lambda_d: 38
Autocorrelation lambda_d: 39
Autocorrelation lambda_d: 40
Sample Autocorrelation
Lag

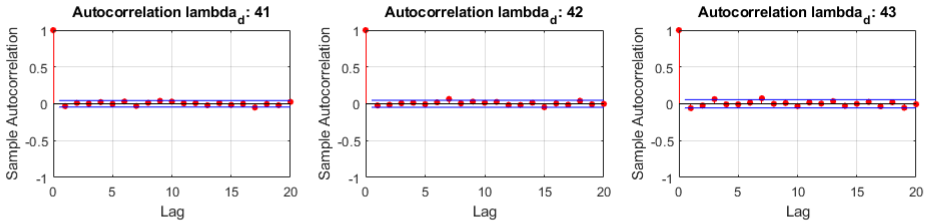
Autocorrelation lambda$_d$: 41
Autocorrelation lambda$_d$: 42
Autocorrelation lambda$_d$: 43
Sample Autocorrelation
Lag
1
0.5
0
-0.5
-1
0
5
10
15
20

J.2 Correlogram of PS formation times

Correlograms for PS inter-formation event times (or simply referred to as formation times) in all human persistent AF epochs (n = 43) are provided on the following pages.

Correlograms provide a visual representation of the autocorrelation (the cross-correlation between a variable and itself) over various lags. The correlograms below are calculated from a lag of 0 to 20 for PS formation-times treated as an ordered time series.

In all correlograms, the highest autocorrelation (of 1) was found at lag 0 as the variable will have perfect autocorrelation with itself. However, as the variable is shifted in time, the autocorrelation is close to 0 for all lags.

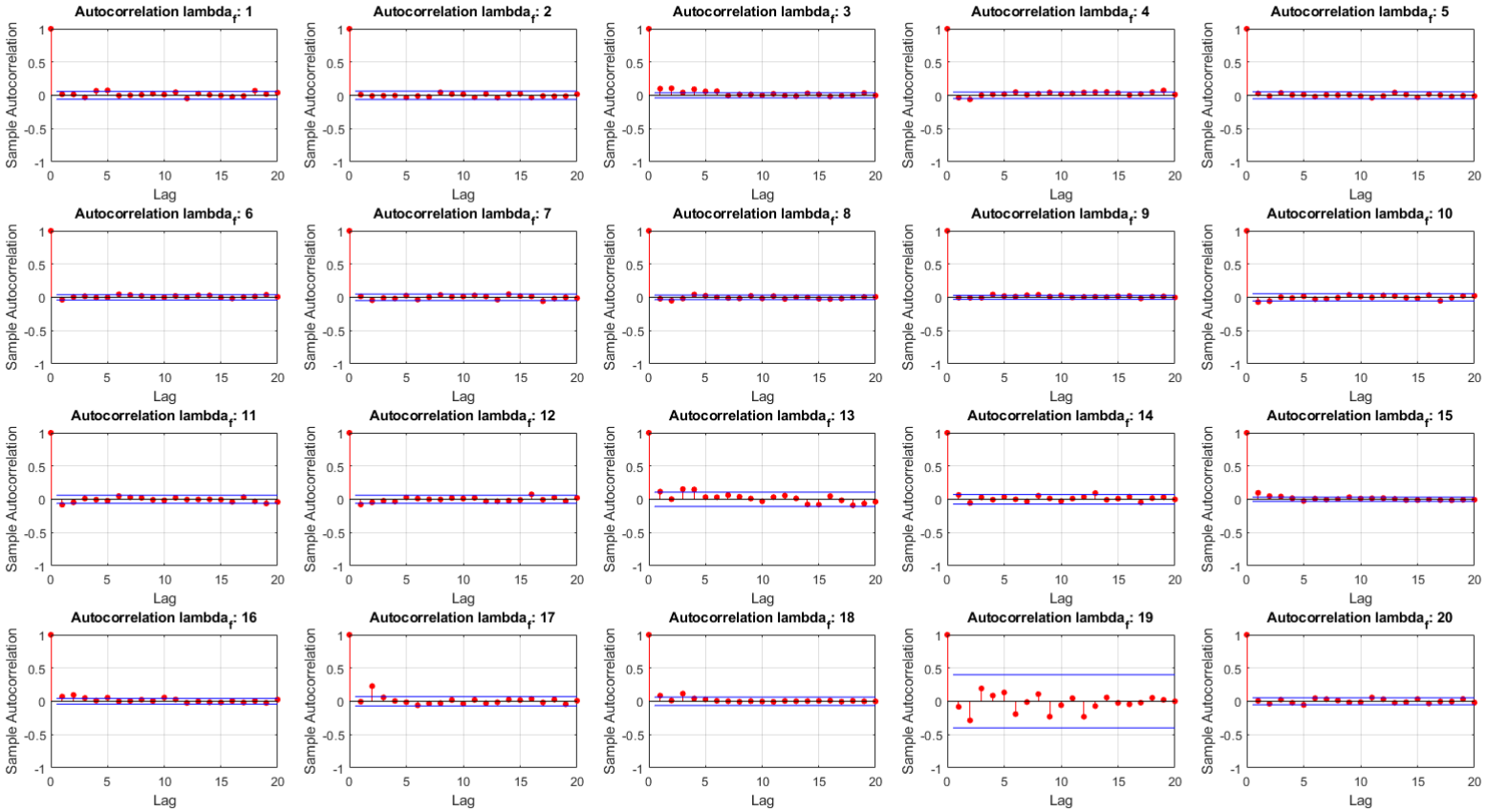
Autocorrelation lambda$_f$: 1
Autocorrelation lambda$_f$: 2
Autocorrelation lambda$_f$: 3
Autocorrelation lambda$_f$: 4
Autocorrelation lambda$_f$: 5
Autocorrelation lambda$_f$: 6
Autocorrelation lambda$_f$: 7
Autocorrelation lambda$_f$: 8
Autocorrelation lambda$_f$: 9
Autocorrelation lambda$_f$: 10
Autocorrelation lambda$_f$: 11
Autocorrelation lambda$_f$: 12
Autocorrelation lambda$_f$: 13
Autocorrelation lambda$_f$: 14
Autocorrelation lambda$_f$: 15
Autocorrelation lambda$_f$: 16
Autocorrelation lambda$_f$: 17
Autocorrelation lambda$_f$: 18
Autocorrelation lambda$_f$: 19
Autocorrelation lambda$_f$: 20
Sample Autocorrelation
Lag

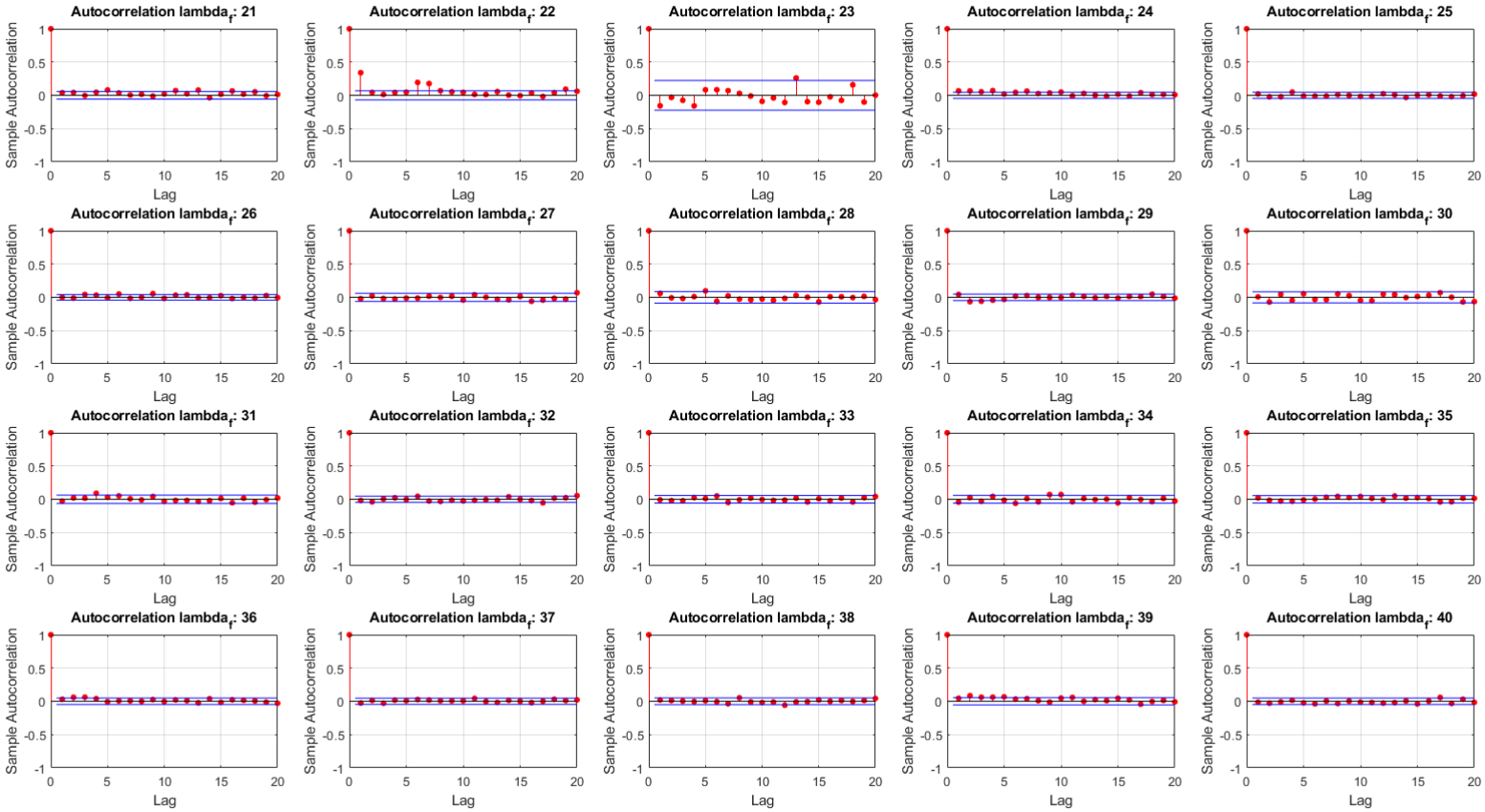
Autocorrelation lambda$_f$: 21
Autocorrelation lambda$_f$: 22
Autocorrelation lambda$_f$: 23
Autocorrelation lambda$_f$: 24
Autocorrelation lambda$_f$: 25
Autocorrelation lambda$_f$: 26
Autocorrelation lambda$_f$: 27
Autocorrelation lambda$_f$: 28
Autocorrelation lambda$_f$: 29
Autocorrelation lambda$_f$: 30
Autocorrelation lambda$_f$: 31
Autocorrelation lambda$_f$: 32
Autocorrelation lambda$_f$: 33
Autocorrelation lambda$_f$: 34
Autocorrelation lambda$_f$: 35
Autocorrelation lambda$_f$: 36
Autocorrelation lambda$_f$: 37
Autocorrelation lambda$_f$: 38
Autocorrelation lambda$_f$: 39
Autocorrelation lambda$_f$: 40
Sample Autocorrelation
Lag

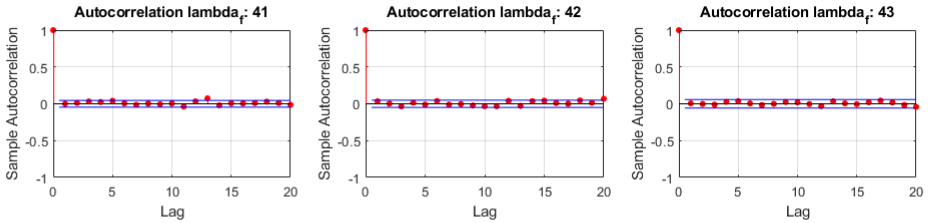
Autocorrelation lambda$_f$: 41
Autocorrelation lambda$_f$: 42
Autocorrelation lambda$_f$: 43
Sample Autocorrelation
Lag
1
0.5
0
-0.5
-1
0
5
10
15
20

Supplement K

Patient VF baseline characteristics- Part II

For the Markov birth-death study detailed in chapter 8 of this dissertation, patient baseline characteristics are as shown below in Table K.1.

Characteristics (patients n = 10)	
Age	70 ± 10
Gender	
Male	70% (7)
Female	3% (3)
Echocardiographic parameters	
EF (%)	66.10 ± 4.93
LVDd (cm^2)	3.88 ± 0.39
LVDs (cm^2)	3.58 ± 1.42
LVPWd (cm^2)	1.30 ± 0.14
IVSd (cm^2)	2.03 ± 0.85

Table K.1: Patient Baseline Characteristics

Part IV

Additional publications during candidature

Comparative spatial resolution of 12-lead electrocardiography and an automated algorithm

Comparative spatial resolution of 12-lead electrocardiography and an automated algorithm

Dhani Dharmaprani, BEng (Biomedical)(Hons),[*1] Anandaroop Lahiri, MD,[†1] Anand N. Ganesan, MBBS, PhD, FRACP,[*†‡] Nicole Kyriacou, BSc (Biomedical Science),[§] Andrew D. McGavigan, MBChB, MD, FRCP (Glas), FRACP, FCSANZ[*†]

*From the *Faculty of Medicine, Flinders University, Bedford Park, South Australia, Australia, †Department of Cardiology, Flinders Medical Centre, Bedford Park, South Australia, Australia, ‡South Australian Health and Medical Research Institute, Adelaide, South Australia, Australia, and §Biosense Webster (Clinical Specialist), Adelaide, South Australia, Australia.*

BACKGROUND The spatial resolution of pacemapping using 12-lead electrocardiography (ECG) or PaSo software is unknown.

OBJECTIVE The purpose of this study was to determine the spatial resolution of traditional ECG pacemapping and pacemapping using the PaSo coefficients.

METHODS Seventeen patients undergoing ablation of supraventricular tachycardias or atrioventricular node were included. After ablation, chamber (right ventricular outflow tract/rest of the right ventricle/left ventricle) geometry was created with Carto 3. Pacing was performed from any point in these cardiac regions, the QRS morphology being the template and the point being considered as arrhythmia "origin." Subsequently, pacing was performed from points around the "origin" (1538 points). The QRS of these tagged points were compared by traditional ECG pacemapping and PaSo coefficients. The spatial resolution was calculated using correlations between the distance away from the origin (measured by 3 computational methods) and traditional ECG pacemapping and PaSo coefficients, independently.

RESULTS A 0.01-unit decrease in the PaSo coefficient resulted in 1.1 mm increased Cartesian distance (95% confidence interval [CI] 0.9–1.3 mm; $P < .001$) and 2.4 mm increased geodesic distance (95% CI 1.9–2.9 mm; $P < .001$) and 664 mm^3 increase in convex hull volume (95% CI 423–906 mm^3; $P < .0001$). For traditional ECG pacemapping, each decrease in lead match resulted in 1.7 mm increased Cartesian distance (95% CI 1.5–2.0 mm; $P < .001$) and 3.4 mm increased geodesic distance (95% CI 2.8–4.1 mm; $P < .001$) and 712 mm^3 increase in convex hull volume (95% CI 599–830 mm^3; $P < .0001$). Both PaSo coefficients and traditional pacemapping showed a significant inverse linear correlation with distance from the "origin."

CONCLUSION The resolution of mapping using the Paso software is better than that of traditional pacemapping.

KEYWORDS Automated algorithm; ECG; Pacemapping; Spatial resolution; Ventricular ectopy

(Heart Rhythm 2019;■:1–8)

Introduction

Pacemapping, where endocardial sites are stimulated to reproduce the QRS morphology of the clinical ventricular arrhythmia (VA), has been used to ablate focal VAs[1] and identify the exit sites of reentrant ventricular tachycardia.[2] It is especially useful in poorly tolerated VAs or where ventricular ectopy (VE) occurs at low frequency.[3]

Traditionally, pacemapping has examined each lead of the 12-lead electrocardiogram (ECG) scoring the paced QRS morphology in a binary fashion (0 or 1) as identical or not identical to the QRS morphology of the VA. Summed lead scores give a pace-match score out of 12, with 12/12 being considered a perfect pace map and 11/12 and 10/12 being considered modest matches.

The clinical utility and accuracy of pacemapping to guide ablation depend on its spatial resolution. Although this will be influenced by areas of fixed or dynamic conduction block,[4] researchers have reported a resolution of 18 ± 6 mm in the structurally normal heart for bipolar recordings.[5,6] Unipolar pacemapping has been less well studied with respect to spatial resolution, with a resolution of 5–10 mm.[7] However, a significant limitation is that ECG morphology was classified qualitatively as having minor or major differences rather than semiquantitative ECG scoring. Man et al[8] also reported a 17–32 mm resolution of unipolar atrial pacing. However, in the electrophysiology laboratory, bipolar stimulation is the most common pacing stimulation protocol.

Recently, quantitative morphology matching software has become commercially available (PaSo software, Carto 3,

This research was conducted with support from the investigator-initiated study program of Biosense Webster, Inc. Ms Kyriacou is an employee of Biosense Webster, which has designed the PaSo software. The rest of the authors report no conflicts of interest. [1]Ms Dharmaprani and Dr Lahiri are joint first authors. **Address reprint requests and correspondence:** Dr Andrew D. McGavigan, Department of Cardiology, Flinders Medical Centre, Flinders Dr, Bedford Park, SA 5042, Australia. E-mail address: Andrew.McGavigan@sa.gov.au.

1547-5271/$-see front matter https://doi.org/10.1016/j.hrthm.2019.08.029

Biosense Webster, Diamond Bar, CA), producing a correlation coefficient for the degree of match. To our knowledge, there are no published data on the spatial resolution of this technology and its relation to traditional qualitative pacemapping.

Furthermore, previous studies examining the spatial resolution of traditional pacemapping have used a simple Cartesian method, where the distance between 2 points producing identical pace maps is simply calculated by measuring the shortest straight line connecting the points.[5,6] However, this may not be the most appropriate method for examining spatial resolution within a 3-dimensional (3D) structure.[9,10]

In this study, we characterize the spatial resolution of quantitative morphology mapping using the PaSo software in comparison to traditional qualitative pacemapping using binary scoring for each lead. In addition, we explore the use of validated computational geometric methods in a novel way to improve the quantification of spatial accuracy in pacemapping.

Methods

Study population

Seventeen patients undergoing electrophysiology study and ablation for supraventricular tachycardia or undergoing ablation of the atrioventricular node were recruited. All patients had a normal echocardiogram. All patients provided written consent, and the study was approved by the institutional review board.

Mapping protocol

Electrophysiology studies were performed under general anesthesia using the Bard system (Boston Scientific, Fremont, CA) with a decapolar catheter in the coronary sinus and quadripolar catheters at the His Bundle and right ventricular apex. Standard ablation protocols were followed in all patients.

After ablation, a virtual geometry of the chamber of interest was created using a NaviStar catheter and the Carto 3 system (Biosense Webster, Diamond Bar, CA). A random site was selected within this allocated geometry and was paced at a drive train of 400 ms with an output just above the threshold to minimize the capture of the surrounding myocardium.[11] The site was tagged as the "origin" and the subsequent paced template used in the Bard and Carto systems. Thereafter, a minimum of 50 pace maps were acquired serially in different regions of the same chamber in a random fashion, pacing at just above the threshold. While acquiring these pace-map sites (both with PaSo matching and with conventional 12-lead ECG matching), pacing was performed at identical cycle lengths of 400 ms to minimize QRS morphology variations.[12]

PaSo correlation pacemapping

Quantitative correlation to an ECG template was assessed with the PaSo module in real time. Once a site was tagged as the "origin" by pacing, in the PaSo module this paced ECG template was taken as the reference induced signal (IS). For each captured IS in the PaSo module, 62.5 seconds for all body surface ECG leads are recorded: 2.5 seconds after acquisition are used for correlation calculation and 60 seconds before acquisition serve as an ECG buffer. After recording an IS, the PaSo module automatically sets the morphology of interest (MOI) at a fixed width of ±150 ms. The MOI is set around the first peak of the last 2.5 seconds of the lead II channel. The MOI window was manually changed if required to bracket the QRS complex. Pace mapped (PM) signals are always associated with a selected point in a Carto 3 map. When a PM is captured, 10 seconds are recorded for all body surface leads: 2.5 seconds after the acquisition and 7.5 seconds before the acquisition. An active interval of 2.5 seconds is used for calculating the correlation coefficient by PaSo. By default, the active interval is the last 2.5 seconds of the PM; however, the active interval was moved as required to any part of the captured signal. Each PM is automatically compared with the reference IS. When comparing 2 sets of signals, the PaSo module provides the correlation value of each lead in 1 signal set (PM) with the corresponding lead in the other set (reference IS). The average correlation is calculated by summing these values and dividing the sum by the number of leads (12) to generate the correlation coefficient. The 3D geometry was exported from Carto 3, along with the triangulated mesh view and PaSo correlation coefficient values. The ACCURESP software (Biosense Webster) was used when collecting points to make sure that we were taking each point only at end expiration to eliminate catheter location movement that occurs during inspiration.

Traditional ECG pacemapping

A simultaneous traditional pace map was created in real time using the same paced ECG data. To replicate the process of ECG annotation under clinical conditions, the observer was blinded to PaSo data, geometry, and fluoroscopy and scored the ECG match in real time. Pace maps were annotated conventionally from scores ranging from 0/12 to 12/12. They were displayed as timing points on the Carto geometry (12/12 = −120 ms, 11/12 = −110 ms, 10/12 = −100 ms, etc). The 3D geometry was exported from Carto 3, along with the triangulated mesh view and activation times representing the degree of the match on the pace map.

Spatial resolution of pacemapping

The spatial resolution of pacemapping using the Carto 3 system was quantified using 3 computational geometric measures implemented in a custom software environment developed in MATLAB (The MathWorks, Natick, MA). Namely, these measures were as follows: (1) the Cartesian distance across the Carto 3 3D mesh; (2) the geodesic distance across the Carto 3 3D mesh, computed with a novel greedy algorithm based on Dijkstra's theorem[9]; and (3) the spatial volume occupied by the convex hull of the 3D point cloud of pace maps. Statistical analysis using multilevel linear mixed models was performed to give a measure of spatial resolution. For comparison, the spatial resolution of traditional ECG matching was also

quantified using the same 3 measures and statistical approaches. The methodology used for each computational geometric measure, as well as the statistical analysis, is further described in the following sections.

Cartesian distance

The Cartesian or Euclidean distance measures the straight-line distance between 2 points on a Euclidean plane. If 2 given points are on a Cartesian coordinate system with the coordinates (x_1, y_1, z_1) and (x_2, y_2, z_2), respectively, then the 3D distance between these points can be calculated using the following distance formula:

$$\text{Distance} = \sqrt{(x_2-x_1)^2+ (y_2-y_1)^2+ (z_2-z_1)^2}$$

Using the Carto 3 3D geometry exported for each patient, which specifies the 3D coordinates of the primary template point and pace maps, the relative Cartesian distance between the template and each pace map was calculated, as illustrated in Figure 1. It will be noted that these distances are given in millimeters. As such, a Cartesian distance was obtained for each of the pace maps for each patient. The computed Cartesian distances were later used in statistical analysis to allow the computation of spatial accuracy.

Geodesic distance

Geodesic distance measures the shortest path between 2 vertices or nodes. Specifically, the implemented algorithm used a novel greedy approach based on Dijkstra's theorem[9] to find the shortest path from the template point to each pace map, using the Carto 3 3D geometry and triangulated mesh of each patient. Like computation of the Cartesian distances, 3D coordinates of the template point and pace maps were extracted from the Carto 3 3D geometry. Vertices and edges of the triangulated 3D mesh were exported from Carto 3 to calculate the distances (in millimeters) of all possible paths along the mesh, from the template to the pace map as shown in Figure 1. The shortest of these distances was assigned as the geodesic distance. In effect, this method takes into consideration the curvature of the 3D mesh when compared to the Cartesian distance, as shown in Figure 1. The geodesic distances were later used in statistical analysis for the computation of spatial accuracy.

Convex hull volume

The convex hull, also known as the convex envelope, determines the smallest convex set that contains a set of points in a Euclidean space.[10] The convex hull volume is the volume within the point cloud that contains all sites with the same value whether expressed as PaSo correlation match or conventional 12-lead ECG pace-map match (Figure 1). Using pace-map coordinates provided by the 3D geometries exported from Carto 3, the boundary of the convex hull containing pace maps associated with PaSo correlation coefficients ranging from 0.85 to 1 was computed, in increments of 0.01. The convex hull associated with the number of lead matches out of 12 was also computed, incrementing from 4/12 to 12/12 matches. The corresponding volume of the 3D point cloud bounded by the convex envelope was then computed in MATLAB. Convex hull volumes were later used in statistical analysis for the computation of spatial accuracy.

Statistical analysis

Multilevel linear mixed models were used to analyze the relationships between the PaSo correlation coefficient and the Cartesian distance, geodesic distance, and convex hull volume. Specifically, a fixed effects estimate was used to measure the change in convex hull volume, Cartesian distance, and geodesic distance for every unit decrease in the PaSo correlation coefficient value, which in turn gave a measure of spatial resolution for the PaSo pacemapping technique. The patient was considered as a random effect in these models.

Similarly, the changes in distances and volume associated with a 1-lead decrease in matches were obtained using the same approaches, giving an estimate of spatial resolution for traditional ECG matching. SPSS version 23 (IBM Corporation, Armonk, NY) was used for statistical analysis, and a P value of $<.05$ was deemed to be significant.

Results

Baseline characteristics

Seventeen patients were included: 12 with supraventricular tachycardia (6 atrioventricular nodal reentry tachycardia [AVNRT], 5 atrioventricular reentry tachycardia [AVRT], and 1 cristal atrial tachycardia), 3 with typical atrial flutter, and 2 undergoing atrioventricular node ablation. Clinical mapping data were acquired in all (1538 points; mean 90.47 $\pm$ 19.125 points per patient; range 48–106 points per patient) during the waiting period after ablation. In 14 patients, the right ventricle was accessed with random allocation for mapping the right ventricular outflow tract or other portions of the right ventricle (7 in each group). In 3 patients, the clinical arrhythmia was AVRT using a left-sided accessory pathway; so the left ventricle, which could be accessed antegradely through the existing transseptal puncture, was mapped.

PaSo mapping

Decreasing PaSo coefficients demonstrated an inverse linear relationship with all 3 methods: Cartesian distances, geodesic distances, and convex hull volumes, as shown in Figure 2. Using linear mixed models (refer to Table 1), it was found that a 0.01-unit decrease in the PaSo correlation coefficient value resulted in a 1.1 mm increased Cartesian distance (95% confidence interval [CI] 0.9–1.3 mm; $P < .001$) and a 2.4 mm increased geodesic distance (95% CI 1.9–2.9 mm; $P < .001$). Similarly, a 0.01-unit decrease in the Paso correlation coefficient resulted in a 664 mm^3 increased convex hull volume (95% CI 423–906 mm^3; $P < .0001$). This inverse linear relationship, wherein a decrease in the PaSo correlation coefficient results in increased distances and volume, is as expected as illustrated on the heart maps shown in Figure 3.

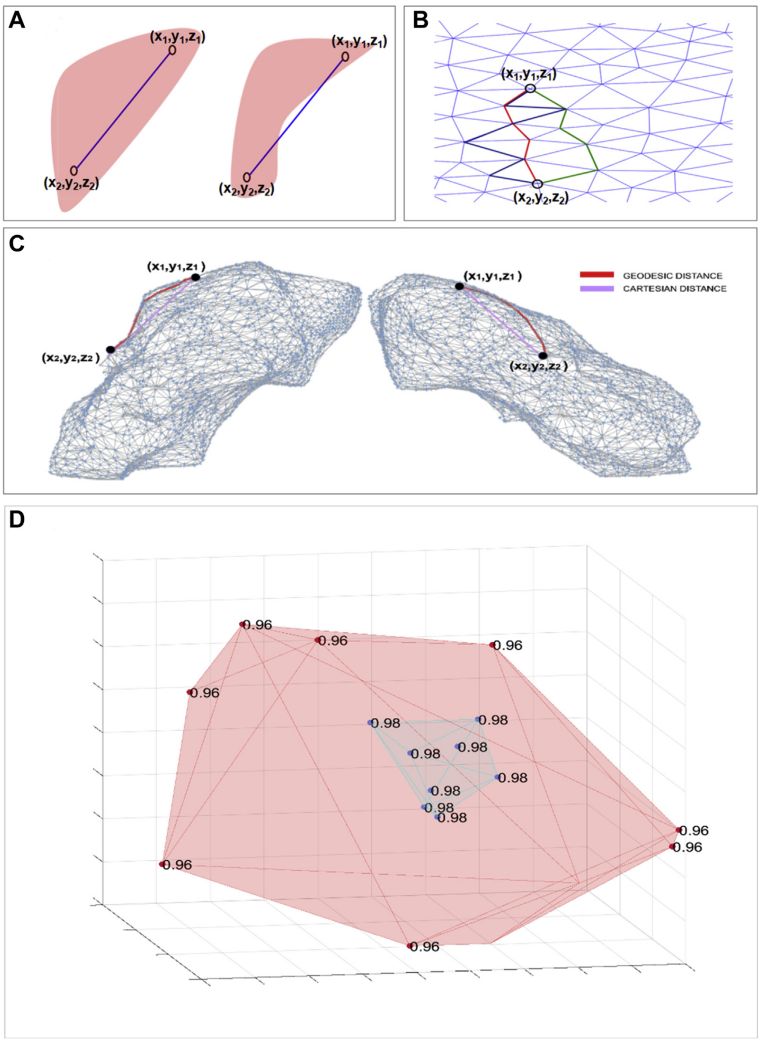

Figure 1 Calculation of computational geometric methods. **A:** Plotting of the Cartesian distance between 2 points ($x_1y_1z_1$ and $x_2y_2z_2$) in an illustrative scenario. The same putative geometry is shown in 2 views. Drawing a straight line between the 2 points is oversimplistic, ignoring the curvature of the surface, with the line exiting the geometry in the right-hand panel. **B:** Calculation of the geodesic distance. Each point of the point cloud has a relationship with every adjacent point. There are multiple potential paths between points $x_1y_1z_1$ and $x_2y_2z_2$. Three potential paths are illustrated in *red*, *blue*, and *green*. The model automatically chooses the shortest possible distance across the surface: in this case, the *red path*. **C:** A 3-dimensional mesh export from Carto 3, shown in 2 rotations (left and right), illustrating both the geodesic (*red*) and Cartesian (*purple*) distances between points $x_1y_1z_1$ and $x_2y_2z_2$. The Cartesian distance is a direct line between the 2 points, with the geodesic distance taking into account the surface curvature of the geometry. **D:** Two representative convex hull volumes. The convex hull depicted in *pink* is the volume within the point cloud that contains all sites with a PaSo correlation of 0.96; similarly, the volume in *light green* (smaller than the previous volume) contains all sites with a correlation of 0.98. Similar hulls can be created with 12-lead electrocardiogram matches.

Traditional ECG matching

Using the same linear mixed model approaches, the number of ECG matches also demonstrated inverse linear relationships with Cartesian distance, geodesic distance, and convex hull volume, as shown in Figure 2. In comparison to PaSo mapping, human ECG matching revealed poorer spatial resolution (refer

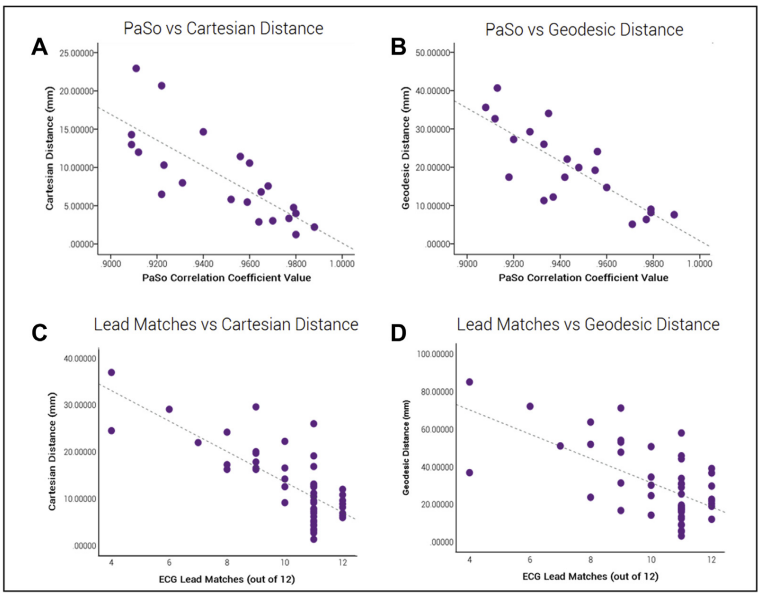

Figure 2 PaSo correlation coefficient vs Cartesian and geodesic distances. Relationship of Cartesian and geodesic distances with pacemapping using PaSo (**A and B**, representative cases) and traditional 12-lead electrocardiographic (ECG) criteria (**C and D**, representative cases) is shown. There is an inverse relationship between the PaSo correlation coefficient and the Cartesian distance (in millimeters) (panel A) with a spatial resolution of 1.1 mm per 0.01-unit decrease in PaSo coefficient (95% confidence interval [CI] 0.9–1.3 mm; $P < .001$). An inverse linear relationship is also reported between the PaSo correlation coefficient and the geodesic distance (panel B) with a spatial resolution of 2.4 mm per 0.01-unit decrease in PaSo coefficient (95% CI 1.9–2.9 mm; $P < .001$). Panel C demonstrates the inverse linear relationships between lead ECG matches (out of 12) and the Cartesian distance (in millimeters) with a spatial resolution of 1.7 mm (95% CI 1.5–2.0 mm; $P < .001$). Likewise, panel D shows the inverse relationship of 12-lead ECG matches and geodesic distance with a spatial resolution of 3.4 mm (95% CI 2.8–4.1 mm; $P < .001$).

to Table 1), with each decrease in lead matches resulting in 1.7 mm increased Cartesian distance (95% CI 1.5–2.0 mm; $P < .001$) and 3.4 mm increased geodesic distance (95% CI 2.8–4.1 mm; $P < .001$). A decrease in lead matches also resulted in a 712 mm^3 increased convex hull volume (95% CI 599–830 mm^3; $P < .0001$), further demonstrating poorer spatial accuracy in comparison to PaSo mapping.

Comparing PaSo and traditional ECG pacemapping

We considered comparing the resolution of PaSo and traditional pacemapping by statistical methods. Given that the measuring scales of the 2 systems are different (PaSo with up to 1000 possible values and traditional ECG pacemapping with up to 12 or 24 values), a statistical comparison is probably inappropriate. However, they can be compared from a clinical viewpoint. Pacemapping with PaSo produces a clinically relevant finer resolution than does traditional ECG pacemapping, potentially improving localization of the focus, which may translate into better outcomes. Spatial resolution for specific locations can be found in the Supplemental Material.

Discussion

Key findings

This study sought to quantify and compare the spatial resolution of PaSo mapping and traditional 12-lead ECG pacemapping by various computational measures of distance.

Table 1 Spatial resolution of traditional 12-lead ECG and PaSo pacemapping—corresponds to a 1-unit decrease in lead match and 0.01-unit decrease in PaSo

	Traditional 12-lead ECG pacemapping			PaSo pacemapping		
Variable	Resolution	95% confidence interval	*P*	Resolution	95% confidence interval	*P*
Cartesian distance (mm)	1.7	1.5–2.0	<.001	1.1	0.9–1.3	<.001
Geodesic distance (mm)	3.4	2.8–4.1	<.001	2.4	1.9–2.9	<.001
Convex hull volume (mm^3)	712	599–830	<.0001	664	423–906	<.0001

ECG = electrocardiographic.

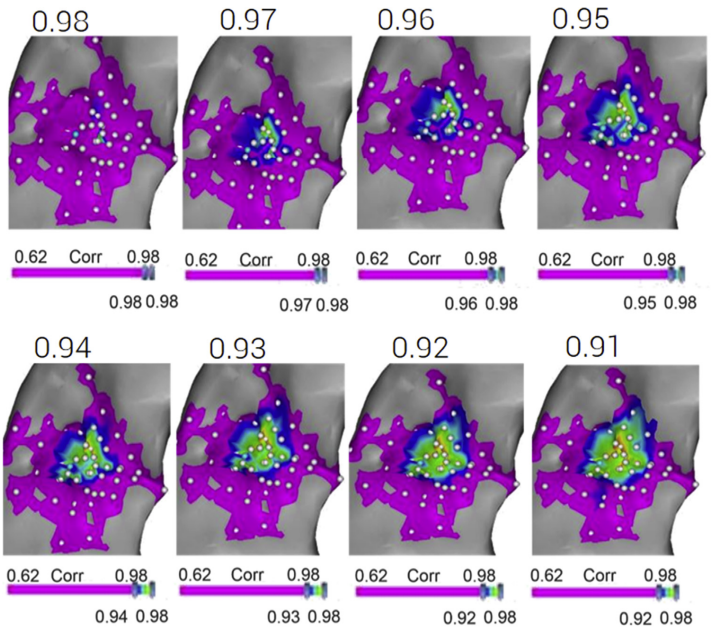

Figure 3 Carto 3 3-dimensional heart maps. Heart map of the right ventricular outflow tract generated by Carto 3 is shown. Each panel shows PaSo coefficient values decreasing in 0.01 increments, ranging from 0.98 to 0.91. The *blue dot* represents the "origin," and correlations below the assigned value are in *purple*, with the best correlation coefficient in *red*, moving through *yellow*, *green*, and *blue*. One can see that there is spatial correlation in a radial fashion from the origin.

Quantitative pacemapping with PaSo has a better spatial resolution in all 3 parameters of distance than does qualitative 12-lead ECG pacemapping. A 0.01-unit decrease in the PaSo correlation coefficient value resulted in a 1.1 mm increased Cartesian distance and a 2.4 mm increased geodesic distance. Similarly, a 0.01-unit decrease in the Paso correlation coefficient resulted in a 664 mm^3 increase in convex hull volume. For traditional ECG pacemapping, each decrease in lead match resulted in 1.7 mm increased Cartesian distance and 3.4 mm increased geodesic distance. A decrease in the lead match also resulted in a 712 mm^3 increased convex hull volume.

Utility of pacemapping

Pacemapping is good for mapping focal VEs. It has been studied systematically for ablation of VA.[13] The ideal strategy is to combine both activation mapping and pacemapping for maximizing the chance of success.[14] However, sometimes, premature ventricular contractions may have a low burden or may not be inducible in the laboratory. This is especially pertinent in children, in whom general anesthesia is essential.[3] In situations with a low burden of PVCs in the laboratory, pacemapping may be the only option available and can be effective.[3,15–18]

Furthermore, pacemapping is useful in the identification of the exit sites of VA.[19–21] It can also be used for determining channels in reentrant poorly tolerated ventricular tachycardia circuits.[2,22]

There are limited data on the utility of automated algorithms, but early results have shown some promise.[3,16]

Significance of spatial resolution

The utility of pacemapping depends on its spatial resolution. Pacing from 2 closely located but distinctly different sites may produce the same QRS complexes on the ECG on the basis of the conduction properties of the underlying myocardium and the extent of stimulus capture.[23] Thus, there would be a region *around* the point of origin of a focal arrhythmia, where pace capture will generate an identical QRS; however, ablation only *at the origin* ideally is what is desired to eliminate the focus. This spatial resolution, therefore, is a key factor in determining the extent to which pacemapping can aid in successfully localizing the exit and the most probable site of successful suppression of the arrhythmia. Traditional pacemapping, involving looking for a match on the 12-lead ECG, is routine but is qualitative. It is subjective and its reproducibility is uncertain.

Available data on spatial resolution

There are limited data on the spatial resolution of traditional pacemapping. Azegami et al[5] looked at the spatial resolution of traditional pacemapping and activation mapping for right

ventricular outflow tract VAs. The greatest mean distance between 2 points with the best pace-map matches was 18 ± 5 mm (range 11–26 mm). They concluded that traditional pacemapping had a modest spatial resolution, comparable to the resolution of activation mapping. While this study was one of the few that attempted to quantify spatial resolution, it was performed in a relatively simplistic manner—where the distances between points were measured in straight lines (Cartesian distances). Cartesian distance measurements may not be the most appropriate, as distances within cardiac chambers need to be considered on a 3D plane rather than as straight lines.

Pacemapping software module

The PaSo module is an algorithm for calculating correlation coefficients of matches in 12-lead ECGs. It is semiquantitative, more objective, and reproducible as it is based on a mathematically derived formula. It may overcome some of the limitations of qualitatively matching 12-lead ECGs (traditional pacemapping).

Use of different computational methods for distance

The data on the spatial resolution of traditional ECG pacemapping are modest at best, using the fairly simplistic approach of the Cartesian distance between points in 3D space displayed on a 3D monitor.[5] This study uses computational techniques to accurately determine spatial resolution between points in a true 3D geometry with measurements by 3 mathematical techniques: Cartesian distance, geodesic distance, and convex hull volume.

The same computational and mathematical techniques were used to systematically examine the resolution of the PaSo module, which has not been previously explored.

Using 3 methods to study spatial resolution has advantages:

1. The validation of the results is more comprehensive if the same relationship is shown by all 3 methods.
2. Cartesian distances may be too simplistic to apply in 3D cardiac chambers—geodesic distance and the convex hull volume schemes would be superior to it in giving a realistic idea of distances.

Implications of our results

The results show that traditional 12-lead ECG pacemapping is good with a spatial resolution of 1.7 mm (by Cartesian distance; 95% CI 1.5–2.0 mm; $P < .001$), with a statistically significant inverse linear relationship between matching lead numbers and the distance away from the source. The spatial resolution is lower if using non-Cartesian approaches; the resultant spatial resolution then drops to 3.4 mm (by geodesic distance; 95% CI 2.8–4.1 mm; $P < .001$) and 712 mm^3 (by convex hull volume; 95% CI 599–830 mm^3; $P < .001$).

In comparison, with the use of PaSo, the spatial resolution is 1.1 mm (by Cartesian distance; 95% CI 0.9–1.3 mm; $P < .001$), again with a significant inverse linear relationship between the correlation coefficient and the distance away from the source. By non-Cartesian methods, the spatial resolution of PaSo is 2.4 mm (by geodesic distance; 95% CI 1.9–2.9 mm; $P < .001$) and 664 mm^3 (by convex hull volume; 95% CI 423–906 mm^3; $P < .001$). Numerically, the strength of correlations appears to be more robust with PaSo than with pacemapping.

The use of geodesic distance rather than Cartesian distance may be particularly pertinent in VAs originating from structures such as the papillary muscles and the moderator band. Given that these project from the walls of the ventricles into the cavities, determination of the distance from a point on one of these structures to the adjacent ventricular walls by linear Cartesian methods would be oversimplistic and erroneous, giving false impressions of either "nearness" or "farness." The use of the geodesic method (which takes into account the 3D contour of the structure) may be useful in assigning distance with more accuracy and validity. However, this was not specifically examined in this study and would be an interesting area of further work. Regional spatial resolution is discussed in the Supplemental Material.

Summary

This is the first study to quantify the spatial resolution of pacemapping using mathematically sound techniques using both traditional qualitative 12-lead ECG criteria and the semiquantitative automated algorithm of the PaSo module. Knowledge of the spatial resolution is critical to allow better interpretation of pace maps and facilitate targeting areas of interest. Furthermore, PaSo appears to provide numerically better spatial resolution than does traditional pacemapping, which may have an impact in the clinical arena. One of the key strengths of this study is that the acquisition of an ECG was done in real time with the interpretation of the 12-lead pace match decided while the case was being performed (while being blinded to fluoroscopy and the electroanatomic geometry), which closely resembles a real-world clinical scenario—this adds to the validity of the results.

Limitations

In this study, the site of arrhythmia origin was "mimicked" using pacing at an output just above the capture threshold. This would have ensured only local capture at the site owing to the low output. Although these were not truly intrinsic arrhythmias, this approach has been used in the past for attempting to determine spatial resolution[8] and for localizing VEs by the ECG.[24]

Conclusion

We have provided data on the spatial resolution of the traditional 12-lead ECG pacemapping system and the Paso module by 3 computational methods of distance. The resolution of mapping using the Paso software is better than that of traditional pacemapping, which may have implications for clinical practice.

Appendix

Supplementary data

Supplementary data associated with this article can be found in the online version at https://doi.org/10.1016/j.hrthm.2019.08.029

References

1. Calkins H, Kalbfleisch SJ, el-Atassi R, Langberg JJ, Morady F. Relation between efficacy of radiofrequency catheter ablation and site of origin of idiopathic ventricular tachycardia. Am J Cardiol 1993;71:827–833.
2. Stevenson WG, Sager PT, Natterson PD, Saxon LA, Middlekauff HR, Wiener I. Relation of pace mapping QRS configuration and conduction delay to ventricular tachycardia reentry circuits in human infarct scars. J Am Coll Cardiol 1995;26:481–488.
3. Moak JP, Sumihara K, Swink J, Hanumanthaiah S, Berul CI. Ablation of the vanishing PVC, facilitated by quantitative morphology-matching software. Pacing Clin Electrophysiol 2017;40:1227–1233.
4. Sinno MC, Yokokawa M, Good E, et al. Endocardial ablation of postinfarction ventricular tachycardia with nonendocardial exit sites. Heart Rhythm 2013;10:794–799.
5. Azegami K, Wilber DJ, Arruda M, Lin AC, Denman RA. Spatial resolution of pacemapping and activation mapping in patients with idiopathic right ventricular outflow tract tachycardia. J Cardiovasc Electrophysiol 2005;16:823–829.
6. Bogun F, Taj M, Ting M, et al. Spatial resolution of pace mapping of idiopathic ventricular tachycardia/ectopy originating in the right ventricular outflow tract. Heart Rhythm 2008;5:339–344.
7. Kadish AH, Childs K, Schmaltz S, Morady F. Differences in QRS configuration during unipolar pacing from adjacent sites: implications for the spatial resolution of pace-mapping. J Am Coll Cardiol 1991;17:143–151.
8. Man KC, Chan KK, Kovack P, et al. Spatial resolution of atrial pace mapping as determined by unipolar atrial pacing at adjacent sites. Circulation 1996;94:1357–1363.
9. Dijkstra EW. A note on two problems in connexion with graphs. Numer Math 1959;1:269–271.
10. Graham RL. An efficient algorithm for determining the convex hull of a finite planar set. Inf Process Lett 1972;1:132–133.
11. Kadish AH, Schmaltz S, Morady F. A comparison of QRS complexes resulting from unipolar and bipolar pacing: implications for pace-mapping. Pacing Clin Electrophysiol 1991;14:823–832.
12. Goyal R, Harvey M, Daoud EG, et al. Electrophysiology/pacing: effect of coupling interval and pacing cycle length on morphology of paced ventricular complexes: implications for pace mapping. Circulation 1996;94:2843–2849.
13. Hutchinson MD, Garcia FC. An organized approach to the localization, mapping, and ablation of outflow tract ventricular arrhythmias. J Cardiovasc Electrophysiol 2013;24:1189–1197.
14. Haqqani HM, Roberts-Thomson KC. Radiofrequency catheter ablation for ventricular tachycardia. Heart Lung Circ 2012;21:402–412.
15. Coggins DL, Lee RJ, Sweeney J, et al. Radiofrequency catheter ablation as a cure for idiopathic tachycardia of both left and right ventricular origin. J Am Coll Cardiol 1994;23:1333–1341.
16. Fedida J, Strisciuglio T, Sohal M, et al. Efficacy of advanced pace-mapping technology for idiopathic premature ventricular complexes ablation. J Interv Card Electrophysiol 2018;51:271–277.
17. Noheria A, Deshmukh A, Asirvatham SJ. Ablating premature ventricular complexes: justification, techniques, and outcomes. Methodist Debakey Cardiovasc J 2015;11:109–120.
18. Adams JC, Srivathsan K, Shen WK. Advances in management of premature ventricular contractions. J Interv Card Electrophysiol 2012;35:137–149.
19. Josephson ME, Waxman HL, Cain ME, Gardner MJ, Buxton AE. Ventricular activation during ventricular endocardial pacing. II. Role of pace-mapping to localize origin of ventricular tachycardia. Am J Cardiol 1982;50:11–22.
20. Li A, Davis JS, Wierwille J, et al. Relationship between distance and change in surface ECG morphology during pacemapping as a guide to ablation of ventricular arrhythmias: implications for the spatial resolution of pacemapping. Circ Arrhythm Electrophysiol 2017;10.
21. Nof E, Stevenson WG, John RM. Catheter ablation for ventricular arrhythmias. Arrhythm Electrophysiol Rev 2013;2:45–52.
22. Brunckhorst CB, Delacretaz E, Soejima K, Maisel WH, Friedman PL, Stevenson WG. Identification of the ventricular tachycardia isthmus after infarction by pace mapping. Circulation 2004;110:652–659.
23. Moreno M, Perez-Castellano N, Villacastin J. Pacemapping. Indian Pacing Electrophysiol J 2005;5:35–42.
24. Dixit S, Gerstenfeld EP, Lin D, et al. Identification of distinct electrocardiographic patterns from the basal left ventricle: distinguishing medial and lateral sites of origin in patients with idiopathic ventricular tachycardia. Heart Rhythm 2005;2:485–491.

Bibliography

[1] M. Abbas, Y. Bai, M. Rashidi, and M. Bhatti, *Analysis of entropy generation in the flow of peristaltic nanofluids in channels with compliant walls*, Entropy, 18 (2016), p. 90.

[2] L. J. Acierno, *The history of cardiology*, CRC Press, 1994.

[3] O. Aftab, P. Cheung, A. Kim, S. Thakkar, and N. Yeddanapudi, *Information theory and the digital age*, Bandwagon, pgs, (2001), pp. 9–11.

[4] M. Aguilar, F. Xiong, X. Y. Qi, P. Comtois, and S. Nattel, *Potassium channel blockade enhances atrial fibrillation–selective antiarrhythmic effects of optimized state-dependent sodium channel blockade*, Circulation, 132 (2015), pp. 2203–2211.

[5] N. Akoum, M. Daccarett, C. McGann, N. Segerson, G. Vergara, S. Kuppahally, T. Badger, N. Burgon, T. Haslam, and E. Kholmovski, *Atrial fibrosis helps select the appropriate patient and strategy in catheter ablation of atrial fibrillation: A de[U+2010]mri guided approach*, Journal of cardiovascular electrophysiology, 22 (2011), pp. 16–22.

[6] S. M. Al-Khatib, W. G. Stevenson, M. J. Ackerman, W. J. Bryant, D. J. Callans, A. B. Curtis, B. J. Deal, T. Dickfeld, M. E. Field, and G. C. Fonarow, *2017 aha/acc/hrs guideline for management of patients with ventricular arrhythmias and the prevention of sudden cardiac death: a report of the american college of cardiology/american heart association task force on clinical practice guidelines and the heart rhythm society*, Journal of the American College of Cardiology, 72 (2018), pp. e91–e220.

[7] P. Albrecht, R. Cohen, and R. Mark, *A stochastic characterization of chronic ventricular ectopic activity*, IEEE transactions on biomedical engineering, 35 (1988), pp. 539–550.

[8] A. Alcaine, M. Mase, A. Cristoforetti, F. Ravelli, G. Nollo, P. Laguna, J. P. Martínez, and L. Faes, *A multi-variate predictability framework to assess invasive cardiac activity and interactions during atrial fibrillation*, IEEE Transactions on Biomedical Engineering, 64 (2017), pp. 1157–1168.

[9] R. Alcaraz and J. Rieta, *A novel application of sample entropy to the electrocardiogram of atrial fibrillation*, Nonlinear Analysis: Real World Applications, 11 (2010), pp. 1026–1035.

[10] R. Alcaraz and J. J. Rieta, *Non-invasive organization variation assessment in the onset and termination of paroxysmal atrial fibrillation*, Computer methods and programs in biomedicine, 93 (2009), pp. 148–154.

[11] R. Alcaraz and J. J. Rieta, *Sample entropy of the main atrial wave predicts spontaneous termination of paroxysmal atrial fibrillation*, Medical engineering and physics, 31 (2009), pp. 917–922.

[12] M. A. Allessie, *Experimental evaluation of moe's multiple wavelet hypothesis of atrial fibrillation*, Cardiac electrophysiology and arrhythmias, (1985), pp. 265–275.

[13] M. A. Allessie, F. Bonke, and F. Schopman, *Circus movement in rabbit atrial muscle as a mechanism of tachycardia. ii. the role of nonuniform recovery of excitability in the occurrence of unidirectional block, as studied with multiple microelectrodes*, Circulation Research, 39 (1976), pp. 168–177.

[14] M. A. Allessie, F. Bonke, and F. Schopman, *Circus movement in rabbit atrial muscle as a mechanism of tachycardia. iii. the" leading circle" concept: a new model of circus movement in cardiac tissue without the involvement of an anatomical obstacle*, Circulation research, 41 (1977), pp. 9–18.

[15] D. Amar, H. Zhang, S. Miodownik, and A. H. Kadish, *Competing autonomic mechanisms precedethe onset of postoperative atrial fibrillation*, Journal of the American College of Cardiology, 42 (2003), pp. 1262–1268.

[16] E. M. Annoni, S. P. Arunachalam, S. Kapa, S. K. Mulpuru, P. A. Friedman, and E. G. Talkachova, *Novel quantitative analytical approaches for rotor identification and associated implications for mapping*, IEEE Transactions on Biomedical Engineering, (2017).

[17] S. P. Arunachalam, S. K. Mulpuru, P. A. Friedman, and E. G. Tolkacheva, *Feasibility of visualizing higher regions of shannon entropy in atrial fibrillation patients*, in Engineering in Medicine and Biology Society (EMBC), 2015 37th Annual International Conference of the IEEE, IEEE, pp. 4499–4502.

[18] F. Atienza, J. Almendral, J. Jalife, S. Zlochiver, R. Ploutz-Snyder, E. G. Torrecilla, A. Arenal, J. Kalifa, F. Fernández-Avilés, and O. Berenfeld, *Real-time dominant frequency mapping and ablation of dominant frequency sites in atrial fibrillation with left-to-right frequency gradients predicts long-term maintenance of sinus rhythm*, Heart Rhythm, 6 (2009), pp. 33–40.

[19] F. Atienza, J. Almendral, J. M. Ormaetxe, [U+FFFD] Moya, J. D. Martínez-Alday, A. Hernández-Madrid, E. Castellanos, F. Arribas, M. [U+FFFD] Arias, and L. Tercedor, *Comparison of radiofrequency catheter ablation of drivers and circumferential pulmonary vein isolation in atrial fibrillation: a noninferiority randomized multicenter radar-af trial*, Journal of the American College of Cardiology, 64 (2014), pp. 2455–2467.

[20] V. B Traykov, R. Pap, and L. Sághy, *Frequency domain mapping of atrial fibrillation-methodology, experimental data and clinical implications*, Current cardiology reviews, 8 (2012), pp. 231–238.

[21] J. Babaud, A. P. Witkin, M. Baudin, and R. O. Duda, *Uniqueness of the gaussian kernel for scale-space filtering*, IEEE Transactions on Pattern Analysis & Machine Intelligence, (1986), pp. 26–33.

[22] A. Baldzizhar, E. Manuylova, R. Marchenko, Y. Kryvalap, and M. G. Carey, *Ventricular tachycardias: characteristics and management*, Critical Care Nursing Clinics, 28 (2016), pp. 317–329.

[23] J. R. Banavar, A. Maritan, and I. Volkov, *Applications of the principle of maximum entropy: from physics to ecology*, Journal of Physics: Condensed Matter, 22 (2010), p. 063101.

[24] L. Barnett, A. B. Barrett, and A. K. Seth, *Granger causality and transfer entropy are equivalent for gaussian variables*, Physical review letters, 103 (2009), p. 238701.

[25] M. Baumert, P. Sanders, and A. Ganesan, *Quantitative-electrogram-based methods for guiding catheter ablation in atrial fibrillation*, Proceedings of the IEEE, 104 (2016), pp. 416–431.

[26] B. Beck, J. Bray, P. Cameron, K. Smith, T. Walker, H. Grantham, C. Hein, M. Thorrowgood, A. Smith, and M. Inoue, *Regional variation in the characteristics, incidence and outcomes of out-of-hospital cardiac arrest in australia and new zealand: results from the aus-roc epistry*, Resuscitation, 126 (2018), pp. 49–57.

[27] P. Benharash, E. Buch, P. Frank, M. Share, R. Tung, K. Shivkumar, and R. Mandapati, *Quantitative analysis of localized sources identified by focal impulse and roter modulation mapping in atrial fibrillation*, Circulation: Arrhythmia and Electrophysiology, (2015), p. CIRCEP. 115.002721.

[28] E. J. Benjamin, P. A. Wolf, R. B. D'Agostino, H. Silbershatz, W. B. Kannel, and D. Levy, *Impact of atrial fibrillation on the risk of death*, Circulation, 98 (1998), pp. 946–952.

[29] O. Berenfeld and J. Jalife, *Complex fractionated atrial electrograms: is this the beast to tame in atrial fibrillation?*, 2011.

[30] O. Berenfeld, A. V. Zaitsev, S. F. Mironov, A. M. Pertsov, and J. Jalife, *Frequency-dependent breakdown of wave propagation into fibrillatory conduction across the pectinate muscle network in the isolated sheep right atrium*, Circulation research, 90 (2002), pp. 1173–1180.

[31] A. L. Berger, V. J. D. Pietra, and S. A. D. Pietra, *A maximum entropy approach to natural language processing*, Computational linguistics, 22 (1996), pp. 39–71.

[32] M. Biermann, M. Shenasa, M. Borggrefe, G. Hindricks, W. Haverkamp, and G. Breithardt, *The interpretation of cardiac electrograms*, Cardiac mapping, (1993), pp. 11–34.

[33] G. W. Botteron and J. M. Smith, *A technique for measurement of the extent of spatial organization of atrial activation during atrial fibrillation in the intact human heart*, IEEE Transactions on Biomedical Engineering, 42 (1995), pp. 579–586.

[34] G. Box, G. Jenkins, G. Reinsel, and G. Ljung, *Time series analysis, control, and forecasting . hoboken*, 2015.

[35] P. M. Boyle, T. Zghaib, S. Zahid, R. L. Ali, D. Deng, W. H. Franceschi, J. B. Hakim, M. J. Murphy, A. Prakosa, S. L. Zimmerman, et al., *Computationally guided personalized targeted ablation of persistent atrial fibrillation*, Nature biomedical engineering, (2019), pp. 1–10.

[36] C. P. Bradley, R. H. Clayton, M. P. Nash, A. Mourad, M. Hayward, D. J. Paterson, and P. Taggart, *Human ventricular fibrillation during global ischemia and reperfusion: paradoxical changes in activation rate and wavefront complexity*, Circulation: Arrhythmia and Electrophysiology, 4 (2011), pp. 684–691.

[37] E. Braunwald, D. L. Kasper, S. L. Hauser, D. L. Longo, J. L. Jameson, and J. Loscalzo, *Harrison's principles of internal medicine*, (2001).

[38] M.-A. Bray, S. Lin, R. R. Aliev, B. J. Roth, and J. P. Wikswo Jr, *Experimental and theoretical analysis of phase singularity dynamics in cardiac tissue*, Journal of cardiovascular electrophysiology, 12 (2001), pp. 716–722.

[39] M.-A. Bray and J. P. Wikswo, *Considerations in phase plane analysis for nonstationary reentrant cardiac behavior*, Physical Review E, 65 (2002), p. 051902.

[40] E. Buch, M. Share, R. Tung, P. Benharash, P. Sharma, J. Koneru, R. Mandapati, K. A. Ellenbogen, and K. Shivkumar, *Long-term clinical outcomes of focal impulse and rotor modulation for treatment of atrial fibrillation: A multicenter experience*, Heart Rhythm, 13 (2016), pp. 636–641.

[41] N. Burioka, M. Miyata, G. Cornélissen, F. Halberg, T. Takeshima, D. T. Kaplan, H. Suyama, M. Endo, Y. Maegaki, T. Nomura, et al., *Approximate entropy in the electroencephalogram during wake and sleep*, Clinical EEG and neuroscience, 36 (2005), pp. 21–24.

[42] M. A. Busa and R. E. van Emmerik, *Multiscale entropy: A tool for understanding the complexity of postural control*, Journal of Sport and Health Science, 5 (2016), pp. 44–51.

[43] H. Calkins, G. Hindricks, R. Cappato, Y.-H. Kim, E. B. Saad, L. Aguinaga, J. G. Akar, V. Badhwar, J. Brugada, and J. Camm, *2017 hrs/ehra/ecas/aphrs/solaece expert*

consensus statement on catheter and surgical ablation of atrial fibrillation, Ep Europace, 20 (2017), pp. e1–e160.

[44] A. Capucci, G. Q. Villani, D. Aschieri, and M. Piepoli, *Effects of class iii drugs on atrial fibrillation*, Journal of cardiovascular electrophysiology, 9 (1998), pp. S109–20.

[45] M. Carrara, L. Carozzi, T. J. Moss, M. De Pasquale, S. Cerutti, M. Ferrario, D. E. Lake, and J. R. Moorman, *Heart rate dynamics distinguish among atrial fibrillation, normal sinus rhythm and sinus rhythm with frequent ectopy*, Physiological measurement, 36 (2015), p. 1873.

[46] D. Chamchad, J. C. Horrow, L. E. Samuels, and L. Nakhamchik, *Heart rate variability measures poorly predict atrial fibrillation after off-pump coronary artery bypass grafting*, Journal of clinical anesthesia, 23 (2011), pp. 451–455.

[47] J. Chen, Y. Lin, L. Chen, J. Yu, Z. Du, S. Li, Z. Yang, C. Zeng, X. Lai, and Q. Lu, *A decade of complex fractionated electrograms catheter-based ablation for atrial fibrillation: Literature analysis, meta-analysis and systematic review*, IJC Heart Vessels, 4 (2014), pp. 63–72.

[48] J. Chen, R. Mandapati, O. Berenfeld, A. C. Skanes, R. A. Gray, and J. Jalife, *Dynamics of wavelets and their role in atrial fibrillation in the isolated sheep heart*, Cardiovascular research, 48 (2000), pp. 220–232.

[49] Q. Chen, G. E. Kirsch, D. Zhang, R. Brugada, J. Brugada, P. Brugada, D. Potenza, A. Moya, M. Borggrefe, and G. Breithardt, *Genetic basis and molecular mechanism for idiopathic ventricular fibrillation*, Nature, 392 (1998), p. 293.

[50] N. Child, R. H. Clayton, C. R. Roney, J. I. Laughner, A. Shuros, P. Neuzil, J. Petru, T. Jackson, B. Porter, and J. Bostock, *Unraveling the underlying arrhythmia mechanism in persistent atrial fibrillation: Results from the starlight study*, Circulation: Arrhythmia and Electrophysiology, 11 (2018), p. e005897.

[51] J. Christoph, M. Chebbok, C. Richter, J. Schröder-Schetelig, P. Bittihn, S. Stein, I. Uzelac, F. Fenton, G. Hasenfuss, and R. Gilmour Jr, *Electromechanical vortex filaments during cardiac fibrillation*, Nature, 555 (2018), p. 667.

[52] S. S. Chugh, R. Havmoeller, K. Narayanan, D. Singh, M. Rienstra, E. J. Benjamin, R. F. Gillum, Y.-H. Kim, J. H. McAnulty, Z.-J. Zheng, M. H. Forouzanfar, M. Naghavi, G. A. Mensah, M. Ezzati, and C. J. Murray, *Worldwide epidemiology of atrial fibrillation*, A Global Burden of Disease 2010 Study, 129 (2014), pp. 837–847.

[53] K. L. Chung, *A course in probability theory*, Academic press, 2001.

[54] S. Ciaroni, L. Cuenoud, and A. Bloch, *Clinical study to investigate the predictive parameters for the onset of atrial fibrillation in patients with essential hypertension*, American heart journal, 139 (2000), pp. 814–819.

[55] E. Cirugeda–Roldán, D. Novak, V. Kremen, D. Cuesta–Frau, M. Keller, A. Luik, and M. Srutova, *Characterization of complex fractionated atrial electrograms by sample entropy: an international multi-center study*, Entropy, 17 (2015), pp. 7493–7509.

[56] J. A. Clarnette, A. G. Brooks, R. Mahajan, A. D. Elliott, D. J. Twomey, R. K. Pathak, S. Kumar, D. A. Munawar, G. D. Young, and J. M. Kalman, *Outcomes of persistent and long-standing persistent atrial fibrillation ablation: a systematic review and meta-analysis*, EP Europace, (2017).

[57] R. H. Clayton and A. V. Holden, *A method to quantify the dynamics and complexity of re-entry in computational models of ventricular fibrillation*, Physics in Medicine & Biology, 47 (2002), p. 225.

[58] M. Costa, A. L. Goldberger, and C.-K. Peng, *Multiscale entropy analysis of complex physiologic time series*, Physical review letters, 89 (2002), p. 068102.

[59] ——, *Multiscale entropy analysis of biological signals*, Physical review E, 71 (2005), p. 021906.

[60] T. M. Cover and J. A. Thomas, *Entropy, relative entropy and mutual information*, Elements of information theory, 2 (1991), pp. 1–55.

[61] J. L. Cox, J. P. Boineau, R. B. Schuessler, K. M. Kater, and D. G. Lappas, *Five-year experience with the maze procedure for atrial fibrillation*, The Annals of thoracic surgery, 56 (1993), pp. 814–824.

[62] J. L. Cox, T. Canavan, R. Schuessler, M. Cain, B. Lindsay, C. Stone, P. Smith, P. Corr, and J. Boineau, *The surgical treatment of atrial fibrillation. ii. intraoperative electrophysiologic mapping and description of the electrophysiologic basis of atrial flutter and atrial fibrillation*, The Journal of thoracic and cardiovascular surgery, 101 (1991), pp. 406–426.

[63] X. Cui, E. Chang, W.-H. Yang, B. C. Jiang, A. C. Yang, and C.-K. Peng, *Automated detection of paroxysmal atrial fibrillation using an information-based similarity approach*, Entropy, 19 (2017), p. 677.

[64] S. Dash, K. Chon, S. Lu, and E. Raeder, *Automatic real time detection of atrial fibrillation*, Annals of biomedical engineering, 37 (2009), pp. 1701–1709.

[65] G. Dawes, M. Moulden, O. Sheil, and C. Redman, *Approximate entropy, a statistic of regularity, applied to fetal heart rate data before and during labor*, Obstetrics and gynecology, 80 (1992), pp. 763–768.

[66] J. M. de Bakker and F. H. Wittkampf, *The pathophysiologic basis of fractionated and complex electrograms and the impact of recording techniques on their detection and interpretation*, Circulation: Arrhythmia and Electrophysiology, 3 (2010), pp. 204–213.

[67] N. M. de Groot, R. P. Houben, J. L. Smeets, E. Boersma, U. Schotten, M. J. Schalij, H. Crijns, and M. A. Allessie, *Electropathological substrate of longstanding persistent atrial fibrillation in patients with structural heart disease: epicardial breakthrough*, Circulation, 122 (2010), pp. 1674–1682.

[68] D. Dharmaprani, L. Dykes, A. D. McGavigan, P. Kuklik, K. Pope, and A. N. Ganesan, *Information theory and atrial fibrillation (af): A review*, Frontiers in physiology, 9 (2018).

[69] D. Dharmaprani, A. D. McGavigan, D. Chapman, R. Kutlieh, S. Thanigaimani, L. Dykes, J. Kalman, P. Sanders, K. Pope, and P. Kuklik, *Temporal stability and specificity of high bipolar electrogram entropy regions in sustained atrial fibrillation: Implications for mapping*, Journal of electrocardiology, 53 (2019), pp. 18–27.

[70] D. Dharmaprani, M. Schopp, P. Kuklik, D. Chapman, A. Lahiri, L. Dykes, F. Xiong, M. Aguilar, B. Strauss, L. Mitchell, K. Pope, C. Meyer, S. Willems, F. G. Akar, S. Nattel, A. D. McGavigan, and A. N. Ganesan, *Renewal theory provides a universal quantitative framework to characterise the continuous regeneration of rotational events in cardiac fibrillation*, bioRxiv, (2019), p. 599142.

[71] W. F. Doolittle, *Phylogenetic classification and the universal tree*, Science, 284 (1999), pp. 2124–2128.

[72] R. Durrett, *Probability: theory and examples*, vol. 49, Cambridge university press, 2019.

[73] J.-P. Eckmann and D. Ruelle, *Ergodic theory of chaos and strange attractors*, Springer, 1985, pp. 273–312.

[74] W. Einthoven, *Weiteres über das elektrokardiogramm*, Pflügers Archiv European Journal of Physiology, 122 (1908), pp. 517–584.

[75] M. S. Eisenberg, A. P. Hallstrom, M. K. Copass, L. Bergner, F. Short, and J. Pierce, *Treatment of ventricular fibrillation: emergency medical technician defibrillation and paramedic services*, JAMA, 251 (1984), pp. 1723–1726.

[76] A. Elvan, A. C. Linnenbank, A. R. R. Misier, P. P. H. Delnoy, W. P. Beukema, and M. Jacques, *Dominant frequency of atrial fibrillation correlates poorly with atrial fibrillation cycle length*, Circulation: Arrhythmia and Electrophysiology, (2009), p. CIRCEP. 108.843284.

[77] L. Faes, A. Porta, M. Javorka, and G. Nollo, *Efficient computation of multiscale entropy over short biomedical time series based on linear state-space models*, Complexity, 2017 (2017).

[78] W. Feller, *An introduction to probability theory and its applications*, vol. 2, John Wiley & Sons, 2008.

[79] L. A. Fleisher, J. A. Dipietro, T. R. Johnson, and S. Pincus, *Complementary and non-coincident increases in heart rate variability and irregularity during fetal development*, Clinical Science, 92 (1997), pp. 345–349.

[80] S. A. Frank, *The common patterns of nature*, Journal of evolutionary biology, 22 (2009), pp. 1563–1585.

[81] R. G. Gallager, *Discrete stochastic processes*, vol. 321, Springer Science & Business Media, 2012.

[82] C. Gallagher, J. Hendriks, L. Giles, A. Elliott, M. Middeldorp, R. Mahajan, D. Lau, P. Sanders, and C. Wong, *Twenty-year national trends in hospitalisations due to atrial fibrillation in australia: A relentless rise*, Heart, Lung and Circulation, 26 (2017), p. S175.

[83] A. N. Ganesan, P. Kuklik, A. Gharaviri, A. Brooks, D. Chapman, D. H. Lau, K. C. Roberts-Thomson, and P. Sanders, *Origin and characteristics of high shannon entropy at the pivot of locally stable rotors: insights from computational simulation*, PloS one, 9 (2014), p. e110662.

[84] A. N. Ganesan, P. Kuklik, D. H. Lau, A. G. Brooks, M. Baumert, W. W. Lim, S. Thanigaimani, S. Nayyar, R. Mahajan, and J. M. Kalman, *Bipolar electrogram shannon entropy at sites of rotational activation: implications for ablation of atrial fibrillation*, Circulation: Arrhythmia and Electrophysiology, (2012), p. CIRCEP. 112.976654.

[85] A. N. Ganesan, P. Kuklik, D. H. Lau, A. G. Brooks, M. Baumert, W. W. Lim, S. Thanigaimani, S. Nayyar, R. Mahajan, J. M. Kalman, K. C. Roberts-Thomson, and P. Sanders, *bipolar electrogram shannon entropy at sites of rotational activationclinical perspective*, Implications for Ablation of Atrial Fibrillation, 6 (2013), pp. 48–57.

[86] P. Ganesan, K. E. Shillieto, and B. Ghoraani, *Simulation of spiral waves and point sources in atrial fibrillation with application to rotor localization*, in 2017 IEEE 30th International Symposium on Computer-Based Medical Systems (CBMS), IEEE, 2017, pp. 379–384.

[87] A. Garfinkel, P.-S. Chen, D. O. Walter, H. S. Karagueuzian, B. Kogan, S. J. Evans, M. Karpoukhin, C. Hwang, T. Uchida, and M. Gotoh, *Quasiperiodicity and chaos in cardiac fibrillation*, The Journal of clinical investigation, 99 (1997), pp. 305–314.

[88] A. Garfinkel, M. L. Spano, W. L. Ditto, and J. N. Weiss, *Controlling cardiac chaos*, Science, 257 (1992), pp. 1230–1235.

[89] W. E. Garrey, *The nature of fibrillary contraction of the heart: its relation to tissue mass and form*, Am J physiol, 33 (1914), pp. 397–414.

[90] R. Gaspo, R. F. Bosch, M. Talajic, and S. Nattel, *Functional mechanisms underlying tachycardia-induced sustained atrial fibrillation in a chronic dog model*, Circulation, 96 (1997), pp. 4027–4035.

[91] C. Glinge, S. Sattler, R. Jabbari, and J. Tfelt-Hansen, *Epidemiology and genetics of ventricular fibrillation during acute myocardial infarction*, Journal of geriatric cardiology: JGC, 13 (2016), p. 789.

[92] A. L. Goldberger, J. E. Mietus, D. R. Rigney, M. L. Wood, and S. M. Fortney, *Effects of head-down bed rest on complex heart rate variability: response to lbnp testing*, Journal of Applied Physiology, 77 (1994), pp. 2863–2869.

[93] E. Goldberger, *A simple, indifferent, electrocardiographic electrode of zero potential and a technique of obtaining augmented, unipolar, extremity leads*, American Heart Journal, 23 (1942), pp. 483–492.

[94] P. Grassberger, *Finite sample corrections to entropy and dimension estimates*, Physics Letters A, 128 (1988), pp. 369–373.

[95] P. Grassberger and I. Procaccia, *Estimation of the kolmogorov entropy from a chaotic signal*, Physical review A, 28 (1983), p. 2591.

[96] R. A. Gray, J. Jalife, A. V. Panfilov, W. T. Baxter, C. Cabo, J. M. Davidenko, A. M. Pertsov, P. Hogeweg, and A. T. Winfree, *Mechanisms of cardiac fibrillation*, Science, 270 (1995), pp. 1222–1226.

[97] R. A. Gray, A. M. Pertsov, and J. Jalife, *Correction: Spatial and temporal organization during cardiac fibrillation*, Nature, 393 (1998), p. 191.

[98] R. A. Gray, A. M. Pertsov, and J. Jalife, *Spatial and temporal organization during cardiac fibrillation*, Nature, 392 (1998), pp. 75–8.

[99] R. M. Gray, *Entropy and information theory*, Springer Science Business Media, 2011.

[100] N. Habel, P. Znojkiewicz, N. Thompson, J. G. Müller, B. Mason, J. Calame, S. Calame, S. Sharma, G. Mirchandani, and D. Janks, *The temporal variability of dominant frequency and complex fractionated atrial electrograms constrains the validity of sequential mapping in human atrial fibrillation*, Heart Rhythm, 7 (2010), pp. 586–593.

[101] M. Haissaguerre, M. Hocini, A. Denis, A. J. Shah, Y. Komatsu, S. Yamashita, M. Daly, S. Amraoui, S. Zellerhoff, and M.-Q. Picat, *Driver domains in persistent atrial fibrillation*, Circulation, (2014), p. CIRCULATIONAHA. 113.005421.

[102] M. Haissaguerre, P. Jaïs, D. C. Shah, A. Takahashi, M. Hocini, G. Quiniou, S. Garrigue, A. Le Mouroux, P. Le Métayer, and J. Clémenty, *Spontaneous initiation of atrial fibrillation by ectopic beats originating in the pulmonary veins*, New England Journal of Medicine, 339 (1998), pp. 659–666.

[103] M. Haissaguerre, A. J. Shah, H. Cochet, M. Hocini, R. Dubois, I. Efimov, E. Vigmond, O. Bernus, and N. Trayanova, *Intermittent drivers anchoring to structural heterogeneities as a major pathophysiological mechanism of human persistent atrial fibrillation*, The Journal of physiology, 594 (2016), pp. 2387–2398.

[104] J. D. Hamilton, *Time series analysis*, vol. 2, Princeton university press Princeton, NJ, 1994.

[105] J. Harte and E. A. Newman, *Maximum information entropy: a foundation for ecological theory*, Trends in ecology evolution, 29 (2014), pp. 384–389.

[106] R. M. Hayward, G. A. Upadhyay, T. Mela, P. T. Ellinor, C. D. Barrett, E. K. Heist, A. Verma, N. K. Choudhry, and J. P. Singh, *Pulmonary vein isolation with complex fractionated atrial electrogram ablation for paroxysmal and nonparoxysmal atrial fibrillation: a meta-analysis*, Heart Rhythm, 8 (2011), pp. 994–1000.

[107] M. Hinescu, M. Gherghiceanu, E. Mandache, S. M. Ciontea, and L. Popescu, *Interstitial cajal[U+2010]like cells (iclc) in atrial myocardium: ultrastructural and immunohistochemical characterization*, Journal of cellular and molecular medicine, 10 (2006), pp. 243–257.

[108] M. Hocini, S. Y. Ho, T. Kawara, A. C. Linnenbank, M. Potse, D. Shah, P. Jaïs, M. J. Janse, M. Haïssaguerre, and J. M. De Bakker, *Electrical conduction in canine pulmonary veins: electrophysiological and anatomic correlation*, Circulation, 105 (2002), pp. 2442–2448.

[109] C. W. Hogue, P. P. Domitrovich, P. K. Stein, G. D. Despotis, L. Re, R. B. Schuessler, R. E. Kleiger, and J. N. Rottman, *Rr interval dynamics before atrial fibrillation in patients after coronary artery bypass graft surgery*, Circulation, 98 (1998), pp. 429–434.

[110] M. Hwang, J.-S. Song, Y.-S. Lee, C. Li, E. B. Shim, and H.-N. Pak, *Electrophysiological rotor ablation in in-silico modeling of atrial fibrillation: comparisons with dominant frequency, shannon entropy, and phase singularity*, PloS one, 11 (2016), p. e0149695.

[111] P. A. Iaizzo, *Handbook of cardiac anatomy, physiology, and devices*, Springer Science Business Media, 2009.

[112] Z. Ilkan, B. Strauss, C. Campana, and F. G. Akar, *Optical Action Potential Mapping in Acute Models of Ischemia–Reperfusion Injury: Probing the Arrhythmogenic Role of the Mitochondrial Translocator Protein*, Springer, 2018, pp. 133–143.

[113] A. N. Iyer and R. A. Gray, *An experimentalist's approach to accurate localization of phase singularities during reentry*, Annals of biomedical engineering, 29 (2001), pp. 47–59.

[114] R. Jabbari, T. Engstrøm, C. Glinge, B. Risgaard, J. Jabbari, B. G. Winkel, C. J. Terkelsen, H. Tilsted, L. O. Jensen, and M. Hougaard, *Incidence and risk factors of ventricular fibrillation before primary angioplasty in patients with first st[U+2010]elevation myocardial infarction: a nationwide study in denmark*, Journal of the American Heart Association, 4 (2015), p. e001399.

[115] J. Jalife, *Ventricular fibrillation: mechanisms of initiation and maintenance*, Annual review of physiology, 62 (2000), pp. 25–50.

[116] ——, *Déjà vu in the theories of atrial fibrillation dynamics*, Cardiovascular Research, 89 (2011), pp. 766–775.

[117] J. Jalife, O. Berenfeld, and M. Mansour, *Mother rotors and fibrillatory conduction: a mechanism of atrial fibrillation*, Cardiovascular research, 54 (2002), pp. 204–216.

[118] J. Jalife, O. Berenfeld, A. Skanes, and R. Mandapati, *Mechanisms of atrial fibrillation: mother rotors or multiple daughter wavelets, or both?*, Journal of cardiovascular electrophysiology, 9 (1998), pp. S2–12.

[119] J. W. Jarman, T. Wong, P. Kojodjojo, H. Spohr, J. E. Davies, M. Roughton, D. P. Francis, P. Kanagaratnam, V. Markides, and D. W. Davies, *Spatiotemporal behavior of high dominant frequency during paroxysmal and persistent atrial fibrillation in the human left atrium*, Circulation: Arrhythmia and Electrophysiology, 5 (2012), pp. 650–658.

[120] E. T. Jaynes, *Information theory and statistical mechanics*, Physical review, 106 (1957), p. 620.

[121] M. E. Josephson, *Clinical cardiac electrophysiology: techniques and interpretations*, Lippincott Williams Wilkins, 2008.

[122] W. B. Kannel, P. A. Wolf, E. J. Benjamin, and D. Levy, *Prevalence, incidence, prognosis, and predisposing conditions for atrial fibrillation: population-based estimates 1*, The American Journal of Cardiology, 82 (1998), pp. 2N–9N.

[123] S. Karlin, *A first course in stochastic processes*, Academic press, 2014.

[124] M. W. Kay, G. P. Walcott, J. D. Gladden, S. B. Melnick, and J. M. Rogers, *Lifetimes of epicardial rotors in panoramic optical maps of fibrillating swine ventricles*, American Journal of Physiology-Heart and Circulatory Physiology, (2006).

[125] P. Kirchhof, S. Benussi, D. Kotecha, A. Ahlsson, D. Atar, B. Casadei, M. Castella, H.-C. Diener, H. Heidbuchel, J. Hendriks, et al., *2016 esc guidelines for the management of atrial fibrillation developed in collaboration with eacts*, European journal of cardio-thoracic surgery, 50 (2016), pp. e1–e88.

[126] L. Kleinrock, *Queueing systems, volume 2: Computer applications*, vol. 66, wiley New York, 1976.

[127] D. C. Knill and W. Richards, *Perception as Bayesian inference*, Cambridge University Press, 1996.

[128] N. L. Komarova, A. Sengupta, and M. A. Nowak, *Mutation–selection networks of cancer initiation: tumor suppressor genes and chromosomal instability*, Journal of theoretical biology, 223 (2003), pp. 433–450.

[129] K. Konings, C. Kirchhof, J. Smeets, H. Wellens, O. C. Penn, and M. A. Allessie, *High-density mapping of electrically induced atrial fibrillation in humans*, Circulation, 89 (1994), pp. 1665–1680.

[130] E. V. Koonin, L. Aravind, and A. S. Kondrashov, *The impact of comparative genomics on our understanding of evolution*, Cell, 101 (2000), pp. 573–576.

[131] C. A. Kowalewski, F. Shenasa, M. Rodrigo, P. Clopton, G. Meckler, M. I. Alhusseini, M. A. Swerdlow, V. Joshi, S. Hossainy, J. A. Zaman, et al., *Interaction of localized drivers and disorganized activation in persistent atrial fibrillation: Reconciling putative mechanisms using multiple mapping techniques*, Circulation: Arrhythmia and Electrophysiology, 11 (2018), p. e005846.

[132] K. Kośna, D. Steven, S. Willems, J. J. Żebrowski, and P. Kuklik, *Causality in atrial fibrillation determined by transfer entropy*, in Computing in Cardiology Conference (CinC), 2015, IEEE, pp. 909–912.

[133] I. L. Kron, B. B. Lerman, D. E. Haines, T. L. Flanagan, and J. P. DiMarco, *Coronary artery bypass grafting in patients with ventricular fibrillation*, The Annals of thoracic surgery, 48 (1989), pp. 85–89.

[134] D. Krummen, M. Anawati, D. Ahn, K. Peng, C. Briggs, and W. Rappel, *Correlation of electrical rotors and focal sources with sites of centrifugal stepdown in dominant frequency in human atrial fibrillation*, Heart Rhythm, 8 (2011), p. S176.

[135] P. Kuklik, S. Zeemering, B. Maesen, J. Maessen, H. J. Crijns, S. Verheule, A. N. Ganesan, and U. Schotten, *Reconstruction of instantaneous phase of unipolar*

atrial contact electrogram using a concept of sinusoidal recomposition and hilbert transform, IEEE transactions on biomedical engineering, 62 (2015), pp. 296–302.

[136] P. Kuklik, S. Zeemering, A. van Hunnik, B. Maesen, L. Pison, D. H. Lau, J. Maessen, P. Podziemski, C. Meyer, and B. Schäffer, *Identification of rotors during human atrial fibrillation using contact mapping and phase singularity detection: technical considerations*, IEEE Transactions on Biomedical Engineering, 64 (2017), pp. 310–318.

[137] K. Kumagai, C. Khrestian, and A. L. Waldo, *Simultaneous multisite mapping studies during induced atrial fibrillation in the sterile pericarditis model: insights into the mechanism of its maintenance*, Circulation, 95 (1997), pp. 511–521.

[138] S. S. Kuppahally, E. Foster, S. Shoor, and A. E. Steimle, *Short-term and long-term success of electrical cardioversion in atrial fibrillation in managed care system*, International Archives of Medicine, 2 (2009), pp. 39–39.

[139] C. Lafuente-Lafuente, S. Mouly, M. A. Longás-Tejero, I. Mahé, and J.-F. Bergmann, *Antiarrhythmic drugs for maintaining sinus rhythm after cardioversion of atrial fibrillation: a systematic review of randomized controlled trials*, Archives of internal medicine, 166 (2006), pp. 719–728.

[140] D. E. Lake and J. R. Moorman, *Accurate estimation of entropy in very short physiological time series: the problem of atrial fibrillation detection in implanted ventricular devices*, American Journal of Physiology-Heart and Circulatory Physiology, 300 (2010), pp. H319–H325.

[141] J. R. Landis and G. G. Koch, *The measurement of observer agreement for categorical data*, biometrics, (1977), pp. 159–174.

[142] S. Lazar, S. Dixit, F. E. Marchlinski, D. J. Callans, and E. P. Gerstenfeld, *Presence of left-to-right atrial frequency gradient in paroxysmal but not persistent atrial fibrillation in humans*, Circulation, 110 (2004), pp. 3181–3186.

[143] G. Lee, S. Kumar, A. Teh, A. Madry, S. Spence, M. Larobina, J. Goldblatt, R. Brown, V. Atkinson, and S. Moten, *Epicardial wave mapping in human long-lasting persistent atrial fibrillation: transient rotational circuits, complex wavefronts, and disorganized activity*, European heart journal, 35 (2013), pp. 86–97.

[144] J. Lee, D. McManus, and K. Chon, *Atrial fibrillation detection using time-varying coherence function and shannon entropy*, in 2011 Annual International Conference of the IEEE Engineering in Medicine and Biology Society, IEEE, 2011, pp. 4685–4688.

[145] S. Lee, J. Sahadevan, C. M. Khrestian, I. Cakulev, A. Markowitz, and A. L. Waldo, *Simultaneous biatrial high-density (510–512 electrodes) epicardial mapping of persistent and long-standing persistent atrial fibrillation in patients: new insights into the mechanism of its maintenance*, Circulation, 132 (2015), pp. 2108–2117.

[146] C. Li, B. Lim, M. Hwang, J.-S. Song, Y.-S. Lee, B. Joung, and H.-N. Pak, *The spatiotemporal stability of dominant frequency sites in in-silico modeling of 3-dimensional left atrial mapping of atrial fibrillation*, PloS one, 11 (2016), p. e0160017.

[147] Y.-J. Lin, M.-T. Lo, L.-W. Lo, F.-P. Chung, and S.-A. Chen, *Rotor mapping and ablation in persistent atrial fibrillation*, Cardiac Mapping, (2019), pp. 496–505.

[148] G. Y. Lip and D. G. Beevers, *Abc of atrial fibrillation. history, epidemiology, and importance of atrial fibrillation*, Bmj, 311 (1995), pp. 1361–3.

[149] L. A. Lipsitz, S. M. Pincus, R. J. Morin, S. Tong, L. P. Eberle, and P. M. Gootman, *Preliminary evidence for the evolution in complexity of heart rate dynamics during autonomic maturation in neonatal swine*, Journal of the autonomic nervous system, 65 (1997), pp. 1–9.

[150] O. Lombardi, F. Holik, and L. Vanni, *What is shannon information?*, Synthese, 193 (2016), pp. 1983–2012.

[151] B. Lown, J. Neuman, R. Amarasingham, and B. V. Berkovits, *Comparison of alternating current with direct current electroshock across the closed chest*, The American journal of cardiology, 10 (1962), pp. 223–233.

[152] D. Ludhwani and M. Jagtap, *Rhythm, Ventricular Fibrillation*, StatPearls Publishing, 2018.

[153] M. Lynch and J. S. Conery, *The evolutionary fate and consequences of duplicate genes*, Science, 290 (2000), pp. 1151–1155.

[154] J. Malmivuo and R. Plonsey, *Bioelectromagnetism: principles and applications of bioelectric and biomagnetic fields*, Oxford University Press, USA, 1995.

[155] R. Mandapati, A. Skanes, J. Chen, O. Berenfeld, and J. Jalife, *Stable microreentrant sources as a mechanism of atrial fibrillation in the isolated sheep heart*, Circulation, 101 (2000), pp. 194–199.

[156] N. F. Marrouche, D. Wilber, G. Hindricks, P. Jais, N. Akoum, F. Marchlinski, E. Kholmovski, N. Burgon, N. Hu, and L. Mont, *Association of atrial tissue fibrosis identified by delayed enhancement mri and atrial fibrillation catheter ablation: the decaaf study*, Jama, 311 (2014), pp. 498–506.

[157] L. M. Martyushev and V. D. Seleznev, *Maximum entropy production principle in physics, chemistry and biology*, Physics reports, 426 (2006), pp. 1–45.

[158] F. Masani, *Node-like cells in the myocardial layer of the pulmonary vein of rats: an ultrastructural study*, Journal of anatomy, 145 (1986), p. 133.

[159] M. Masè, L. Faes, R. Antolini, M. Scaglione, and F. Ravelli, *Quantification of synchronization during atrial fibrillation by shannon entropy: validation in patients and computer model of atrial arrhythmias*, Physiological measurement, 26 (2005), p. 911.

[160] M. M. Meerschaert and E. Scalas, *Coupled continuous time random walks in finance*, Physica A: Statistical Mechanics and its Applications, 370 (2006), pp. 114–118.

[161] G. R. Mines, *On circulating excitations in heart muscle and their possible relation to tachycardia and fibrillation*, Trans R Soc Can, 8 (1914), pp. 43–52.

[162] Y. Miyasaka, M. E. Barnes, B. J. Gersh, S. S. Cha, J. B. Seward, K. R. Bailey, T. Iwasaka, and T. S. Tsang, *Time trends of ischemic stroke incidence and mortality in patients diagnosed with first atrial fibrillation in 1980 to 2000*, Stroke, 36 (2005), pp. 2362–2366.

[163] G. Moe and J. Abildskov, *Atrial fibrillation as a self-sustaining arrhythmia independent of focal discharge*, American heart journal, 58 (1959), pp. 59–70.

[164] G. K. Moe, *On the multiple wavelet hypothesis of atrial fibrillation*, Arch Int Pharmacodyn Ther, 140 (1962), p. 183.

[165] G. K. Moe, W. C. Rheinboldt, and J. Abildskov, *A computer model of atrial fibrillation*, American heart journal, 67 (1964), pp. 200–220.

[166] K. Nademanee, J. McKenzie, E. Kosar, M. Schwab, B. Sunsaneewitayakul, T. Vasavakul, C. Khunnawat, and T. Ngarmukos, *A new approach for catheter ablation of atrial fibrillation: mapping of the electrophysiologic substrate*, Journal of the American College of Cardiology, 43 (2004), pp. 2044–2053.

[167] K. Nademanee and N. Oketani, *The role of complex fractionated atrial electrograms in atrial fibrillation ablation: moving to the beat of a different drum*, 2009.

[168] K. Nanthakumar, G. P. Walcott, S. Melnick, J. M. Rogers, M. W. Kay, W. M. Smith, R. E. Ideker, and W. Holman, *Epicardial organization of human ventricular fibrillation*, Heart Rhythm, 1 (2004), pp. 14–23.

[169] S. M. Narayan, D. E. Krummen, K. Shivkumar, P. Clopton, W.-J. Rappel, and J. M. Miller, *Treatment of atrial fibrillation by the ablation of localized sources: Confirm (conventional ablation for atrial fibrillation with or without focal impulse and rotor modulation) trial*, Journal of the American College of Cardiology, 60 (2012), pp. 628–636.

[170] M. P. Nash, A. Mourad, R. H. Clayton, P. M. Sutton, C. P. Bradley, M. Hayward, D. J. Paterson, and P. Taggart, *Evidence for multiple mechanisms in human ventricular fibrillation*, Circulation, 114 (2006), pp. 536–542.

[171] S. Nattel, *New ideas about atrial fibrillation 50 years on*, Nature, 415 (2002), p. 219.

[172] S. Nattel and D. Dobrev, *Controversies about atrial fibrillation mechanisms: aiming for order in chaos and whether it matters*, Circulation research, 120 (2017), pp. 1396–1398.

[173] J. C. Nelson, M. P. Griffin, and J. R. Moorman, *Probing the order within neonatal heart rate variability*, Pediatric research, 43 (1998), p. 823.

[174] J. Ng, A. H. Kadish, and J. J. Goldberger, *Effect of electrogram characteristics on the relationship of dominant frequency to atrial activation rate in atrial fibrillation*, Heart Rhythm, 3 (2006), pp. 1295–1305.

[175] M. A. Nielsen and I. Chuang, *Quantum computation and quantum information*, 2002.

[176] R. Nieuwlaat, M. H. Prins, J.-Y. Le Heuzey, P. E. Vardas, E. Aliot, M. Santini, S. M. Cobbe, J. W. Widdershoven, L. H. Baur, and S. Lévy, *Prognosis, disease progression, and treatment of atrial fibrillation patients during 1 year: follow-up of the euro heart survey on atrial fibrillation*, European heart journal, (2008).

[177] S. F. Noujaim, D. S. Auerbach, and J. Jalife, *Ventricular fibrillation*, Circulation journal, 71 (2007), pp. A1–A11.

[178] A. S. Novozhilov, G. P. Karev, and E. V. Koonin, *Biological applications of the theory of birth-and-death processes*, Briefings in bioinformatics, 7 (2006), pp. 70–85.

[179] M. A. Nowak, F. Michor, N. L. Komarova, and Y. Iwasa, *Evolutionary dynamics of tumor suppressor gene inactivation*, Proceedings of the National Academy of Sciences, 101 (2004), pp. 10635–10638.

[180] H. Ocak, *Automatic detection of epileptic seizures in eeg using discrete wavelet transform and approximate entropy*, Expert Systems with Applications, 36 (2009), pp. 2027–2036.

[181] T. G. Oesterlein, M. W. Keller, S. Schuler, A. Luik, M. Krüger, G. Seemann, G. Seemann, C. Schmitt, and O. Dössel, *Determination of local activation time in bipolar endocardial electrograms: a comparison of clinical criteria and a new method based on the non-linear energy operator*, Journal of Electrocardiology, 46, p. e18.

[182] S. Ohno, *Evolution by gene duplication. berlin, new york: Springer-verlag.*, xv, 160 p, (1970).

[183] A. V. Oppenheim and G. C. Verghese, *Signals, systems and inference*, Pearson, 2015.

[184] H. Oral, A. Chugh, E. Good, T. Crawford, J. F. Sarrazin, M. Kuhne, N. Chalfoun, D. Wells, W. Boonyapisit, and N. Gadeela, *Randomized evaluation of right atrial ablation after left atrial ablation of complex fractionated atrial electrograms for long-lasting persistent atrial fibrillation*, Circulation: Arrhythmia and Electrophysiology, 1 (2008), pp. 6–13.

[185] H. Oral, A. Chugh, E. Good, A. Wimmer, S. Dey, N. Gadeela, S. Sankaran, T. Crawford, J. F. Sarrazin, and M. Kuhne, *Radiofrequency catheter ablation of*

chronic atrial fibrillation guided by complex electrograms, Circulation, 115 (2007), pp. 2606–2612.

[186] H. Oral, A. Chugh, K. Yoshida, J. F. Sarrazin, M. Kuhne, T. Crawford, N. Chalfoun, D. Wells, W. Boonyapisit, and S. Veerareddy, *A randomized assessment of the incremental role of ablation of complex fractionated atrial electrograms after antral pulmonary vein isolation for long-lasting persistent atrial fibrillation*, Journal of the American College of Cardiology, 53 (2009), pp. 782–789.

[187] H. Oral, B. P. Knight, H. Tada, M. O¨zaydin, A. Chugh, S. Hassan, C. Scharf, S. W. Lai, R. Greenstein, and F. Pelosi Jr, *Pulmonary vein isolation for paroxysmal and persistent atrial fibrillation*, Circulation, 105 (2002), pp. 1077–1081.

[188] A. Orozco-Duque, J. P. Ugarte, C. Tobón, J. Saiz, and J. Bustamante, *Approximate entropy can localize rotors, but not ectopic foci during chronic atrial fibrillation: A simulation study*, in Computing in Cardiology Conference (CinC), 2013, IEEE, pp. 903–906.

[189] A. Ott, M. M. Breteler, M. C. de Bruyne, F. van Harskamp, D. E. Grobbee, and A. Hofman, *Atrial fibrillation and dementia in a population-based study*, Stroke, 28 (1997), pp. 316–321.

[190] D. L. Packer, D. B. Mark, R. A. Robb, K. H. Monahan, T. D. Bahnson, K. Moretz, J. E. Poole, A. Mascette, Y. Rosenberg, N. Jeffries, et al., *Catheter ablation versus antiarrhythmic drug therapy for atrial fibrillation (cabana) trial: study rationale and design*, American heart journal, 199 (2018), pp. 192–199.

[191] J. Pan and W. J. Tompkins, *A real-time qrs detection algorithm*, IEEE Trans. Biomed. Eng, 32 (1985), pp. 230–236.

[192] S. V. Pandit and J. Jalife, *Rotors and the dynamics of cardiac fibrillation*, Circulation research, 112 (2013), pp. 849–862.

[193] A. Panfilow and A. Pertsov, *Ventricular fibrillation: evolution of the multiple–wavelet hypothesis*, Philosophical Transactions of the Royal Society of London. Series A: Mathematical, Physical and Engineering Sciences, 359 (2001), pp. 1315–1325.

[194] S. M. Pincus, *Approximate entropy as a measure of system complexity*, Proceedings of the National Academy of Sciences, 88 (1991), pp. 2297–2301.

[195] E. S. Platou and H. Refsum, *Class iii antiarrhythmic action in experimental atrial fibrillation and flutter in dogs*, Journal of cardiovascular pharmacology, 4 (1982), pp. 839–846.

[196] M. Porter, W. Spear, J. G. Akar, R. Helms, N. Brysiewicz, P. Santucci, and D. J. Wilber, *Prospective study of atrial fibrillation termination during ablation guided by automated detection of fractionated electrograms*, Journal of cardiovascular electrophysiology, 19 (2008), pp. 613–620.

[197] S. Purwani, J. Nahar, and C. Twining, *Analyzing bin-width effect on the computed entropy*, in AIP Conference Proceedings, vol. 1868, AIP Publishing, p. 040008.

[198] S. Puwal, B. J. Roth, and D. Garfinkle, *Spherical topology in cardiac simulations*, HFSP journal, 3 (2009), pp. 124–129.

[199] Z. Qu, J. N. Weiss, and A. Garfinkel, *Spatiotemporal chaos in a simulated ring of cardiac cells*, Physical review letters, 78 (1997), p. 1387.

[200] ——, *Cardiac electrical restitution properties and stability of reentrant spiral waves: a simulation study*, American Journal of Physiology-Heart and Circulatory Physiology, 276 (1999), pp. H269–H283.

[201] A. Ratnaparkhi, *A simple introduction to maximum entropy models for natural language processing*, IRCS Technical Reports Series, (1997), p. 81.

[202] S. I. Resnick, *Adventures in stochastic processes*, Springer Science Business Media, 2013.

[203] J. S. Richman, D. E. Lake, and J. R. Moorman, *Sample entropy*, Methods in enzymology, 384 (2004), pp. 172–184.

[204] J. S. Richman and J. R. Moorman, *Physiological time-series analysis using approximate entropy and sample entropy*, American Journal of Physiology-Heart and Circulatory Physiology, 278 (2000), pp. H2039–H2049.

[205] C. H. Roney, J. D. Bayer, S. Zahid, M. Meo, P. M. Boyle, N. A. Trayanova, M. Haïssaguerre, R. Dubois, H. Cochet, and E. J. Vigmond, *Modelling methodology of atrial fibrosis affects rotor dynamics and electrograms*, EP Europace, 18 (2016), pp. iv146–iv155.

[206] S. M. Ross, J. J. Kelly, R. J. Sullivan, W. J. Perry, D. Mercer, R. M. Davis, T. D. Washburn, E. V. Sager, J. B. Boyce, and V. L. Bristow, *Stochastic processes*, vol. 2, Wiley New York, 1996.

[207] O. A. Rosso, S. Blanco, J. Yordanova, V. Kolev, A. Figliola, M. Schürmann, and E. Başar, *Wavelet entropy: a new tool for analysis of short duration brain electrical signals*, Journal of neuroscience methods, 105 (2001), pp. 65–75.

[208] S. M. Ryan, A. L. Goldberger, S. M. Pincus, J. Mietus, and L. A. Lipsitz, *Gender- and age-related differences in heart rate dynamics: are women more complex than men?*, Journal of the American College of Cardiology, 24 (1994), pp. 1700–1707.

[209] J. Ródenas, M. García, R. Alcaraz, and J. J. Rieta, *Wavelet entropy automatically detects episodes of atrial fibrillation from single-lead electrocardiograms*, Entropy, 17 (2015), pp. 6179–6199.

[210] B. Sakmann, *Single-channel recording*, Springer Science & Business Media, 2013.

[211] P. Sanders, O. Berenfeld, M. Hocini, P. Jaïs, R. Vaidyanathan, L.-F. Hsu, S. Garrigue, Y. Takahashi, M. Rotter, and F. Sacher, *Spectral analysis identifies sites of high-frequency activity maintaining atrial fibrillation in humans*, Circulation, 112 (2005), pp. 789–797.

[212] D. Scherr, D. Dalal, A. Cheema, A. Cheng, C. A. Henrikson, D. Spragg, J. E. Marine, R. D. Berger, H. Calkins, and J. Dong, *Automated detection and characterization of complex fractionated atrial electrograms in human left atrium during atrial fibrillation*, Heart Rhythm, 4 (2007), pp. 1013–1020.

[213] E. Schneidman, M. J. Berry II, R. Segev, and W. Bialek, *Weak pairwise correlations imply strongly correlated network states in a neural population*, Nature, 440 (2006), p. 1007.

[214] U. Schotten, S. Verheule, P. Kirchhof, and A. Goette, *Pathophysiological mechanisms of atrial fibrillation: a translational appraisal*, Physiological reviews, 91 (2011), pp. 265–325.

[215] T. Schreiber, *Measuring information transfer*, Physical review letters, 85 (2000), p. 461.

[216] S. A. C. Schuckers, *Use of approximate entropy measurements to classify ventricular tachycardia and fibrillation*, Journal of electrocardiology, 31 (1998), pp. 101–105.

[217] R. B. Schuessler, T. M. Grayson, B. I. Bromberg, J. L. Cox, and J. P. Boineau, *Cholinergically mediated tachyarrhythmias induced by a single extrastimulus in the isolated canine right atrium*, Circulation research, 71 (1992), pp. 1254–1267.

[218] J. Seitz, C. Bars, G. Théodore, S. Beurtheret, N. Lellouche, M. Bremondy, A. Ferracci, J. Faure, G. Penaranda, and M. Yamazaki, *Af ablation guided by spatiotemporal electrogram dispersion without pulmonary vein isolation: a wholly patient-tailored approach*, Journal of the American College of Cardiology, 69 (2017), pp. 303–321.

[219] C. E. Shannon, *A mathematical theory of communication*, Bell system technical journal, 27 (1948), pp. 379–423.

[220] M. Shenasa, G. Hindricks, D. J. Callans, J. M. Miller, and M. E. Josephson, *Cardiac mapping*, Wiley Online Library, 2003.

[221] L. Sherwood, *Human physiology: from cells to systems*, Cengage learning, 2015.

[222] D.-G. Shin, C.-S. Yoo, S.-H. Yi, J.-H. Bae, Y.-J. Kim, J.-S. Park, and G.-R. Hong, *Prediction of paroxysmal atrial fibrillation using nonlinear analysis of the rr interval dynamics before the spontaneous onset of atrial fibrillation*, Circulation Journal, 70 (2006), pp. 94–99.

[223] S. Shkurovich, A. V. Sahakian, and S. Swiryn, *Detection of atrial activity from high-voltage leads of implantable ventricular defibrillators using a cancellation technique*, IEEE Transactions on Biomedical Engineering, 45 (1998), pp. 229–234.

[224] S. Sibisi, J. Skilling, R. G. Brereton, E. D. Laue, and J. Staunton, *Maximum entropy signal processing in practical nmr spectroscopy*, Nature, 311 (1984), p. 446.

[225] A. C. Skanes, R. Mandapati, O. Berenfeld, J. M. Davidenko, and J. Jalife, *Spatiotemporal periodicity during atrial fibrillation in the isolated sheep heart*, Circulation, 98 (1998), pp. 1236–1248.

[226] R. S. Snell, *Clinical anatomy: an illustrated review with questions and explanations*, Lippincott Williams Wilkins, 2004.

[227] J. S. Steinberg, Y. Shah, A. Bhatt, T. Sichrovsky, A. Arshad, E. Hansinger, and D. Musat, *Focal impulse and rotor modulation: acute procedural observations and extended clinical follow-up*, Heart Rhythm, 14 (2017), pp. 192–197.

[228] W. G. Stevenson and K. Soejima, *Recording techniques for clinical electrophysiology*, Journal of cardiovascular electrophysiology, 16 (2005), pp. 1017–1022.

[229] R. Sungnoon, S. Muengtaweepongsa, P. Kitipawong, K. Suwanprasert, and T. Ngarmukos, *Increased sample entropy in atrial fibrillation relates to cardiac autonomic dysfunction determined by heart rate variability: a preliminary study*, in Biomedical Engineering International Conference (BMEiCON), 2012, IEEE, pp. 1–4.

[230] A. Suzuki and H. Konno, *Stochastic dynamics of phase singularities under ventricular fibrillation in 2d beeler-reuter model*, AIP Advances, 1 (2011), p. 032103.

[231] U. B. Tedrow and W. G. Stevenson, *Recording and interpreting unipolar electrograms to guide catheter ablation*, Heart Rhythm, 8 (2011), pp. 791–796.

[232] K. H. Ten Tusscher and A. V. Panfilov, *Alternans and spiral breakup in a human ventricular tissue model*, American Journal of Physiology-Heart and Circulatory Physiology, 291 (2006), pp. H1088–H1100.

[233] P. Thoft-Cristensen and M. J. Baker, *Structural reliability theory and its applications*, Springer Science & Business Media, 2012.

[234] M. P. Tulppo, T. Makikallio, T. Takala, T. Seppanen, and H. V. Huikuri, *Quantitative beat-to-beat analysis of heart rate dynamics during exercise*, American journal of physiology-heart and circulatory physiology, 271 (1996), pp. H244–H252.

[235] V. Tuzcu, S. Nas, T. Börklü, and A. Ugur, *Decrease in the heart rate complexity prior to the onset of atrial fibrillation*, Europace, 8 (2006), pp. 398–402.

[236] J. P. Ugarte, A. Orozco-Duque, C. Tobón, V. Kremen, D. Novak, J. Saiz, T. Oesterlein, C. Schmitt, A. Luik, and J. Bustamante, *Dynamic approximate entropy electroanatomic maps detect rotors in a simulated atrial fibrillation model*, PloS one, 9 (2014), p. e114577.

[237] K. Umapathy, K. Nair, S. Masse, S. Krishnan, J. Rogers, M. P. Nash, and K. Nanthakumar, *Phase mapping of cardiac fibrillation*, Circulation: Arrhythmia and Electrophysiology, 3 (2010), pp. 105–114.

[238] S. Vajapeyam, *Understanding shannon's entropy metric for information*, arXiv preprint arXiv:1405.2061, (2014).

[239] A. Vakkuri, A. Yli[U+2010]Hankala, P. Talja, S. Mustola, H. Tolvanen[U+2010]Laakso, T. Sampson, and H. Viertiö[U+2010]Oja, *Time[U+2010]frequency balanced spectral entropy as a measure of anesthetic drug effect in central nervous system during sevoflurane, propofol, and thiopental anesthesia*, Acta Anaesthesiologica Scandinavica, 48 (2004), pp. 145–153.

[240] J. F. Valencia, A. Porta, M. Vallverdu, F. Claria, R. Baranowski, E. Orlowska-Baranowska, and P. Caminal, *Refined multiscale entropy: Application to 24-h holter recordings of heart period variability in healthy and aortic stenosis subjects*, IEEE Transactions on Biomedical Engineering, 56 (2009), pp. 2202–2213.

[241] L. J. van der Does, C. Kik, A. J. Bogers, M. A. Allessie, and N. M. de Groot, *Dynamics of endo-and epicardial focal fibrillation waves at the right atrium in a patient with advanced atrial remodelling*, Canadian Journal of Cardiology, 32 (2016), pp. 1260. e19–1260. e21.

[242] I. C. Van Gelder, H. J. Crijns, R. G. Tieleman, J. Brügemann, P. J. De Kam, A. M. Gosselink, F. W. Verheugt, and K. I. Lie, *Chronic atrial fibrillation: success of serial cardioversion therapy and safety of oral anticoagulation*, Archives of Internal Medicine, 156 (1996), pp. 2585–2592.

[243] I. C. Van Gelder, H. J. Crijns, W. H. Van Gilst, R. Verwer, and K. I. Lie, *Prediction of uneventful cardioversion and maintenance of sinus rhythm from direct-current electrical cardioversion of chronic atrial fibrillation and flutter*, The American journal of cardiology, 68 (1991), pp. 41–46.

[244] M. Vaquero, D. Calvo, and J. Jalife, *Cardiac fibrillation: from ion channels to rotors in the human heart*, Heart rhythm, 5 (2008), pp. 872–879.

[245] R. Ventura, T. Rostock, H. U. Klemm, B. Lutomsky, C. Demir, C. Weiss, T. Meinertz, and S. Willems, *Catheter ablation of common-type atrial flutter guided by three-dimensional right atrial geometry reconstruction and catheter tracking using cutaneous patches: A randomized prospective study*, Journal of cardiovascular electrophysiology, 15 (2004), pp. 1157–1161.

[246] S. Verdu, *Fifty years of shannon theory*, IEEE Transactions on information theory, 44 (1998), pp. 2057–2078.

[247] S. Verheule, E. E. Wilson, R. Arora, S. K. Engle, L. R. Scott, and J. E. Olgin, *Tissue structure and connexin expression of canine pulmonary veins*, Cardiovascular research, 55 (2002), pp. 727–738.

[248] A. Verma, C.-y. Jiang, T. R. Betts, J. Chen, I. Deisenhofer, R. Mantovan, L. Macle, C. A. Morillo, W. Haverkamp, and R. Weerasooriya, *Approaches to catheter ablation for persistent atrial fibrillation*, New England Journal of Medicine, 372 (2015), pp. 1812–1822.

[249] A. Verma, D. Lakkireddy, Z. Wulffhart, J. Pillarisetti, D. Farina, M. Beardsall, B. Whaley, D. Giewercer, B. Tsang, and Y. Khaykin, *Relationship between complex fractionated electrograms (cfe) and dominant frequency (df) sites and prospective assessment of adding df[U+2010]guided ablation to pulmonary vein isolation in persistent atrial fibrillation (af)*, Journal of cardiovascular electrophysiology, 22 (2011), pp. 1309–1316.

[250] A. Verma, P. Novak, L. Macle, B. Whaley, M. Beardsall, Z. Wulffhart, and Y. Khaykin, *A prospective, multicenter evaluation of ablating complex fractionated electrograms (cfes) during atrial fibrillation (af) identified by an automated mapping algorithm: acute effects on af and efficacy as an adjuvant strategy*, Heart rhythm, 5 (2008), pp. 198–205.

[251] A. Verma, P. Sanders, J. Champagne, L. Macle, G. M. Nair, H. Calkins, and D. J. Wilber, *Selective complex fractionated atrial electrograms targeting for atrial fibrillation study (select af)*, Circulation: Arrhythmia and Electrophysiology, 7 (2014), pp. 55–62.

[252] R. Vicente, M. Wibral, M. Lindner, and G. Pipa, *Transfer entropy—a model-free measure of effective connectivity for the neurosciences*, Journal of computational neuroscience, 30 (2011), pp. 45–67.

[253] S. Vikman, T. H. Mäkikallio, S. Yli-Mäyry, S. Pikkujämsä, A.-M. Koivisto, P. Reinikainen, K. J. Airaksinen, and H. V. Huikuri, *Altered complexity and correlation properties of rr interval dynamics before the spontaneous onset of paroxysmal atrial fibrillation*, Circulation, 100 (1999), pp. 2079–2084.

[254] J. W. Waks and M. E. Josephson, *Mechanisms of atrial fibrillation–reentry, rotors and reality*, Arrhythmia electrophysiology review, 3 (2014), p. 90.

[255] T. J. Wang, M. G. Larson, D. Levy, R. S. Vasan, E. P. Leip, P. A. Wolf, R. B. D'Agostino, J. M. Murabito, W. B. Kannel, and E. J. Benjamin, *Temporal relations of atrial fibrillation and congestive heart failure and their joint influence on mortality*, Circulation, 107 (2003), pp. 2920–2925.

[256] J. G. Webster and J. W. Clark, *Medical instrumentation: application and design*, vol. 200, John Wiley Sons, 1995.

[257] P. Welch, *The use of fast fourier transform for the estimation of power spectra: a method based on time averaging over short, modified periodograms*, IEEE Transactions on audio and electroacoustics, 15 (1967), pp. 70–73.

[258] J. L. Wells, R. B. Karp, N. T. Kouchoukos, W. A. Maclean, T. N. James, and A. L. Waldo, *Characterization of atrial fibrillation in man: studies following open heart surgery*, Pacing and clinical electrophysiology, 1 (1978), pp. 426–438.

[259] R. H. Whitaker, *Anatomy of the heart*, Medicine, 34 (2006), pp. 163–165.

[260] C. J. Wiggers, *The mechanism and nature of ventricular fibrillation*, American Heart Journal, 20 (1940), pp. 399–412.

[261] F. N. Wilson, A. G. Macleod, and P. S. Barker, *The potential variations produced by the heart beat at the apices of einthoven's triangle*, American Heart Journal, 7 (1931), pp. 207–211.

[262] A. Winfree, *Electrical turbulence in three-dimensional heart muscle*, Science, 266 (1994), pp. 1003–1006.

[263] A. T. Winfree, *Spiral waves of chemical activity*, Science, 175 (1972), pp. 634–636.

[264] ——, *When time breaks down: the three-dimensional dynamics of electrochemical waves and cardiac arrhythmias*, vol. 14, Princeton University Press Princeton, 1987.

[265] A. M. Wink and J. B. Roerdink, *Denoising functional mr images: a comparison of wavelet denoising and gaussian smoothing*, IEEE transactions on medical imaging, 23 (2004), pp. 374–387.

[266] F. X. Witkowski, L. J. Leon, P. A. Penkoske, W. R. Giles, M. L. Spano, W. L. Ditto, and A. T. Winfree, *Spatiotemporal evolution of ventricular fibrillation*, Nature, 392 (1998), p. 78.

[267] P. A. Wolf, R. D. Abbott, and W. B. Kannel, *Atrial fibrillation as an independent risk factor for stroke: the framingham study*, Stroke, 22 (1991), pp. 983–988.

[268] P. A. Wolf, J. B. Mitchell, C. S. Baker, W. B. Kannel, and R. B. D'agostino, *Impact of atrial fibrillation on mortality, stroke, and medical costs*, Archives of internal medicine, 158 (1998), pp. 229–234.

[269] C. X. Wong, A. Brown, D. H. Lau, S. S. Chugh, C. M. Albert, J. M. Kalman, and P. Sanders, *Epidemiology of sudden cardiac death: global and regional perspectives*, Heart, Lung and Circulation, 28 (2019), pp. 6–14.

[270] S. H. Wright, *Generation of resting membrane potential*, Advances in physiology education, 28 (2004), pp. 139–142.

[271] S.-D. Wu, C.-W. Wu, S.-G. Lin, C.-C. Wang, and K.-Y. Lee, *Time series analysis using composite multiscale entropy*, Entropy, 15 (2013), pp. 1069–1084.

[272] D. G. Wyse and B. J. Gersh, *Atrial fibrillation: a perspective: thinking inside and outside the box*, Circulation, 109 (2004), pp. 3089–3095.

[273] W. Xiong, L. Faes, and P. C. Ivanov, *Entropy measures, entropy estimators, and their performance in quantifying complex dynamics: Effects of artifacts, nonstationarity, and long-range correlations*, Physical Review E, 95 (2017), p. 062114.

[274] J. M. Yentes, N. Hunt, K. K. Schmid, J. P. Kaipust, D. McGrath, and N. Stergiou, *The appropriate use of approximate entropy and sample entropy with short data sets*, Annals of biomedical engineering, 41 (2013), pp. 349–365.

[275] L. A. Zadeh, *Fuzzy logic= computing with words*, in Computing with Words in Information/Intelligent Systems 1, Springer, 1999, pp. 3–23.

[276] W. Zeng and L. Glass, *Statistical properties of heartbeat intervals during atrial fibrillation*, Physical Review E, 54 (1996), p. 1779.

[277] Y.-C. Zhang, *Complexity and 1/f noise. a phase space approach*, Journal de Physique I, 1 (1991), pp. 971–977.

[278] X. Zhou, H. Ding, B. Ung, E. Pickwell-MacPherson, and Y. Zhang, *Automatic online detection of atrial fibrillation based on symbolic dynamics and shannon entropy*, Biomedical engineering online, 13 (2014), p. 18.

[279] D. P. Zipes and J. JalitTe, *Cardiac electrophysiology from cell to bedside, 2nd*, (1989).